UNIVERSITÀ DEGLI STUDI DI NAPOLI FEDERICO II

Department of Civil, Building and Environmental Engineering

Ph.D. in Civil Systems Engineering

XXXVI Cycle

Sara Tuozzo

WAVE OVERTOPPING OF VERTICAL SEAWALLS IN THE SURF ZONE

Ph.D Coordinator:

Prof. Andrea Papola

Tutor:

Prof. Mariano Buccino

ABSTRACT

The present Thesis analyzed in depth the wave overtopping of vertical walls in the surf zone. Seawalls are evergreen solutions commonly adopted to protect assets from coastal risks, such as flooding. The wave overtopping, hence, is an essential phenomenon to account for in designing coastal structures to guarantee their efficacy in protecting coastal zones from flooding risks.

However, even though wave overtopping is one of the main issues in the coastal scientific community, a critical review of the literature has revealed that our knowledge about the overtopping of seawalls in shallow water is still rough and unaccomplished. In particular, a few reliable data on the overtopping of vertical walls in the surf zone are available in the literature.

The work, hence, moves from these shortcomings and aims to fill this gap through a combined analysis of experimental and numerical data.

The study firstly analyzes the laboratory data of an experimental campaign carried out at the University of Naples Federico II that have been also numerically reproduced via the non-hydrostatic model, SWASH, and the CFD-RANS model, FLOW-3D. On one hand, such analysis has shown that the phase-resolving models can capture, to a good extent, the physical processes (despite different levels of accuracy) and, thus, they significantly contribute to extending our comprehension of the wave overtopping in the surf-zone. On the other hand, the joint laboratory and numerical analysis has shed some light on the hydraulic variables that influence the wave overtopping in the surf zone.

Specifically, the results have revealed that, unlike the literature assumption, the wave overtopping process of vertical walls does not depend on the wave energy distribution in the frequency domain but on the wave displacement distribution at the toe of the wall. Therefore, a new hydraulic variable has been introduced, which expresses the influence of the upper tail of the distribution on wave overtopping.

Consequently, the work has attempted to provide a new overtopping model based on this hydraulic variable. To this end, an extensive parametric study has been carried out via SWASH; indeed, using a numerical model allowed the experimental conditions to vary smoothly, thus creating a wide and varied dataset and avoiding the typical limitation of laboratory experiments.

The numerical investigation has ensured the identification of the main variables involved in the wave overtopping process, and thus, a new overtopping parametrization has been proposed. According to the new parametrization, a predictive model has been inferred from the numerical data.

Numerical findings have been verified against 270 laboratory data from different datasets, including 70 physical model tests performed in this work to examine the wave overtopping of seawalls with very and extremely shallow foreshores and fill the void found in the literature.

According to the numerical findings, the laboratory data follow a unique trend and exhibit a uniform behavior, demonstrating the large explanatory power of the new parametrization introduced.

Finally, the work provides a unique generalized formula for estimating the wave overtopping of seawalls in shallow water, valid for both breaking and non-breaking waves.

The last phase of the work has investigated the wind effect on wave overtopping at vertical seawalls in shallow water. By gathering numerical and laboratory data provided by the literature, this study provides a new empirical formula to quantify the flow rate enhancement due to the presence of the wind.

RIASSUNTO

Il presente lavoro di tesi analizza il fenomeno di wave overtopping di muri verticali nella surf-zone. I seawall sono da sempre tra le soluzioni più adottate per proteggere le aree costiere dai rischi legati all'azione del moto ondoso, tra cui quello di inondazioni. È dunque fondamentale tener conto del fenomeno di overtopping nelle fasi progettuali dell'opera, così da garantirne l'efficacia in termini di protezione dalle inondazioni.

Tuttavia, sebbene si tratti di uno dei fenomeni di maggiore interesse per la comunità scientifica, un'analisi critica della letteratura ha evidenziato come la nostra conoscenza sul processo di tracimazione di seawall in acque basse presenti, in realtà, molte incertezze a causa della mancanza di dati sperimentali affidabili che permettano di comprendere più a fondo il fenomeno.

Ricostruito tale stato dell'arte, il lavoro di tesi si propone di colmare alcune delle lacune emerse dalla letteratura scientifica, utilizzando un'analisi combinata di dati sperimentali e di dati numerici.

In particolare, lo studio parte dall'analisi di una campagna sperimentale condotta presso l'Università degli Studi di Napoli Federico II, i cui esperimenti sono stati riprodotti numericamente mediante due diversi modelli risolti in fase: un modello che integra le equazioni di Navier-Stokes mediate alla Reynolds (RANS) ed un modello a pressione non idrostatica, SWASH. La combinazione di dati sperimentali e numerici ha permesso, da un lato, di apprezzare la capacità dei due modelli di catturare la fisica del fenomeno, seppure con due diversi gradi di accuratezza, e, dall'altro, di fare maggiore chiarezza riguardo l'influenza di diverse variabili idrauliche sulla portata di overtopping.
In particolare, la tracimazione delle strutture non dipende dalla distribuzione dell'energia nel dominio delle frequenze, bensì dalla distribuzione dell'oscillazione ondosa al piede dell'opera nel dominio del tempo. È stata quindi introdotta una nuova variabile idrauliche che esprime l'effetto della coda più alta della distribuzione sulla portata di tracimazione.

Il riscontro di quanto emerso è stato approfondito con un'approfondita indagine sperimentale mediante il modello numerico SWASH. L'utilizzo di un modello numerico permette, infatti, di variare con facilità le caratteristiche geometriche ed idrauliche rispetto alla modellazione fisica, creando così un vasto e vario dataset. Lo studio numerico ha quindi permesso di indentificare le variabili chiave per la stima della portata di overtopping in acque basse, e, sulla base di queste, di introdurre una nuova parametrizzazione. Dai dati numerici è stata ricavata, inoltre, una formula generale di predizione della portata di overtopping per seawall in acque basse.

Per confermare ed avvalorare i risultati numerici, sono stati utilizzati circa 270 dati di laboratorio appartenenti a diversi dataset. Di questi, 70 dati sono il frutto dell'attività sperimentale, svolta nell'ambito di questo lavoro di tesi, volta ad analizzare la tracimazione di muri verticali in acque estremamente basse.

I dati di laboratori hanno confermato i risultati osservati nel corso della campagna sperimentale numerica, facendo emergere il forte potere esplicativo della nuova parametrizzazione introdotta. Le formule di previsione

derivate dai dati numerici sono state, infine, ricalibrate sulla base dei dati sperimentali, ottenendo così una formula empirica generale per i muri in acqua basse, valida sia per condizioni impulsive che non impulsive.

L'ultima fase del lavoro, infine, si è concentrata sullo studio dell'influenza del vento sul fenomeno di overtopping. In ultimo, utilizzando dati numerici e di laboratorio forniti dalla letteratura, è stata ricavata una formula per la stima dell'effetto del vento sulla portata media di tracimazione.

Acknowledgements

I would like to express my gratitude to those whose support and guidance have been instrumental in the completion of this doctoral thesis. My profound gratitude goes to Professor Mariano Buccino, his enthusiasm and competence deeply inspired and encouraged my progresses.

I sincerely thank Professor Mario Calabrese for his availability and openness and the suggestions provided.

I am grateful to Angela Di Leo for her helping hand and sound advice during this journey.

11th March 2024, Naples Sara

Table of Contents

List of Figures

List of Tables

1. INTRODUCTION

1.1. Research context

Coastal areas are the meeting place between sea and land, and thus, they have always been vulnerable. One of the main issues for coastal engineers is, therefore, protecting people, infrastructures and properties that populate coastal zones. Among the risks that affect the shore, engineers have to face the wave-induced flooding. Sea defense structures, such as seawalls or dikes, are used to hinder the wave action and reduce the inundation.

Wave overtopping is, hence, an essential process in designing coastal structures, as underlined by the large body of literature that has dealt with this phenomenon over the last century; from the pioneering work of Saville (1955), to the crucial works of Goda et al. (1975) and Owen (1980), up to the significant EU-funded project CLASH (Crest Level Assessment of Coastal Structures by Full-scale Monitoring, Neural Network Prediction and Hazard Analysis on Permissible Wave Overtopping), wave overtopping has a leading role for coastal scientific community.

Despite the literature's efforts and progress, the ongoing interest in wave overtopping demonstrates that many aspects need to be clarified. The present work will highlight and concern some of them.

Specifically, this study focuses on vertical seawalls, an evergreen solution for preventing coastal risks and protecting assets from wave action (Allsop et al., 2005; Kraus and McDougal, 1996). These coastal defenses are common in urban landscapes since they require little space and can be placed on the backshore, reducing the aesthetic and environmental impact and avoiding alteration of the nearshore circulation.

1.2. Background and research aims

The wave overtopping is typically described through different parameters that allow coastal engineers to assess flooding-related risks and damages. These parameters include the mean overtopping discharge, q, the maximum individual overtopping volume, V_{MAX}, the overtopping flow velocity and thickness over the structure (or the leeward slope). Although the overtopping volume and the flow velocity and depth account for the complex random nature of this phenomenon (such variables are related to the individual overtopping events), the mean overtopping discharge is still generally used as the main criterion for the structure design.

The estimation of q is historically entrusted to the regression formulae (e.g. Owen, 1980; Van der Meer and Janssen, 1994; TAW, 2002; EurOtop Manual, 2018), even if these have been recently supported by new predictive tools, such as machine-learning techniques (see the Artificial Neural Network developed by Zanuttigh et al., 2016) or phase-resolving models with a different degrees of complexity.

As emerged from the literature review, the empirical formulae substantially differ depending on the hydraulic variable adopted. On one hand, the flow rate is related to a run-up height statistic (Yuhi et al., 2021; Hedge

and Reis, 1998; de Waal and Van der Meer, 1992); thus, these models are affected by the uncertainties related to the estimation of the predictive variable. On the other hand, the wave parameters are used to estimate q (EurOtop, 2018). Commonly, according to the findings of Van Gent (1999a,b), the spectral wave height and period at the toe of the structure are used to describe the wave overtopping process. However, their assessment becomes tough within the surf zone, especially for T_{m-10}, because of the occurrence of the surf-beats (Symonds et al., 1982). Indeed, in case of very shallow water and heavy wave breaking, the EurOtop Manual recommends resorting to phase-resolving numerical models to evaluate the harmonic spectral period. Paradoxically, using a simplified overtopping predictive model needs quite sophisticated numerical models for assessing the hydraulic predictors. Recently, Lashley et al. (2021) provided a deepwater-wave-based overtopping model that avoids such drawbacks; nevertheless, its application presumes regular topographic conditions and, therefore, it is less general compared to the use of incident quantities.

As mentioned above, this work investigates the wave overtopping of vertical walls in shallow water. A closer inspection of the literature has revealed that our knowledge of the overtopping process of seawalls in the surf zone is still rough and, therefore, the available predictive empirical tools are affected by significant uncertainties. In particular, the evaluation of literature datasets (i.e. CLASH) has shown a lack of reliable data concerning vertical seawalls in extremely shallow water.

Furthermore, the comprehension of the phenomenon to a greater extent requires the analysis of secondary factors, such as the onshore wind that blows during storms; indeed, the presence of wind can significantly enhance the wave overtopping, increasing the risk of coastal flooding and jeopardizing people and vehicles safety. However, the assessment of this crucial effect is still challenging.

Hence, the present Thesis moves from the uncertainties and drawbacks of the literature and aims to analyze this coastal process in depth; the research pursues the following objectives:

- to provide a deeper insight into the physics of this wave-structure interaction phenomenon and sheds some light on the most efficient hydraulic variables that role the overtopping process in a surf zone;
- to extend our comprehension of wave overtopping of vertical walls with extremely shallow foreshores and provide new laboratory data;
- to develop a trustworthy design equation that predicts the mean overtopping discharge at vertical seawalls in a wide range of hydraulic, structural and topographic conditions;
- to evaluate the influence of the wind on the mean overtopping discharge.

To achieve these research aims, the works combines numerical modelling, physical experiments and analysis of existing data.

In particular, the analysis of the laboratory experiments carried out at the University of Naples Federico II (Cordova et al., 2015;2016), along with the numerical experiments that reproduce the laboratory ones, allowed

us to attain the first aim. The numerical tests have been performed via the CFD-RANS model FLOW-3D and the non-hydrostatic model SWASH. It is worth mentioning that some of the CFD experiments have been conducted by Angela Di Leo within her PhD Thesis (Di Leo, 2021); additional CFD experiments have been performed in this work to extend the analysis.
The research of the variables that truly affect the overtopping in the surf zone has continued with a numerical investigation conducted via SWASH. An extensive parametric study ensured the identification of the key parameters and, successively, the development of a new design formula that uniformly predicts the overtopping rate at vertical seawalls in shallow water.

The analysis of three laboratory datasets has corroborated the numerical findings; among them, new laboratory data have been provided in this work. In particular, 70 physical model tests have been conducted in the small-scale flume of the University of Naples Federico II on vertical seawalls with very and extremely shallow foreshores. Hence, the physical experimental campaign has allowed us to extend our comprehension of wave overtopping of seawalls in the surf zone.

Finally, the influence of the wind on wave overtopping process has been studied via numerical experiments, which include the CFD tests performed in Di Leo (2021) and the SWASH experiments presented in this work. Furthermore, by gathering the CFD numerical data and the laboratory experiments conducted by Durbridge (2021), this work provides a new empirical formula to quantify the wind effect on the mean overtopping discharge of vertical walls.

1.3.Outline of the dissertation

The Thesis is organized as follows:

- Chapter 2 provides the literature review, analyzing the fundamental works and the empirical formulae of wave overtopping;
- Chapter 3 discusses the drawbacks of the hydraulic variables commonly adopted to estimate the mean overtopping discharge;
- Chapter 4 focuses on the existing empirical tool for vertical seawalls in shallow water;
- Chapter 5 briefly describes the phase-resolving models employed in this work;
- Chapter 6 performs a joint analysis of laboratory and numerical data and identifies the new hydraulic variable adopted in this work;
- Chapter 7 deepens the results of Chapter 6 by analyzing literature data and performing *ad hoc* numerical experiments;
- Chapter 8 accomplishes a wide parametric study via the non-hydrostatic model SWASH. The Chapter introduces new dimensionless variables that account for the main parameters involved in the overtopping process. Moreover, a new predictive model is provided;

- Chapter 9 attempts to identify a suitable equivalent slope representative of irregular foreshores;
- Chapter 10 describes the physical experimental campaign conducted at the University of Naples Federico II;
- Chapter 11 analyzes the UniNA dataset and studies the wave overtopping behavior of seawalls in extremely shallow water;
- Chapter 12 verifies the numerical findings against three laboratory datasets, a unique generalized formula is provided to estimate the mean overtopping discharge of seawalls in shallow water;
- Chapter 13 studies the influence of the wind on wave overtopping process and provides an empirical formula to quantify its effect on the flow rate;
- Chapter 14 provides the main conclusions of the work.

2. WAVE OVERTOPPING IN ENGINEERING APPLICATIONS

The wave overtopping phenomenon occurs when wave-structure interaction produces a volume of water that reaches the crest structure and flows over it. Therefore, it is strictly related to the wave run-up process; wave overtopping arises when run-up levels exceed the crest freeboard. The literature typically distinguishes between two overtopping dynamics, referred to as "green" and "white" overtopping (EurOtop, 2018). The former describes a sheet of water that overflows the crest, while the white overtopping is a non-continuous overtopping due to wave breaking seaward or into the face of the structure, generating an amount of spray carried over the crest by its own momentum or by the onshore wind. Additional spray can be generated by wind blowing directly on wave crests, but it is negligible and not considered in the overtopping process.

Although the complexity of the process – wave overtopping is a stochastic, dynamic, temporally variable phenomenon with intermittent events during the whole storm duration – engineering community adopts two simple descriptive parameters to design any coastal defense: the mean overtopping discharge, q, and the individual maximum overtopping volume, V_{MAX}. The former is the ratio between the volume overtopped during a sea state and the sea state duration per linear meter of width, so it is expressed as $m^3/s/m$ or l/s/m. On the other hand, the second parameter allows taking the process's randomness into account. The overtopping volumes are not uniform during a sea state; few waves can lead to significantly larger overtopping volumes. Thus V_{MAX}, expressed as m^3/m or l/m, is used.

The design process has to satisfy the criteria for functional and structural safety by complying with thresholds for q and V_{MAX} specified in the guidelines (see EurOtop, 2018; Rock Manual, 2007). According to the literature (Allsop et al., 2008; Franco et al., 1994), the volume represents the more suitable parameter to describe the hazard related to wave overtopping; however, since the mean rate has been historically used, it is still considered a key parameter for coastal flood risks assessment and sea defenses design. It is worth mentioning that researchers have recently attended to further parameters, such as flow velocity and thickness, which allow to better establish a safe scenario for pedestrians and vehicles safety (Van der Meer et al., 2022; Altomare et al., 2020; Mares-Nasarre et al., 2019; Sandoval and Bruce, 2017; Nørgaard et al., 2013; Schüttrumpf and Van Gent, 2003).

The present work focuses on the mean overtopping discharge, the leading parameter engineers have dealt with when designing structures and assessing coastal risks.

2.1. The maximum individual overtopping volume

In the design process of sea defenses, the mean overtopping discharge has been historically considered the primary parameter; nonetheless, the maximum individual overtopping volume, V_{MAX}, is handled as a key variable as well. Indeed, in many cases, individual overtopping volumes can be significantly larger than the

mean volume; hence, this variable must be addressed to guarantee the safety of pedestrians, vehicles and properties.

However, unlike q, assessing V_{MAX} is quite challenging since it is related to individual wave overtopping events and requires a wave-by-wave analysis.

Individual overtopping events are described by the exceedance probability distribution by virtue of their random nature. Such an exceedance probability distribution is commonly related to the mean overtopping discharge, the storm duration and the probability of overtopping, P_{OW} (the number of overtopping waves to the number of incident wave ratio). As first stated by Van der Meer and Janssen (1994) and Franco et al. (1994), the wave-by-wave overtopping volumes follow a two-parameter Weibull distribution:

$$P(V_i \leq V) = 1 - exp\left[-\left(\frac{V}{a}\right)^b\right] \tag{2.1}$$

Eq. (2.1) expresses the non-exceedance probability, where V_i is the individual overtopping volume and a and b are the Weibull's distribution scale and shape parameters, respectively. Specifically, a normalizes the distribution, while the dimensionless parameter b determines the shape of the probability distribution. A smaller shape factor describes few overtopping waves giving large overtopping volumes, whereas the larger value of b corresponds to more uniform overtopping volumes during a sea state. A particular case is $b = 2$, which defines a Rayleigh distribution.

To assign an exceedance probability to every V_i, a Weibull plotting position can be used:

$$P(V_i) = 1 - \frac{i}{N_{ow}} \tag{2.2}$$

with i the rank of the individual overtopping volumes sorted in descending order ($i = 1$ corresponds to V_{MAX}) and N_{OW} is the actual number of overtopping waves. Therefore, the maximum individual overtopping volume can be derived:

$$V_{MAX} = a \cdot [\ln(N_{OW})]^{\frac{1}{b}} \tag{2.3}$$

However, for a few overtopping waves, Eq. (2.3) could predict an unreliable value of V_{MAX}. In particular, Lykke-Andersen et al. (2009) warned that for $N_{OW} = 1$, Eq. (2.3) would predict an inconsistent $V_{MAX} = 0$. Thus, they adopted a different plotting position and obtained an alternative formula to estimate the maximum individual overtopping volume:

$$V_{MAX} = a \cdot [\ln(N_{OW} + 1)]^{\frac{1}{b}} \tag{2.4}$$

By assuming the equality of the theoretical and the measured mean overtopping volumes, Franco and Franco (1999) derived the scale factor of Weibull distribution as:

$$a = \frac{1}{\Gamma\left(1+\frac{1}{b}\right)} \cdot \frac{qN_W T_m}{N_{OW}} \tag{2.5}$$

where Γ is the mathematical gamma function. Eq. (2.5) highlights that the scale and the shape parameters are mutually related and that q is a key variable in the distribution of the individual overtopping volume.

The early studies that dealt with the analysis of the overtopping volumes proposed a constant value of $b = 0.75$ for sloped and vertical structures in non-breaking wave conditions (Van der Meer and Janssen, 1994; Franco et al., 1994). In its detailed analysis of the individual wave overtopping volumes for vertical walls, sloped structures and composite structures, Besley (1999) found an influence of the deepwater wave steepness on the shape parameter. On the other hand, Victor et al. (2012) observed no effect of the wave steepness for steep impermeable low-crested structures, while they proposed a formula that relates b to the slope angle and the relative crest freeboard, while Hughes et al. (2012) found that, for sloped impermeable structures, the shape factor depends only on the relative crest freeboard, R_C/H_{m0}. Zanuttigh et al. (2013) studied smooth-slope and rubble mound breakwater and derived an empirical formula that relates b to the mean overtopping discharge and the incident wave conditions, H_{m0} and T_{m-10}. Nørgaard et al. (2014) analyzed the distribution of individual wave overtopping volumes of rule mound breakwaters in shallow water conditions and observed that the existing formulae led to an overestimation of b for the largest overtopping volumes in depth-limited waves; thus, the authors proposed a correction term which is a function of the incident spectral wave height and the average of the 1/10 highest incident waves, $H_{1/10}$. Salauddin et al. (2022) extensively analyzed the overtopping volume distribution for vertical walls and derived a unique predictive formula to estimate b under impulsive and pulsating waves.

Besides the scale and shape parameters of the Weibull distribution, the estimation of the individual maximum overtopping volume depends on the number of the overtopping waves, N_{OW} (Eq. (2.3)). The latter quantity is usually expressed as the probability of overtopping:

$$P_{OW} = \frac{N_{OW}}{N_W} \tag{2.6}$$

where N_W is the number of incident waves.

The literature provides several empirical formulae depending on the sea defense structure. Some models relate P_{OW} for sloping structures to the relative crest freeboard and the wave run-up (Van der Meer and Janssen, 1994; EurOtop, 2018), while Victor et al. (2012) considered only the relative crest freeboard and the slope of the structure. For vertical walls, P_{OW} depends on the incident wave conditions and the crest freeboard (Besley, 1999; EurOtop, 2018).

2.2. Overtopping flow thickness and velocity

For a proper assessment of people and vehicle safety at the crest of structures, neither the mean overtopping discharge nor the maximum individual overtopping volume are satisfactory parameters. On the other hand, the flow depth, h, and velocity, u, of an overtopping event need to be established. Moreover, these parameters may be useful to assess the potential damage at the crest or the leeward slope of dikes (Koosheh et al., 2021).

The most common parameter to define the safety limits for different hazard regimes is the product of h and u; some studies provide this product's safety limits for both pedestrians and vehicles (e.g. Smith et al., 2019; Ball et al., 2019).

The overtopping flow depth and velocity are temporally and spatially variable over the structure; different empirical equations have been proposed for estimating these variables at the edge of the crest's structure, along the berm and at the leeward side (Schüttrumpf and Van Gent, 2003; EurOtop, 2018; Mares-Nasarre et al., 2019; Formentin et al., 2019; Nørgaard et al., 2014). These models suggest that the flow thickness and velocity depend on the difference between the run-up height and the freeboard crest. Altomare et al. (2020) found a correlation between the overtopping flow depth and velocities and the maximum overtopping volume, but the large scattering of the data has prevented any regression analysis.

However, the ongoing research indicates that a greater understanding of these overtopping parameters is essential to assessing coastal risk.

2.3. The mean overtopping discharge: predictive tools

Flow rate estimation typically resorts to three different types of tools, namely:

- numerical models are physical-based tools, as they integrate mathematical equations to describe the physics of the analyzed processes. In particular, the Navier-Stokes equations well describe the complex hydrodynamics related to wave propagation and transformation along with the wave-structure interactions phenomena. By using either mesh-based or mesh-less (SPH) approaches to solve Navier-Stokes equations, a large amount of literature has dealt with the overtopping process (among them Stagnitti et al., 2023; Chen et al., 2021; Liu et al. 2021; Altomare et al., 2021; Mokos et al., 2020; Akbari et al., 2017; Ni and Feng, 2013; Losada et al., 2008; Shao, 2006). Furthermore, more simplified phase-resolving models, such as Non Linear Shallow Water models, non-hydrstatic models or Boussinesq-type models can be employed to estimate the mean overtopping discharge (Suzuki et al., 2023; Henderson et al., 2022; Tuozzo et al., 2022; Zhang et al., 2020; Suzuki et al., 2017; Tonelli and Petti, 2013; Lynett et al., 2010).
- machine learning techniques, on the opposite side, are regarded as data-driven models. In fact, the predictive ability of such tools is due to the acquisition and integration of a large amount of data, which assemble their knowledge. The larger and more varied the number of observations, the greater the knowledge. Among the others, one of the most important was the Neural Network (NN) developed by

Van Gent et al. (2007), as it was based on the largest dataset containing about 10000 physical model tests on wave overtopping, i.e. the CLASH database that includes different datasets collected during the CLASH European project. The NN structure is organized into several layers, each of them composed of neurons (e.g., the number of neurons in the first layer is equal to the input parameters), connected in only one direction. After several hidden layers, representing the core of NN, the last one provides the mean overtopping discharge. Zanuttigh et al. (2016) have provided the EurOtop Artificial Neural Network (ANN), optimizing the existing one. The authors have trained the ANN by using more than 13500 overtopping tests (including those of the CLASH database). By using the same database, Den Bieman et al. (2021) have proposed the XGBoost, an alternative machine learning method of the type gradient boosting decision trees. It is composed of an ensemble of regression trees that provides the mean overtopping discharge;

- empirical formulae can be seen as a compromise between the previous predictive tools.

2.3.1. The mean overtopping discharge: structural and hydraulic variables

The mean overtopping discharge depends on the structural and hydraulic variables required to describe the wave-interaction process properly.

The formers include all the geometric features that could affect the overtopping (some of them are depicted in Figure 2.1):

- the crest freeboard, R_C, is the vertical height of the structure relative to the Still Water Level (SWL) and represents the main structural variable in the empirical predictive formulae. For specific structures, such as a rubble mound breakwater with a storm wall, we need to discern between the wall's freeboard and the armour's freeboard, A_C (Figure 2.1). Empirical formulae usually require the maximum of the two;
- the promenade, G_C, and the berm, B, are the horizontal sections of the structure. The former is located above the SWL, while the berm is situated near the SWL and used to split the slope of the structure;
- the slope of the sloping structures, $tan(\alpha)$;
- the surface characteristics, as structures may be either smooth or rough;
- a bullnose or a return wall is usually designed at the top of the wall to return the up-rushing waves seaward.

For plain vertical walls, such as those investigated in this work, the crest freeboard is the only structural feature involved in the overtopping process.

Furthermore, the water depth at the toe of the structure, h_{TOE}, is a crucial parameter since it allows distinguishing between deep and shallow water.

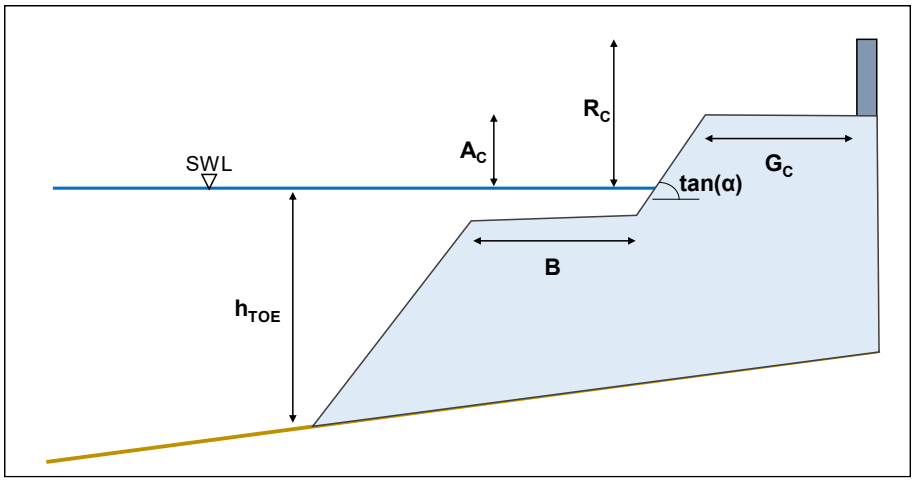

Figure 2.1 *– Sketch of some geometric features needed to estimate the mean overtopping discharge.*

Regarding the hydraulic variables, two fronts can be distinguished in the literature, as can be appreciated by the state-of-the-art review reported below. The first front relates the flow rate to the wave run-up (Figure 2.2a), as the overtopping generally occurs when the up-rush jet is higher than the crest freeboard. It is worth noting that the run-up height refers to the height reached by the water if the structure were high enough to preclude the overtopping. The second considers instead the wave conditions, measured either in deep water or at the toe of the structure (Figure 2.2b). Table 2.1 summarizes the dimensionless predictor variables adopted in the main works to estimate the mean overtopping discharge.

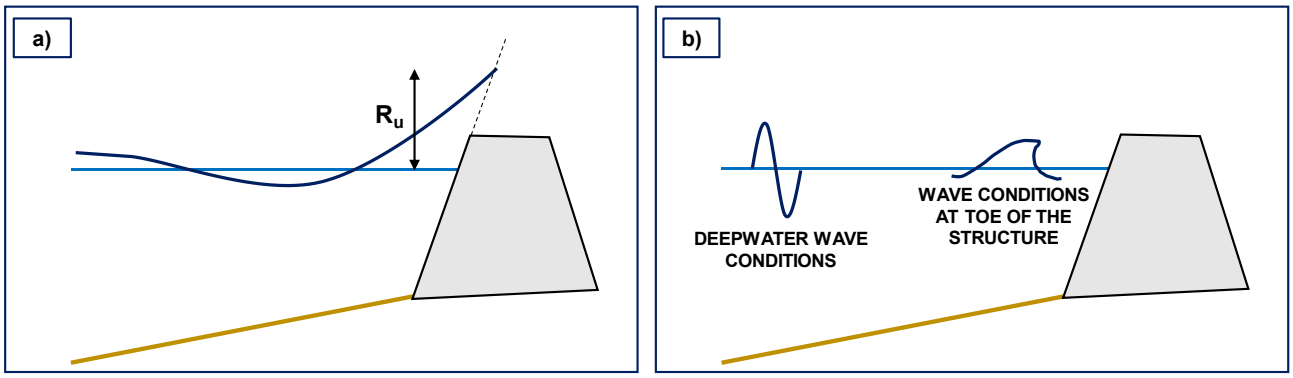

Figure 2.2 *– Sketch of hydraulic variables used to estimate the flow rate. Panel a): wave run-up; panel b): wave conditions.*

Based on the laboratory experimental campaign of Saville (1955) on the overtopping of monochromatic waves, Weggel (1976) readdressed the results in dimensionless form, so providing an empirical equation that relates the overtopping rate to the wave run-up, R_u. Ahrens (1977) has successively extended Weggel's formula to irregular sea states by assuming a Rayleigh distribution of run-up; thus, a wave run-up associated with a particular probability of exceedance, $p_{\%}$, is used.

Battjes (1974) related the overtopping volume per wave to the wave run-up through a "deficit in crest freeboard", $1 - R_C/R$, where a monochromatic run-up formula was used. The empirical equation was derived using Seville's data.

On the other hand, in the same years, Goda et al. (1975) model resorts to deepwater wave conditions. In particular, the authors have provided design diagrams to estimate the mean overtopping discharge of vertical walls in terms of crest freeboard, deepwater significant wave height, H_S, water depth at the toe of the wall, h_{TOE}, the wave steepness, s_0, and foreshore slope, $tan(m)$.

Owen (1980) adopted the wave characteristics at the toe of the structure instead. An extensive experimental campaign conducted at the Hydraulic Research Station of Wallingford led to an exponential-type predictive formula for wave overtopping, which is characterized by new dimensionless variables (Table 2.1). According to Owen, the estimation of the flow rate requires significant wave height, $H_{1/3}$, or an equivalent post-breaking wave height when wave breaking occurs ($H_{sb} = \gamma \cdot h_{TOE}$), and the mean zero-crossing wave period, T_m, at the toe of the structure.
Both Goda et al. and Owen take the effect of wave steepness into account; thus, the influence of wave period has been observed. Specifically, their models state that longer waves lead to larger flow rates.

Although with different dimensionless variables, Aminti and Franco (1988) and Pedersen and Burchart (1993) have related the mean overtopping discharge to the incident significant wave height and the mean zero-crossing period as well.

In the re-analysis of Owen's approach, de Waal and Van der Meer (1992) have observed a different behavior for plunging and surging waves, so an overtopping formula based on a new variable has been proposed. Specifically, the authors have related R_C to an expected value of run-up, the so-called "shortage in crest height". This concept has been successively exploited by Schüttrumpf and Van Gent (2003) to estimate the overtopping rate exceeded by 2% of the incoming waves and by Etemad-Shahidi et al. (2022) to provide a new formula for estimating q of rubble mound structures.

Van der Meer and Janssen (1994) have distinguished between braking and non-breaking waves by providing two different formulae that adopt the incident wave conditions. In particular, the overtopping for non-breaking waves depends only on the significant wave height, H_S, while in the case of breaking waves, the peak period, T_p, is required as well.
Franco et al. (1994) investigated the wave overtopping of vertical breakwaters and provided a design formula with the same structure.

In 1998, Hedge and Reis have proposed a new overtopping model based on the maximum run-up induced by random waves, R_{MAX}. The overtopping model considers the physical boundary conditions that the flow rate

should be zero when the crest freeboard is quite larger than the level of wave uprush and that should be large, but finite, when the crest freeboard is zero.
Based on this approach, Mase et al. (2013) and Yuhi et al. (2020) have slightly modified the Hedge and Reis model and related the mean overtopping discharge to the maximum run-up and the deepwater wave height.

At the end of the last century, Van Gent (1999a,b) investigated in depth the wave run-up and overtopping of sea dikes in shallow water through an extensive numerical and physical experimental campaign. The author has suggested using the spectral wave condition at the toe of the structure to estimate the wave overtopping. In particular, this work first introduced the harmonic spectral period T_{m-10} to describe the wave-structure interaction processes in shallow water conditions.
Altomare et al. (2016) have successively extended the analysis to sea dikes characterized by shallower foreshores and stressed the significant role of the foreshore slope in the overtopping process. Indeed, they have revisited Van Gent's model by introducing an equivalent slope concept that takes into account either the dike slope or the foreshore slope.

In 2020, Ibrahim and Baldock have somehow resumed the Battjes method (1974) by proposing the positive volume flux of the incident waves and the deficit in freeboard as scaling parameters. Therefore, the overtopping process is related to the wave run-up phenomenon. The analysis of experimental data on the swash overtopping of truncated plane beaches has demonstrated that the use of these dimensionless variables, instead of those widely adopted in literature (EurOtop, 2018), significantly diminishes the scatter of data around the best fit. Altomare et al. (2020) have employed the Evolutionary Polynomial Regression technique – a data-driven approach – to detect the most important explanatory variables that describe the mean overtopping discharge of smooth sea dikes and vertical walls. To this end, 1679 data from five different datasets have been used. This study has verified that both the dimensionless crest freeboard, $R_C/H_{m0,TOE}$, and the deficit in crest freeboard are key variables. However, the latter parameter requires the estimation of wave run-up, which includes the influence of wave period, local water depth, and foreshore and dike slopes. Thus, it accounts for a proper consideration of the wave transformation process.

Based on Goda's approach, Lashley et al. (2021) have provided predictive formulae that require deepwater wave conditions. On the other hand, unlike its previous model, Goda (2009) have related the flow rate to the significant wave height at the toe of the structure.

In the last two decades, based on Van Gent' findings (2001;1999a,b), the scientific community has typically adopted the spectral wave height, H_{m0}, and the harmonic wave period, T_{m-10}, at the toe of the structure, as proved by the overtopping manuals (EurOtop, 2018; EurOtop, 2007; TAW, 2002) and the main machine learning tools (Den Bieman et al., 2021; Zanuttigh et al., 2016; Van Gent et al., 2007).

Finally, it should be noted that structures with an emerged toe (i.e. located above the still water level) make empirical models based on incident wave conditions useless. Therefore, those require either models based on

wave run-up (Yuhi et al. 2020; Altomare et al., 2016; Mase et al., 2013) or deep water wave parameters (Lashley et al., 2021).

Table 2.1 *– List of dimensionless flow rate and predictor variables used in the literature over the years.*

	Dimensionless flow rate	**Predictor variables**
Weggel, 1976	$\frac{q}{\sqrt{gH_0^3}}$	$\frac{R_C}{R_u}$
Ahrens, 1977	$\frac{q}{\sqrt{gH_S^3}}$	$\frac{R_C}{R_{u,p\%}}$
Battjes, 1974	$\frac{V}{HL_0\sqrt{tan\beta}}$	$\frac{R-R_C}{R}$
Goda et al., 1975	$\frac{q}{\sqrt{2gH_{1/3}^3}}$	$\frac{R_C}{H_{1/3}}$; $\frac{h_{TOE}}{H_{1/3}}$; s_0; $\tan(m)$
Owen, 1980	$\frac{q}{gT_mH_{1/3}}$	$\frac{R_C}{T_m\sqrt{gH_{1/3}}}$
Aminti and Franco, 1988	$\frac{q}{gT_mH_S}$	$\frac{R_C}{H_S}$
Pedersen and Burchart, 1993	$\frac{qT_m}{L_m}$	$\frac{R_C}{H_S}$
de Wall and Van der Meer, 1992 *Etemad-Shahidi et al., 2022*	$\frac{q}{\sqrt{gH_S^3}}$	$\frac{R_{u,2\%}-R_C}{H_S}$
Van der Meer and Janssen, 1994	$\frac{q}{\sqrt{gH_{1/3}^3}}\cdot\sqrt{\frac{s_{0,p}}{\tan(\alpha)}}$; $\frac{q}{\sqrt{gH_{1/3}^3}}$	$\frac{R_C}{H_{1/3}}\cdot\frac{\sqrt{s_{0,p}}}{\tan(\alpha)}$; $\frac{R_C}{H_{1/3}}$
Hedge and Reis, 1998	$\frac{q}{\sqrt{g\cdot {R_{MAX}}^3}}$	$\frac{R_{MAX}-R_C}{R_{MAX}}$
*Van Gent, 1999**	$\frac{q}{\sqrt{gH_{m0,TOE}^3}}$	$\frac{R_C}{H_{m0,TOE}(b-c\cdot\xi_{m-10})}$
Goda, 2009	$\frac{q}{\sqrt{gH_{S,TOE}^3}}$	$\frac{R_C}{H_{S,TOE}}$
Mase et al., 2013 *Yuhi et al., 2020*	$\frac{q}{\sqrt{g\cdot {H_{S,DEEP}}^3}}$	$\frac{R_{MAX}-R_C}{R_{MAX}}$; $\frac{R_{MAX}}{H_{S,DEEP}}$

*Altomare et al., 2016**	$\frac{q}{\sqrt{gH_{m0,TOE}^3}}$	$\frac{R_C}{H_{m0,TOE}(b - c \cdot \xi_{m-10})}$
Lashley et al., 2021	$\frac{q}{\sqrt{gH_{m0,DEEP}^3}}$	$\frac{R_C}{H_{m0,DEEP}}$; $\frac{h_{TOE}}{H_{m0,DEEP}}$; s_{m-10} ; $\tan(m)$; $\tan(\alpha)$

* the predictor variables of Van Gent (1999) and Altomare et al. (2016) differ for the slope used in the surf-similarity parameters.

In the following, the main empirical formulae are described in detail.

2.3.2. Empirical formulae related to wave parameters

Goda et al. (1975)

Goda et al. (1975) performed laboratory tests of wave overtopping on vertical structures located on two foreshore slopes, *cot(m)* = 10 and 30, with conditions at the toe varying from shallow to emergent. Irregular wave trains, characterized by a single value of wave height and three different wave periods, have been generated to investigate the effect of wave steepness on the overtopping. In particular, the authors refer to the time-domain wave characteristics, $H_{1/3}$ and $T_{1/3}$.

The results have been collected in design diagrams, as shown in Figure 2.3. For each wave steepness and foreshore slope investigated, the dimensionless mean overtopping discharge depends on both the dimensionless crest freeboard and the relative water depth ($h_{TOE}/H_{1/3,DEEP}$). These diagrams summarize the main characteristics of wave overtopping observed by the authors:

- the higher the relative crest freeboard, the lower the mean overtopping discharge;
- different zones can be distinguished to express the relationship between the relative water depth and q, so a univocal behavior has not been observed;
- longer waves produce higher flow rates;
- milder slopes reduce q.

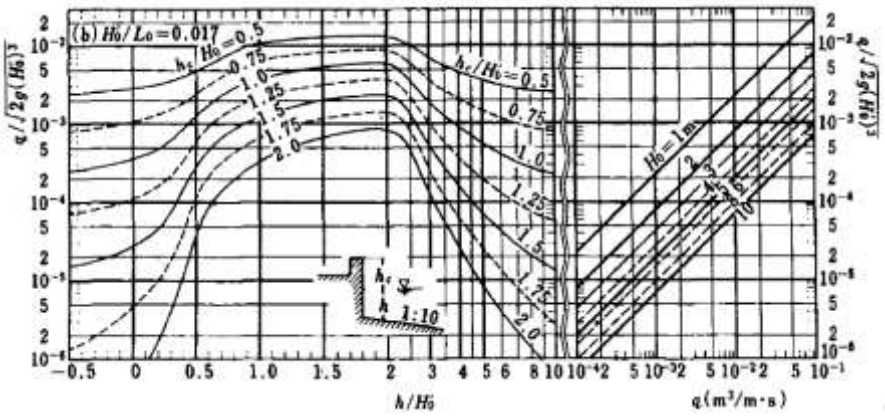

Figure 2.3 *– Design diagram reported in Goda (2000).*

Owen (1980)

The fundamental work of Owen collects the results of an extensive experimental campaign carried out at the Hydraulic Research Station of Wallingford (UK), which aimed to determine the overtopping discharge of different types of seawalls (e.g. vertical, sloped, etc..) by examining the influence of both hydraulic and geometric features.

The outcomes of these laboratory tests resulted in the following exponential-type predictive formula:

$$\frac{q}{gT_m H_{1/3,TOE}} = a \cdot exp\left(-b \cdot \frac{R_C}{T_m\sqrt{gH_{1/3,TOE}}}\right) \tag{2.7}$$

where the mean flow rate has been related to the time-domain wave conditions. In particular, the model refers to the incident significant wave height, $H_{1/3}$, and the mean zero-crossing wave period in deep water, T_m.
When wave breaking occurs, the author has suggested using an equivalent post-breaking wave height, $H_{sb} = \gamma h_{TOE}$, where the breaking coefficient depends both on the foreshore slope and the relative water depth h_{TOE}/L_{0m}. It is worth specifying that H_{sb} is the equivalent wave height that provides the correct overtopping discharge but can differ from the effective height. On the other hand, the deepwater mean zero-crossing period is used for structures located in the surf zone as well.
The Owen's model highlights the influence of wave period on wave overtopping; indeed, the longer the wave, the higher the discharge. Nonetheless, by re-writing the dimensionless variables as in Eq. (2.8), the model assumes that for a given wave steepness, the incident significant wave height is the hydraulic parameter that rules the overtopping process:

$$\frac{q}{gT_m H_{1/3,TOE}} = \frac{q}{\sqrt{gH_{1/3,TOE}{}^3}} \cdot \sqrt{\frac{s_{0,m}}{2\pi}} \tag{2.8a}$$

$$\frac{R_C}{T_m\sqrt{gH_{1/3,TOE}}} = \frac{R_C}{H_{1/3,TOE}} \cdot \sqrt{\frac{s_{0,m}}{2\pi}} \tag{2.8b}$$

Finally, the empirical coefficients a and b in Eq. (2.7) depend on the geometric characteristics.

Van der Meer and Janssen (1994)

Van der Meer and Janssen have analyzed several laboratory data about the overtopping of dikes and sloping structures, including those obtained by Owen (1980). Unlike the previous models, the authors distinguished between the overtopping behavior of breaking and non-breaking waves; thus, two formulae have been provided.
When waves break on the structure slope ($\xi_{0,p} < 2$), the authors have suggested Eq. (2.9a); otherwise, they refer to Eq. (2.9b):

$$\frac{q}{\sqrt{gH_{1/3,TOE}^3}} \cdot \sqrt{\frac{s_{0,p}}{\tan(\alpha)}} = a \cdot exp\left(-b \cdot \frac{R_C}{H_{1/3,TOE}} \cdot \frac{\sqrt{s_{0,p}}}{\tan(\alpha)}\right) \qquad \xi_{0,p} < 2 \qquad (2.9a)$$

$$\frac{q}{\sqrt{gH_{1/3,TOE}^3}} = a' \cdot exp\left(-b' \cdot \frac{R_C}{H_{1/3,TOE}}\right) \qquad \xi_{0,p} \geq 2 \qquad (2.9b)$$

where *a*, *b*, *a'* and *b'* are empirical coefficients; the significant wave height in the time domain (the average of the highest one-third) at the toe of the structure and the peak period of the wave spectrum have been adopted as wave parameters.

The Van der Meer and Janssen's predictive model assumes that both the structure slope and the wave steepness affect only the overtopping process of breaking waves; in particular, the mean flow rate increases as either the wave period increases or the structure slope becomes steeper. Their influence disappears in a non-breaking regime, and the wave overtopping depends only on the relative crest freeboard, i.e. the significant wave height is the only hydraulic parameter that affects the process.

It is worth highlighting that the distinction above does not refer to waves that break on the foreshore, namely in front of the sea defense (broken waves that reach the structure), but on the structure's slope. However, an empirically-based coefficient γ_h allows taking the influence of shallow foreshore into account. Specifically, the relative crest freeboard $R_C/H_{1/3,TOE}$ is divided by this reduction factor, which considers that waves in shallow water no longer follow a Rayleigh distribution.

Van Gent (1999)

In 1999, Van Gent performed an extensive experimental campaign to investigate wave-structure interaction phenomena in shallow water. Laboratory tests carried out at the research institute Delft Hydraulic, along with numerical experiments, ensured the analysis of the wave run-up and overtopping of sea dikes in shallow foreshore.

Specifically, Van Gent has reproduced two different sea dikes, *tan(α)* = 1/2.5 and 1/4, on two mild foreshore slopes, *tan(m)* = 1/100 and 1/250. Furthermore, the water depth at the toe of the structure, the deepwater wave steepness and the spectral shape have been varied. The overtopping predictive model obtained is:

$$\frac{q}{\sqrt{gH_{m0,TOE}^3}} = a \cdot exp\left(-\frac{R_C}{H_{m0,TOE}(b - c \cdot \xi_{m-10})}\right) \qquad (2.10)$$

where the surf similarity parameter is the dike slope to the square of wave steepness ratio, $tan\alpha/\sqrt{H_{m0}/L_{m-10}}$.

Beyond the empirical formula, the main aim of the work was to identify the more suitable wave parameters to describe the wave-structure interaction phenomena in shallow water. To this end, Van Gent examined three different characteristics wave heights (the spectral wave height, H_{m0}, the significant wave height, $H_{1/3}$, and the wave height exceeded by 2% of the incident waves, $H_{2\%}$) and five different characteristics periods (the spectral periods, T_{m-10}, T_{m-02}, T_{m01}, the peak period, T_p, and the mean zero-crossing period, T_m). This approach differs from that of Van der Meer and Janssen (1994), which resorts to an empirical reduction coefficient to take the effects of shallow foreshore into account.

Unlike the findings about the characteristic wave height, where no significant differences have been observed between those examined, the appropriate wave period seems to be crucial. In particular, the author has stressed the role of the harmonic spectral period, T_{m-10}, as will be discussed in the next chapter. As reported in Eq. (2.10), Van Gent suggested adopting the incident spectral wave conditions to estimate the mean overtopping discharge.

Following the findings of Van Gent (1999a,b; 2001), many researchers have adopted spectral wave parameters to describe wave run-up and overtopping (e.g. EurOtop Manual 2007, 2018).

Goda (2009)

In 2009, Goda provided a new unified overtopping formula for both vertical and inclined walls, based on data from the CLASH database. In particular, 715 data for vertical walls and 1254 for inclined seawalls have been selected to derive the predictive model. The author aimed to overcome some drawbacks that have been observed in the EurOtop (2007) formulae: for sloping seawalls, the model does not account for the role of water depth at toe of the structure, while the estimation of the mean overtopping discharge at vertical walls requires different empirical equations depending on the breaking regime. A different overtopping behavior has been observed for impulsive and pulsating (non-breaking) wave conditions (Allsop et al., 1995). On the other hand, Goda has differed from this assumption since the overtopping process is due to non-breaking, breaking and broken waves within a single train of random waves.

The unique exponential formula proposed in this work reads:

$$\frac{q}{\sqrt{gH_{S,TOE}^3}} = exp\left[-\left(a + b \cdot \frac{R_C}{H_{S,TOE}}\right)\right] \tag{2.11}$$

The coefficients a and b are equal to 3.64 and 2.21, respectively, in deep water (where h_{TOE} does not affect the overtopping), while in shallower water, they depend on the seabed slope, the relative water depth, $h_{TOE}/H_{s,TOE}$, and the structure slope. Different formulations have been suggested for vertical and inclined seawalls.

According to Goda's model, the flow rate just depends on the significant wave height at toe of the wall, the wave period has no role. It is worth specifying that in Eq. (2.11), the incident significant wave height has been indicated with the general symbol $H_{s,TOE}$, since in Goda (2009), the difference between $H_{1/3}$ and H_{m0} was disregarded.

Altomare et al. (2016)

The work of Altomare et al. (2016) has examined in depth the wave overtopping of sea dike with very shallow foreshores. The authors indeed stated that the process was still unclear, especially with structures located on gentle foreshore in very shallow water conditions, and that the existing formula (Van Gent, 1999 – Eq. (2.10)) does not take the foreshore slope explicitly into account, which is an essential parameter instead. Although the foreshore slope indirectly appears in the empirical formulae that adopt incident wave parameters, since it affects the wave transformation, Altomare et al. have demonstrated that a proper estimation of the mean flow rate requires this parameter.

The findings reported in this work mainly derive from five different experimental campaigns, four carried out at Flanders Hydraulics Research and one at Ghent University, resulting in 204 data. During the experiments, two foreshore slopes ($tan(m)$ = 1/35 and 1/50) and three dike slopes ($tan(\alpha)$ = 1/2, 1/3 and 1/6) have been examined. Moreover, 75 data from the CLASH dataset have been analyzed as well; 69 out of 75 data are characterized by milder foreshores ($tan(m)$ = 1/100 and 1/250), while the same range of dike slope has been considered. The whole dataset includes either dikes with shallow and very shallow foreshore or with emerged toe; since this dataset examined dikes located in shallower water compared to those of Van Gent (1999b), such a work ensured to analyze in more detail the influence of very shallow foreshore on the wave overtopping process.

The formula proposed has the same Eq. (2.10) structure, but the surf similarity parameter is related to an equivalent slope, $tan\delta$. Thus, the overtopping process depends on the spectral incident wave conditions, the geometric features of the dike and the foreshore slope. Such a variable is accounted for in the equivalent slope concept (Figure 2.4):

$$tan\delta = \frac{1.5 \cdot H_{m0,TOE} + R_{u,2\%}}{L_{slope}} \tag{2.12}$$

where L_{slope} is the horizontal distance the SWL – $1.5 \cdot H_{m0,TOE}$ and SWL + $R_{u,2\%}$, and, in case of emerged toe, it can be calculated as:

$$L_{slope} = \frac{h_{TOE} + R_{u,2\%}}{\tan(\alpha)} + \frac{1.5 \cdot H_{m0,TOE} - h_{TOE}}{\tan(m)} \tag{2.13}$$

However, when the water depth at toe of the dike is larger than $1.5 \cdot H_{m0,TOE}$, the Van Gent's model (Eq. (2.10)) is applied.

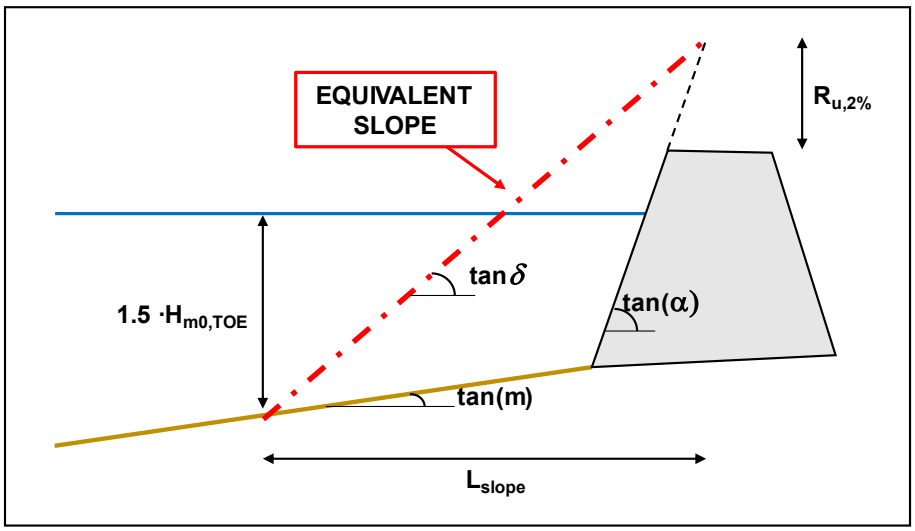

***Figure 2.4** – The equivalent slope proposed by Altomare et al. (2016).*

Nevertheless, since the wave run-up $R_{u,2\%}$ is determined using a formula that correlates it with the surf similarity parameter, which in turn depends on wave run-up, an iterative procedure is required to use such a predictive equation.

Therefore, the Altomare et al. overtopping model mainly depends on the spectral wave condition at toe of the wall, but it also requires the estimation of wave run-up. Furthermore, the use of the significant spectral wave height also allows accounting for the energy of broken waves or bores (along a gentle and shallow foreshore, waves can lose their oscillatory nature when they reach the toe of the structure); thus, $H_{m0,TOE}$ represents a sort of equivalent wave height.

Lashley et al. (2021)

Recently, Lashley et al. have proposed an overtopping model for vertical and sloping seawalls in very shallow water inspired by the Goda et al. (1975) approach, namely an overtopping model based on deep water wave conditions. The authors pointed out the difficulty in estimating the incident wave conditions required in much of the existing empirical overtopping formulae when either complex bathymetries or very shallow foreshores are involved.

Several datasets have been used to infer the predictive equations; in particular, 465 and 161 data for inclined and vertical walls, respectively. Specifically, the dike slope investigated varies between 1/2 and 1/7, while the foreshore slope range is 1/10 ÷ 1/250 and 1/10 ÷ 1/100 for sloping and vertical structures, respectively. Seawalls are characterized by a very shallow foreshore up to an emergent toe.

The predictive overtopping model reads:

$$\frac{q}{\sqrt{gH_{m0,DEEP}^3}} = a \cdot exp\left(-b \cdot \frac{R_C}{H_{m0,DEEP}} + c \cdot \frac{h_{TOE}}{H_{m0,DEEP}}\right) \tag{2.14}$$

where the coefficients *a*, *b* and *c* depend on the foreshore, *tan(m)*, the seawall slopes, *tan(α)*, and the deep water wave steepness related to the harmonic spectral period, s_{m-10}. In particular, both the foreshore slope and the relative water depth are necessary to take somehow the wave transformation process into account.

According to Lashley et al., the deep water significant wave height is the main hydraulic variable that rules the wave overtopping process. However, the wave period appears through the coefficients of Eq. (2.14); in particular, the longer the waves the higher the discharge. Furthermore, the formula shows that steeper foreshore and/or slope lead to larger *q*.

2.3.3. Empirical formulae related to wave run-up

de Waal and Van der Meer (1992)

The Owen's overtopping model has been verified against a large amount of laboratory data, including those used in Owen (1980) and more than 350 tests performed at the Delft Hydraulics Institute on various coastal structures. However, de Waal and Van der Meer observed a different behavior according to the breaking regime – the overtopping model appeared unsuitable for surging waves. Therefore, they have proposed a new unified model that resorts to different dimensionless variables:

$$\frac{q}{\sqrt{gH_{1/3,TOE}^3}} = a \cdot exp\left(b \cdot \frac{R_{u,2\%} - R_C}{H_{1/3,TOE}}\right) \tag{2.15}$$

The term at the right-hand side is called "shortage in crest height", namely the dimensionless excess of the crest level above the 2% run-up level; thus, the mean overtopping discharge is related to an expected run-up level on a non-overtopped slope, $R_{u,2\%}$, which can be derived from wave run-up formula provided in the same work.

Eq. (2.15) assumes that negative values of the shortage in crest height lead to low overtopping discharge, as the crest freeboard is higher than the expected run-up height; on the other hand, smaller crest freeboards compared to $R_{u,2\%}$ causes a larger amount of wave overtopping.

Hedges and Reis (1998)

Hedges and Reis (1998) have developed an overtopping model that satisfies two physical boundary conditions: when the crest freeboard is higher than the up-rush level, the flow rate should be zero (keeping out the white

overtopping); when the crest freeboard is zero, the discharge may be large but should remain finite. The formula assumes that the structure acts as a weir. Therefore, the overtopping model is:

$$\frac{q}{\sqrt{g \cdot {R_{MAX}}^3}} = \begin{cases} a \cdot exp\left[b \cdot \left(1 - \frac{R_C}{R_{MAX}}\right)\right] & 0 \leq R_C < R_{MAX} \\ 0 & R_{MAX} < R_C \end{cases} \quad (2.16)$$

According to the first boundary condition, the overtopping estimation is strictly related to the run-up level. In particular, Hedges and Reis refer to the maximum run-up induced by random waves, R_{MAX}, which differs from the run-up due to a significant wave height.

Assuming a Rayleigh distribution may describe that run-up, the $p_{\%}$ confidence value of maximum run-up is related to the significant wave run-up. For instance, the maximum run-up not exceeded in 37% of the cases can be determined as $R_{MAX,37\%} = 1.52 \cdot R_S = C \cdot H_{S,TOE}$. Hence, the maximum run-up is related to the incident significant wave height; the coefficient C depends on the specified confidence level associated with R_{MAX} and accounts for the seawall's features, such as the slope.

The coefficient a represents the dimensionless discharge when the dimensionless crest freeboard is zero. The coefficient b depends on the behavior of the water surface at the seaward face of the structure, specifically, it increases as front slopes become flatter. The values of these coefficients have been obtained by applying the least absolute deviations fitting to Owen's data (1980) of simple inclined seawalls.

Mase et al. (2013)

Mase et al. aimed to provide empirical formulae to determine the wave run-up and overtopping of seawalls on land or in very shallow water. Specifically, the overtopping model is based on that of Hedge and Reis (1998); thus, the overtopping process is related to the wave run-up process. The original structure of the Hedge and Reis' model has been slightly modified by introducing the deepwater significant wave height:

$$\frac{q}{\sqrt{g \cdot {H_{s,DEEP}}^3}} = \begin{cases} a \cdot \left(\frac{R_{MAX}}{H_{s,DEEP}}\right)^{\frac{3}{2}} \left[1 - \frac{\left(\frac{R_C}{H_{s,DEEP}}\right)}{\left(\frac{R_{MAX}}{H_{s,DEEP}}\right)}\right]^b & 0 \leq R_C < R_{MAX} \\ 0 & R_{MAX} < R_C \end{cases} \quad (2.17)$$

As mentioned above, Mase et al. has provided predictive formulae for wave run-up as well. It has been expressed as a function of the deep water wave steepness and an equivalent slope, $tan\beta$. The latter considers a cross-sectional area that includes seawall and foreshore slopes, from the wave breaking location to the run-up level (Figure 2.5).

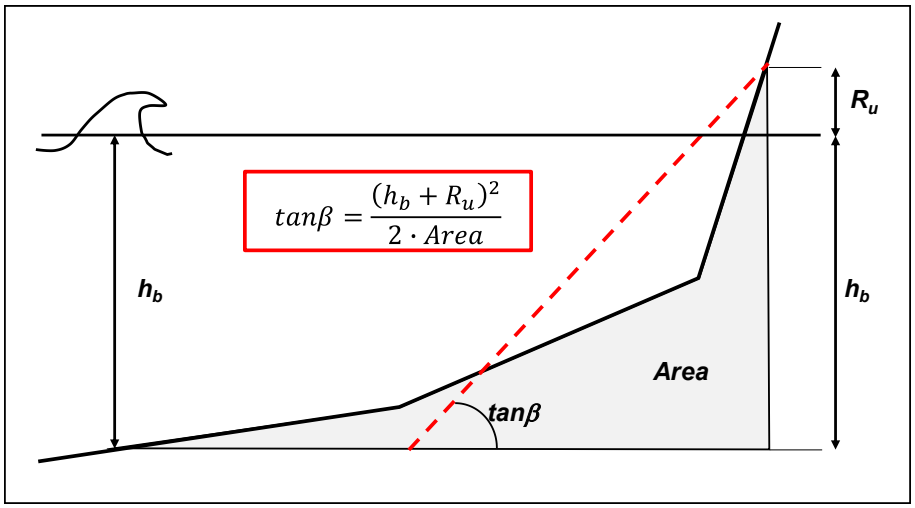

Figure 2.5 *– The equivalent slope proposed by Mase et al. (2013).*

As the equivalent slope of Altomare et al. (2016), the estimation of $tan\beta$ requires an iterative procedure. The run-up value depends on the equivalent slope, which in turn depends on the run-up level. Furthermore, the presence of water depth at the breaking location represents an additional drawback since the irregular wave train does not have a unique breaking point. However, the authors have provided a graph to determine h_b for a given value of deep water wave steepness and foreshore slope.

It is worth specifying that Mase et al. adopt deep water wave conditions because estimating wave conditions at the toe of the structure may be anything but easy, especially for seawalls constructed on the land.

The coefficients *a* and *b* in Eq. (2.17) have been inferred by a regression analysis of the dataset of Tamada et al. (2002), which contains 150 laboratory experiments on the overtopping of sloping seawalls. In particular, three different slopes were investigated ($tan(\alpha)$ = 1/3, 1/5 and 1/7), the dikes were located on two foreshore slopes ($tan(\alpha)$ = 1/10 and 1/30) from very shallow water up to the emerged land.
Recently, Yuhi et al. (2021) have re-calibrated the empirical coefficients by using 132 laboratory data from Altomare et al. (2016) and 270 data from the CLASH database.

2.3.4. Discussion

The mean overtopping discharge is still a key parameter in sea defense design and coastal risk assessment. However, the literature overview has revealed the lack of a unified definition of the hydraulic boundary conditions that better describe the overtopping process.

As clearly indicated in Table 2.1, from the first to the more recent empirical models, the wave parameters (wave height and period) or the wave run-up level alternate for estimating the flow rate. Moreover, an additional difference exists for the overtopping models that resort to the wave parameters; indeed, authors adopt either the incident wave conditions (at the toe of the structure) or the deep water ones.

The predictive models based on a run-up level (among them, Etemad-Shahidi et al., 2022; Mase et al., 2013; Hedge and Reis, 1998) are physically consistent since wave overtopping occurs when the run-up height exceeds the crest height of the structure. However, they are affected by several drawbacks; using a wave-structure interaction process to predict another wave-structure interaction process is an arduous path.

The primary weakness is thus related to the previous estimation of wave run-up before estimating q. Various empirical formulae can be employed (e.g. Hughes, 2004; Pillai et al., 2019; EurOtop 2018) and, as observed by Altomare et al. (2020), the wave run-up model adopted will affect the prediction of the mean overtopping discharge.

Furthermore, the uncertainties related to the empirical formulae employed to derive the predictors can sabotage even the most robust overtopping model, as shown by Yuhi et al. (2021). Although the authors have refined the Mase et al.' overtopping model to obtain conservative predictions generally, the validation process revealed some underestimations of q that result from the underestimation of the predictive variable, R_{MAX}. Hence, providing an empirical formula to assess the run-up height previously does not exonerate the overtopping model from the uncertainties that typically affect every empirical model.

Finally, some of the models that adopt R_u are based on iterative procedures – see the equivalent slope determination in either Mase et al. (2013) or Altomare et al. (2016) – that make demanding the use of the predictive model.

On the other hand, the overtopping models that require the wave conditions (either in deep waters or at the toe of the structure) are also affected by several uncertainties.

The use of incident wave conditions assumes that these hydraulic variables already accounted for the effects of the foreshore (uniform or uneven) on wave transformation. However, this is an illusory advantage since estimating wave parameters in very shallow water and heavy breaking conditions is challenging, especially for the harmonic spectral period, as will be highlighted in the next Chapter.

To overcome this limitation, deepwater-wave-based models have been developed (see Lashley et al., 2021). Using wave characteristics in deep water avoids the difficulties related to the appropriate estimation of the incident wave parameters. Nevertheless, this type of overtopping model is typically calibrated with uniform foreshores; they do not account for the effect of uneven beaches on wave transformation and then on wave overtopping. Thus, predictions of q presume regular topographic conditions and are, therefore, less general compared to the use of incident parameters.

3. SPECTRAL BASED PREDICTORS AND RELATED DRAWBACKS

Chapter 2 highlights that a large number of predictive models (e.g., EurOtop manual and machine learning techniques) relate the mean overtopping discharge to the spectral wave conditions. Specifically, the extensive work of Van Gent (1999a,b) on wave overtopping in shallow water first introduces the use of these variables, which the literature has successively embraced.

3.1. Wave height

The significant wave height, either at the toe of the structure or in deep water, is the main variable of the predictive models that adopt wave conditions to estimate the flow rate.

However, while the significant wave height can be equally derived from a frequency or time domain analysis in deep waters, in depth-limited conditions the Rayleigh distribution fails. Therefore, for structures located in shallow waters, it is necessary to resort to either the spectral analysis or to an alternative distribution valid in the surf zone (e.g. Battjes and Groenendijk, 2000; Buccino and Calabrese, 2002).
It is worth noting that also alternative approaches have been adopted to consider a suitable wave height. Owen (1980) used an equivalent wave height, $H_{sb}= \gamma h_{TOE}$, which properly describes the overtopping process in the surf zone (Section 2.3.2). de Waal and Van der Meer (1992), Van der Meer and Janssen (1994) and Van der Meer (1997) resorted to an empirical reduction coefficient to take the effect of shallow foreshore on wave height into account.

Van Gent (1999b) performed a sensitive analysis to find the characteristic wave height more suitable for estimating wave run-up and overtopping in shallow water conditions. The author has examined the relationship between the surf-similarity parameter, ξ, and either wave run-up or overtopping with three different wave heights, namely H_{m0}, $H_{1/3}$ and $H_{2\%}$. The wave period used to derive the surf similarity parameter was T_{m-10}. Although slight differences occur by varying wave heights, each of them appears suitable to describe wave run-up and overtopping processes; the work of Van Gent introduced the use of spectral wave conditions in the overtopping estimation.

Since the beginning of the new century, when the study of wave overtopping in shallow waters has become more widespread, H_{m0} has been accepted as the characteristic wave height, as reported in various manuals (EurOtop, 2018; EurOtop, 2007; TAW, 2002). The significant spectral wave height can be determined by the total variance of the process, m_0, as specified in Van Gent and Giarrusso (2003):

$$H_{m0} = 4\sqrt{m_0} \tag{3.1}$$

Waves experience the breaking phenomenon, which induces both a reduction in wave energy and a variation in the energy distribution along the spectral bandwidth, with the appearance of low-frequency components.

Van Gent and Giarrusso have explored the influence of these components on the overtopping phenomenon. With a study based on field measurements at Patten Sea-defense (The Netherlands) and a numerical analysis, the authors pointed out that proper estimation of wave overtopping requires the whole wave energy rather than just that related to short waves. This has been demonstrated by comparing the numerical overtopping results obtained with and without the low-frequency energy in the incident wave trains. The analysis revealed that when the percentage of low-frequency energy in the wave spectrum is higher than 20%, the flow rate significantly increases if the whole amount of energy is considered. Therefore, the total variance of the process needs to be accounted for to avoid underestimations of the mean overtopping discharge.

Several approaches exist to estimate the spectral wave height at the toe of the structure with shallow foreshores. Physical model tests or sophisticated numerical models may provide accurate estimation even for very shallow water conditions with heavy wave breaking. However, phase-averaged numerical models equipped with breaking models that also account for long-wave components (e.g. Battijes and Janssen, 1978) or suitable empirical formulae are valid tools. Among the latter, either the predictive formula of Kamphuis (1996) or Lashley et al. (2021) could be used.

Kamphuis's formula is the outcome of an extensive experimental campaign carried out at the Queen's University Coastal Engineering Research Laboratory, which investigated the transformation of irregular waves on 1/50 foreshore slope. The formula reads:

$$H_{m0,TOE} = 0.56 \cdot \exp[3.5 \cdot \tan(m)] \cdot (h_{TOE} + 0.1 H_{m0,b}) \tag{3.2}$$

where $H_{m0,b}$ is the spectral wave height at the breaking point. Actually, Eq. (3.2) represents a slight variation of the formula proposed by Kamphuis (1991) for regular waves. Such a modification includes the effects of wave set-up and low-frequency components on the wave height at the toe of the structure in very shallow waters.

Recently, Lashely et al. (2021) have gathered about 1000 data from numerical and physical model tests to derive an empirical formula that allows to easily estimate $H_{m0,TOE}$:

$$\frac{H_{m0,TOE}}{H_{m0,DEEP}} = M \cdot \frac{h_{TOE}}{H_{m0,DEEP}} + C \tag{3.3}$$

with

$$M = 0.35 \cdot \frac{\tan(m)^{0.1}}{s_{m-1,0}^{0.2}} \tag{3.4}$$

$$C = 0.95 \cdot \tan(m)^{0.15} - 0.3 \tag{3.5}$$

Hence, in Eq. (3.3), the spectral wave height at the toe of the structure depends on the deep water wave condition (through the deepwater wave height and steepness) and the foreshore slope. However, although the

investigated range of *tan(m)* varies between 1/10 and 1/1000, the predictive formula has been derived with uniform slopes only.

The Lashley et al.' model assumes that the wave steepness barely affects the wave height as water becomes shallower, and the water depth governs $H_{m0,TOE}$. Furthermore, the steeper the foreshore, the higher the wave height in the surf zone – lower energy decay occurs. Finally, consistent with the model of Goda (2000), Eq. (3.3) provides a finite value of the spectral wave height even if $h_{TOE} = 0$.
It is worth specifying that, unlike Goda's model that considers IG-waves through the increase of the mean water level, Lashley et al. directly included them in $H_{m0,TOE}$.

3.2. Wave period

The historical analysis of the predictor variables accomplished in Section 2.3.1 has pointed out the clear role of wave period on the overtopping process. From the design diagrams of Goda et al. (1975) or the predictive model of Owen (1980) to the recent works of Altomare et al. (2016) or Lashley et al. (2021), the large amount of literature agrees that longer waves produce larger overtopping discharges.

However, Table 2.1 shows that different wave periods have been adopted over the years. Owen used the mean zero-crossing wave period, T_m, while Van der Meer and Janssen (1994) referred to the peak period, T_p. Nevertheless, as highlighted by Hofland et al. (2017), in the last two decades, the harmonic spectral period, T_{m-10}, has been accepted as the characteristic wave period to describe the wave-structure interaction processes, such as wave overtopping.

At the end of the last century, researchers wondered how to account for the effects of different wave energy spectra and which characteristic period was better suited to predict wave run-up and wave overtopping. The coexistence of swell and sea waves or the presence of shallow foreshores indeed involve that wave energy spectra at the toe of coastal structures are no longer characterized by a narrow spectral band but often experience double or multi-peaked. Therefore, the adequacy of the deepwater peak period in the overtopping models was questioned by researchers.

Hence, two different approaches have been adopted to identify a more suitable wave period.

The first was the geometric approach of Van der Meer (1997), which proposes an equivalent peak period determined by a weighted average of peaks of the energy spectrum, $T_{p,eq}$. Specifically, the double-peaked spectrum is split into two areas, and then the wave energy and peak frequency are detected for each of them (Figure 3.1). Thus, $T_{p,eq}$ can be determined:

$$T_{p,eq} = \sqrt[4]{\frac{m_{0\_1}}{m_0} \cdot T_{p\_1}^4 + \frac{m_{0\_2}}{m_0} \cdot T_{p\_2}^4} \tag{3.6}$$

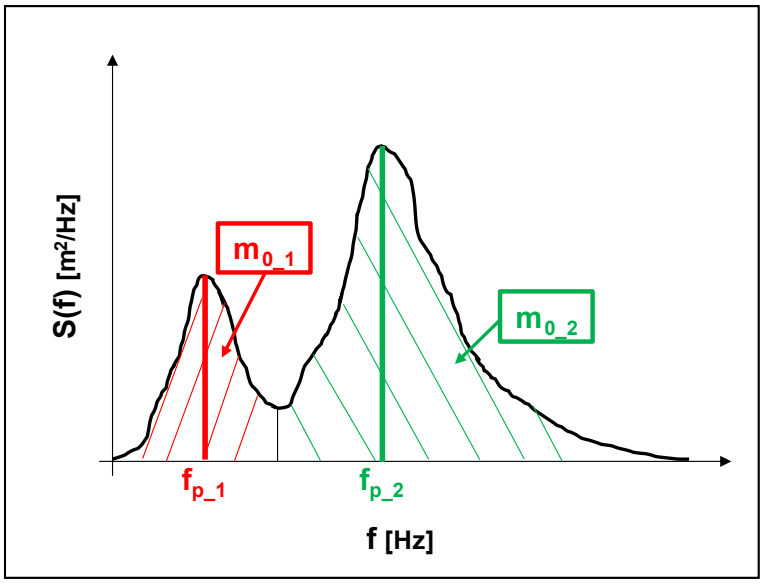

Figure 3.1 – Geometric approach of van der Meer (1997) to identify the equivalent peak period.

On the other hand, inspired by the work of Holterman (1998), Van Gent (2001, 1999a,b) used a spectral moments-based approach, which allows predictions of wave run-up and overtopping either regardless the shape of spectra (single, double or multi-peaked) or without the need for detection of local peaks in the wave energy spectrum.

In its first study (Van Gent, 1999a), the author has numerically investigated the effects of wave energy spectra on wave run-up and wave overtopping, focusing on double-peaked spectra and verifying whether a characteristic wave period can be determined.

A Non Linear Shallow Water model was used to reproduce these wave-structure interaction phenomena. Numerical experiments considered two sloping dikes with a constant value of h_{TOE}; the total wave energy was kept constant, while the peak period was significantly varied (the range of wave steepness is 0.001÷0.04). Both single and double-peaked spectra were examined. The latter were obtained by the superimposition of two TMA spectra, which are characterized by different amounts of wave energy per peak and a variation in their mutual distance (Figure 3.2).

Van Gent qualitatively examined the scatter plots showing the relationship between the surf-similarity parameter relative to various wave periods, ξ, and both wave run-up height and mean overtopping discharge to determine which period was more suitable to characterize these phenomena. Specifically, these relationships were analyzed in dimensionless form (i.e. $R_{2\%}/H_s = f(\xi)$ and $q/\sqrt{gH_s^3} = f(R_C/H_s \cdot \xi)$ for wave run-up and overtopping, respectively).

In addition to the peak period, both periods based on time-domain analysis (the mean wave period, T_m) and spectral analysis were examined. It is worth pointing out that T_p is defined as the period relative to the global maximum of the wave energy spectrum. Regarding the spectral periods, the basic idea was that spectral moments can be easily predicted, regardless of the spectrum's shape. Moreover, spectral periods based on

negative moments (e.g. $T_{m-1,0}$) were carefully investigated because they emphasize the low-frequency components of the spectrum. Since the wave run-up of individual waves with longer periods is higher than that with shorter periods, the author considered that lower frequencies are likely more important than higher ones. Numerical results showed that both $T_{m-1,0}$ and $T_{m-2,0}$ significantly reduce the scatter around the main trend compared to T_p; furthermore, contrary to the results obtained using T_m, no influence of the distance between the peaks of the spectrum was observed. Finally, $T_{m-1,0}$ and $T_{m-2,0}$ appeared more suitable than $T_{m0,1}$ and $T_{m0,2}$ to predict wave run-up with double-peaked energy spectra. Analogous results were obtained for wave overtopping.

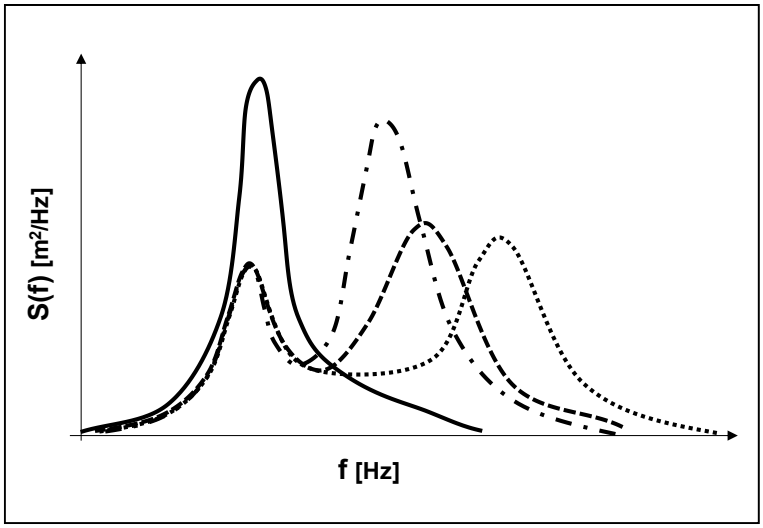

***Figure 3.2** – Example of single and double-peaked wave spectra used in Van Gent (1999a) numerical analysis; the picture shows the variation in the distance between the spectrum peaks and in the amount of wave energy per peak.*

Subsequently, Van Gent (2001, 1999b) has extended the analysis to the influence of wave spectra on wave run-up and overtopping of dikes with shallow foreshores. Indeed, due to both the wave breaking and triad interaction phenomena during wave propagation, the presence of foreshores leads to a substantial transformation in the shape of spectra. The milder the foreshore, the greater the shape change.

Physical experiments have been performed at the Scheldt Flume of Deltares to study the evolution of single and double-peaked energy spectra on two different mild foreshores (inclined 1/100 and 1/250 to the horizontal plane), along with the wave run-up and overtopping at dikes characterized by two different slopes (1/4 and 1/2.5). The water depth at the toe of the dike has been varied in order to obtain deep, intermediate and shallow water conditions (according to the definition provided in Van Gent, 1999b). Both single-peaked JONSWAP and double-peaked spectra (obtained by superimposing two JONSWAP spectra) were investigated. The procedure was similar to that used in the numerical investigation (Van Gent, 1999a).

The aim was to analyze the influence of wave spectra and wave height distribution on wave run-up and overtopping in shallow waters. As in the previous work, the author's conclusions were derived from the relationships between the dimensionless run-up height (dimensionless flow rate) and the surf-similarity

parameter related to different wave periods at the toe of the dike, i.e. T_p, T_m and spectral periods. A scatter plots inspection confirmed that $T_{m-1,0}$ is the appropriate period to describe run-up and overtopping phenomena, whatever the shape of the incident wave spectrum.

Furthermore, Van Gent performed a quantitative analysis by evaluating the scatter of the data around the run-up and predictive models proposed in the work (see Section 2.3.2). Using the harmonic spectral period in the surf-similarity parameter provided the lower values of the root mean square error, confirming the conclusions drawn from the visual inspection.

The works of Van Gent represented a tipping point in coastal engineering. Thenceforth, the harmonic mean spectral period $T_{m-1,0}$ has been considered the characteristic period in wave-structure interaction processes (Hofland et al., 2017). This has been preferred due to the greater weight given to longer periods in the spectrum (Altomare et al., 2016). Particularly in case of very shallow foreshore and heavy wave breaking, the spectrum becomes flattened – no well-defined peaks can be identified – so $T_{m-1,0}$ appears to be the "obvious parameter", as reported in TAW (2002).

3.2.1. Uncertainties about the estimation of T_{m-10}

Although the harmonic period seems crucial for predicting the flow rate in shallow waters, its estimation is far from straightforward. In fact, $T_{m-1,0}$ is defined as:

$$T_{m-10} = \frac{m_{-1}}{m_0} \tag{3.7}$$

where m_n is the n^{th} order of the wave spectrum; thus, it is necessary to assess both the total amount of wave energy, m_0, and where this energy gathers along the frequency bandwidth, m_{-1}. In particular, since the -1 spectral moment lends weight to the low-frequency energy, T_{m-10} strictly depends on the presence of the infragravity waves.

Munk (1949) and Tucker (1950) first observed the presence of these low-frequency waves, which have been successively sparked a growing interest in many researchers (among them Longuet-Higgins and Stewart, 1962; 1964; Guza and Thornton, 1982; Symonds et al., 1982; Ruessink et al., 1998; Baldock et al., 2000; van Dogeren et al., 2007; De Bakker et al., 2016; Bertin et al., 2018) due to their significant effects on many coastal phenomena (e.g. nearshore hydrodynamics, sediments transports, dune and barrier breaching).

As first stated by Munk (1949) and Tucker (1950), the IG-waves are related to the presence of the groupness in the incident short wave trains. Specifically, two main generation mechanisms can be distinguished.
The first concerns the so-called bound waves, which are secondary wave of a similar frequency as the group, as demonstrated by Longuet-Higgins and Stewart (1962). This generation mechanism already occurs in deep water, where the modulation of the waves causes a variation in radiation stress at the time scale of incident group that forces a slight undulation in the mean sea level that can be seen as a wave itself; this is a set down

wave that travels phase-locked (in antiphase) to the wave group, so it is called bound wave. As the wave train moves shoreward, the phase difference between short and bound waves shifts away from 180 ° so that the long waves lag behind the wave groups (Masselink, 1995; Janssen et al., 2003; De Bakker et al., 2013); such a phase shift ensures growth of the bound waves due to the energy transfer from short waves (Van Dongeren et al.,2007). In shallower water, when wave breaking occurs, the bound IG-waves are released and propagate as free waves (Masselink, 1995; Janssen et al., 2003; Battjes et al., 2004; Baldock, 2012).

The second generation mechanism is due to the time-varying breaking point. Within an irregular wave train, the higher waves break seaward than the shorter ones, leading to a time variation in the breaking position that generates waves at the group period, i.e. surf beats. Hence, the source of wave energy at lower frequencies is due to a time variation of the radiation stress gradient that is balanced by a time-varying mean sea level. This generation mechanism was first analyzed by Symonds et al. (1982), which dealt with it as a wave-maker type problem; the zone between the minimum and maximum breaking point positions represents a forcing region that radiates seaward and shoreward these free long waves. The simplified analytical approach of Symonds et al. was successively enhanced by Shaffer and Svendsen (1988) and Shaffer (1993).

In addition to these main generation mechanisms, the bore merging in the inner surf zone of gentle dissipative beaches can contribute to the energy transfer from short waves to low frequency waves. However, it is considered a minor mechanism for IG-wave generation (Tissier et al.,2017; Bertin et al., 2018).

Once generated, the free long waves propagating shoreward can be fully reflected at the shoreline or dissipated through different mechanisms (Battjes et al., 2004). In particular, Battjes et al. introduced a normalized bed slope parameter that distinguishes between a “mild-slope” and a “steep slope” regime; the steeper the regime, the longer waves tend to a nearly full reflection. These findings have been successively corroborated by several studies (Van Dongeren et al., 2007; De Bakker et al., 2014; Inch et al., 2017). The reflection of IG-waves at the shoreline can lead to refractively trapped motions which could turn into periodic alongshore-travelling patterns, also referred to as edge waves.

In mild-slope regimes, surf beats can be dissipated near the shoreline, as observed in field, laboratory and numerical studies (e.g. Ruessink, 1998; Henderson et al., 2006; Van Dongeren et al., 2007; De Bakker et al., 2014; Inch et al., 2017). Three dissipation sinks have been discerned: the bottom friction, which does not have significant effect on the natural beaches; the energy transfer back to the higher frequencies and the breaking of the higher IG-harmonics (see Pomeroy et al., 2012; De Bakker et al., 2014; Fielder et al., 2015).

Overall, the correct estimation of the harmonic spectral period within the surf zone requires tools able to account for the complex behaviors of the surf beats described above.

3.2.2. Empirical tools for estimating T_{m-10}

The brief overview of the surf beat features makes the difficulties in the harmonic spectral period’s estimation emerge.

While in deep water, T_{m-10} can be easily derived from the peak period (according to the deepwater relationship $T_{m-1,0}/T_p$ = 0.9 for narrow band process), shallow water cases require either physical model measurements or phase-resolving numerical models.

However, some researchers have recently attempted to simplify the estimation process by providing empirical formulae. In particular, Hofland et al. (2017) pursued this aim and proposed an engineering tool.
The formula has been derived by gathering information from different datasets, which include the results obtained by Van Gent (1999b) on two mild foreshore slopes (*tan(m)* = 1/100 and 1/250) along with the data of Chen et al. (2015) and Altomare et al. (2016) carried out at the Flanders Hydraulic Research on a foreshore slope inclined 1/35 to the horizontal. Steeper seabeds have not been considered. The data are characterized by a wave steepness range between 0.01 and 0.045. The experiments include wave measurements from shallow to extremely shallow water. According to the normalized bed slope parameter introduced in Battijes et al. (2004), the datasets used to derive the empirical tool make it valid for a mild-slope regime.
The empirical equation obtained by fitting the data reads:

$$\frac{T_{m-1,0,TOE}}{T_{m-1,0,DEEP}} - 1 = 6 \cdot exp\left(-4 \cdot \tilde{h}\right) + exp\left(-\tilde{h}\right) \tag{3.8}$$

where $\tilde{h}$ is:

$$\tilde{h} = \frac{h_{TOE}}{H_{mo,DEEP}} \cdot \left(\frac{\cot(m)}{100}\right)^{0.2} \tag{3.9}$$

Thus, Hofland et al. relate $T_{m-1,0,TOE}$ to the deepwater wave conditions and take the wave evolution process into account by means of the water depth and the foreshore slope, *cot(m)*. An exponential growth of the harmonic spectral period has been observed as the water decreases. Specifically, the authors adopted two exponential terms to fit the data well for shallow and extremely shallow foreshores; indeed, the harmonic spectral period can be eight times larger than the value in deep water.
Nevertheless, Eq. (3.9) has been derived using long-crested wave data. Thus, Hofland et al. performed a series of numerical experiments by means of the non-hydrostatic model XBeach (Smit et al., 2013) to acquire information on the harmonic spectral period with short-crested conditions. Such an analysis reveals that the directional spreading ensures a slower increase in the harmonic spectral period that occurs much closer to the shoreline; hence, the authors proposed an additional formula that takes the directional spreading effect into account:

$$\frac{T_{m-1,0,TOE}}{T_{m-1,0,DEEP}} - 1 = 6 \cdot exp\left(-6 \cdot \tilde{h}\right) + 0.25 \cdot exp\left(-0.75 \cdot \tilde{h}\right) \tag{3.10}$$

More recently, Mahmoudof et al. (2023) have tried to investigate the realistic shoreward variation of the harmonic spectral period over a complex bathymetry since the Hofland et al.' formula has only been derived from uniform slopes. In particular, Mahmoudof et al. analyzed the field measurements carried out on a mild barred beach in the Southern Caspian Sea with four events, including two high-energy and two moderate-energy events.

The comparison with field measurements has shown that the Hofland et al.' empirical tool underestimates the harmonic spectral period. According to the authors, this is due to the presence of offshore generated IG-waves – missing in physical model experiments – which enhance the value of T_{m-10}. Therefore, Mahmoudof et al. have provided a new predicted formula:

$$\frac{T_{m-1,0,TOE}}{T_{m-1,0,DEEP}} - 1 = 6.084 \cdot exp\left(-1.207 \cdot \frac{h_{TOE,s}}{H_{m0,DEEP}}\right) \tag{3.11}$$

where $h_{TOE,s}$ includes wave set-up (set-down) to better describe the foreshore depth. Otherwise, following the approach of Hofland et al. that adopts the still water level (i.e. neglecting the wave set-up), field observations can be fitted by the following equation:

$$\frac{T_{m-1,0,TOE}}{T_{m-1,0,DEEP}} - 1 = 6.691 \cdot exp\left(-1.657 \cdot \frac{h_{TOE}}{H_{m0,DEEP}}\right) \tag{3.12}$$

Figure 3.3 plots Eqs. (3.8) and (3.12); the comparison confirms that the Hofland et al.'s model may underestimate field values of the harmonic spectral period.

However, this work analyzed a single site, thus the model neglects the foreshore slope effect pointed out in Hofland et al. (2017). Mahmoudof et al. indeed recommend to investigate different natural beaches to evaluate the seabed's influence on the shoreward growth of the harmonic spectral period.

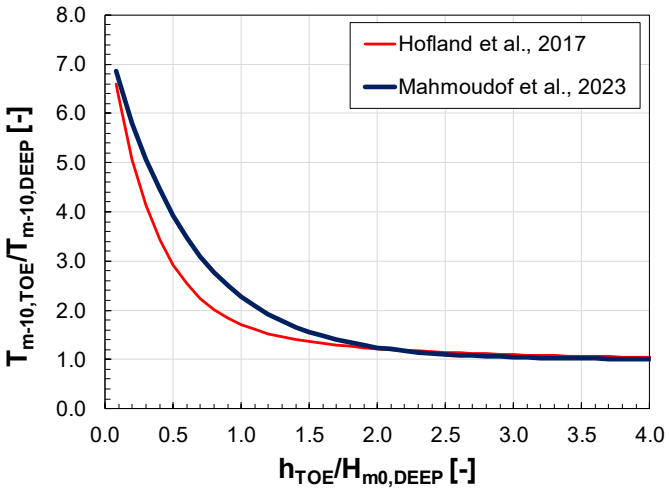

Figure 3.3 *– Comparison between Eq. (3.12) and Eq. (3.8); the latter has been plotted by considering a foreshore slope equals 1/30.*

Hence, although some authors have tried to simplify it by providing empirical formulae (see Eqs. (2.9-2.13)), some drawbacks weaken their utility. The Hofland et al.' formula has been derived from laboratory experiments conducted on planar beaches; indeed, it may not take into account the complex processes described above, as demonstrated in Mahmoudof et al. (2023), leading to underestimation of T_{m-10}. On the other hand, the latter have proposed an empirical formula based on field observations. However, it requires a more in-depth analysis as only one case study has been investigated.

Therefore, the available empirical formulae may be a helpful tool for the engineering community. However, they can easily lead to incorrect estimations that can compromise the design of sea defense structures.
The overtopping formulae based on spectral predictors need either physical or phase-resolving models as these ensure an accurate estimation of spectral variables in very shallow water conditions, as also specified in the EurOtop manual. In particular, more sophisticated numerical models (i.e. phase-resolving type) are essential since phase-averaged models provide any information about the wave energy distribution along the spectral bandwidth. This makes the overtopping estimation process in shallow water conditions more challenging and demanding. Paradoxically, using a simplified overtopping predictive model, such as an empirical formula, needs quite sophisticated numerical models for assessing the hydraulic predictors.

4. WAVE OVERTOPPING AT VERTICAL SEAWALLS

Seawalls are shore-parallel structures designed to prevent coastal risks, such as further shoreline erosion and flooding, and to protect infrastructures or roads from wave action (Allsop et al., 2005; Kraus and McDougal, 1996). In particular, these coastal defenses are critical in protecting communities and infrastructure from the risks of wave run-up and overtopping during storm events. Indeed, seawalls are common in urban landscapes since they need little space to be built and can be located landward of the mean high water shoreline as well. Moreover, an environmental advantage characterizes them since seawalls placed on the backshore do not alter the nearshore circulation, compromise water quality, or affect visual impact, preserving the aesthetic and environmental value of the beach.

However, despite their defensive scope and advantages, seawalls could have a negative impact on the coasts, producing erosion. In particular, passive and active erosion can be distinguished. The former occurs regardless of the presence of the structure, whereas the active erosion is due to the interaction of the wall with local coastal processes (Kraus and McDougal, 1996; Griggs 2010; Nordstrom, 2014; Schoonees et al., 2019). Moreover, this mutual interaction can even lead to seawall failure (e.g. the scour at the toe of the structure due to the wave reflection may result in the overturning of the wall). Hence, seawalls must be carefully designed so that they do not break in their defensive function.

The primary stress acting on a seawall is due to waves, which challenge the structure's stability and integrity. Thus, designers must take wave effects on seawalls into account to ensure adequate protection against flooding risks.

Wave overtopping is one of the main failure mechanisms of seawalls; it may subsequently cause hinterland flooding and jeopardize assets and human safety. Hence, overtopping-related variables are used in the design process to determine the crest freeboard of the wall. In particular, the latter has to ensure that the mean overtopping discharge and the maximum individual overtopping volume do not exceed the limits indicated in the guidelines (e.g. EurOtop, 2018; Rock Manual, 2007).

4.1. Prediction of mean overtopping discharge at vertical walls with shallow foreshore

This Section focuses on the existing empirical formulae for estimating the mean overtopping discharge of vertical walls with shallow foreshores.

However, as argued by Goda (2009), the terminology of "foreshore" can be somehow confusing as the literature includes different definitions (e.g., EurOtop, 2018; Van Gent, 1999b). Among them, this work refers to Hofland et al. (2017), which assumes that the shallowness of the foreshore can be characterized by combining the local water depth and the deep water significant wave height ($h_{TOE}/H_{m0,DEEP}$). Specifically, Hofland et al. classify the foreshore as:

- *deep* ($h_{TOE}/H_{m0,DEEP} > 4$): where no depth-induced wave breaking occurs;

- *shallow* ($1 < h_{TOE}/H_{m0,DEEP} < 4$): the water depth starts to influence the wave breaking, even if the wave spectrum still experiences a clear single peak;
- *very shallow* ($0.3 < h_{TOE}/H_{m0,DEEP} < 1$): the energy at the high frequencies (near the deep water peak frequency) has been mainly dissipated and large amount of energy at lower frequencies arises;
- *extremely shallow* ($h_{TOE}/H_{m0,DEEP} < 0.3$): most of the high frequency part of the spectrum has been dissipated and the low-frequency energy is dominant.

EurOtop 2018

The EurOtop Manual (2018) provides different predictive formulae depending on several factors, as proved by the decision chart – recalled in Figure 4.1 – that launches the Manual's chapter regarding vertical walls. As can be appreciated in Figure 4.1, the primary division excludes the structures in relatively deep water, which are not affected by the presence of the foreshore. Such a division has been introduced in the second edition of the EurOtop manual, resulting from the analysis of Van der Meer and Bruce (2014). The analysis only concerns the left side of the decision chart (delimited with the red rectangle in Figure 4.1), as this work focuses on seawalls in shallow water.

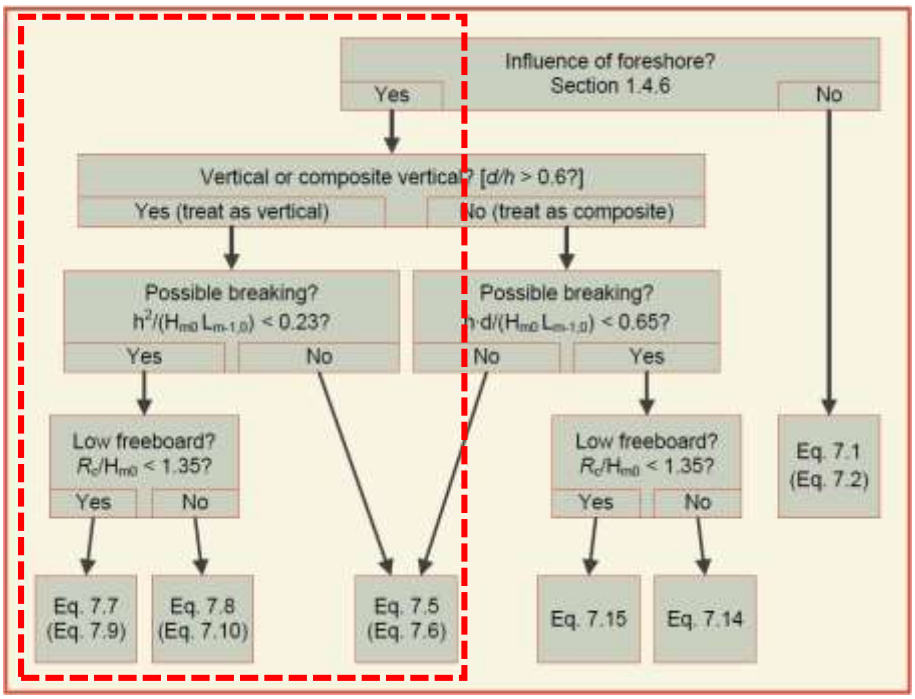

***Figure 4.1** – Decision chart reported in the Chapter 7 of the EurOtop manual (2018); the delimited part includes the empirical formulae analyzed in this work.*

Beyond the presence of the small toe berm (the so-called composite vertical wall), further discriminations characterize the design process of vertical walls. The Manual first distinguishes between breaking and non-breaking waves; then, in the former group, the predictive model varies depending on the relative crest freeboard's height. It is worth noting that the EurOtop Manual 2007 already included these distinctions.

To discriminate between breaking and non-breaking waves, the impulsiveness parameter, h^*, is used, which distinguishes between "non-impulsive" or "pulsating" ($h^* > 0.23$) and "impulsive" conditions ($h^* \leq 0.23$). The former occurs when waves are relatively small relative to the local water depth, while the impulsive condition describes waves that break along the foreshore or against the wall. The equation of the impulsiveness parameter reads:

$$h^* = \frac{{h_{TOE}}^2}{H_{mo,TOE} \cdot L_{m-10,TOE}} \tag{4.1}$$

where $L_{m-10,TOE}$ is the deep water wavelength related to $T_{m-10,TOE}$.

For non-breaking waves, $h^* > 0.23$, the EurOtop 2018 suggests:

$$\frac{q}{\sqrt{g \cdot {H_{m0,TOE}}^3}} = 0.05 \cdot exp\left(-2.78 \frac{R_C}{H_{mo,TOE}}\right) \tag{4.2}$$

which is depicted in Figure 4.2a. The two coefficients in Eq. (4.2) refer to the mean value approach, which provides the mean value of the stochastic parameters; in the design (semi-probabilistic) approach, the uncertainty related to the prediction is included, so the coefficients become 0.062 and 2.61, respectively.

On the other hand, two equations are used to describe the overtopping of breaking waves depending on the relative crest freeboard value (Figure 4.2b). For low-crested structure, an exponential formula is provided; otherwise, the overtopping model follows a power law:

$$\frac{q}{\sqrt{g \cdot {H_{m0,TOE}}^3}} = \begin{cases} 0.011 \cdot \sqrt{\frac{L_{m-10,TOE}}{h_{TOE}}} \cdot exp\left(-2.2 \frac{R_C}{H_{mo,TOE}}\right) & \frac{R_C}{H_{mo,TOE}} < 1.35 \quad \text{(4.3a)} \\ 0.0014 \cdot \sqrt{\frac{L_{m-10,TOE}}{h_{TOE}}} \cdot \left(\frac{R_C}{H_{mo,TOE}}\right)^{-3} & \frac{R_C}{H_{mo,TOE}} \geq 1.35 \quad \text{(4.3b)} \end{cases}$$

The coefficients in Eq. (4.3) are those relative to the mean value approach; in the design approach, the coefficients are 0.0155 in Eq. (4.3a) and 0.002 in Eq. (4.3b).

Unlike the predictive model for pulsating waves (Eq. (4.2)), the EurOtop formulae relate the mean overtopping discharge in impulsive conditions to both the significant wave height and the harmonic spectral period.

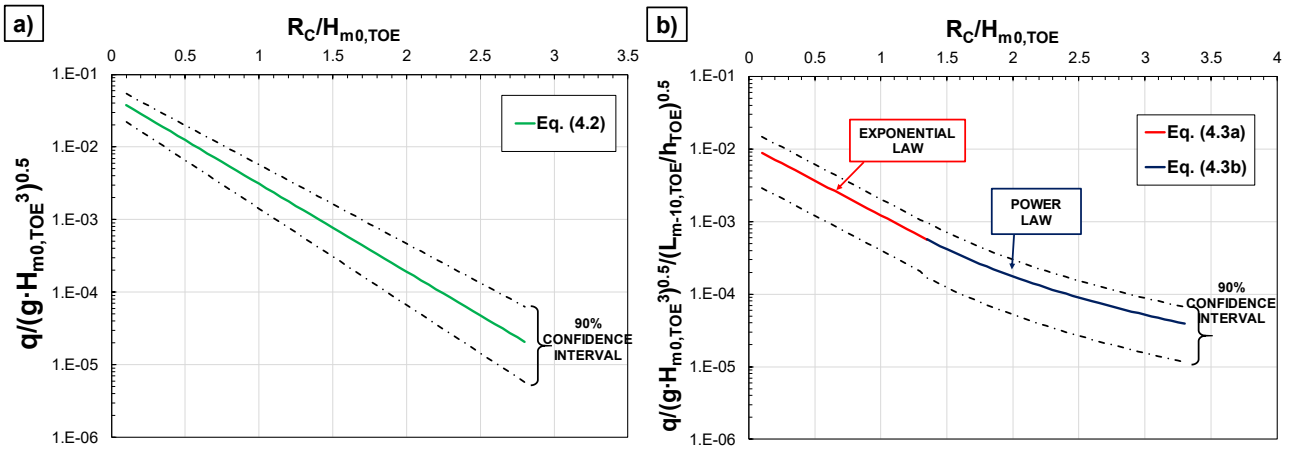

Figure 4.2 *– EurOtop formulae. Panel a) depicts the empirical equation for pulsating wave conditions; panel b) refers to impulsive loadings. Solid curves represent the formulae determined using the mean values of the empirical coefficients, while the dash-dotted lines are the 90% confidence bands.*

Goda (2009)

Goda (2009) questioned the division between impulsive and pulsating behaviors in the EurOtop Manual (2007) and proposed instead a unique predictive model (Eq. (4.4)). The author indeed argued that the wave overtopping is due to a train of random waves, including non-breaking, breaking and broken waves.

Furthermore, Goda verified the performances of the EurOtop formula and observed a biased tendency of overestimation for large overtopping rates and underestimation for small overtopping rates; thus, the author aimed to provide a predictive model lacking bias.

The new predictive formula is valid for both vertical and sloping seawalls built at any depth from deep water to the shoreline. For the sake of clarity, the formula is recalled here:

$$\frac{q}{\sqrt{g \cdot {H_{s,TOE}}^3}} = exp\left[-\left(a + b\frac{R_c}{H_{s,TOE}}\right)\right] \tag{4.4}$$

Similar to Eq. (4.2), Goda's model takes only the incident wave height into account; the wave period does not appear in the formula. It is worth noting that, in this work, the author employed the significant wave height to denote either $H_{1/3}$ or H_{m0}, where $H_{1/3}$ can be determined with Goda's formula (2000).

The coefficients a and b in Eq. (4.4) have been determined based on selected CLASH datasets, which count 715 and 1254 data for vertical and sloping seawalls, respectively. These depend on the relative toe depth, $h_{TOE}/H_{s,TOE}$, on the foreshore slope, $tan(m)$, and on the surface slope for inclined seawalls. In the case of vertical wall, the expressions of a and b are:

$$a = 3.4 \cdot tanh\left[(0.956 + 4.44 \cdot \tan(m)) \cdot \left(\frac{h_{TOE}}{H_{s,TOE}} + 1.242 - 2.032 \cdot \tan(m)^{0.25}\right)\right] \tag{4.5a}$$

$$b = 2.3 \cdot tanh\left[(0.822 - 2.22 \cdot \tan(m))\left(\frac{h_{TOE}}{H_{s,TOE}} + 0.578 + 2.22 \cdot \tan(m)\right)\right] \quad (4.5b)$$

As verified in the work, the performances of Eq. (4.4) decreases for lower flow rates; indeed, Goda recommended to use its prediction formula for preliminary design only

IFORM – Mase et al. (2013), Yuhi et al. (2021)

On the other hand, Mase et al. (2013) relate the wave overtopping to the wave run-up. Hence, unlike the previous models, Mase et al.' formula adopts a run-up statistics as hydraulic variable; it was named later as IFORM (Integrated Formula of Overtopping and Run-up Modeling). As specified in Chapter 2, the IFORM is based on the approach of Hedges and Reis (1998), which considers two physical restraints: wave overtopping does not occur when the maximum run-up is lower than the crest of the seawall, and the flow rate remains finite when the crest freeboard is zero.

The predictive formula, reported in Chapter 2 (Eq. (2.17)), allows to estimate the mean overtopping discharge of seawalls located on land or in very shallow water. The flow rate depends on the maximum run-up, the crest freeboard and the deepwater significant wave height:

$$\frac{q}{\sqrt{g \cdot {H_{s,DEEP}}^3}} = f\left(\frac{R_{MAX}}{H_{s,DEEP}}; \frac{R_C}{H_{s,DEEP}}\right) \quad (4.6)$$

where the maximum run-up, namely the run-up height not exceeded in 99% of cases in runs of 100 waves assuming a Rayleigh distribution, is related to $R_{2\%}$ and can be determined by means of the following equation:

$$R_{MAX} = 1.54 \cdot R_{2\%} = 1.54 \cdot H_{s,DEEP}\left[2.99 - 2.73exp\left(-0.57 \cdot tan\beta / \sqrt{H_{s,DEEP}/L_{0,DEEP}}\right)\right] \quad (4.7)$$

It is worth noting that Mase et al. also provided a predictive model that refers to a most probable maximum run-up, namely the value not exceeded in 37% of the (cases assuming a Rayleigh distribution). However, for the sake of clarity, this work only refers to the run-up statistics in Eq. (4.7).

The term $tan\beta$ is the imaginary slope descripted in Figure 2.5 that takes into account a cross-sectional area of seawall and foreshore between the wave breaking point, h_b, and the run up level, $R_{2\%}$. Thus, an iterative approach is necessary. Furthermore, the model requires the water depth at breaking point, that is anything but easy to estimate for irregular wave trains. The authors provided a graph to estimate h_b based on the outcomes of the wave transformation model of Mase and Kirby (1993); however, it has been inferred with planar beaches only.

The Mase et al.' model has been successively modified by Tamada et al. (2015), which aimed to extend the applicability of the empirical formula to vertical or steep walls. They have introduced a coefficient that depends

on the structure's slope and is equal to 0.5 in case of vertical seawalls. The other two coefficients in Eq. (2.17) derive from a regression analysis of the laboratory data of Tamada et al. (2002); in particular, the regression analysis has been performed to obtain a conservative estimation for design purposes (regression line passes close to the upper limit of most of the experimental data). Nonetheless, the model significantly underestimates the flow rate for higher values of R_C/R_{MAX}, as shown in Figure 4.3.

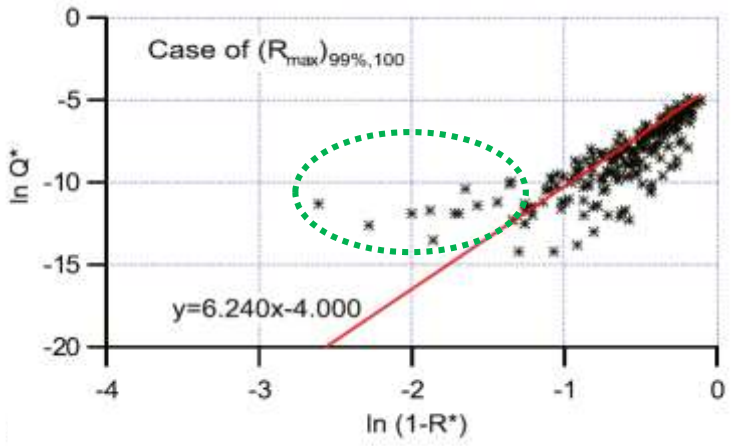

Figure 4.3 *– Figure 17b of Mase et al. (2013) that shows the experimental data and the regression line used to derive the empirical coefficients of the IFORM; the green ellipse highlights the underestimation of flow rates with higher relative crest freeboards.*

To extend the conservative performance of the model even to higher values of R_C/R_{MAX}, so providing reliable predictions under a broader range of overtopping conditions, Yuhi et al. (2021) have recently performed a new regression analysis and slightly modified the Mase et al.' model by using 132 laboratory data of Altomare et al. (2016) and 270 data of CLASH database. The formulation of the coefficients has been reconstructed with a set of piecewise formulas for three ranges of the relative crest freeboard (Figure 4.4):

$$ln\left(\frac{q}{\sqrt{gR_{MAX}{}^3}}\right) = 6.24 \cdot ln\left(1-\frac{R_C}{R_{MAX}}\right) - 4 \qquad ln\left(1-\frac{R_C}{R_{MAX}}\right) \geq -0.5 \qquad (4.8a)$$

$$ln\left(\frac{q}{\sqrt{gR_{MAX}{}^3}}\right) = ln\left(1-\frac{R_C}{R_{MAX}}\right) - 8.98 \qquad ln\left(1-\frac{R_C}{R_{MAX}}\right) \leq -1.4 \qquad (4.8b)$$

$$ln\left(\frac{q}{\sqrt{gR_{MAX}{}^3}}\right) = 2.91 \cdot ln\left(1-\frac{R_C}{R_{MAX}}\right)^2 + 9.15 \cdot ln\left(1-\frac{R_C}{R_{MAX}}\right) - 3.27 \qquad -0.5 \leq ln\left(1-\frac{R_C}{R_{MAX}}\right) \leq -1.4 \qquad (4.8c)$$

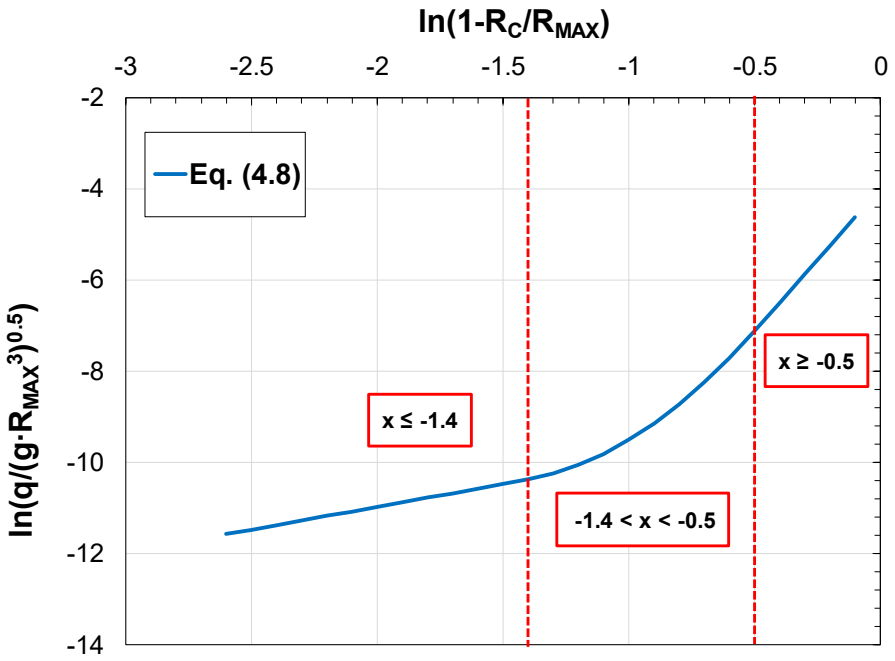

***Figure 4.4** – The new predictive model proposed in Yuhi et al. (2021).*

Lashley et al. (2021)

Lashley et al. (2021) have proposed a new predictive model for seawalls with very shallow foreshores based on deep water wave conditions to provide an alternative to the more common approaches, which require wave parameters at the toe of the structure as hydraulic predictors (e.g. EurOtop, 2018). As discussed in Chapter 2, estimating spectral wave parameters becomes tough with surf beats dominant conditions.
Overall, a deepwater-wave-based model avoids the drawbacks related to the use of either the incident wave conditions or the run-up level (see Section 2.3.4).

The authors revisited the graphical approach of Goda et al. (1975) and modelled the flow rate as a function the relative water depth, the relative crest freeboard, the foreshore slope and the deep water wave steepness. In particular, the presence of the seabed slope and the relative water depth ensures to adopt the deep water conditions instead of the incident one; indeed, consistent with Hofland et al. (2017), Lashley et al. have demonstrated that the foreshore effects on wave conditions at the toe of the structure can be accounted for by means of *tan(m)* and $h_{TOE}/H_{m0,DEEP}$.
By gathering three different datasets that include laboratory experiments of vertical walls with very and extremely shallow foreshores and emerged toe as well, the new proposed formula reads:

$$\frac{q}{\sqrt{gH_{m0,DEEP}^3}} = a \cdot exp\left(-b\frac{R_C}{H_{m0,DEEP}} + c\frac{h_{TOE}}{H_{m0,DEEP}}\right) \tag{4.9}$$

where the coefficients *a*, *b* and *c* rely on the deep water wave steepness and the foreshore slope and vary depending on the relative foreshore depth. In particular, the authors have identified three different regimes.
In very shallow regime ($0.5 \leq h_{TOE}/H_{m0,DEEP} < 1$), coefficients in Eq. (4.9) can be determined as follow:

$$a_1 = 0.90 \cdot \frac{\tan(m)^{2.05}}{s_{0,m-10}^{0.2}} \tag{4.10a}$$

$$b_1 = 5.1 \cdot \frac{s_{0,m-10}^{0.25}}{\tan(m)^{0.15}} \tag{4.10b}$$

$$c_1 = 0.70 \cdot \frac{s_{0,m-10}^{0.1}}{\tan(m)^{0.55}} \tag{4.10c}$$

whereas for extremely shallow regime ($0.1 \leq h_{TOE}/H_{m0,DEEP}$):

$$a_2 = 0.09 \cdot \frac{\tan(m)^{2.35}}{s_{0,m-10}^{1.25}} \tag{4.11a}$$

$$b_2 = 5.4 \cdot \frac{s_{0,m-10}^{0.3}}{\tan(m)^{0.45}} \tag{4.11b}$$

$$c_2 = 0.75 \cdot \frac{s_{0,m-10}^{0.5}}{\tan(m)^{0.6}} \tag{4.11c}$$

In case of transition zone, namely a third regime between very and extremely shallow foreshore ($0.1 < h_{TOE}/H_{m0,DEEP} < 0.5$) identified by the authors, the work suggests to use an exponential interpolation between the flow rates obtained using the coefficients of Eq. (4.10) and Eq. (4.11). On the other hand, the EurOtop formulae can be employed for seawalls with shallow and deep foreshores ($h_{TOE}/H_{m0,DEEP} >1$).
The functional form of the coefficients is in line with existing models that use the breaker parameter (i.e. the seabed slope to the square of wave steepness ratio), while the values of their exponents have been obtained using a trial-and-error approach to minimize the scatter. By means of these coefficients, the authors express the correlation between the overtopping discharge and the wavelength (the longer the waves, the larger the flow rates); moreover, steeper foreshores lead to the overtopping discharge increases.
The overtopping model has been derived assuming a straight uniform foreshore slope, so the authors did not recommend its direct feasibility on highly irregular bathymetry. A complex foreshore can indeed significantly affect the wave transformation, increasing the uncertainties related to a deepwater-wave-based overtopping model. However, Lashley et al. (2023) have recently introduced a new hypothetical slope that can be used in case of irregular bathymetry; it is a constant slope angle extending from a water depth equal to $H_{m0,DEEP}$ to the

toe of the structure. Nonetheless, such an equivalent slope has been validated against only a single event that occurred at the beach of Crosby (UK).

4.2.Discussion on the reliability of the available datasets

As mentioned above, the reliability of this type of predictive tool depends partially on the database used to calibrate them. Indeed, beyond the range of applicability, the data used to derive an empirical equation affects, to some extent, its validity. Therefore, the datasets employed by the previous models deserve to be discussed.

Figure 4.5 reports the dataset's characteristics (i.e. number of data and shallowness conditions) for the four predictive models previously discussed.

It is worth noting that the following Figure refers only to the data obtained in shallow water.

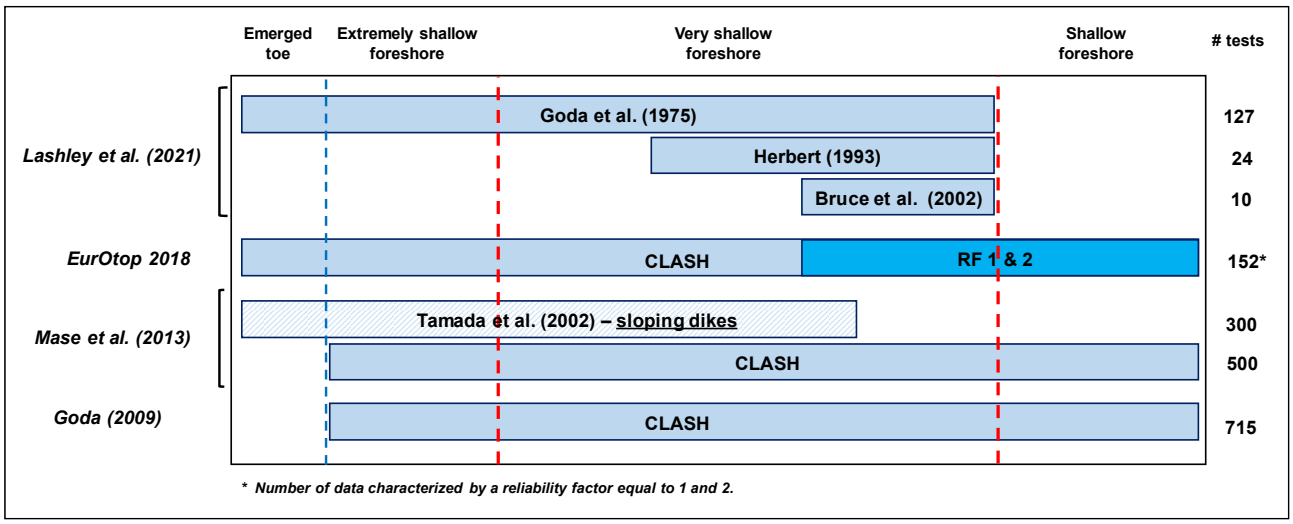

***Figure 4.5** – Datasets employed by the existing empirical formulae for estimating the mean overtopping discharge of vertical seawalls.*

Except for Mase et al. (2013), all the predictive models have used data on vertical walls contained in the CLASH database. On the other hand, Mase et al. have inferred the formula based on the dataset of Tamada et al. 2002, which refers to sloping dikes. Nevertheless, Tamada et al. (2015) have also resorted to the CLASH data to extend the formula to vertical structures.

However, despite the remarkable size, a large part of the database is characterized by low reliability. Analyzing in detail the shallow water data used in the EurOtop Manual, only 152 are labelled as "reliable", i.e. with a Reliability Factor (RF) equal to 1 and 2. During the data collection within the CLASH project, indeed, high RF was assigned to data when all required experiment information was available in the corresponding reports, and measurements and analysis were performed reliably. Conversely, no acceptable measurements and uncertainty tests led to low RF values (i.e., 3 or 4). Further information on the data classification can be found in Verhaeghe et al. (2008).

Moreover, just 9 out of 152 reliable data are in very shallow foreshore, with the lower value ($h_{TOE}/H_{m0,DEEP}$ = 0.82) near the shallow foreshore condition (Figure 4.6a). Thus, the reliable data used to derive the EurOtop formulae seem to contain a paucity of information on the overtopping process of vertical walls in shallow waters. Figure 4.6b confirms this assertion; the histogram shows that the whole reliable EurOtop dataset exhibits the harmonic spectral period at the toe of the structure to the deep water peak period ratio included between 0.8 and 1.1, namely the typical value for a single-peaked wave spectrum in deep water.

On the other hand, the presence of surf beats (Symonds et al., 1982; Shaffer and Svendsen, 1988), along with triad-interaction phenomena, implies that the energy spreads towards lower frequencies of the wave spectrum, increasing the harmonic spectral period. Hofland et al. (2017) have indeed observed a growth of the $T_{m-10,TOE}/T_{p,DEEP}$ ratio up to a factor of 8 in extremely shallow waters. Thus, the relationship between the harmonic spectral period and the mean overtopping discharge accounted for in these empirical formulae seems to be anything but the relationship between the offshore peak period and q.

Therefore, all the empirical formulae derived from the CLASH database (e.g. Goda, 2009) suffer from significant uncertainties regarding the flow rate estimation at vertical seawalls with very shallow foreshores.

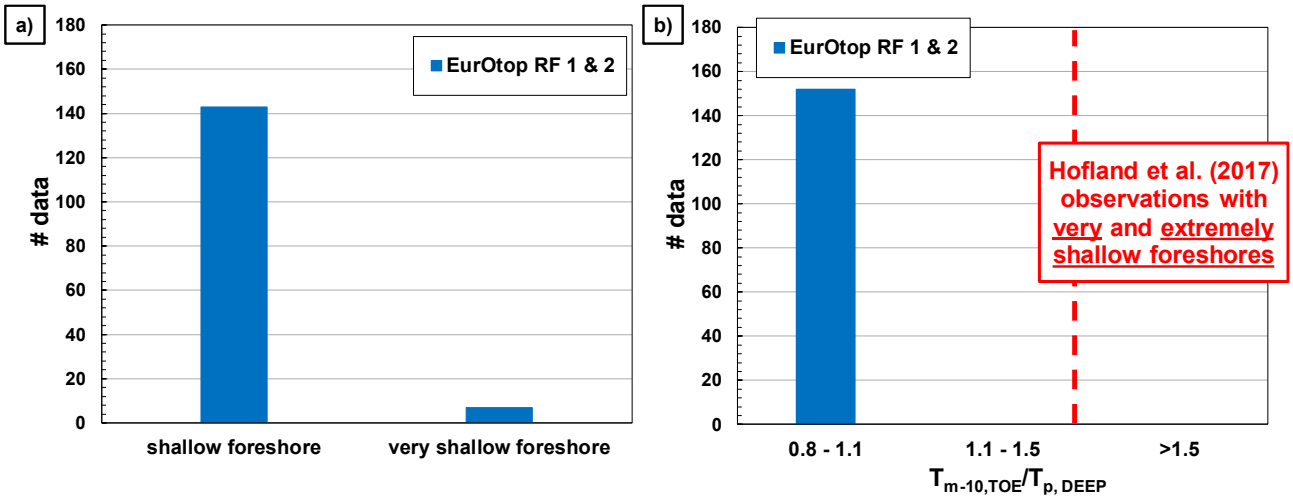

Figure 4.6 – *EurOtop reliable data characteristics. Panel a): shallow foreshore conditions; panel b); the harmonic spectral period at toe of the structure and the deepwater peak period ratio.*

Regarding Lashley et al. (2021), a large part of the data is derived from the experimental campaign of Goda et al. (1975). However, although the specific data sources have been specified in Figure 4.5, they are all included in the CLASH database. Hence, a paucity of them can be considered reliable. In particular, 151 out of 161 data (about 94%) used by the authors are characterized by RF = 3 and 4, namely "less reliable or not reliable enough to be used" (EurOtop, 2018).

A clear proof of the Goda et al. database's low reliability has been expressed in the own work of Lashley et al. (2021). Specifically, the geometrical features of the seawalls, i.e. the crest freeboards and water depth at the

toe of the walls, were modified by Goda to compensate for the (unrealistic) growth of the surf beats and wave setup due to the re-reflection of the waves in the laboratory channel. However, these modifications were based on “engineering judgment”, not measurements.

Therefore, such a deeper analysis of the data used to derive the existing predictive equations casts a shadow on their reliability. In particular, it highlights our inadequate knowledge about the overtopping of vertical seawalls in shallow water.

Finally, it points to the need for both a more detailed study of this coastal process and a more reliable predictive tool.

5. PHASE-RESOLVING MODELS

This Chapter briefly introduces the general features of the phase-resolving models employed in this work.

5.1.FLOW-3D

FLOW-3D HYDRO is a sophisticated and versatile Computational Fluid Dynamics platform developed by Flow Science Inc. (2009).

5.1.2. Governing equations

The software integrates the incompressible Reynolds-Averaged Navier-Stokes Equations (RANS) for a single fluid that flows in the *x,z* vertical plane; the *x*-axis is directed toward the shore, whereas *z* points upwards.

The equations for the conservation of mass and momentum then read:

$$\frac{\partial u_x}{\partial x} + \frac{\partial u_z}{\partial z} = 0 \tag{5.1}$$

$$\frac{\partial u_x}{\partial t} + u_x \frac{\partial u_x}{\partial x} + u_z \frac{\partial u_x}{\partial z} + \frac{1}{\rho}\frac{\partial p}{\partial x} - 2\frac{\partial}{\partial x}\left[(\nu + \nu_T)\left(\frac{\partial u_x}{\partial x}\right)\right] - \frac{\partial}{\partial z}\left[(\nu + \nu_T)\left(\frac{\partial u_x}{\partial z} + \frac{\partial u_z}{\partial x}\right)\right] = 0 \tag{5.2}$$

$$\frac{\partial u_z}{\partial t} + u_x \frac{\partial u_z}{\partial x} + u_z \frac{\partial u_z}{\partial z} + g + \frac{1}{\rho}\frac{\partial p}{\partial z} - \frac{\partial}{\partial x}\left[(\nu + \nu_T)\left(\frac{\partial u_x}{\partial z} + \frac{\partial u_z}{\partial x}\right)\right] - 2\frac{\partial}{\partial z}\left[(\nu + \nu_T)\left(\frac{\partial u_z}{\partial z}\right)\right] = 0 \tag{5.3}$$

where **u** (u_x; u_z) denotes the turbulence-averaged velocity field, *p* is the turbulence-averaged pressure, **g** (0;*g*) is gravity, ρ is the water density, and ν and ν_T indicate, respectively, kinematic and eddy viscosity.
To calculate ν_T, RANS models resort to turbulence closures; among them there are the standard *k-ε* model (Harlow and Nakayama, 1967), the ReNormalization Group model (Yakhot and Smith, 1992), the k-ω model (Wilcox, 1998) and the Large Eddy Simulation model (REF).

In this work, ReNormalization Group model (Yakhot and Smith, 1992) has been employed. Hence, two additional transport equations must be solved, which express the balance of the turbulent kinetic energy, *k*, and the dissipation rate, ε:

$$\frac{\partial k}{\partial t} + u_x \frac{\partial k}{\partial x} + u_z \frac{\partial k}{\partial z} - \frac{\partial}{\partial x}\left[\frac{(\nu + \nu_T)}{\sigma_k}\left(\frac{\partial k}{\partial x}\right)\right] - \frac{\partial}{\partial z}\left[\frac{(\nu + \nu_T)}{\sigma_k}\left(\frac{\partial k}{\partial z}\right)\right] + \epsilon - P = 0 \tag{5.4}$$

$$\frac{\partial \epsilon}{\partial t} + u_x \frac{\partial \epsilon}{\partial x} + u_z \frac{\partial \epsilon}{\partial z} - \frac{\partial}{\partial x}\left[\frac{(\nu + \nu_T)}{\sigma_\epsilon}\left(\frac{\partial \epsilon}{\partial x}\right)\right] - \frac{\partial}{\partial z}\left[\frac{(\nu + \nu_T)}{\sigma_\epsilon}\left(\frac{\partial \epsilon}{\partial z}\right)\right] + c_2\frac{\epsilon^2}{k} - c_1\frac{\epsilon}{k}\nu_T P = 0 \tag{5.5}$$

In the equations above, *P* is the shear production:

$$P = \frac{(\nu + \nu_T)}{\rho} \cdot \left[2 \left(\frac{\partial u_x}{\partial x} \right)^2 + \left(\frac{\partial u_x}{\partial z} + \frac{\partial u_z}{\partial x} \right)^2 + 2 \left(\frac{\partial u_z}{\partial z} \right)^2 \right] \quad (5.6)$$

whereas σ_k, σ_ε, c_1 and c_2 are specific coefficients.

Finally, the boundary conditions allow to solving this system of equations. Among them, these involve wave generation theories as inflow boundary, outflow condition that minimizes reflection at the face of the domain, a sponge layer that acts as wave-damping zone, symmetrical condition to nullify the gradients, wall-type condition that nullifies the velocity normal to the boundary.

5.1.3. Free surface tracking

The well-known Volume-of-Fluid (VOF) method (Hirt and Nichols, 1981) allows for tracking the free surface of the fluid. The VOF considers a volume of fluid fraction *F(x,y,z,t)* that defines the fractional volume of water for each cell in the computational domain. Specifically, *F* is evaluated as:

$$F = \frac{V_w}{V_c} \quad (5.7)$$

namely the volume of water (V_W) that occupies the cell's volume (V_c). Thus, *F* varies between 0 (void region) and 1 (a cell full of water).

The free surface is tracked by solving the transport equation for *F*:

$$\frac{dF}{dt} + \frac{\partial(uF)}{\partial x} + \frac{\partial(wF)}{\partial z} = 0 \quad (5.8)$$

5.1.4. Numerical implementation

The numerical domain is divided into a mesh of fixed rectangular cells. FLOW-3D solves the set of PDEs that govern the problem according to a staggered grid finite difference scheme; thus, pressure, turbulent kinetic energy, eddy viscosity, and *F* are computed at the center of the cell, while the velocity components at the cell face.

The presence of obstacles (e.g. walls, curved objectives) are embedded in the mesh by defining the fractional areas of the cells that are open to flow (the FAVOR™ method of Hirt and Sicilian, 1985).

A variable time stepping ensures to maintain the stability and accuracy of the solution. In particular, the n^{th} time step size Δt_n is automatically adjusted to:

$$\Delta t_n = \min\{\Delta t_{CON}^n; \Delta t_s\} \quad (5.9)$$

where Δt_s is a user defined sampling rate which depends on the frequency spectrum of the phenomenon under study, while Δt^n_{CON} is a convergence time step size needed to avoid numerical instabilities. Since the advective fluxes have been computed using a simple first order donor cell, Δt^n_{CON} has to satisfy the following criterion:

$$\Delta t^n_{CON} = \min\left\{0.5 \cdot \Delta t_s; 0.5\frac{\Delta x}{\sqrt{\Delta z \Delta a_z}}\right\} \tag{5.10}$$

The first term is the time step that satisfies the Courant–Friedrichs–Lewy (CFL) stability criterion, while the second ensures surface waves cannot propagate more than one cell per time step (a_z indicates vertical acceleration).

5.2. SWASH

SWASH (acronym for Simulating WAves till SHore) is an open source time domain wave model that ensures to analyze a variety of coastal phenomena (Zijlema et al., 2011); indeed, it has been designed to study propagation of dispersive surface waves from offshore to the beach, surf zone and swash zone dynamics, wave agitation in ports, and coastal-structure interactions.

5.2.1. Governing equations

SWASH integrates the Non-Linear Shallow Water equations extended with a non-hydrostatic pressure term:

$$\frac{\partial \zeta}{\partial t} + \frac{\partial hu}{\partial x} = 0 \tag{5.11}$$

$$\frac{\partial u}{\partial t} + u\frac{\partial u}{\partial x} + g\frac{\partial \zeta}{\partial x} + \frac{1}{2}\frac{\partial p_b}{\partial x} + \frac{1}{2}\frac{p_b}{h}\frac{\partial(\zeta - d)}{\partial x} + c_f\frac{u|u|}{h} = 0 \tag{5.12}$$

$$\frac{\partial \omega_s}{\partial t} = \frac{2p_b}{h} - \frac{\partial \omega_b}{\partial t}, \omega_b = -u\frac{\partial d}{\partial x} \tag{5.13}$$

$$\frac{\partial u}{\partial x} + \frac{\omega_s - \omega_b}{h} = 0 \tag{5.14}$$

where u is the depth-averaged velocity in x-direction, ω_s and ω_b are the velocities in z-direction at the free surface and at the bottom respectively, ζ is the free surface elevation from the still water level, d is the still water depth and h the total depth, p_b is the non-hydrostatic pressure at the bottom, g is the gravitational acceleration and c_f is the dimensionless bottom friction coefficient.

Eqs. (5.11 - 5.12) represent the conservation of mass and momentum for a depth-averaged, non-hydrostatic, free-surface flow; Eqs. (5.13 - 5.14) are the momentum equation for the vertical velocity at free surface, along with the kinematic boundary condition for vertical velocity at the bottom, and the local mass continuity, respectively (see Smit et al.,2014; Zijlema et al., 2011; Zijlema and Stelling, 2008). The addition of the two extra equations and the Keller box scheme ensures that the non-hydrostatic pressure is accounted for.

Such a non-hydrostatic model assumes a single-valued representation of the free surface in the horizontal plane, $\zeta(x,y,t)$, which means that the compute of free surface flow requires no additional treatment methods. This enhances the computational efficiency, although prevents the model reproducing complex processes such as overturning, air-entrainment, and the production of wave-induced turbulence after the incipient breaking.

It is worth to emphasized that SWASH may be run either in depth-averaged mode or in multi-layered mode, i.e. the computational domain is divided vertically into a fixed number of layers. Thus, the vertical structure of the flow should be in a way part of the solution. The higher the number of layers, the better the dispersive properties, in contrast to Boussinesq-type models approach that improves frequency dispersion by increasing the order of derivatives. However, the use of the Keller Box scheme (Lam and Simpson, 1976) to handle the pressure gradients in the vertical momentum equation guarantees good dispersive properties even at low vertical resolution.

The system of equation, Eqs. (5.11 - 5.14), is completed by imposing boundary conditions at the open boundaries of the computational domain. At the offshore boundary, waves are generated by prescribing the horizontal particle velocities normal to the boundary over the vertical. In addition, a weakly reflective condition avoids some reflections. Either periodic or random waves can be generated. The latter could have a specific parametric shape (e.g. JONSWAP); moreover, it can be modified by adding a second-order correction term that allows to generate bound IG-waves (Rijnsdorp et al., 2014). At the onshore boundary, either a Sommerfeld's radiation condition or a sponge layer can be applied to prevent wave reflection.

5.2.2. Wave breaking modelling

As waves travel from deep to shallow waters, wave steepening increases until the wave front becomes unstable or overturns, and the breaking occurs. However, since the free surface is modelled as a single-valued function ($\zeta(x,t)$), SWASH does not reproduce processes such as overturning or air-entrainment. The steepness of the front continues instead to a jump-discontinuity, where the momentum is conserved (i.e. shock capturing scheme) and the energy dissipation rate is then proportional to the cube of the bore height. Nonetheless, prediction of the onset of breaking requires high vertical resolution (10-20 layers).

On the other hand, a coarse vertical resolution leads to an overestimation of the non-hydrostatic pressure gradients, that postpones the transition into the characteristic saw-tooth shape and therefore the onset of dissipation. Thus, depth-uniform velocities and a hydrostatic pressure distribution are required to properly describe the dissipation related to wave breaking. To this end, Smit et al. (2013) developed the Hydrostatic Front Approximation (HFA), which ensures that governing equations locally reduce to the classical NLSW equations, allowing an appropriate reproduction of wave breaking without increasing the number of layers. Hence, imposing a hydrostatic distribution resolution ensures that, due the absence of dispersive effects, the front quickly transitions into a bore like shape.

It is initiated once the rate of change of the free surface exceeds a certain threshold α ($\partial_t\zeta/\sqrt{gh} > \alpha$), which is reduced to β in in neighboring points in order to ensure the persistence of breaking. According to the findings of Smit et al. (2013), α and β are equal to 0.6 and 0.3, respectively. When the crest of wave passes ($(\partial_t\zeta < 0)$, the non-hydrostatic pressure term reappears in the governing equations. Similar to the hybrid approach introduced by Tonelli and Petti (2012), HFA guarantees that during wave breaking vertical accelerations are no longer resolved and the non-hydrostatic pressure is set to zero. Lastly, additional horizontal viscosity is included to prevent generation of high frequency noise in the wave profile due to the discrete activation of the HFA.

5.2.3. Numerical implementation

SWASH adopts an explicit, second order accurate finite difference method for staggered grid that conserves both mass and momentum at the numerical level, and a second-order leapfrog scheme for time integration (Hansen,1956).

The computational domain is discretized in columns of constant width Δx and Δy in x- and y-direction respectively, and in a fixed number of layers between the bottom and the free surface vertically (Figure 5.1). A staggered grid is employed; indeed, the horizontal velocity is defined at the central plane of each layer and at the center of each lateral face of the columns, while vertical velocities are computed at the interfaces of the layers, at the center axis of each column. On the other hand, the pressure is computed at the center of each column, but vertically it depends on the scheme employed to approximate the pressure gradients in the vertical momentum equations: at central plane with the explicit standard layout or at layer interface when the implicit Keller Box scheme is used (Figure 5.2). As specified above, the latter guarantees good dispersive properties with a coarse vertical resolution, since the pressure is defined at both the surface and the bottom. Conversely, the standard layout is more suitable when high vertical resolution is adopted.

Time integration is performed by means of an adaptive time step that satisfies the Courant-Friedrichs-Lewy stability condition.

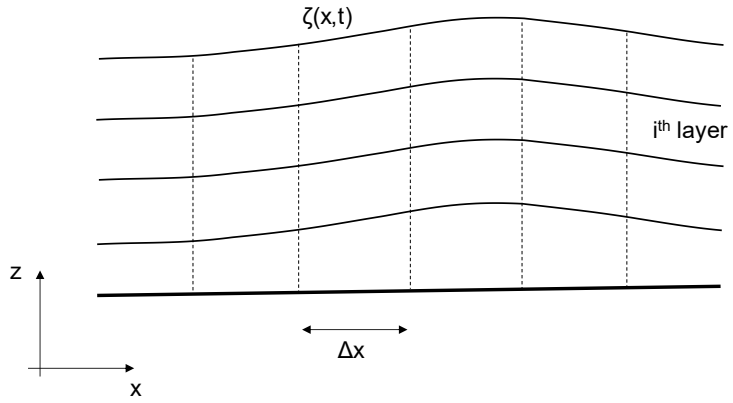

***Figure 5.1** – Spatial discretization of the computational domain.*

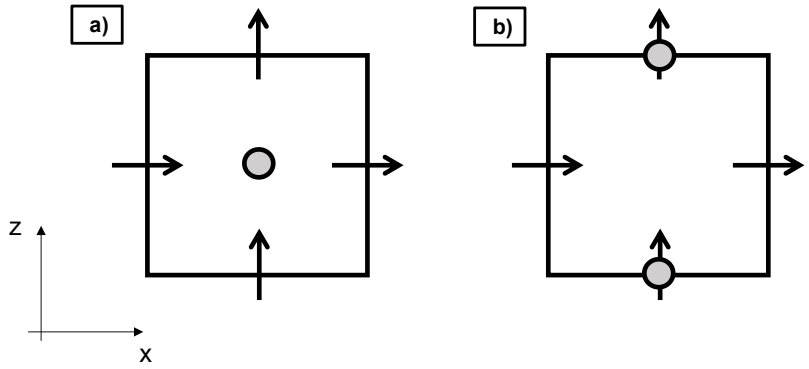

Figure 5.2 – *Panel a): standard scheme; panel b): Keller box scheme. Arrays and circles indicate where the velocity and pressure, respectively, are calculated.*

6. WAVE OVERTOPPING OF A VERTICAL SEAWALL IN A SURF ZONE: A JOINT ANALYSIS OF NUMERICAL AND LABORATORY DATA

The critical review of the existing empirical tools has revealed our lacking knowledge about the wave overtopping process of vertical walls with shallow foreshores. Hence, an in-depth analysis is necessary to both find out the hydraulic variables that role this phenomenon and derive a more appropriate predictive model.
This chapter aims to pursue the first objective, while the new predictive formula will be discussed in the following Chapters.

To this end, a recent dataset of seawall located in the surf zone will be examined; specifically, the Malecòn Tradicional (MT) dataset carried out at the University of Naples Federico II. Simultaneously, the MT experiments are numerically reproduced by two different phase-resolving models: the non-hydrostatic model SWASH and the CFD-RANS model FLOW-3D. The joint analysis of laboratory and numerical data allows to understand the physics of this coastal process. Furthermore, it ensures to verify the ability of phase-resolving models with different degree of complexity in reproducing physical behaviors observed through laboratory experiments.

The study first concerns the spectral variables and their evolution within the surf zone. For a deeper comprehension, the analysis on the steep Malecòn foreshore will be simultaneously performed on a milder beach; indeed, such a comparison will show that the spectral evolution and its effect strongly depend on the seabed slope. To this end, the analysis will be extended to the data of the physical experimental campaign of Van Gent (1999), which involve a mild foreshore ($tan(m)$=1/100).
Then, a deeper insight into the possible correlation between spectral moments sheds some light on their influence on wave overtopping in shallow water. Finally, a new predictive hydraulic variable will be introduced.

6.1. The Malecòn Traditionàl (MT) experimental campaign

An extensive physical experimental campaign has been carried out at the University of Naples Federico II to investigate the wave overtopping at the Malecòn Traditionàl, the vertical wall that protect La Havana city (Cuba) against flooding. The MT experimental campaign has examined the actual sea defense's performances and that of several variants as well, which would mitigate the severe flooding events that periodically afflict the city. Specifically, the alternatives encompass raising the wall height, varying the wall profile (i.e. recurved wall) and adding coastal protective structures, such as rock rubble mounds or low-crested detached breakwaters. The details of the 360 experiments are described in Còrdova Lopez et al. (2015; 2016); among them, this work only handles the 48 experiments relative to the vertical structure.

6.1.1. MT physical model setup

Physical model tests have been conducted at the RAndom wave TAnk of the DICEA of the University of Napoli "Federico II". The facility is 36 m long, 18 m wide, and 1.2 m deep; it is provided with 16 independent piston-type wavemakers – equipped with an active-absorption system – capable of simulating periodic and random waves with different mean angles and directional spreading.

A concrete-walled channel has been constructed within the basin to carry out the experiments in 2D conditions. The channel is 18.4m long and 1.55m wide. Moreover, the basin has been further divided; others walls separates a "dry zone" from a "water-filled zone" surrounding the channel. The former was created for observation purposes, whereas the latter allowed a large compensating volume, controlling the water level variation in the channel.

The multi-slope foreshore of La Havana has been reproduced at a scale of 1:30 (Froude's similitude law) in the 2D channel, as shown in Figure 6.1. The foreshore was modeled from the location of the Malecòn seawall, which is 0.057m below the Mean Water Level (MWL), out to a depth of 0.624m; further towards the wavemaker, the bottom is flat to allow the generated waves to develop appropriately.

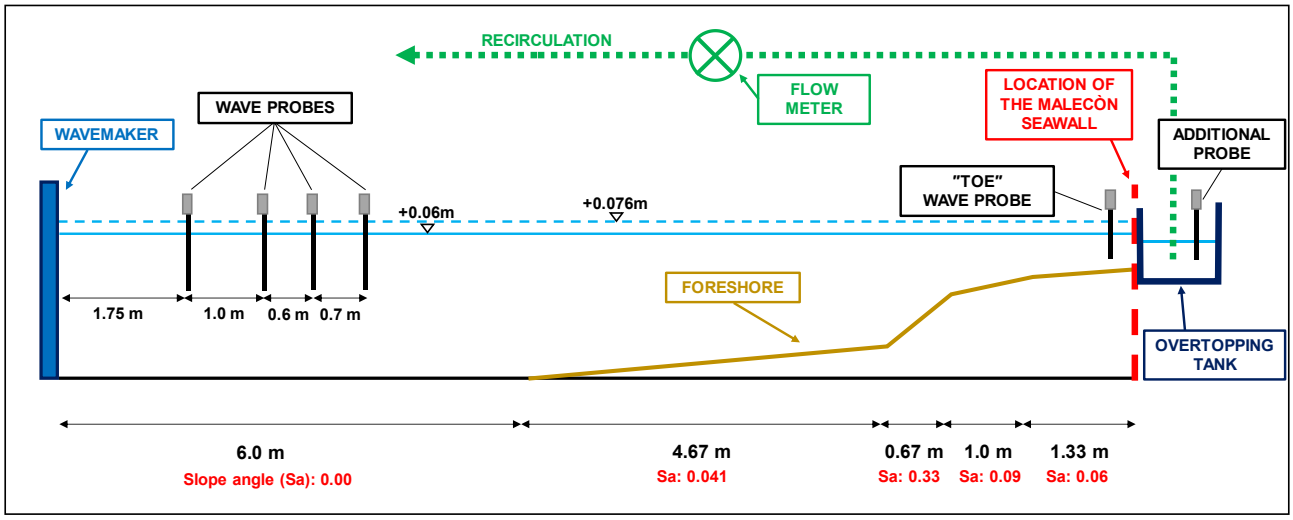

***Figure 6.1** – Sketch of the MT experimental setup.*

To assess the incoming wave conditions at the toe of the wall, the sea-states were run for 200 waves without the structure in the channel (the foreshore was extended above the MWL to perform the wave propagation tests). Simultaneously, this allowed the calibration of the incident wave conditions on the flat bottom that precedes the foreshore, which were estimated by applying the separation method of Zelt and Skjelbreia (1992) to an array of four probes, according to Figure 6.1.

Subsequently, the mean overtopping discharges were estimated on a sequence of 1000 waves with the structure in place. The overtopping water was collected in a tank and then recirculated using two submersible pumps. The pumped water passed through an electromagnetic flow meter, which computed the fluid volume

progressively. The water level in the reservoir at the beginning and at the end of each test was controlled by a supplementary wave probe.

Three different heights of the vertical wall were modelled, namely 3.96m above the MWL (original height of the Malecòn), 4.46m and 4.96m (these values refer to the prototype scale).

6.1.2. MT tests program

The experiments were performed with two water levels, namely +0.06m and +0.076m above the MWL at the model scale, which correspond respectively to the 50 years return period sea level rise (including astronomical tide, storm surge, and climate change effects) and the surge observed during the hurricane Wilma occurred in 2005. The combination between two water levels and three different wall's heights led to investigate six different crest freeboards, R_C.

For each level, eight sea states driven by mean JONSWAP spectra were generated, which are representative of the extreme Cuban climate; in particular, four values of the significant wave height were used (2.5m, 4.0m, 5.4m, and 6.5m in prototype), with two peak periods (10s and 12s in prototype).

The range of the most relevant hydraulic variables is reported in Table 6.1, where the subscripts "*N*" and "*TOE*" denote, respectively, the "*Nearshore"* conditions (measured on the flat bottom) and the conditions at the location of the structure. The values of $H_{m0,DEEP}$ have been obtained by means of the de-shoaling of the nearshore characteristics. The parameter h^* refers to the wave loading conditions at the wall, and indicates the impulsiveness of the overtopping events (consistent with the pressure measurements obtained via four transducers located along the wall during the experimental campaign).

Table 6.1 *– Main characteristics of the MT experiments.*

$H_{m0,N}$ [m]	$T_{p,N}$ [s]	$h_{TOE}/H_{m0,DEEP}$ [-]	$R_C/H_{m0,TOE}$ [-]	h^* [-]
2.7 ÷ 6.5	10, 12	0.52 ÷ 1.52	0.47 ÷ 1.88	0.003 ÷ 0.048

6.1.3. MT dataset peculiarities

As discussed in Chapter 4, the EurOtop reliable dataset in "non-deep waters" ($h_{TOE}/H_{m0,DEEP} \leq 4$, according to the classification Hofland et al., 2017) amounts to 152 data; among them, only nine fall within the very shallow water domain ($0.3 \leq h_{TOE}/H_{m0,DEEP} \leq 1$). Moreover, these nine data have $h_{TOE}/H_{m0,DEEP} \geq 0.82$, which indicates that the breaking process is only in the early stages of its development.

As reported in Table 6.1, the MT dataset allows us to extend the analysis range towards shallower waters (see Figure 6.2a) by adding 36 out of 48 data in the very shallow water domain.

These characteristics reverberate in the ratio $T_{m-10,TOE}/T_{p,DEEP}$ pictured in Figure 6.2b. In contrast to the EurOtop data that lie about a value of 1.1 (corresponding to waves with no or very few surf beats in the energy

wave spectrum), the MT data even reaches values higher than 1.5. Therefore, these data can ensure the establishment of the effective role of the harmonic spectral period on the overtopping rate for vertical seawalls.

The inherent peculiarities of MT dataset are even more evident since 73% of data fall outside the training set boundaries of the EurOtop Artificial Neural Network (Zanuttigh et al., 2016).

It is also worth recalling that the great majority of the data analyzed by Lashley et al. (2021) on vertical seawalls belongs to the "Non-Reliable" part of the EurOtop database; this further renews the interest in the analyses discussed herein.

Overall, the MT dataset can promote the proper assessment of vertical seawalls' behavior subject to many broken waves.

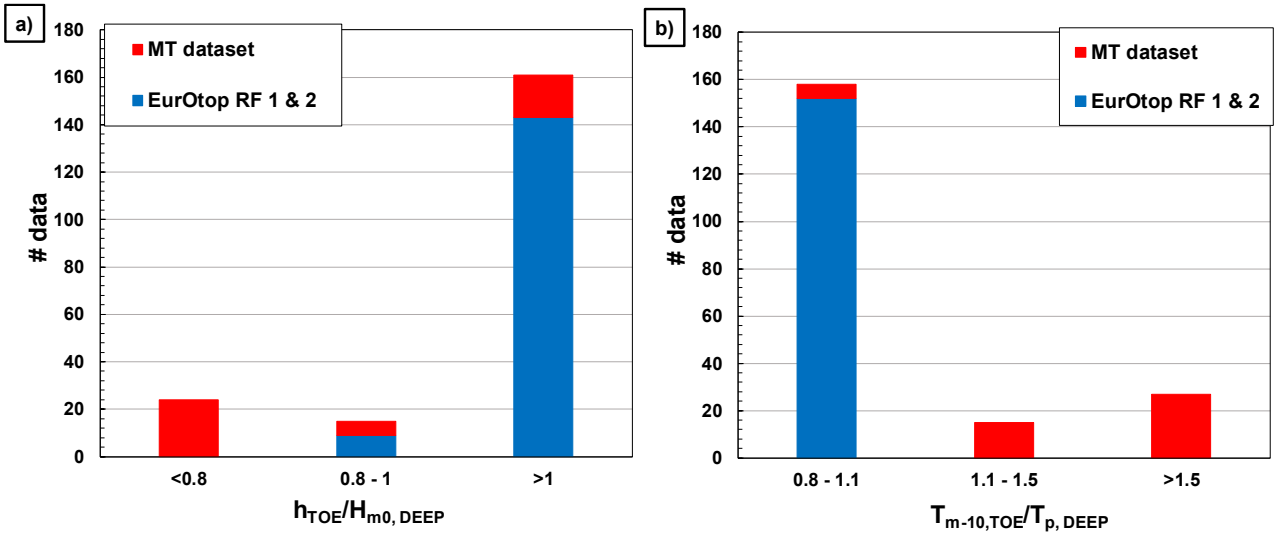

***Figure 6.2** – Comparison between MT and EurOtop (RF 1 & 2) databases for plain vertical walls in shallow waters.*

6.1.4. Numerical study

The primary purpose of the numerical study is to compare the performance of two phase-resolving models with different degrees of complexity: the CFD-RANS software, FLOW-3D, and the non-hydrostatic model, SWASH.

The MT tests numerically reproduced concern only the +0.06m sea level rise (+1.73m at the prototype scale), namely the lower water depth, for which wave breaking is very intense. The laboratory layout was scaled to the prototype (1:1) to check for possible scale effects in the physical experiments and to analyze the models' behavior under "real-life" dimensions.

Furthermore, the parallel analysis "laboratory vs. numerical results" aims to verify to what extent numerical models capture the physics of the processes and their potential use as exploratory tools.

6.1.4.1. CFD-RANS experiments

CFD-RANS simulations have been carried out with FLOW-3D (see Section 5.1), a sophisticated and versatile Computational Fluid Dynamics platform developed by Flow Science Inc. (2009).

It is worth noting that some of the CFD-RANS experiments was performed within the PhD Thesis of Angela Di Leo (Di Leo, 2021), which includes the overtopping tests with the actual Malecòn crest freeboard (R_C = 3.96m). In this work, the numerical dataset has been extended to both the overtopping tests with higher R_C (4.46 and 4.96m), and the wave propagation tests (the main characteristics of the whole CFD-RANS dataset are summarized in Table 6.2).

Table 6.2 *– Main characteristics of the CFD-RANS experiments; the values of $H_{m0,N}$ have been derived using the Zelt and Skjelbreia method (1992).*

Type	***duration***	$H_{m0,N}$ **[m]**	$T_{p,N}$ **[s]**	R_C **[m]**
propagation	200 waves	1.35 ÷ 6.43	10, 12	-
overtopping	500 waves	2.88 ÷ 6.43	10, 12	3.96, 4.46, 4.96

As a result of a grid-sensitive analysis performed in Di Leo (2021), the numerical domain has been discretized into 272,275 rectangular cells. From the wave generation up to 100m from the wall, the cells have $\Delta x = 0.70$m and $\Delta z = 0.30$m, whereas in the rest of the computational domain, the dimensions reduce to $\Delta x = 0.40$m and $\Delta z = 0.15$m. Such a discretization allowed saving computational time (reducing the number of cells) while maintaining adequate vertical resolution both in the innermost surf zone and along the structure.

The boundary conditions employed are schematized in Figure 6.3. At the end of the channel, opposite to the wave generation, two different boundary conditions are used depending on the type of experiment performed: during the overtopping tests, the "*Outflow condition*" allows the waves to leave the domain without any reflections; otherwise, for the wave propagation tests without structure, "*Pressure*" guarantees a constant water level.

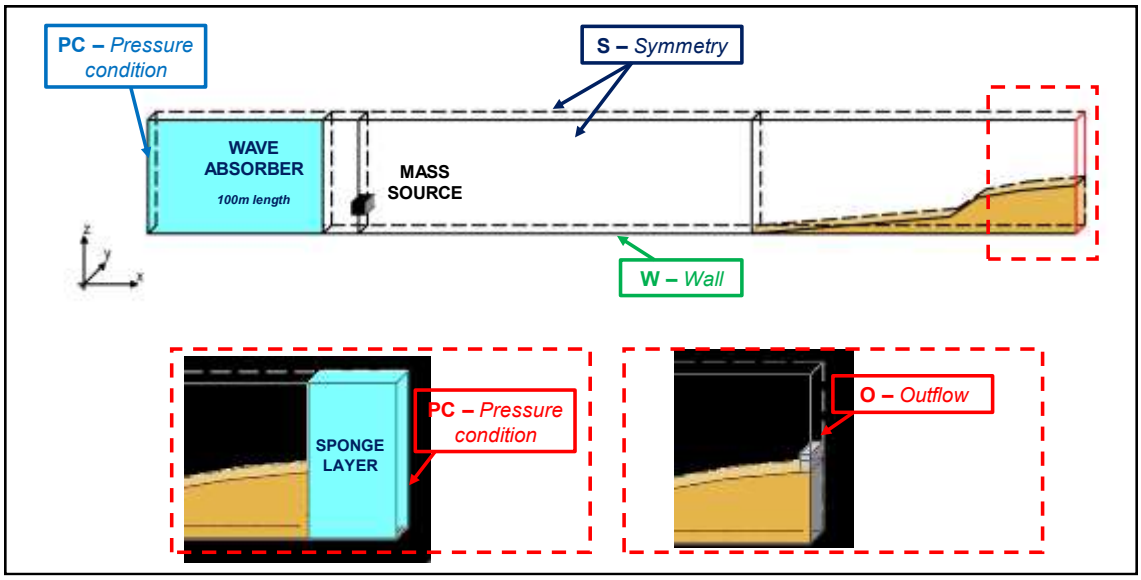

Figure 6.3 *– Boundary conditions employed during the CFD-RANS experiments.*

Wave generation exploits the mass source concept introduced by Lin and Liu (1999), which adds a source term to the continuity equation. The sea-states are generated by an underwater parallelepiped, through which the fluid enters the computational domain at a desired speed. Moreover, a wave-damping zone has been added at the beginning of the flume that acts as an active absorption system. The length of the damping zone is 100m, with a 0.5m x 1.0 m x 0.5m internal mesh. The damping coefficient varied linearly from 0 to 1.

To numerically reproduce the MT experiments, the ReNormalized Group (RNG) extension of the standard κ–ε turbulence closure has been used.

As stated in Table 6.2, the wave propagation tests have been run for 200 waves, while the overtopping experiments for 500 waves (according to the findings of Romano et al., 2015).

However, it should be highlighted that despite the same spectrum shape, the waves generated with FLOW-3D differ from those of the physical model by the values $H_{m0,N}$ and in terms of time-domain properties. Indeed, while the laboratory waves remain approximately Gaussian even for the largest values of the wave height, CFD waves become positively skewed with the crests being increasingly higher than troughs (Figure 6.4). Since wave skewness plays a role in the breaking process, such a peculiarity must be properly accounted for in the analysis of results.

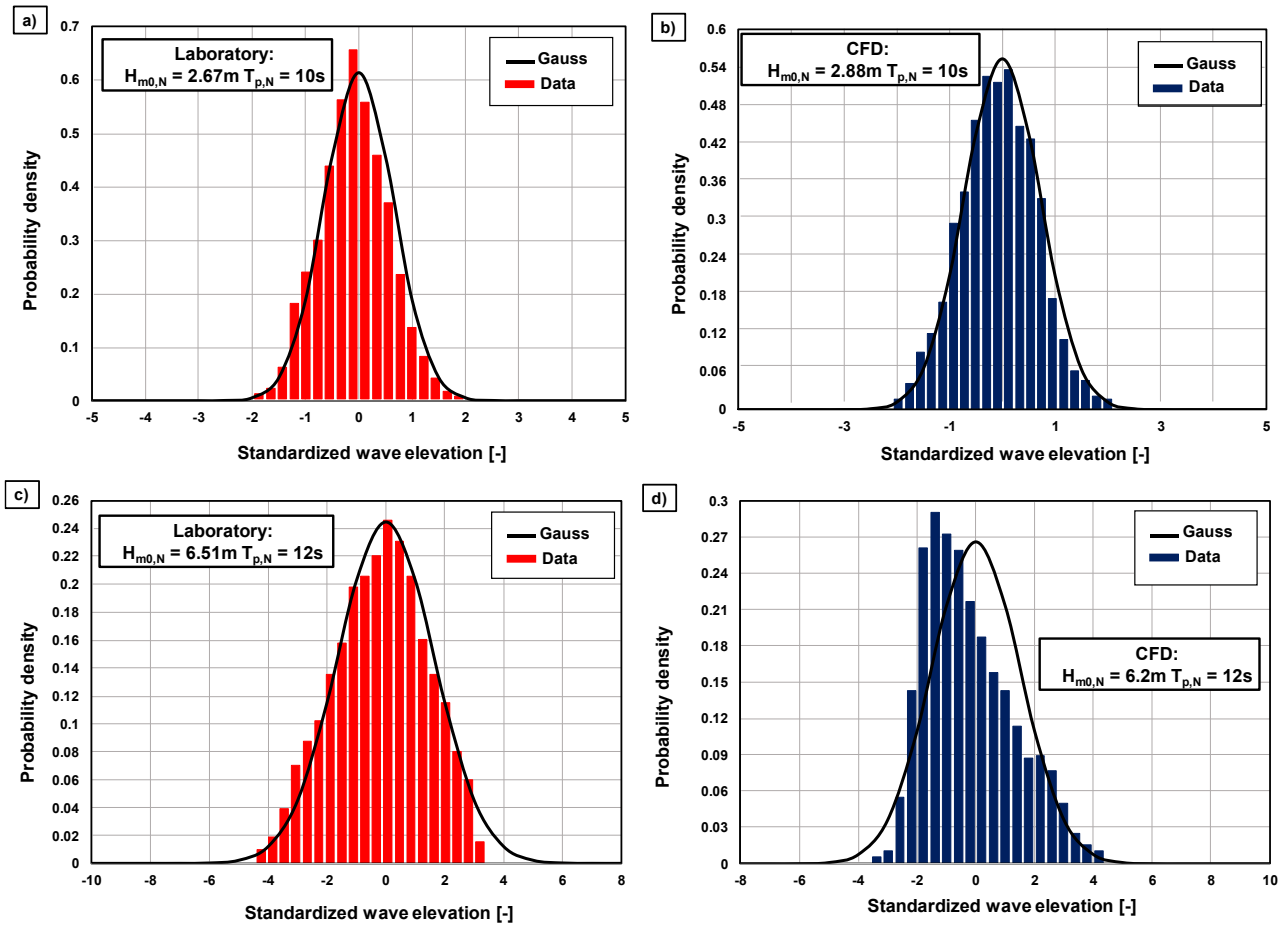

***Figure 6.4** – Distribution of laboratory and CFD wave elevation (standardized) in the Nearshore zone.*

6.1.4.2. SWASH experiments

The MT experiments have been reproduced with the non-hydrostatic model SWASH as well. The numerical tests include eight propagation experiments, which lasted 200 waves, and 24 overtopping tests with a duration of 500 waves.

The MT foreshore has been modelled at the prototype scale. At the generation boundary, the same wave elevation time-series have been imposed as the laboratory experiments, so that numerical and physical sea states match in both the time and frequency domains (Figure 6.5). Conversely, at the opposite end of the channel a Sommerfield boundary condition has been adopted to minimize wave reflection. The wave breaking has been modelled via the HFA method developed by Smit et al. (2013); the default values of the coefficients α and β have been used.

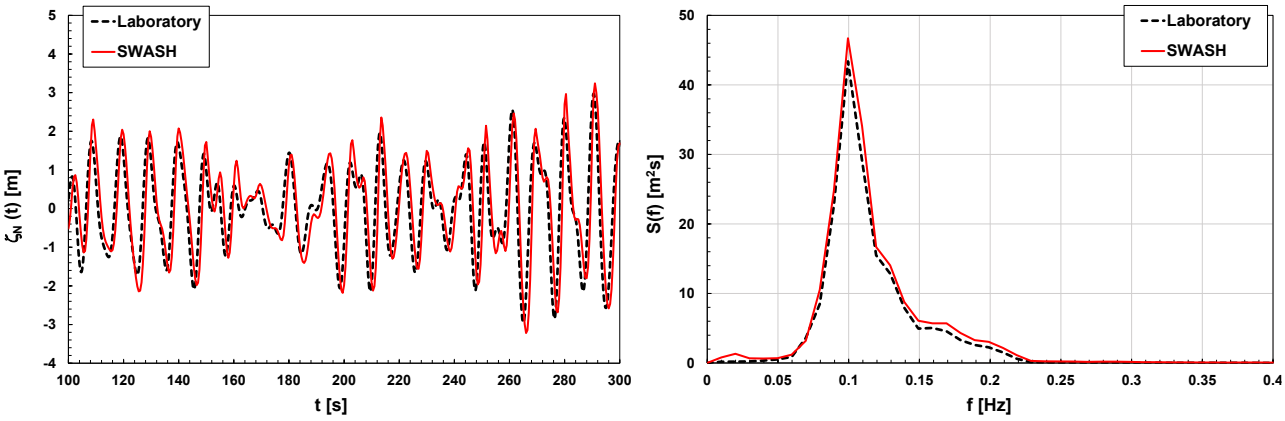

Figure 6.5 - *Laboratory vs SWASH wave elevation time-series (left panel) and wave energy spectra (right panel). These refer to the tests characterized by $H_{m0,N}$ = 5.4m and $T_{p,N}$ = 10s.*

The water depth has been divided into 2 layers; the horizontal discretization has a grid spacing of 1 m, which corresponds to about $L/\Delta x$ = 70 (with L defined as $L = \sqrt{gH_{m0,N}} \cdot T_p$). A Manning coefficient of zero has been used. The maximum Courant number has been set at 0.5.

It is worth specifying that both the Manning coefficient value and the grid spacing derive from a sensitivity analysis.

Specifically, six different values of Δx have been tested, keeping the Manning coefficient $\nu = 0$. The grid spacing ranged from Δx = 0.5m to 3.0m, corresponding to a number of points per shallow-water wavelength ($L/\Delta x$) varying from 20 to 128. The grid effects have been evaluated both for wave transformation and wave overtopping processes. According to previous findings in literature (Suzuki et al., 2014), the convergence is observed solely on wave energy spectra, whereas the overtopping discharge exhibits remarkable scatter (Figure 6.6). When the grid spacing is reduced from 3.0m to 1.0m q more than doubles, while the trend reverses for the finer grids. Thus, wave overtopping becomes saturated at Δx = 1.0m, which was selected as the final grid for testing (Suzuki, 2014).

Successively, the role of the Manning coefficient has been examined, keeping Δx = 1.0m. Figure 6.7 indicates that the impact on wave spectrum is weak overall, and mainly affects the low-frequency components (i.e. the spectral moment m_{-1}). Increasing ν results in a surf-beats dampening, which leads to a reduction of m_{-1} (up to -15%) and a slight variation in m_0 (-5%), while the first order spectral moment increases (up to +11%). On the other hand, the effect on wave overtopping is significant, as highlighted in Suzuki et al. (2011). The mean overtopping discharge indeed decreases linearly with the Manning coefficient. As ν transitions from 0 to 0.1$m^{-1/3}$ s, q decreases by 1/3. The best agreement with the results of the physical model is thus obtained with a zero value of the Manning coefficient.

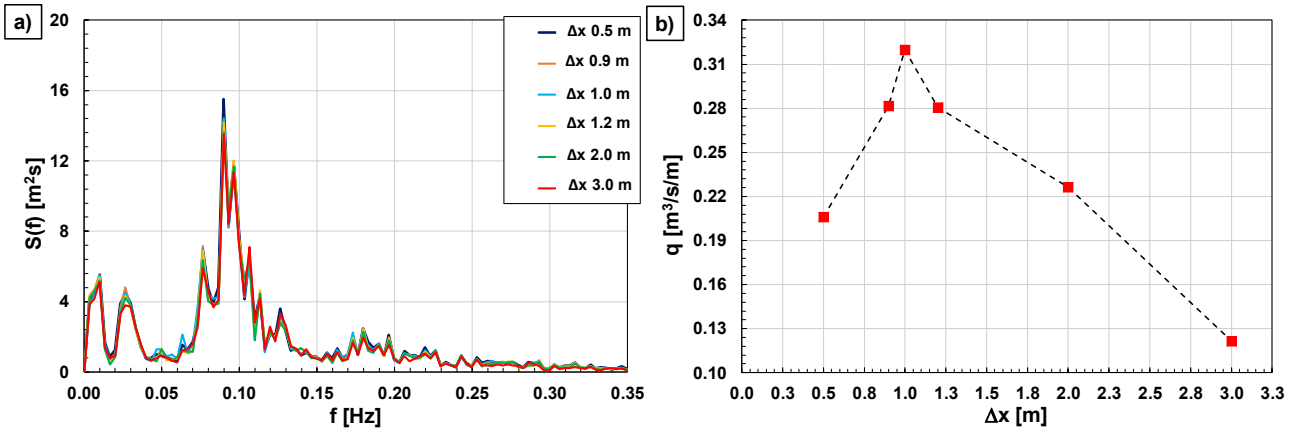

Figure 6.6 *– Panels a) and b) show the effects of grid spacing on wave energy spectra and wave overtopping (Malecon's current height), respectively. These refer to the test characterized by* $H_{m0,N}$ *= 5.4m and* $T_{p,N}$ *= 10s.*

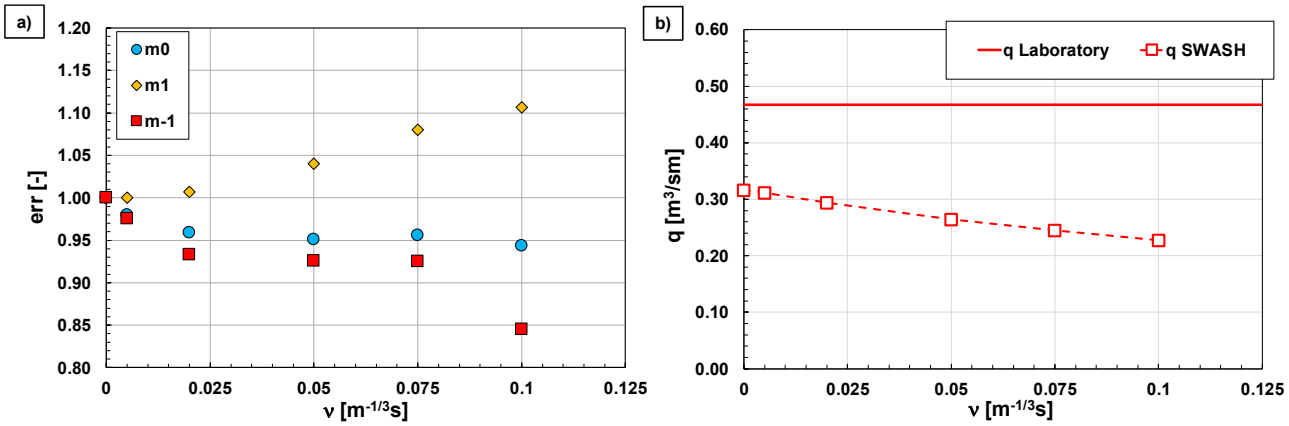

Figure 6.7 *- Effect of Manning coefficient on wave energy spectra (panel a)) and wave overtopping (panel b)). These refer to the test characterized by* $H_{m0,N}$ *= 5.4m and* $T_{p,N}$ *= 10s.*

6.2. The DH experimental campaign

The DH experimental campaign has been conducted at the Scheldt-flume (Delft Hydraulics) and reported in Van Gent (1999). It represents a milestone in coastal engineering; the purpose was to investigate the wave run-up and overtopping of dikes with very shallow foreshores. Van Gent indeed tried to account for the evolution of wave energy spectra due to shallow foreshores in these wave-structure interaction processes.

It is worth specifying that the DH data analysis allows a further comprehension of the spectral evolution process and spectral moments correlation discussed in Section 6.3. Specifically, the milder foreshore examined in Van Gent ensures to compare the behavior of a steep (Malecòn foreshore) and a gentle beach and, therefore, gain a more robust physical explanation of the results.

6.2.1. DH physical model setup

The laboratory tests were performed in a wave flume long 55m, wide 1m and high 1.2m. The facility has a wavemaker able to generate both regular and random sea states and equipped with an active-absorption system.

Two mild foreshores inclined 1/100 and 1/250 to the horizontal were modelled in the flume along with two dikes having a smooth slope of 1/2.5 and 1/4, respectively. Four different water levels allowed to investigate four dike's crest heights (Figure 6.8). The analysis performed in this Chapter refers only to data related to *tan(m)* = 1/100.

The water surface elevation was measured via a set of three gauges located in five different positions (from the flat bottom to the toe of the dike). Along the structure was positioned a step-gauge, namely a beam with a large number of conductive probes, to measure the run-up heights; whereas an overtopping tank rear the dike allowed to measure the flow rate.

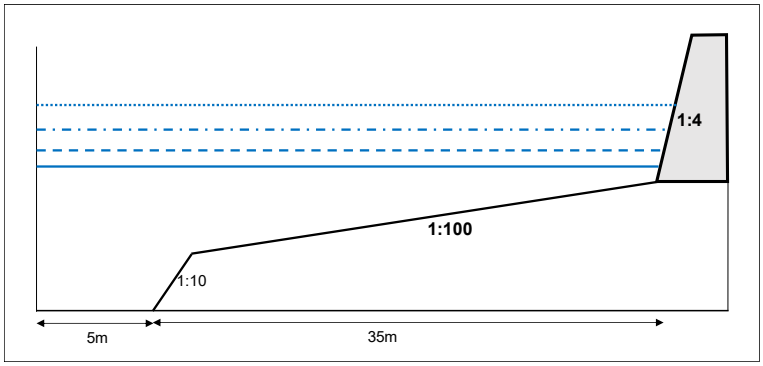

Figure 6.8 – *Physical model setup of the DH experimental campaign; despite the picture only depicts one foreshore and one dike investigated, the model is analogous with tan(m)=1/250 and tan(α)=1/2.5.*

6.2.2. DH tests program

During the DH experimental campaign, Van Gent performed two types of experiment – generating either single-peaked or double-peaked wave energy spectra – in order to examine the influence of spectral frequency distribution on wave run-up and overtopping. However, this work only analyzes 24 out of 174 laboratory tests; in particular, the experiments performed with double-peaked spectra are excluded.

As mentioned above, four water depths at the toe of the dikes were investigated (0.047, 0.094, 0.188 and 0.353m). The JONSWAP spectra generated were characterized by a single spectral wave height equals to 0.14m and three different peak periods (1.6, 2.0 and 2.5s).
The experiments were run for about 1000 waves. It is worth noting that the wave characteristics were measured without the structure in the flume.

Table 6.3 lists the main characteristics of the tests program.

Table 6.3 *– Main characteristics of the DH experiments.*

tan(m)	*tan(α)*	h_{TOE} [m]	$h_{TOE}/H_{m0,DEEP}$ [-]	s_{0p} [-]
1/100	1/2.5, 1/4	0.047 ÷ 0.353	0.33 ÷ 2.5	0.014 ÷ 0.035
1/250	1/2.5	0.047 ÷ 0.353	0.33 ÷ 2.5	0.014 ÷ 0.035

6.3. Analysis of the spectral evolution

As discussed in Chapter 3, Lashley et al. (2021) and Hofland et al. (2017) shows that the wave parameters in the surf zone are strictly related to the offshore wave conditions (see Eqs. (3.3, 3.9)). In their empirically-derived tools for estimating these variable, the authors follow the approach of Goda (2000, 1975) and use the relative water depth, $h_{TOE}/H_{m0,DEEP}$, and the deepwater wave steepness as main predictors.

This approach can be generalized to express the relationship between the spectral moments at the toe of the structure and the wave properties in the "nearshore" zone (Figure 6.9).

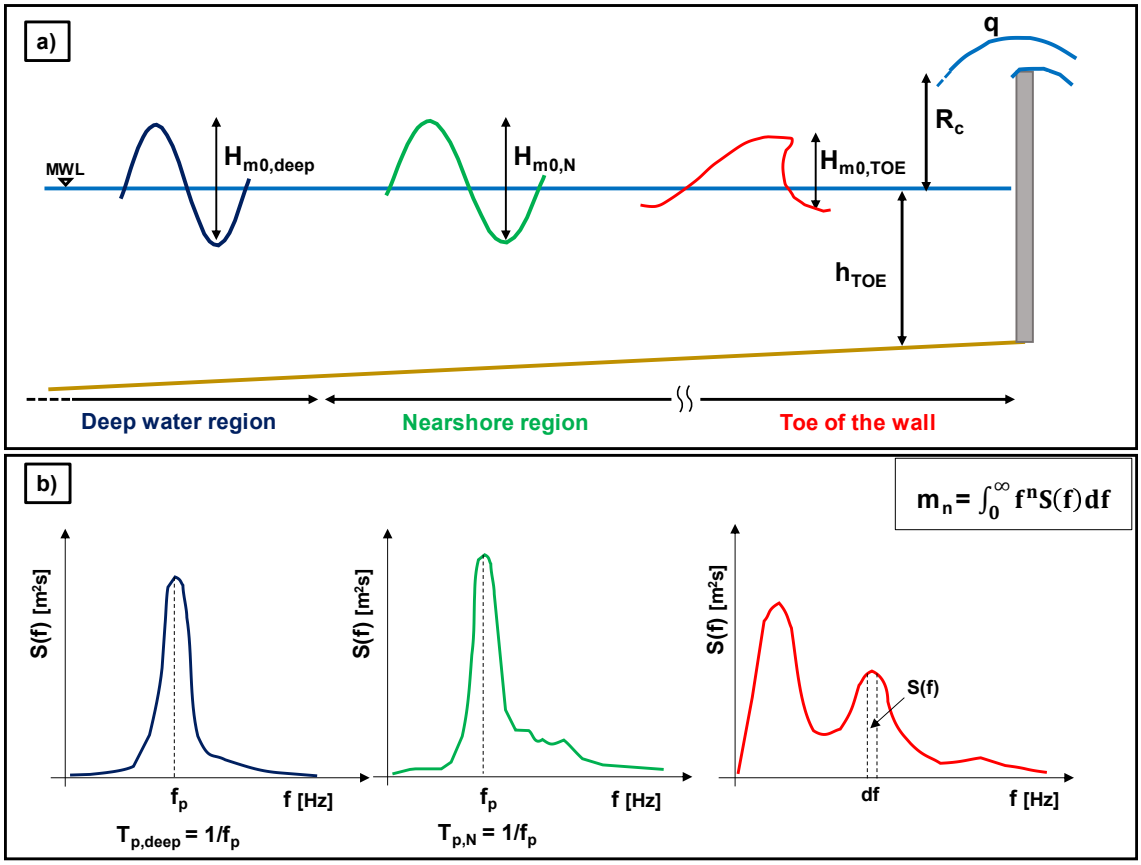

***Figure 6.9** – Sketch of wave transformation from deep waters to the toe of the structure (panel a)) and the relative evolution of the wave energy spectrum (panel b)).*

The analysis shows the correlations between the various spectral moments and the predictors adopted in Eqs. (3.3, 3.9). However, the nearshore wave envelope function $E(t)$ has been used instead of $H_{m0,DEEP}$ to account for a possible skewness of the wave elevation (see the CFD wave elevation characteristics in Figure 6.4), that otherwise would be neglected. The envelope function has been obtained via Hilbert transform of the wave oscillation signals (Figure 6.10).

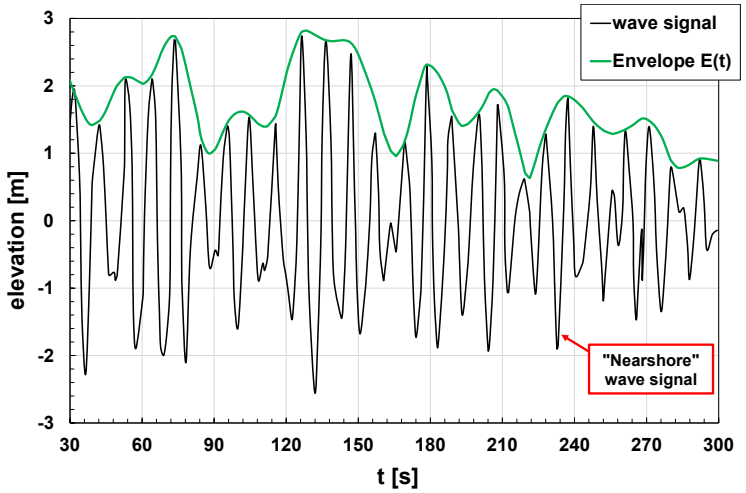

Figure 6.10 *– Envelope of nearshore wave oscillation signal.*

Wave height to depth ratio and wave steepness are thus replaced by the following quantities:

$$r_E = \frac{E_{rms-N}}{h_{TOE}} \tag{6.1}$$

$$s_{E,P} = 2\pi \cdot \frac{E_{rms-N}}{gT_{PN}^2} \tag{6.2}$$

in which $E_{rms\text{-}N}$ denotes the effective envelope value at the nearshore region (as indicated by the subscript *N*); as widely known, $E_{rms\text{-}N} = 1/2 \cdot H_{rms}$ for symmetric Gaussian wave processes (Tayfun and Lo, 1989), and increases as the wave profile becomes skewed. A further advantage of using the effective envelope is that in virtue of the equality:

$$[E_{rms-N}]^2 = [Mean\ E(t)]^2 + VAR\ E(t) \tag{6.3}$$

that explicitly linked $E_{rms\text{-}N}$ to the variance of *E(t),* and then to the modulation of the envelope. The latter is in turn closely related to the generation of surf beats, as the fluctuation of the breaking point from wave to wave represents a main generation mechanism of long waves (Symonds et al., 1982).

The combination of these two variables (Eqs. (6.1,6.2)) leads to the predictors:

$$x_n = \left(\frac{E_{rms-N}}{h_{TOE}}\right)^2 \cdot [s_{E,P}]^{-\frac{n+1}{2}} \tag{6.4}$$

At the ringht-hand side of Eq. (6.4), the first term represents the excess of wave energy propagating from the nearshore zone, while the second one is a weighting function that accounts for the effect of wave steepness on the energy dissipation due to wave breaking (e.g., Battjes and Janssen, 1978). According to the literature (e.g., Battjes and Janssen, 1978), steeper waves result in a more intense breaking process, which in turn primarily affects the high frequencies of the spectrum; thus, the exponent of $s_{E,P}$ increases with the moment order *n*.

The spectral moments at the toe of the structure are expressed in dimensionless form:

$$m'_{n,TOE} = \frac{m_{n,TOE}}{m_{nB,TOE}} \tag{6.5}$$

where

$$m_{nB,TOE} = \frac{1}{2}\,\gamma_b^2\,h_{TOE}^2\,\left(T_{p,N}\right)^{-n} \tag{6.6}$$

Eq. (6.6) represents the n^{th} moment of a linear (narrow band) breaker with amplitude $a_B=\gamma_b \cdot h_{TOE}$. An order of magnitude of $\gamma_b = 0.3$ is adopted for the breaking index, corresponding to a wave height to depth ratio of 0.6 (see Kamphuis 1996; 1991).

Figures 6.11 and 6.12, thus, describe the variation in spectral trends (Eq. (6.5)) depending on the nearshore wave conditions (Eq. (6.4)) for the steeper beach of the Malecon and the DH mild beach (Van Gent, 1999), respectively. In particular, the graphs refer the spectral moments of orders n = -1, 0, 1, 2.

On the steep MT beach, all the four spectral moments increase as the relative abscissa increases; $m'_{n,TOE}$ grows almost linearly with x_n.

Specifically, the increasing trend of $m'_{-1,TOE}$ (Figure 6.11a) suggests that, for a given $E_{rms\text{-}N}$, the shallower the water, the larger the amount of energy at low-frequency components; or still, for a given h_{TOE}, larger values of the effective envelope lead to a greater surf zone, which indicates a larger surf beats forcing zone that contributes to the growth of $m'_{-1,TOE}$ (Symonds et al., 1982).

Concerning $m'_{0,TOE}$, Figure 6.11b indicates that steeper waves reduce wave energy due to the more intense wave breaking; on the other hand, for a given wave steepness, the increasing trend denotes the inability of the steep Malecòn foreshore in dissipating the growing $E_{rms\text{-}N}$.

As shown in Figures 6.11c and 6.11d, analogous results characterize the higher spectral moments. The increasing trends of $m'_{1,TOE}$ and $m'_{2,TOE}$ indicate that the steep foreshore does not ensure the dissipation of wave energy at higher frequencies, which has been developed during the wave evolution process (i.e., wave energy spreads over a larger spectral band compared to the deep/nearshore region).

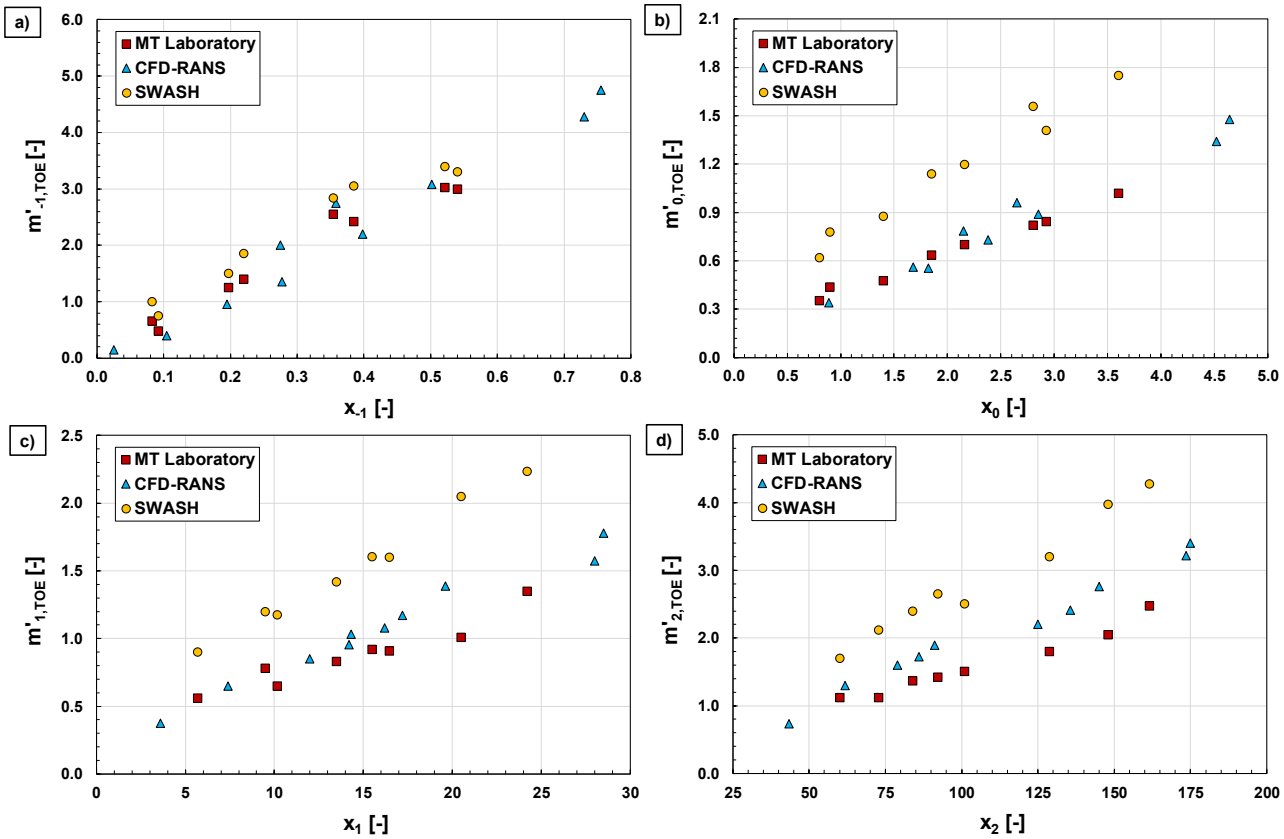

Figure 6.11 *– MT dimensionless spectral moments as a function of* x_n.

Conversely to the increasing trends in Figure 6.11, such linear growth does not always occur for the mild beaches of the DH dataset (Figure 6.12). The comparison between the MT and DH data indeed points out the role of the seabed slope in the spectral moments' behavior.

In particular, whereas the -1 moment still exhibits an increasing trend with the relative abscissa (Figure 6.12a), the zeroth and the first moment of DH data tend toward tend towards a constant value of the order of 0.8, as shown in panels b) and c) of Figure 6.12, respectively. Indeed, the slow growth of dissipation demand due to a small beach angle ($tan(m)$=1/100) ensures that the breakers can dissipate almost all the energy surplus coming from offshore. Hence, m_0 and m_1 reach a "depth-controlled" condition as the nearshore envelope increases. On the other hand, Figure 6.12a shows that $m'_{-1,TOE}$ increases as the offshore energy excess. $E_{rms\text{-}N}/h_{TOE}$, increases. This is due to the fact that m_{-1} depends primarily on the low-frequency spectral components, which are almost unaffected by breaking. As the nearshore envelope grows high, as the long waves generation zone increases, resulting in a growth of $m'_{-1,TOE}$. However, as shown in the Figure 6.12a, the DH increment rate is nearly half that for MT; this is just because the damping of the high-frequency components is more intense on the mild beach.

Hence, the comparison proved that the steeper foreshore of the MT tests and the milder one of Van Gent behave differently, especially for the higher spectral moments investigated. Such a difference is because the energy dissipation rate depends on the foreshore slope, as Le Mehautè (1962) stated in its saturated breakers theory.

According to Le Mehautè, the wave height within the surf zone on a gentle beach is directly related only to the water depth (i.e. depth-controlled condition) since the breaker is able to dissipate the excess energy. Conversely, for steeper and steeper beaches, the breaker becomes saturated and cannot satisfy the demand for energy dissipation; the amount of excess energy still propagates shoreward. These two different theoretical behaviors described can be appreciated by comparing the spectral moments of zeroth and first order of the MT and DH experiments.

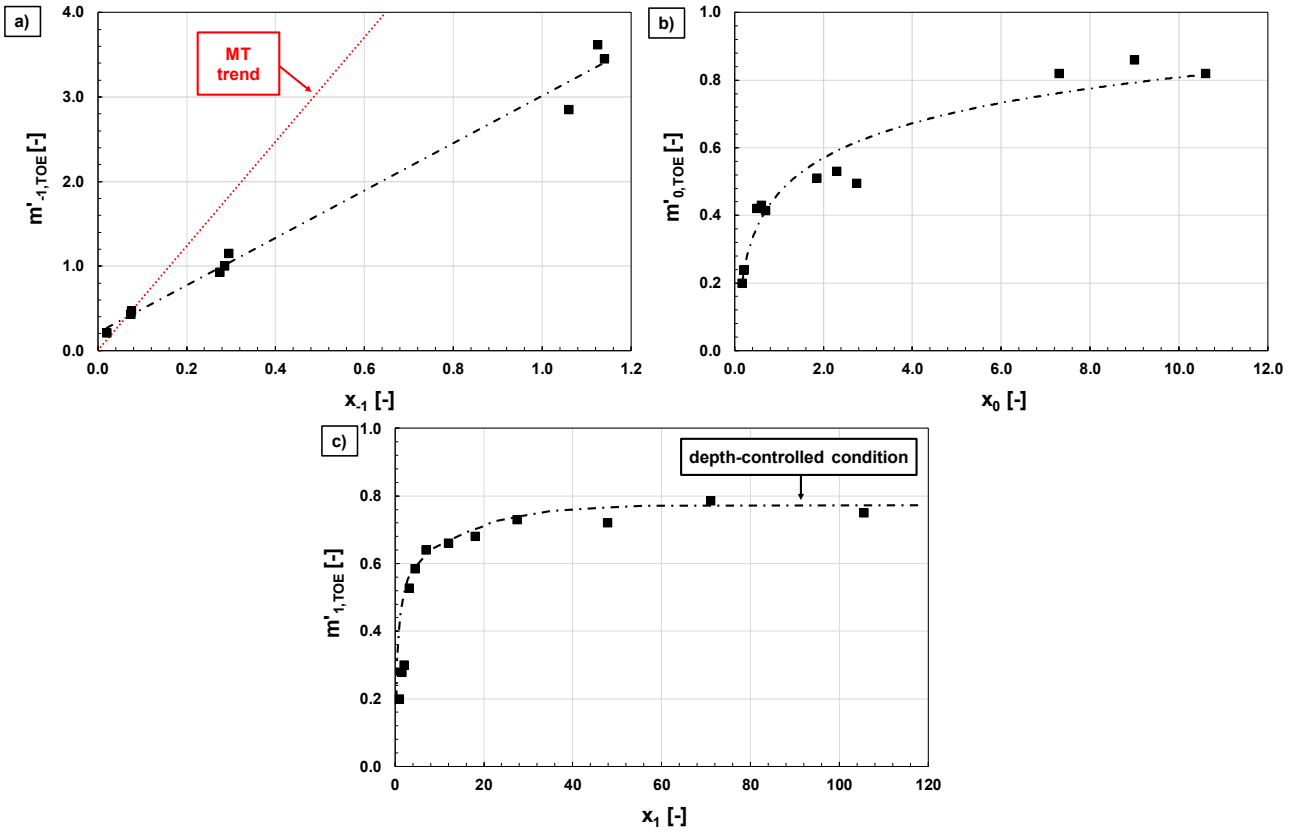

***Figure 6.12** – DH dimensionless spectral moments as a function of x_n.*

Regarding numerical models, Figure 6.11 demonstrates that both the phase-resolving models properly reproduce the qualitative trends of the MT laboratory. However, among the two, the CFD-RANS outcomes appear more consistent – keeping reasonably close to the physical model data – except for a slight systematic overprediction of $m'_{2,TOE}$. On the other hand, SWASH overpredicts all the spectral moments apart from $m'_{-1,TOE}$. Therefore, it underestimates the energy dissipation in the high-frequency range, including around $T_{p,N}$, but correctly simulates the generation of surf beats.

The behavior of the phase-resolving models can be more intuitively by observing Figure 6.13, which shows the wave energy spectra at the toe of the wall for two experiments with the same values of $E_{rms\text{-}N}$ and $T_{p,N}$. Indeed, the figure shows that SWASH overestimates the energy around both the peak period and the higher frequencies; while the agreement of the low-frequency energy is quite satisfactory. On the other hand, CFD-

RANS spectra are rather consistent with laboratory ones, except for the higher frequencies (resulting in the overestimation of Figure 6.11d). The latter observation indicates that, in the CFD-RANS tests, the dampening of the superharmonics in the surf zone is weaker than in the laboratory. This phenomenon may be due to either the "Wall" (slip) condition imposed at the bottom, which affects the boundary layer in the numerical flume, or to a viscosity-related scale effect in the physical model, which augments dissipation.

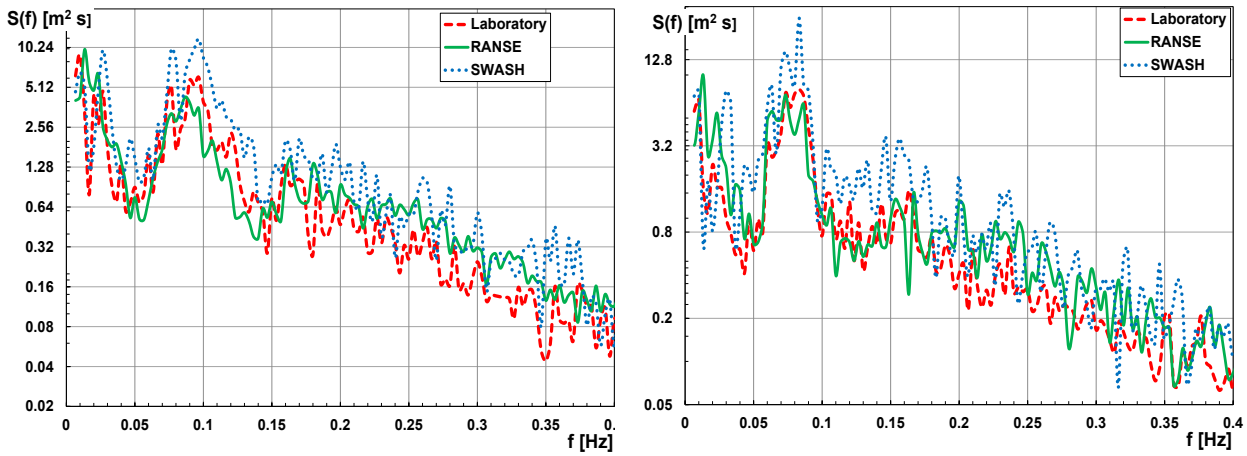

Figure 6.13 *– Laboratory vs. numerical wave spectra at the toe of the wall. Left panel: Erms-N=2.48m, Tp,N = 10s. Right panel Erms-N =2.15m, Tp,N = 12s.*

6.3.1. Spectral moments correlation

Besides the potential trends observed in the previous section, their effects on the correlation between the spectral moments within the surf zone need to be stressed.

In deep or shoaling waters, the wave energy is almost confined in a narrow spectral band (see the sketch in Figure 6.9); thus, mean spectral periods such as T_{m-10} and T_{m01} only depend on T_p, and are independent (at least theoretically) of the wave energy. For the MT laboratory data, Figure 6.14 confirms such statement.

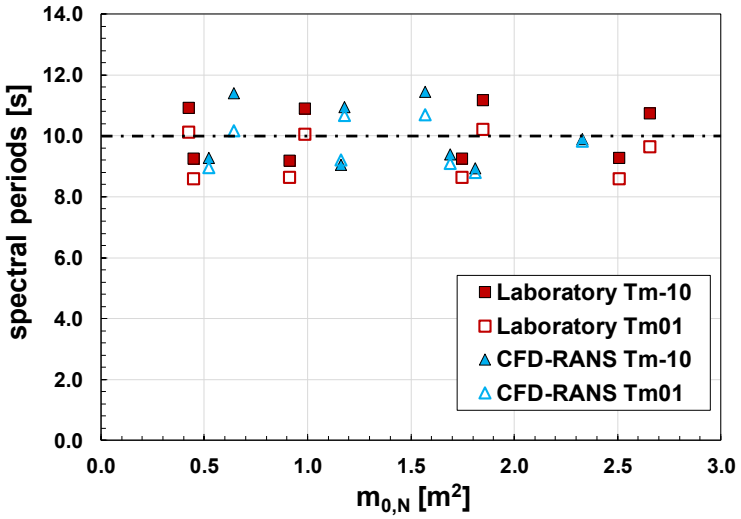

Figure 6.14 *– Spectral periods as a function of wave energy in the nearshore region for MT data.*

However, the narrow band assumption is no longer appropriate in the surf zone since the energy spreads on an increasingly spectral band as the wave train travels shoreward; then, as shown in the following, significant relationships will arise between spectral moments. Conversely to the nearshore region (Figure 6.14), a strong correlation might appear between spectral periods and wave energy within the surf zone.

Nevertheless, such relationships exist as long as the spectral moments increase linearly with the corresponding x_n (Figures 6.11 and 6.12a), while it weakens for a depth-controlled condition (Figures 6.12b and 6.12c).

Figures 6.15 and 6.16 allow discerning between these different behaviors, paying particular attention to the spectral period T_{m01}. In fact, since $m'_{-1,TOE}$ and $m'_{1,TOE}$ increases with the relative x_n for the MT data, the correlation degree between wave energy and mean spectral periods remains globally high (R^2 of the order of 0.8/ 0.9), as shown in Figure 6.15. On the other hand, whereas the correlation between wave energy and harmonic spectral period is high for DH data (R^2 = 0.93 in Figure 6.16a), the fact that the first-order moment in Figure 6.12c tends to become depth-controlled weakens the relationship between m_0 and T_{m01} by far (R^2 = 0.28 in Figure 6.16b).

Hence, the local wave energy tends to be correlated with both the mean spectral periods on steep foreshores (see MT results), while this is only true of T_{m-10} on mild beaches (e.g., DH foreshore).

It is worth noting that, in Figure 6.15, the CFD-RANS outcomes are consistent with laboratory data because of the good agreement observed in Figure 6.11. On the other hand, SWASH reproduces the correlation between $T_{m-10,TOE}$ and $m_{0,TOE}$ fairly well, except for a bias (Figure 6.15a); however, this is anything but surprising since Figure 6.13 has shown that the non-hydrostatic model overestimates wave energy at high-frequency components.

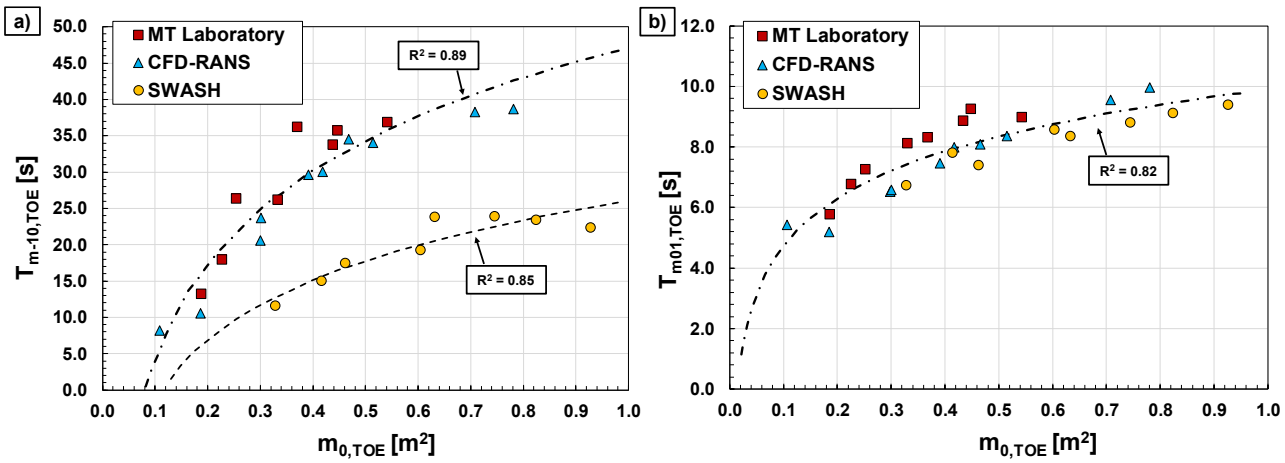

Figure 6.15 – *Relationships between spectral periods and the wave energy at the toe of the wall for MT data.*

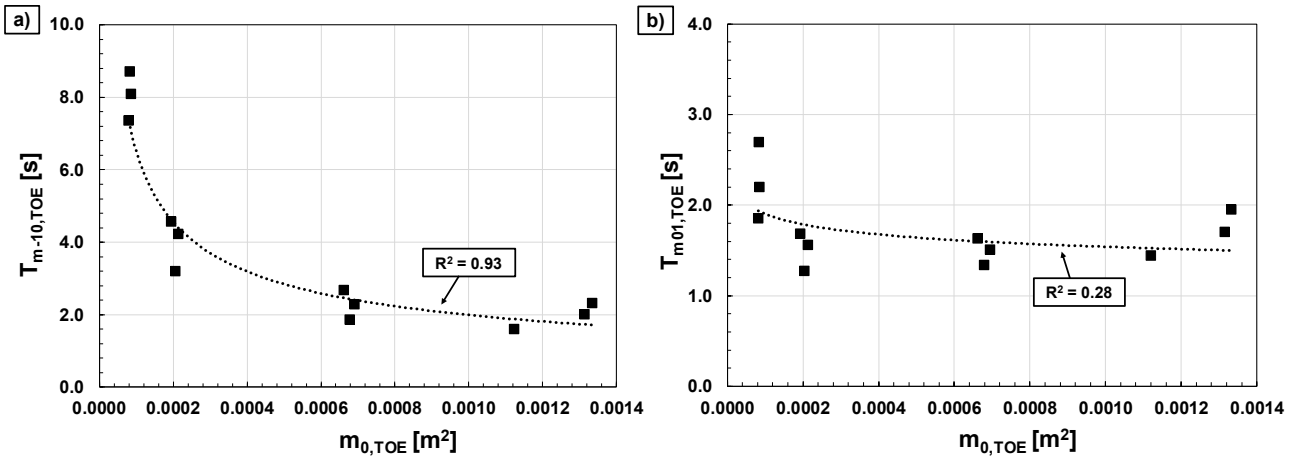

Figure 6.16 – *Relationships between spectral periods and the wave energy at the toe of the wall for DH data.*

It is worth highlighting that signs of the trends (whether increasing or decreasing) only depend on how the experiments were designed. For instance, let us consider the relationship between the harmonic spectral period, $T_{m-10,TOE}$ and wave energy.

MT experiments used a single value of h_{TOE} and varied the wave parameters in the nearshore zone. Hence, larger E_{rms-N} (and so does E_{rms-N}/h_{TOE}) simultaneously results in larger $m_{0,TOE}$ – due to the inability of the steep foreshore to dissipate the growing nearshore energy – and larger $m_{-1,TOE}$ because of the greater long-wave forcing zone (Symonds et al., 1982); since the amount of energy at low-frequency components should increase as E_{rms-N}/h_{TOE} increases (see Hofland et al., 2017), a positive correlation appears between $T_{m-10,TOE}$ and $m_{0,TOE}$ (Figure 6.15a).

On the other hand, DH tests have almost the same offshore wave height, but different local water depth instead. This causes the experimental points to be mirrored. Indeed, for a given surf beats forcing zone, $m_{-1,TOE}$ increases in shallower waters while $m_{0,TOE}$ decreases because the gentle beach ensures the dissipation of wave energy (according to Le Mehautè's theory). Thus, the lower $m_{0,TOE}$ the larger $T_{m-10,TOE}$ (Figure 6.16a).

The analysis of these correlation structures is of great interest for engineering purposes, as either the wave energy or the spectral periods are used as predictors in analyzing wave overtopping and other wave-structure interaction phenomena. Ignoring their mutual relationships can create spurious (false) correlations, which are independent of the physics of the processes.

6.4. Analysis of the mean wave setup

Before turning the wave parameters' influence inside out, this paragraph briefly verifies the ability of the phase-resolving models to reproduce the mean (steady-state) wave setup, $\bar{\zeta}$, namely the average of the wave elevation signal at the location of the wall. As will be shown at the end of this Chapter, its impact on wave overtopping is predictably stringent.

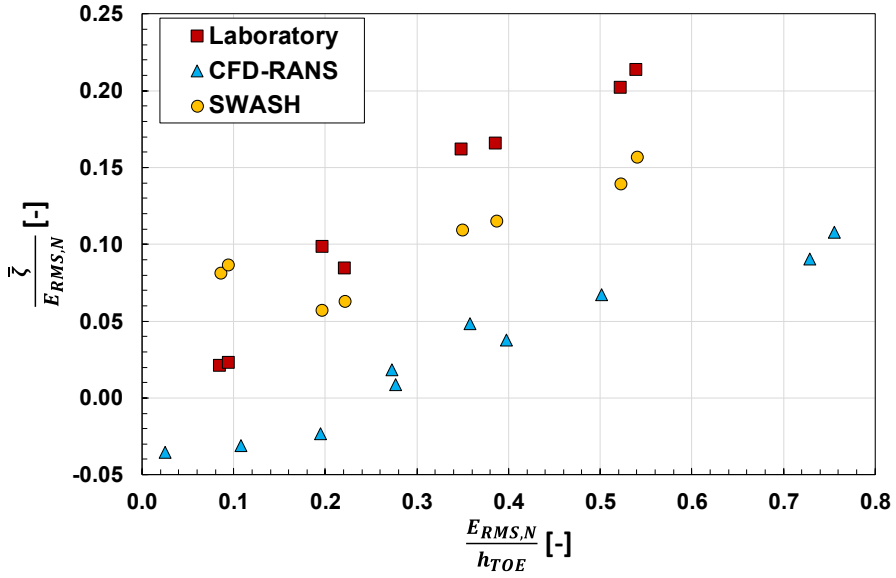

***Figure 6.17** – Laboratory and numerical wave setups at the toe of the wall.*

Figure 6.17 shows that the uneven profile of the Malecòn foreshore led to values of wave setup particularly high, which both the numerical models underestimate. This is particularly true for the CFD-RANS model, most likely because of the mass-source generation condition, which allows the water to leave the domain on the upwave side.

6.4. Predictive variables

As discussed in Chapter 2, a large part of the predictive tools in the literature adopt spectral wave parameters for estimating the flow rate; among them is the EurOtop Manual 2018, a reference point for coastal engineers in designing sea defenses.

However, the previous paragraph has demonstrated that these spectral-based hydraulic variables can be significantly related to each other, leading to some spurious correlations that confuse which variable is truly involved in the wave-structure interaction phenomena.

To assess the effective wave parameters that role the overtopping process, a variant of the Added Variable Plot method (Draper & Smith, 1998) is employed. The relationships between q and the crest freeboard, the wave energy and the mean spectral period at the toe of the wall will be discussed.

The Added Variable Plot (AVP) method exploits a sequence of simple linear regression models that link the flow rate to one predictor at time; step by step, the spurious correlation effects are reduced.
Specifically, let X_1 be a predictor and let Eq. (6.7) represents a regression model, which links it to the overtopping rate variable:

$$q = a + b \cdot X_1 + \varepsilon_1 \tag{6.7}$$

where ε_1 represents the residuals, namely the flow rate without the predictor X_1 influence. To assess the effect of a second predictor, X_2, a regression model that links it to the residuals ε_1 is applied:

$$\varepsilon_1 = a + b \cdot X_2 + \varepsilon_2 \tag{6.8}$$

Such a procedure sheds some light on the role of the different variables involved in the overtopping process, especially for those affected by correlation structures.

The relationship between q and the wave energy at the toe of the wall has been first assessed (Figure 6.18). Since it is significantly nonlinear (halfway between the exponential and the power laws), the data are fitted with a power function, which is linearized into:

$$ln(q) = b \cdot ln\left(m_{0,TOE}\right) + ln(a) + \varepsilon_z \tag{6.9}$$

Successively, the influence of the crest freeboard can be assessed regardless that of wave height by plotting the residuals ε_z in Eq. (6.9) as a function of R_C in Figure 6.19.

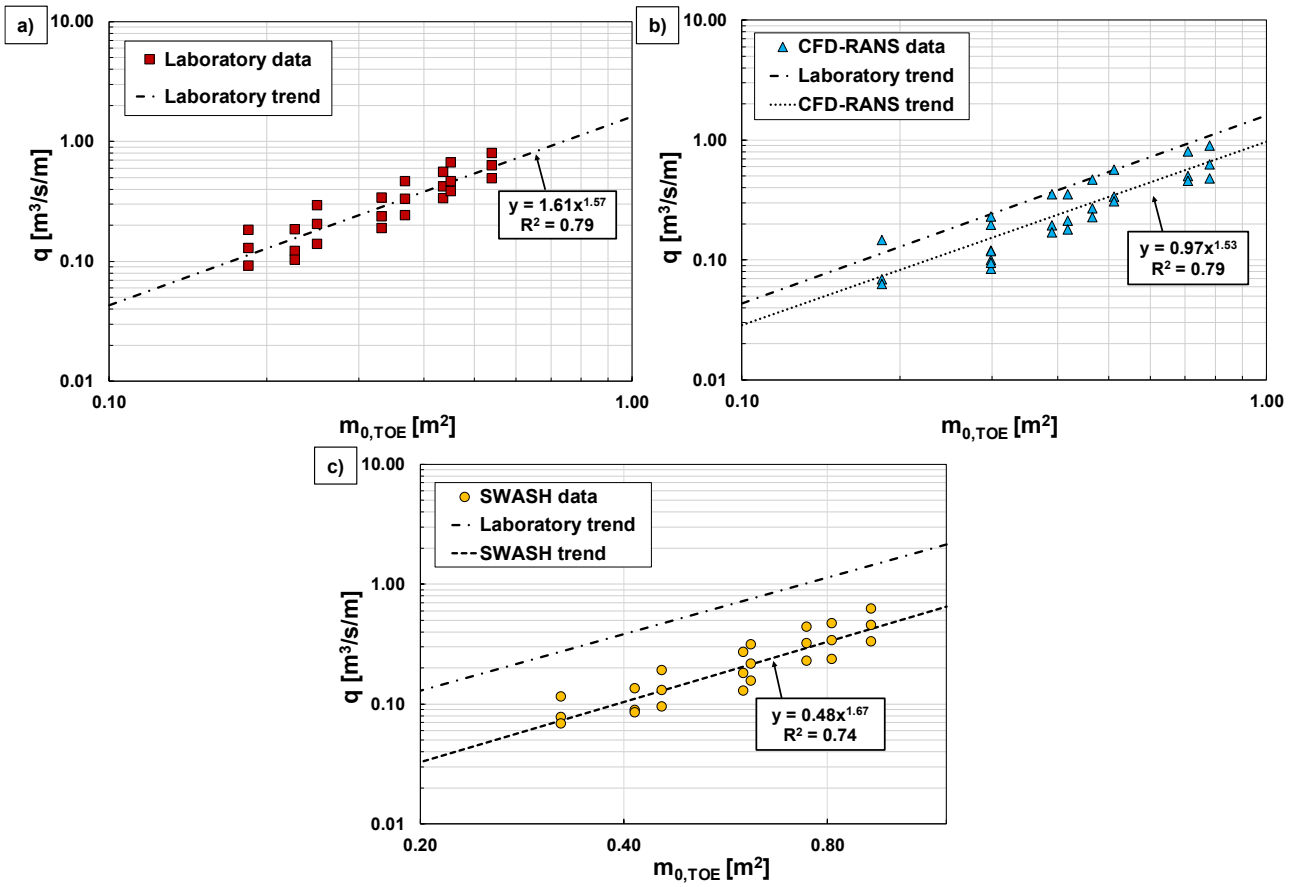

***Figure 6.18**- Laboratory and numerical flow rates vs. wave energy at the toe of the wall.*

The inspection of the graphs suggests that either CFD or the non-hydrostatic model underestimate the flow rate for a given value of wave energy, especially for SWASH. On the other hand, both the numerical account for the effect of the crest freeboard properly; however, RANS model slightly overpredicts q at lower freeboards, as indicated by the green line in Figure 6.19b.

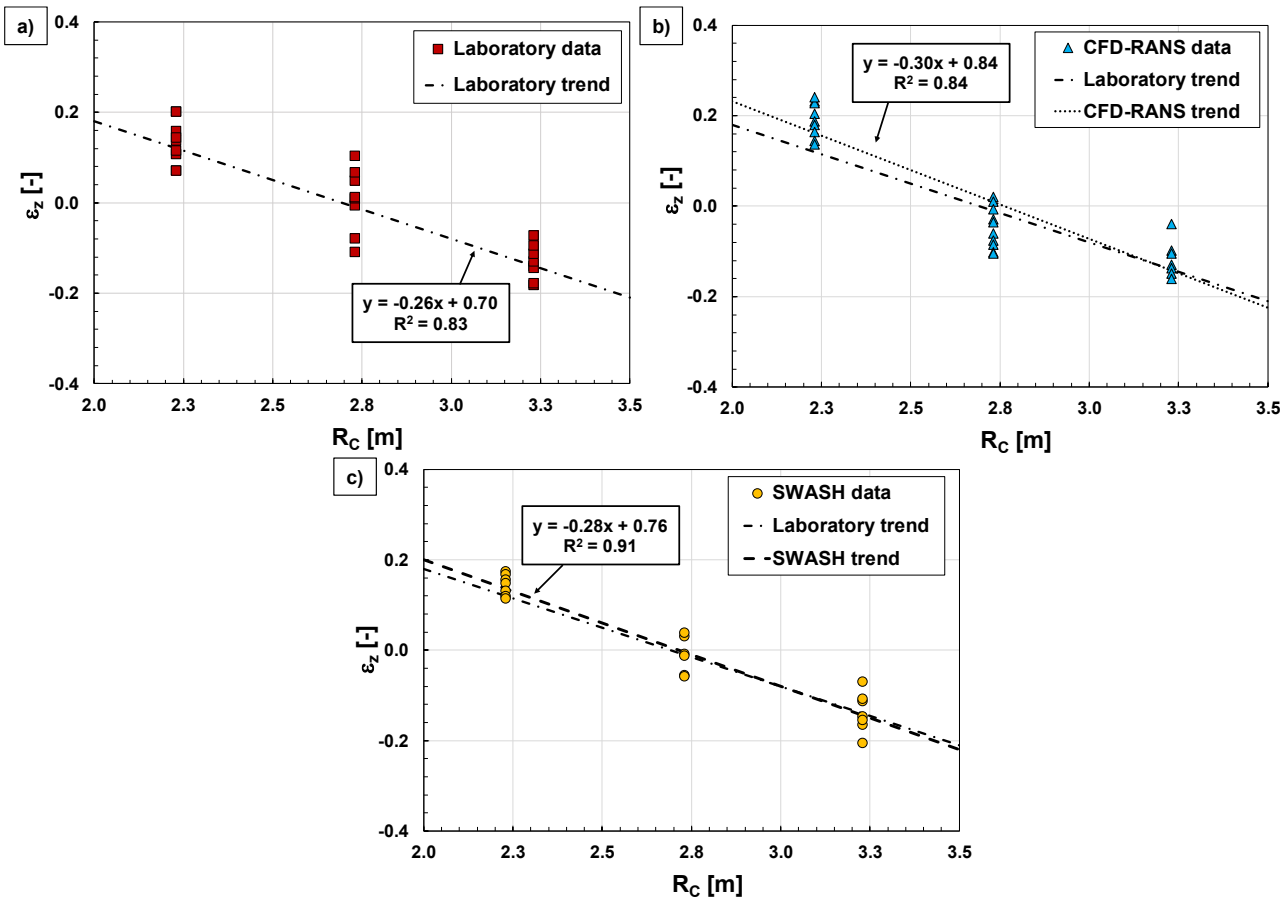

Figure 6.19 - *Reduction of wave overtopping in response to crest freeboard.*

Finally, the role of the spectral periods is investigated. Figure 6.20 plots both the mean spectral periods at the toe of the wall, $T_{m-10,TOE}$ and $T_{m01,TOE}$, against the mean overtopping discharges for the MT experiments. Both the laboratory and numerical outcomes show a significant increasing trends, as observed in the literature (e.g. Van Gent, 1999); furthermore, the relationships are characterized by quite high correlation coefficients. Unlike the nearshore peak period, $T_{p,N}$, that slightly affects the flow rate (see Figure 6.21), the spectral periods seem to have a larger explanatory power.

However, results of the AVP reveals the illusory nature of these relationships. T_{m-10} and T_{m01} take into account the effect of the wave energy distribution in the frequency domain in the long and short-wave range, respectively. Thus, when the dependence of q from $m_{0,TOE}$ is removed, the correlations disappears wherever, as clearly shown by Figure 6.22 that plots the residuals ε_z against the mean spectral periods. This result indicates

that T_{m-10} and T_{m01} do not contribute to the prediction of q more than $T_{p,N}$, and the correlation observed in Figure 6.20 essentially results from the relationship with the wave energy observed in Figure 6.15. It is, therefore, a spurious correlation effect rather than a real physical relationship.

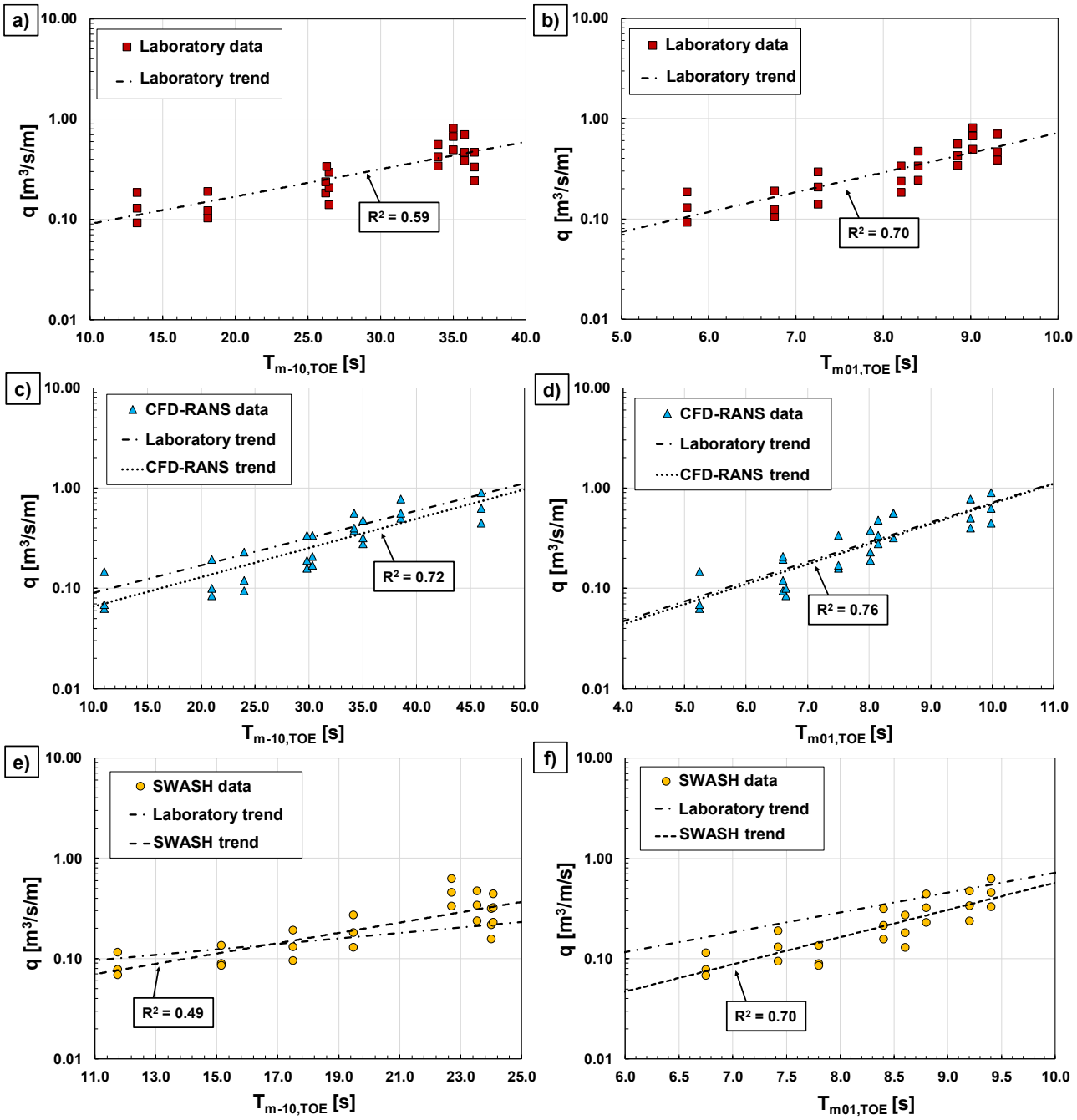

Figure 6.20 - *Laboratory and numerical flow rates as a function of the mean spectral periods.*

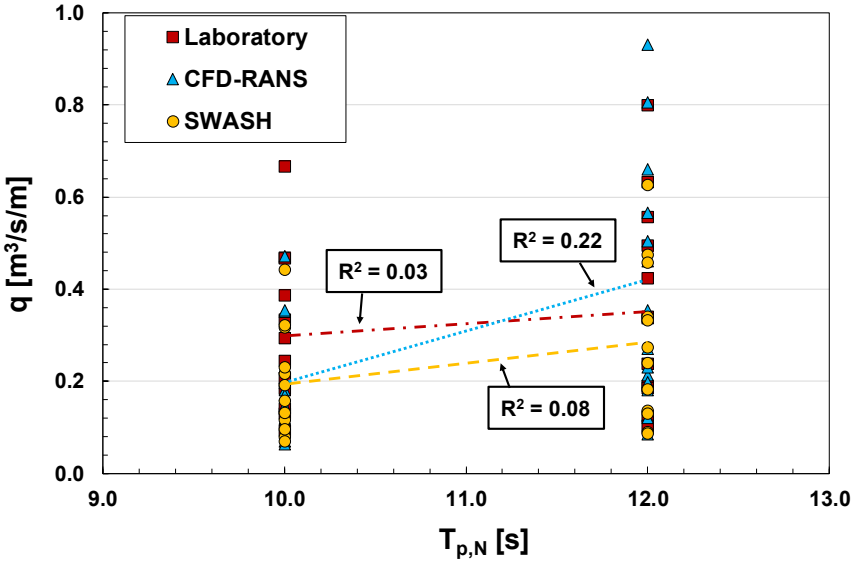

Figure 6.21 - *Laboratory and numerical flow rates as a function of the nearshore peak period.*

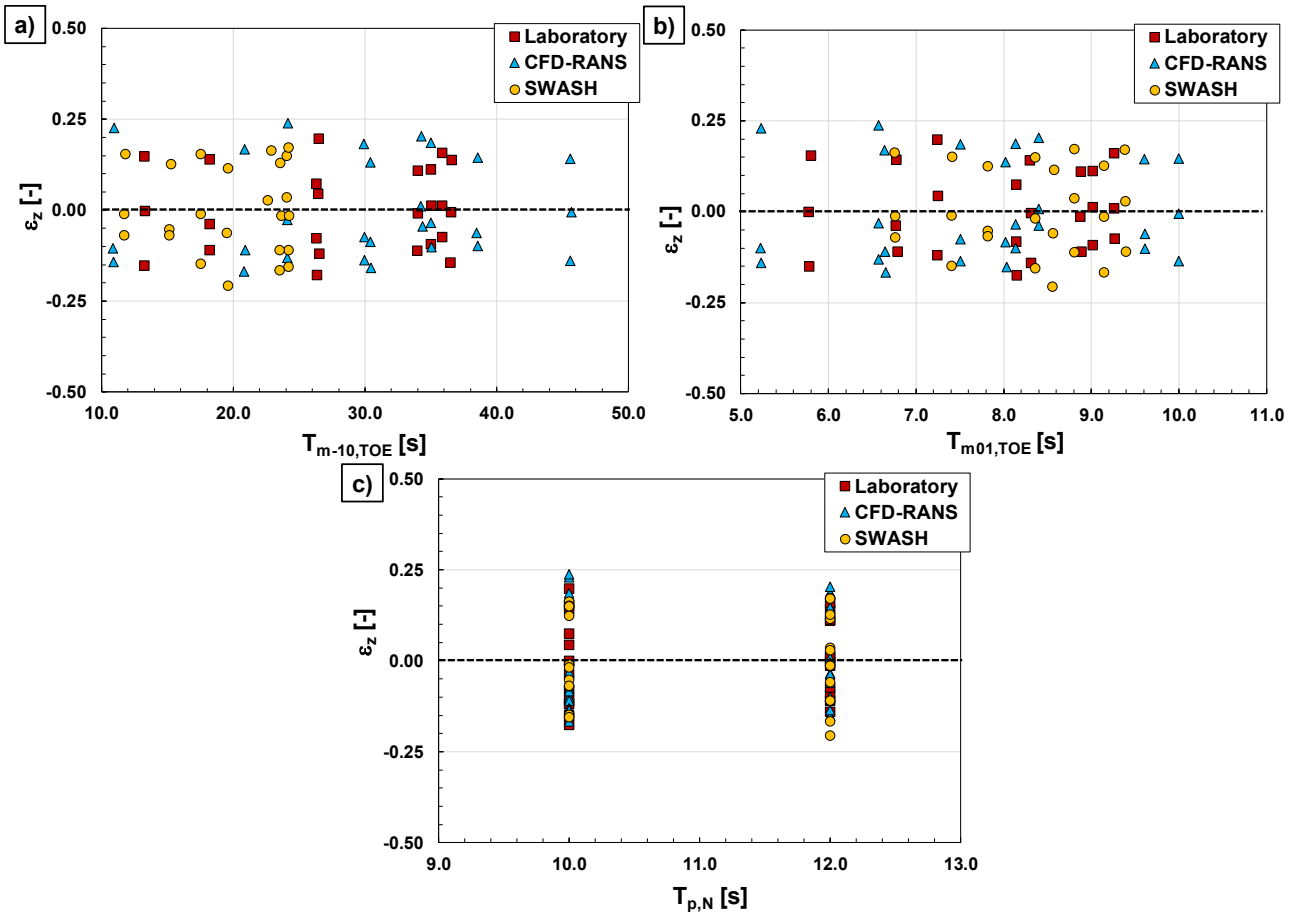

Figure 6.22 *– Panels a) and b) plot residuals of Eq.(6.9) as a function of $T_{m-10,TOE}$ and $T_{m01,TOE}$, respectively; panel c) relates residuals and the nearshore peak periods.*

6.5. The new hydraulic variable

The comparison between laboratory and numerical data with EurOtop's prediction formulae for vertical walls (Eq. (4.3)) is shown in Figure 6.23. The existing tool (solid line) systematically underpredicts the laboratory data (and only 13 out of 24 laboratory points lie within the formula's band) while overestimating the numerical results. However, most points lie within or close to the 90% confidence bands (dash-dotted curves), indicating that the observed scatter is consistent with the inherent variability of the overtopping process. From this perspective, both the numerical approaches predict the overtopping rate reasonably well.

In light of the AVP's results, the fact that numerical data lie systematically beneath the laboratory ones is not surprising. Figures 6.18 and 6.19 have indeed demonstrated that both the numerical models reproduce the relationship between q and R_C quite well while underestimating the role of wave energy.

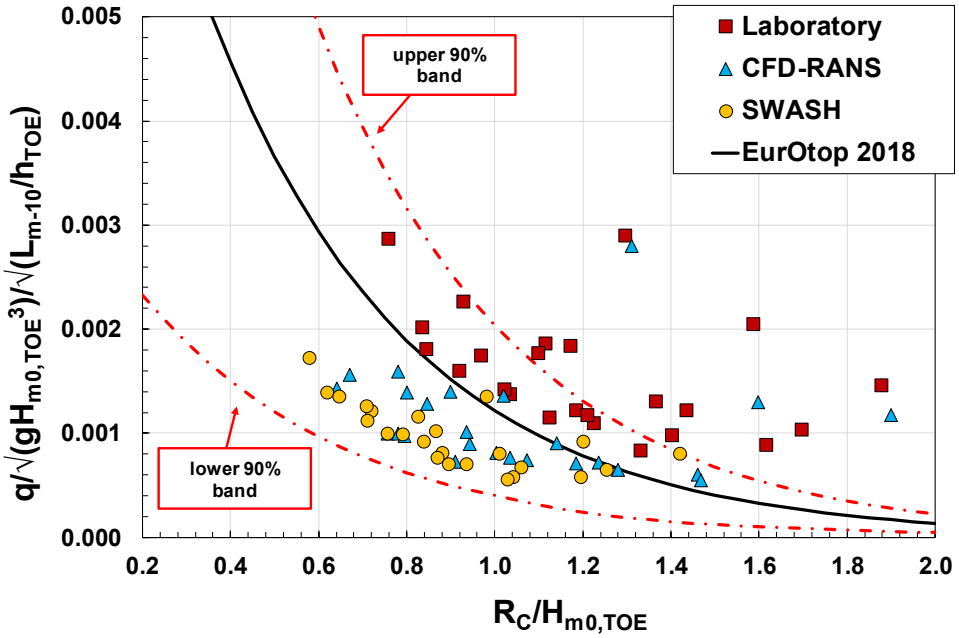

***Figure 6.23** – Laboratory and numerical flow rates on the EurOtop non-dimensional plane; note that all the data are under impulsive conditions. The graph also plots the EurOtop model (black solid line) and the upper and lower 90% bands (red dash-dotted lines).*

Nevertheless, the larger laboratory flow rates are reasonably due to the higher values of wave setup shown in Figure 6.16. To take this effect into account, Figure 6.23 replots the flow rates against the quantity:

$$\zeta_{1/4} = \left(\bar{\zeta} + 1.27\sqrt{m_{0,TOE}}\right) \tag{6.10}$$

which represents the average of the highest one-fourth of water levels in a Gaussian wave process. It is worth noting that Eq. (6.10) can be used for both a Gaussian process and a series of sinewaves.

CFD-RANS and laboratory data follow now approximately the same trend (black line in Figure 6.24), while SWASH lies only moderately below (red line in Figure 6.24).

From a physical point of view, this result expresses the simple concept that the amount of wave overtopping cannot depend solely on the variance of the wave fluctuations, but rather on the upper tail of the distribution. Indeed, this is similar to predictive models that relate the mean overtopping discharge to the run-up heights with low exceedance probability (Etemad-Shahidi, 2022; Yuhi et al., 2020; Hedge and Reis, 1998; de Waal and Van der Meer, 1992), assuming that the wave overtopping occurs when wave uprush reaches the crest of the structure.

Nevertheless, it should be noticed that $\zeta_{1/4}$ is measured in the absence of the wall and is therefore not a run-up statistic.

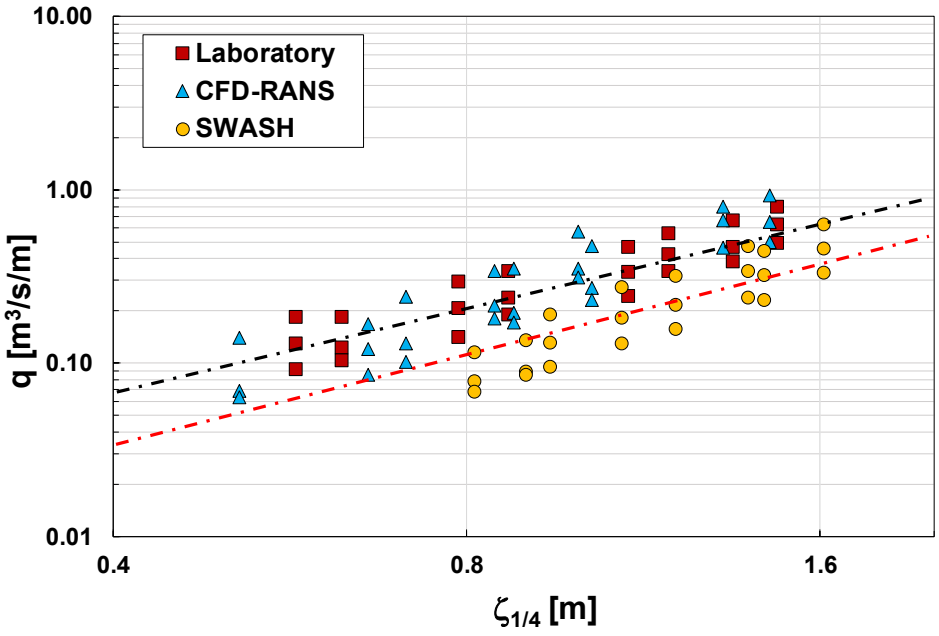

***Figure 6.24** – Laboratory and numerical flow rates as a function of the new hydraulic variable, $\zeta_{1/4}$.*

6.5.1. Predicting the overtopping rate in the surf zone

The analysis of the MT dataset has revealed that the overtopping of a vertical seawall in the surf zone can be predicted in the function of the crest freeboard, and some water level statistics related to the upper tail of the distribution of the wave elevations at the toe of the structure, say $q = q\ (R_C, \zeta_f)$.

A proof is shown in Figure 6.25, which plots the mean overtopping discharges for the entire MT dataset (48 data that include both the surges investigated) against the relative crest freeboard, $R_C/\zeta_{1/4}$; the graph includes the flow rates from the numerical models as well.

The data are indeed characterized by a very predictable trend and a little scatter, resulting in high values of the correlation coefficients (R^2 larger than 0.9). In particular, CFD-RANS experiments follow the same regression equation as the laboratory ones (solid curve), which indicates a satisfactory reproduction of the wave overtopping process by the CFD model. On the other hand, the non-hydrostatic model regression equation lies

systematically below that obtained by gathering laboratory and RANS results, confirming SWASH's tendency to underestimate the flow rate already observed in the literature (e.g. Suzuki et al., 2017).
Furthermore, such a result confirms the crucial role of wave setup for properly estimating wave overtopping in the surf zone. In particular, the wave setup is treated with some ambiguity in the literature, so that it is not included explicitly among the overtopping predictors. This might be either because the EurOtop database includes only few data in the surf zone (as discussed in Section 4.2), or simply because no information on this quantity was available for the analysis.

Further proof of the influence of wave setup clearly emerges by comparing Figures 6.25 and 6.26, as the latter plots q as a function of the sole wave variance, $m_{0,TOE}$. The graphs demonstrate that the data significantly scatter when the wave setup is neglected.

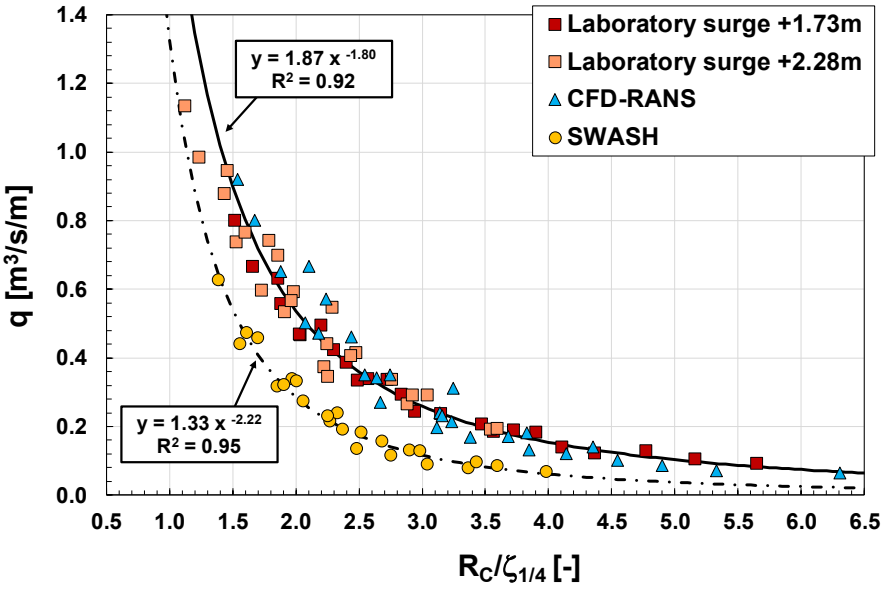

Figure 6.25 - *Laboratory and numerical values of q vs $R_C/\zeta_{1/4}$. The graph plots the whole MT dataset.*

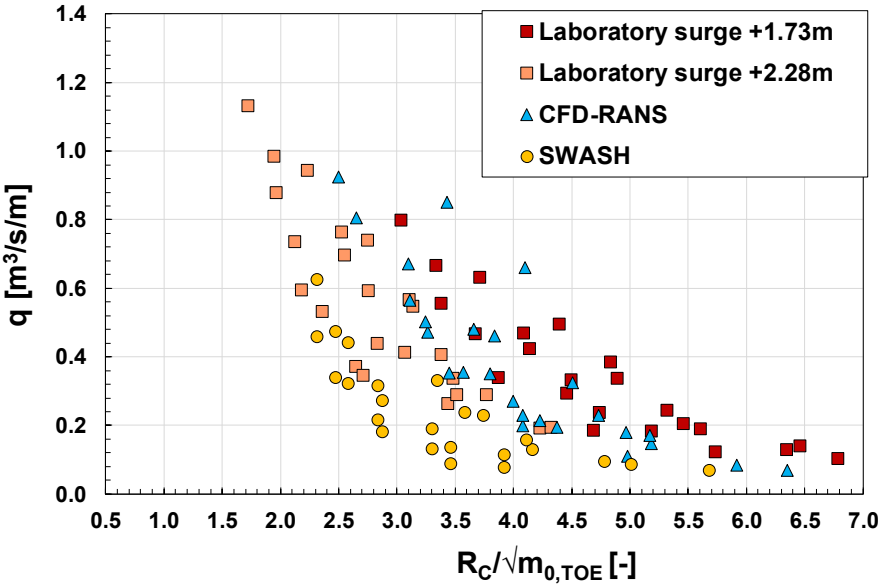

Figure 6.26 - *Laboratory and numerical values of q vs $R_C/(m_{0,TOE})^{0.5}$. The graph plots the whole MT dataset (both the surge investigated during the physical experimental campaign).*

6.6. Discussion

The present Chapter examines the MT dataset to deepen insight into the characteristics of wave overtopping at vertical seawalls in the surf zone. Indeed, as pointed out in Chapter 4, the EurOtop dataset includes a large part of data in shallow water and only a few reliable data in very shallow water; the dataset contains no actual information on vertical walls with very and extremely shallow foreshores. The MT data thus allowed us to extend our knowledge about this wave-structure interaction phenomenon.

These data have been numerically reproduced as well. The numerical experiments exploit two approaches, which differ in vertical resolution and computational time: CFD-RANS and non-hydrostatic model SWASH.

The analysis first focuses on the evolution of spectral moments within the surf zone. The data carried out on the steep uneven MT foreshore have been contemporary compared with those obtained on the mild (1/100) beach of the DH dataset (Van Gent, 1999b); such a comparison ensures the assessment of the influence of the seabed slope on the spectral moments transformation.

The joint analysis of laboratory and numerical data shows a relationship between wave energy and spectral periods (Figures 6.15) despite these quantities being independent outside the surf zone (Figures 6.14). This is true as long as spectral moments attain a "depth-controlled" condition because of breaking. Indeed, as the zeroth and first moments become depth-controlled on the DH mild beach – according to the saturated breakers theory by Le-Mehautè (1962) – the relationship between $m_{0,TOE}$ and $T_{m01,TOE}$ weakens (Figure 6.16b). Conversely, since surf-beats are almost unaffected by wave breaking, the link with T_{m-10} is hardly destroyed (Figure 6.16a). On the other hand, the depth-controlled condition has not been observed on the Malecòn's steep foreshore; wave energy is strictly correlated with both spectral periods.

These correlation structures are relevant because they create spurious relationships with the variables related to the wave-structure interaction processes. The Added Variable Plot analysis of the MT dataset leads to consistent conclusions: the influence of T_{m-10} and T_{m01} on wave overtopping is spurious and depends on their relationship with m_0; once the latter correlation is removed, mean spectral periods do not explain the output variable more than the peak period (Figure 6.22). Such a result may indicate that the shape of wave energy spectra negligibly affects the overtopping process.

Instead of the spectral distribution, the mean overtopping discharge is strongly related to the high percentiles of the distribution of the wave elevations at toe of the wall. Laboratory and numerical flow rates are very well predicted using the variable $\zeta_{1/4}$, namely the average of the highest one-fourth of water levels in a Gaussian wave process. The relationships reported in Figure 6.25 exhibit a very high R^2 index, indicating a remarkable prediction power.
Such a relationship is physically consistent with the approach of many authors in literature who relate overtopping rate and extreme run-up heights (e.g. Mase et al., 2013). However, the new hydraulic variable is much simpler to estimate compared to extreme run-up statistics. According to the Eq. (6.10), $\zeta_{1/4}$ could be even easily determined either with empirical formulae or phase-averaged numerical models.

The results of this Chapter also highlight the role of the wave setup in the overtopping process within the surf zone, although the literature has treated it with some ambiguity. In the EurOtop manual, for instance, the wave setup is considered a "self-accounted" quantity as it is strongly correlated with the height of the breakers and hence implicitly accounted for in the empirical formulae. Nonetheless, the manual suggests taking it explicitly into account when the foreshore is very long and very gentle.

However, the correlation law between wave setup and wave height is not unique. Still, it depends on the seabed's topography as well as, like for CFD-RANS in Figure 6.17, on possible model effects in laboratory or numerical experiments (using mass-source method allowed to better understand the crucial role of $\overline{\zeta}$). Therefore, such variable needs to be explicitly included in the prediction formulae.

Finally, the comparison between laboratory and numerical findings indicates that both CFD-RANS and SWASH model capture the general physics of the processes investigated satisfactorily. Remarkably, this is true for a wide range of phenomena, including the spectral moments' trend with varying nearshore wave conditions (Figure 6.11), the correlation relating wave energy and mean spectral periods (Figure 6.15), and the relationships between the overtopping rate and the wave properties at the toe of the wall, either in the frequency or in the time domain (Figures 6.18, 6.20, 6.24, 6.25). Therefore, the difference between the performance of the numerical approaches is merely quantitative. RANS experiments are, in fact, in good agreement with the physical model, which also leads to excluding the presence of major scale effects in the laboratory experiments.

On the other hand, SWASH suffers from two main biases: it overestimates the high-frequency components of the surf zone spectra and systematically underestimates the overtopping rate. Neither of these, however, are new in the literature.

Indeed, results of Figure 6.13 are similar to those reported in Figure 18 of Zijlema et al. (2011), which refers to the laboratory experiments of Boers (1996). Although the authors do not provide specific comments on this point, Figure shows that the non-hydrostatic model adequately predicts the surf beats, while the high-frequency components are overestimated. However, the ratio between numerical and laboratory spectral moments reaches at most 1.5, whereas for our data we calculated 1.9; this is likely an effect of the beach angle, which in Boers (1996) was as mild as 1:40. In any case, the tendency at overpredicting the shortwave peaks seems an inherent drawback of SWASH (see also Figure 16 of Zijlema et al., 2011).

As concerns the underprediction of the overtopping rate, Suzuki et al. (2017) analyzed 127 experiments of shallow water sloping dikes and found an average underestimation factor of about 0.80; for the Malecòn this factor is 0.69, which is essentially in line. Given the high variability of the overtopping process, these values can be considered reasonably accurate; engineers can readily account for the bias in practical applications by multiplying the numerical overtopping rate by 2.

7. ENERGY SPECTRAL DISTRIBUTION VS. WAVE ELEVATION DISTRIBUTION

The previous Chapter has revealed a crucial issue concerning the role of the harmonic spectral period on the wave overtopping process in shallow water. Contradictory to the literature assumption, which has labelled T_{m-10} as the characteristic period in wave-structure interactions processes, the joint numerical and laboratory analysis of the MT overtopping data has shown that the harmonic spectral period affects the flow rate because of a spurious correlation due to the mutual relationships between spectral within the surf zone.
In particular, the Added Variable Plot analysis has demonstrated that T_{m-10} is strictly related to the mean overtopping discharge as long as the dependence of q from wave energy, $m_{0,TOE}$, is not removed; then, the influence of the harmonic spectral period disappears. According to these findings, T_{m-10} does not contribute to predicting q more than the peak period.

This result may represent a turning point for the coastal engineering community. As already pointed out by Lashley et al. (2021) and discussed in Section 3.2.2. of this work, the assessment of the harmonic spectral period within the surf zone is anything but easy; in fact, some authors overcome this problem by providing a deepwater-wave-based formula for estimating the mean overtopping discharge (Lashley et al., 2021; Mase et al., 2013). Hence, confirming this outcome would ease the flow rate estimation process.

To this end, this Chapter follows two approaches: one applies the AVP method on the run-up and overtopping data of Van Gent (1999b), which is the work that first recommended the use of T_{m-10}; the second resorts to *ad hoc* numerical experiments to obtain direct proofs. Both the statistical and empirical approaches will confirm this significant result.

7.1. The Added Variable Plot analysis on Van Gent data

7.1.1. Run-up data

As described in Section 6.2., Van Gent has measured the wave run-up on two sloping dikes in very shallow foreshore. Specifically, the author has tested two dike's slopes ($tan(\alpha)$ = 1/2.5 and 1/4) located on two mild beaches ($tan(m)$ = 1/100 and 1/250). The AVP analysis is performed on the DH data obtained with single-peak nearshore wave spectra.

According to the AVP procedure reported in Section 6.3.1., a sequence of linear regression models ensures an understanding of the variables involved in this wave-structure interaction process.

The first regression model links wave run-up, $R_{2\%}$, and significant spectral wave heights at the toe of the dikes, the model reads:

$$ln(R_{2\%}) = 0.57 + 0.77 \cdot ln\left(H_{m0,TOE}\right) + \varepsilon_H \tag{7.1}$$

whereas the residuals ε_H can be related to the structures' slope, $tan(\alpha)$, according to the formula:

$$\varepsilon_H = 0.37 + 0.35 \cdot ln(\tan(\alpha)) + \varepsilon_\alpha \tag{7.2}$$

Thus, summing Eq. (7.1) and Eq. (7.2) leads to the following predictive equation:

$$ln(R_{2\%}) = 0.57 + 0.77 \cdot ln\left(H_{m0,TOE}\right) + 0.37 + 0.35 \cdot ln(\tan(\alpha)) + \varepsilon_\alpha = Z + \varepsilon_\alpha \tag{7.3}$$

which explains about 95% of the data variance, as shown in Figure 7.1.

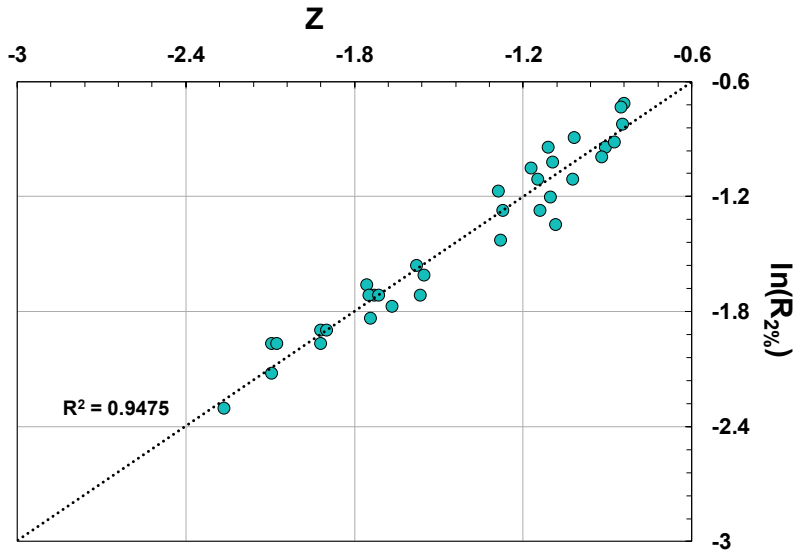

Figure 7.1 *– Regression model reported in Eq. (7.3) for wave run-up DH data.*

The residuals ε_α are then regressed against the nearshore peak period, $T_{p,N}$:

$$\varepsilon_\alpha = -0.33 + 0.47 \cdot ln\left(T_{p,N}\right) + \varepsilon_{Tp} \tag{7.4}$$

The model is statistically significant and explains nearly 62% of the residual scatter (Figure 7.2).

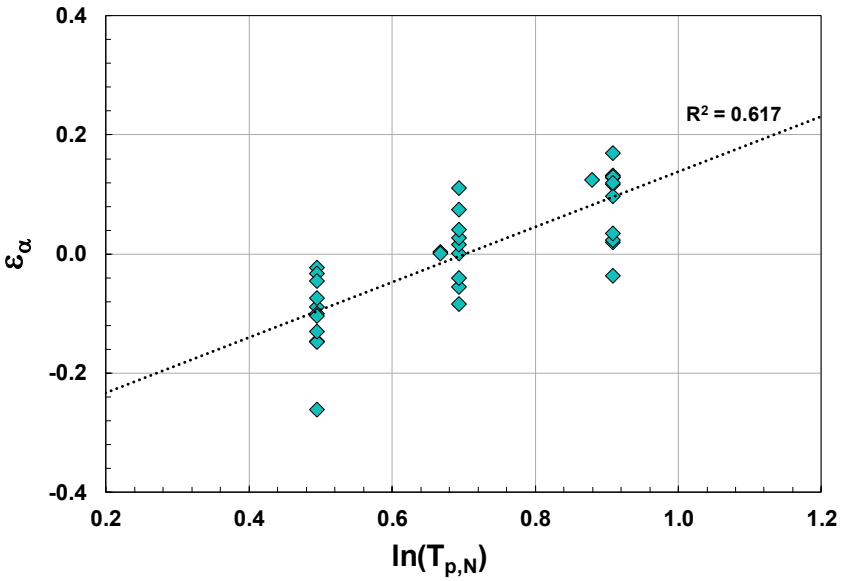

Figure 7.2 *– Regression model between residuals of Eq. (7.3) and the nearshore peak period.*

Finally, residuals of Eq. (7.4) are plotted against the mean spectral periods in Figure 7.3. The latter shows any trend, indicating that the distribution of wave energy in the frequency domain, either in the low or high range, does not actually affect the wave-structure interaction process.

Nevertheless, it is worth highlighting that results do not exclude the influence of the wave period at all; Figure 7.2 indeed points out the role of the peak period.

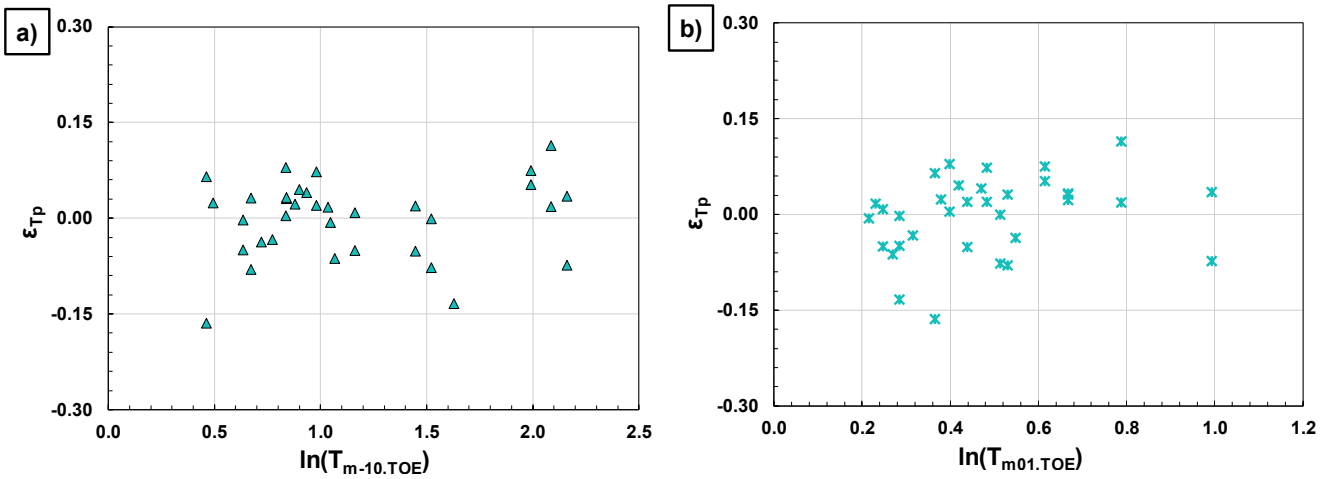

Figure 7.3 *– Panels a) and b) plot the residuals of Eq. (X.4) as a function of* $T_{m\text{-}10,TOE}$ *and* $T_{m01,TOE}$*, respectively.*

However, the influence of the harmonic spectral is the outcome of a spurious correlation, as proved in the following.

Eq. (7.1) can be rewritten as follow by subtracting the wave height from both the hand sides of the equation:

$$ln\left(\frac{R_{2\%}}{H_{m0,TOE}}\right) = 0.57 - 0.23 \cdot ln\left(H_{m0,TOE}\right) \quad (7.5)$$

The relationship between spectral moments at the toe of the structure has already been showed in Section 6.3.1 for 1/100 DH data; here, it is reported for the whole dataset (the effect of the foreshore slope is neglected):

$$ln\left(H_{m0,TOE}\right) = -1.55 - 0.91 \cdot ln\left(T_{m-10,TOE}\right) \quad (7.6)$$

and plotted in Figure 7.4a.

Then, by substituting Eq. (7.6) in the left hand side of Eq. (7.5), the latter becomes:

$$ln\left(\frac{R_{2\%}}{H_{m0,TOE}}\right) = 0.93 + 0.21 \cdot ln\left(T_{m-10,TOE}\right) \quad (7.7)$$

Such a formula expresses the spurious correlation between the relative run-up height, $R_{2\%}/H_{m0,TOE}$, and the harmonic spectral period. Indeed, it does not express an actual (physical) link between the variables but a statistical artifact generated by the correlation between $H_{m0,TOE}$ and $T_{m-10,TOE}$ (Figure 7.4a), i.e. by the presence of a common variable in the input and output terms.

The Eq. (7.7) is shown in Figure 7.4b, where it reasonably fits the data despite some nonlinearity due to the simplifications adopted in the analysis.

The spurious model has a relatively high R^2 statistic (0.48) due to the significant influence of the incident wave height on wave run-up. Furthermore, this correlation appears much higher than those between $R_{2\%}/H_{m0,TOE}$ and the nearshore peak period, which seems to be a weaker predictor, i.e. $R^2 = 0.25$ (Figure 7.5a).

It is worth noting that the spectral period $T_{m01,TOE}$ has no influence on the relative run-up height (Figure 7.5b). Indeed, as the first order moments reach a depth-controlled condition (see Figure 6.12), the relationship between $H_{m0,TOE}$ and $T_{m01,TOE}$ disappears, avoiding any spurious correlation. This leads to the results shown in Figure 7.5b.

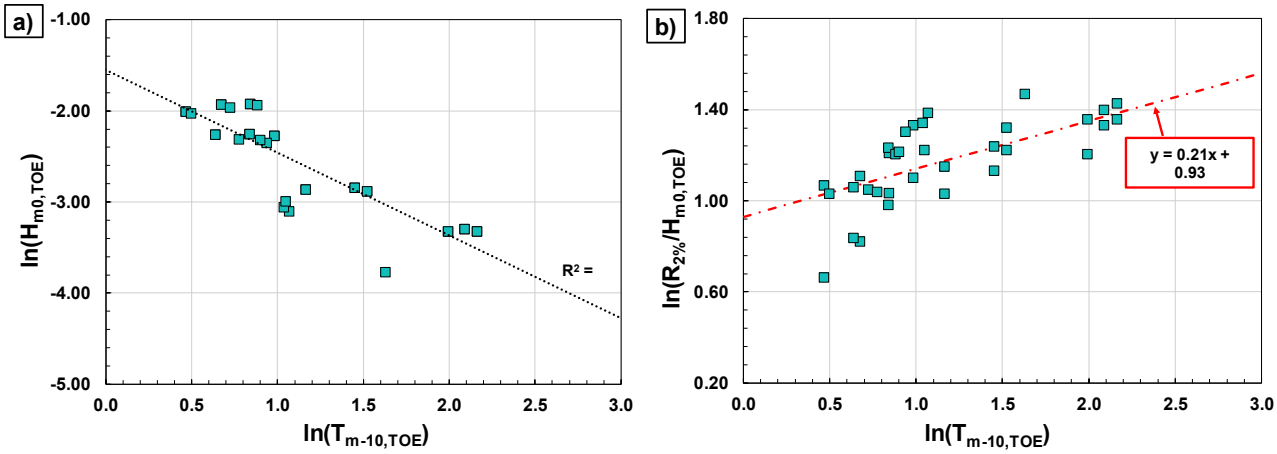

Figure 7.4 *– Panel a) shows the relationship between $H_{m0,TOE}$ and $T_{m-10,TOE}$; panel b) shows the spurious correlation between the relative run-up height and the harmonic spectral period.*

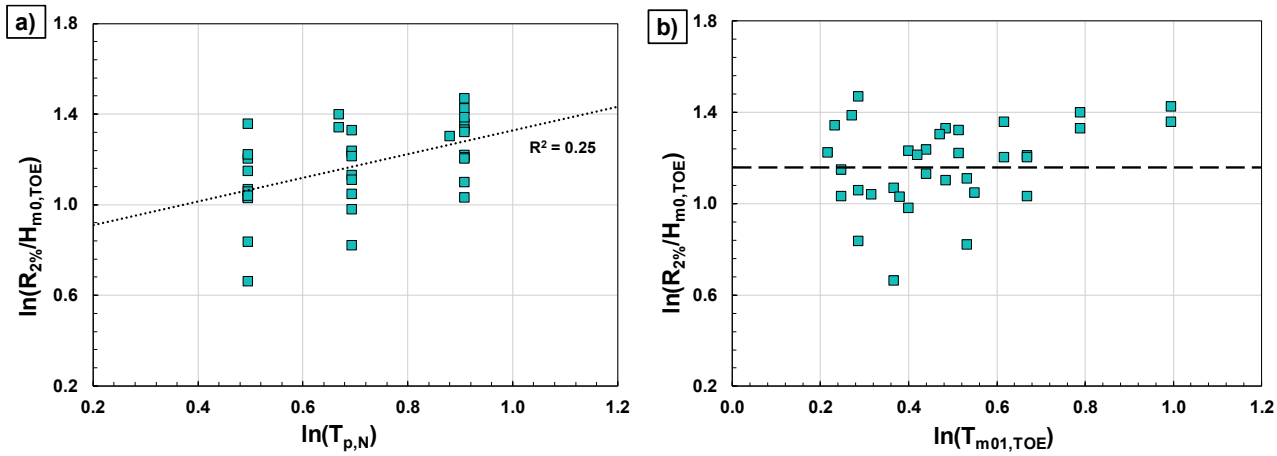

Figure 7.5 *– Relationship between the relative run-up height and either the nearshore peak period (panel a)) or the spectral period $T_{m01,TOE}$ (panel b)).*

The effect of the spurious correlation could be even higher when specific dimensionless variables are used as predictors, as for the predictive model proposed in Van Gent (1999b).

In particular, the author analyzed the relationships between the dimensionless run-up height and the surf-similarity parameter; thus, using the harmonic spectral period to determine the wave steepness means expressing twice the influence of $H_{m0,TOE}$ on $z_{2\%}$ because of the Eq. (7.6), as can be seen in the following:

$$ln\left(\frac{R_{2\%}}{H_{m0,TOE}}\right) = f\left(ln\left(\frac{tan\alpha}{\sqrt{s_{m-10}}}\right)\right) \cong f\left(ln\left(\frac{tan\alpha \cdot T_{m-10,TOE}}{\sqrt{H_{m0,TOE}}}\right)\right) \cong f\left(ln\left(\frac{tan\alpha}{H_{m0,TOE} \cdot \sqrt{H_{m0,TOE}}}\right)\right) \tag{7.8}$$

Hence, the dimensionless predictor variable adopted in Van Gent (1999) amplifies the spurious correlation effects with the dimensionless output variable; indeed, as can be appreciated in Figure 7.6, using the surf-similarity parameter ξ_{m-10} reduces the scattering and leads to a higher correlation coefficient (R^2 = 0.85) compared to that obtained with the dimensional variable $T_{m-10,TOE}$ (see Figure 7.4b).

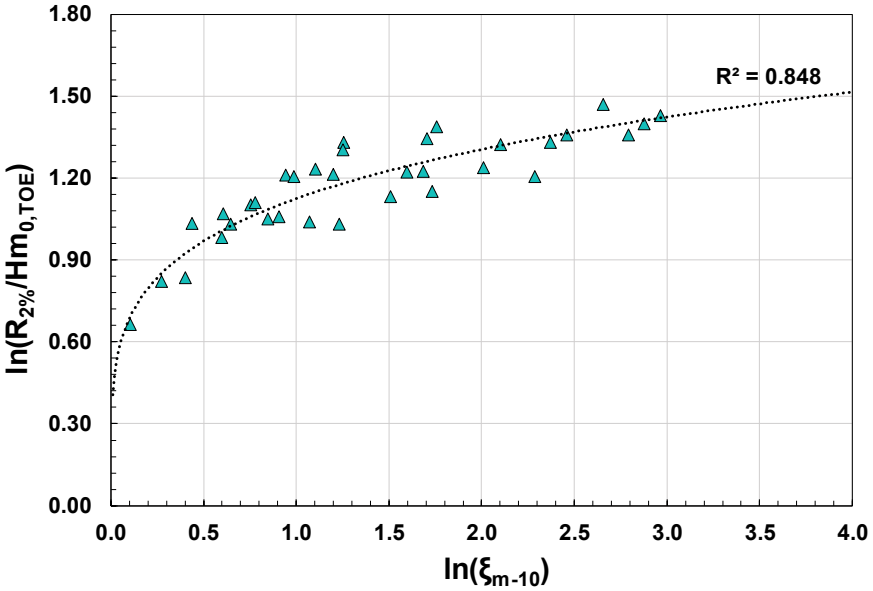

Figure 7.6 *– Relationship between the relative run-up height and the surf-similarity parameter related to the harmonic spectral period.*

7.1.2. Overtopping data

To further prove the conclusion of the previous section, a similar analysis is here applied on the overtopping data with single-peak nearshore wave spectra of DH dataset (Van Gent, 1999b).

According to AVP's results on the MT overtopping data and DH run-up data, the harmonic spectral period influences the output variables as long as a relationship exists between them and the incident wave height. Therefore, the lacking influence of $H_{m0,TOE}$ on q (Figure 7.7a) entails that $T_{m-10,TOE}$ does not affect the mean overtopping discharge, as shown in Figure 7.7b.

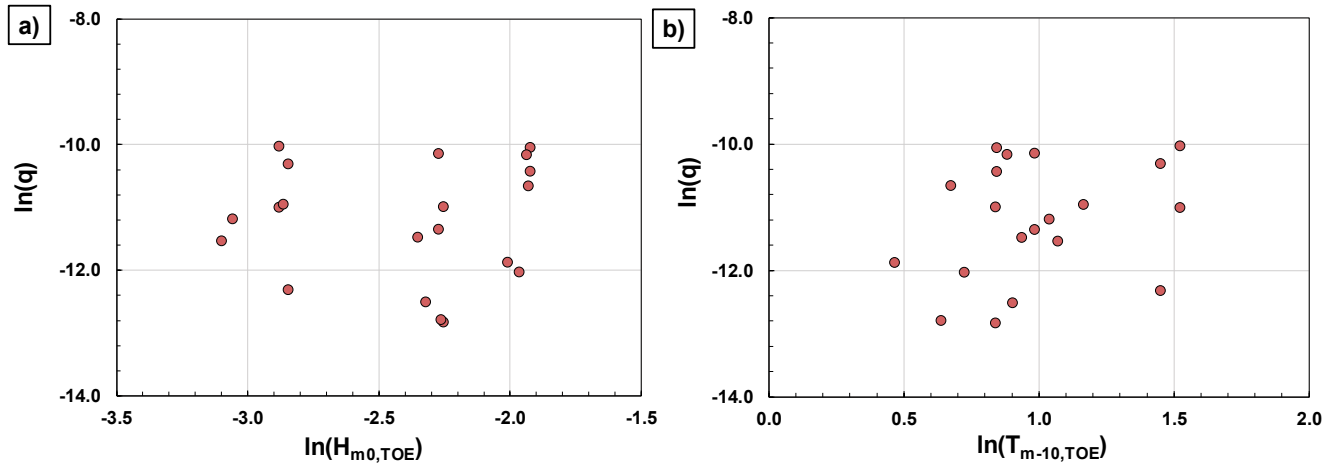

***Figure 7.7** – Flow rate as a function of the incident wave height (panel a)) and the harmonic spectral period (panel b)).*

Still, the conclusions drawn on the role of T_{m-10} are the effect of spurious correlations, as demonstrated in the following.

Despite no correlation exists between q and $T_{m-10,TOE}$, the data in Figure 7.7b can be regressed by this linear model:

$$ln(q) = 0.905 \cdot ln\left(T_{m-10,TOE}\right) - 12.12 \tag{7.9}$$

It is worth specifying that such a linear regression model is not statistically significant and has an R^2 statistic equal to 0.085; however, it has a speculative function.

To obtain the typical dimensionless flow rate (omitting the gravity g for clarity), the term $H_{m0,TOE}^{3/2}$ will be subtracted from both the hand sides of the equation above. Then, the wave height term at the right-hand side is rewritten according to Eq. (7.6), which links wave heights and harmonic spectral periods at the toe of the dikes. Eventually, Eq. (7.9) becomes:

$$ln\left(\frac{q}{\sqrt{H_{m0,TOE}^3}}\right) = \ln(q^*) = 2.27 \cdot ln\left(T_{m-10,TOE}\right) - 9.8 \tag{7.10}$$

The data are fairly fitted by this model, as shown in Figure 7.8 where Eq. (7.10) is depicted as well.

The comparison between Figures 7.7b and 7.8 clearly demonstrates the effects of spurious correlation on predictive models. The dimensionless variable (i.e. the introduction of the incident wave height) has ensured that the harmonic spectral period has become a proper predictor; indeed, the spurious model is statistically significant and has a relatively high R^2 statistic (0.44).

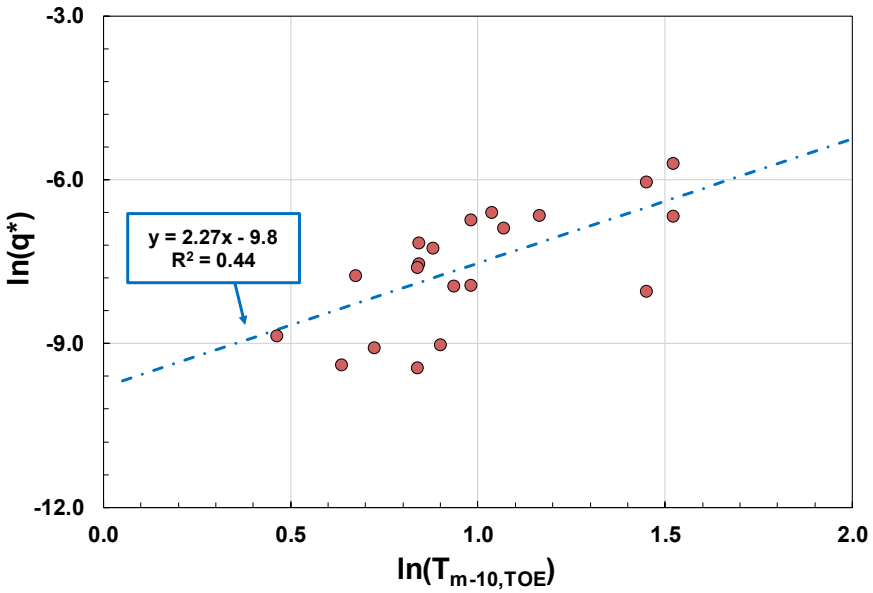

Figure 7.8 *– The dimensionless flow rates as a function of the harmonic spectral; the linear regression model of Eq. (7.10) is depicted as well (blue dash-dotted line).*

It is worth noting that the result shown in Figure 7.7a is consistent with the empirical model that relates the flow rate to the deepwater wave height (Lashley et al., 2021; Goda et al., 1975); thus, as $H_{m0,N}$ was kept constant during the DH experiments, any significant relationship appears between q and $H_{m0,TOE}$.

7.2. The effect of spectral shape on wave overtopping

The outcomes of the AVP analysis on both MT and Van Gent data indicate that the spectral shape does not impact the wave-structure interaction processes; quite the opposite, this Section aims to establish that the upper tail of wave elevation distribution at the toe of the wall – rather than the spectral distribution – roles wave overtopping.

In particular, an experimental analysis is performed to support this conclusion directly. Numerical tests have been carried out via SWASH; they include 8 random wave experiments performed on the Malecòn Tradicionàl foreshore (see Section 6.1.4.2.) and 35 conducted on a planar beach inclined by 1/10 to the horizontal that compare the behavior of random and periodic waves.

The first array of experiments exploits two different generation boundary conditions to conveniently vary the wave spectra characteristics at the location of the structure. In particular, a first- and a second-order generation have been used, referred to as JONSWAP and BOUND, respectively. The JONSWAP wavemaker employs the linear superposition of N harmonic components (i.e., the first term at the right-hand side of Eq. (7.11)); the amplitude of each velocity component, u_n, is derived from the variance of the parametric spectrum (mean JONSWAP spectrum), according to the linear wave theory. The related phase, ϕ_n, is randomly selected instead (Zijlema et al., 2011). The BOUND generation (Rijnsdorp et al., 2014) is based on the weakly nonlinear,

second-order, finite-depth wave theory of Hasselmann (1962) that adds a second-order correction to the linear free wave's contribution:

$$u(x=0,z,t) = \sum_{n=1}^{N} u_n(z)\cos(2\pi f_n t + \phi_n) + \sum_{n=1}^{N}\sum_{m=n+1}^{N} u_{nm} cos[2\pi(f_n - f_m)t + (\phi_n - \phi_m + \pi)] \quad (7.11)$$

The second term on the right-hand side of Eq. (7.11) represents the contribution of the bound IG-waves forced by the difference interaction between the nth and mth free wave components (Longuet-Higgins and Stewart, 1962).

JONSWAP and BOUND boundary conditions can lead to different evolution paths for surf beats, even though the generated spectra have the same energy and approximately the same shape. This property has been exploited to achieve wave spectra at the toes of the walls, which differ solely in terms of long-period wave energy – the same value of *m0* but different m_{-1} (i.e. different $T_{m-10,TOE}$).

Simulations performed on the Malecòn foreshore encompass two different wall crest freeboards, namely R_C = 2.23 and 4.46m above MWL. The water depth at the toe of the wall has been kept constant. The target values of $H_{m0,N}$ are 5.9 and 6.7m, and 7.2 and 8.2m, using JONSWAP and BOUND generation, respectively; the peak period is equal to 12s. Tests' characteristics are summarized in Table 7.1. It is worth mentioning that the incident wave characteristics at the toe of the wall have been derived without the structure in the numerical channel.

Table 7.1. - *Main features of the experiments performed on the Malecòn foreshore.*

wavemaker	h_{DEEP} [m]	$H_{m0,N}$ [m]	T_p [s]	h_{TOE} [m]	R_C [m]
JONSWAP	20.45	5.9, 6.7	12	3.43	2.23, 4.46
BOUND	20.45	7.2, 8.2	12	3.43	2.23, 4.46

Eventually, these two generation tools have led to spectra with the same variance, $m_{0,TOE}$, that differ only by the amount of energy in the low-frequency domain (Figure 7.10), namely in the value of the harmonic spectral period. In particular, $T_{m-10,TOE}$ varies significantly (40% in panels a) and c), and 80% in panels b) and d). For each pair of energy spectra and seawall's height, the mean overtopping discharges are reported in the histograms on the left of the graph.

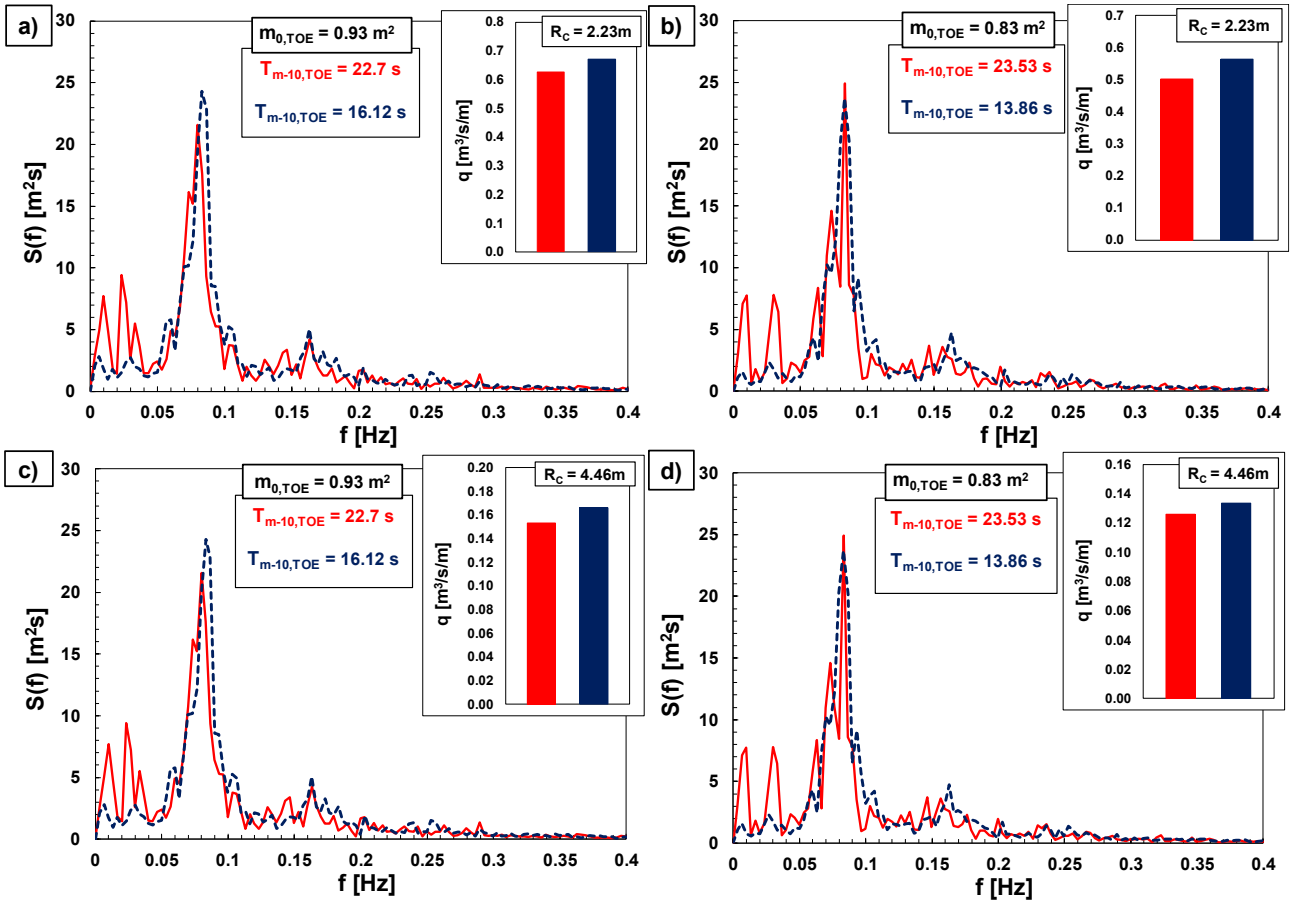

Figure 7.10 *- Comparison between the different wave spectra at toe of the walls (red refers to JONSWAP sea states, while blue to BOUND generation) and the related mean overtopping discharges (shown in the histograms on the right). Panels a) and b) describe the outcomes obtained with R_C = 2.23m; panels c) and d) are related to R_C = 4.46m.*

Unexpectedly, the overtopping rate is systematically higher as the amount of surf beats is low, unlike what is suggested by most of the literature. However, this result becomes clear by considering the values of wave setup. The results observed in Figure 7.10 occur because in BOUND wave experiments, the fluctuations of the wave profile at the toe of the wall reach higher levels than JONSWAP. As the wave variance $m_{0,TOE}$ is the same, this depends on quantities such as wave setup and wave skewness, which are inherently not reflected in the spectrum. Reasonably, then, the overtopping rate is mainly affected by the statistical distribution of the wave elevation, particularly the tail with low exceedance probability.

A second array of experiments helps to further corroborate the assumption above by comparing flow rates of random and periodic sea states as they experience hugely different wave energy distribution along the spectral bandwidth. Moreover, periodic sea states do not exhibit low-frequency components in the energy spectra.

The simulations have been performed on a steep beach inclined 1 to 10 to the horizontal and have investigated two different crest freeboards (R_C = 1 and 2m) located on a constant water depth (h_{TOE} = 1.0m) for a total of 35 data.

The wave height and period of periodic sea states vary between 1.0 and 4.2m and 5 and 12s, respectively. Overall, the deep water wave steepness range investigated is $s_0 = 0.014 \div 0.043$. The irregular sea states are driven by mean JONSWAP spectra characterized by $H_{m0,N} = 1 \div 6.4$m and $T_{p,N} = 7 \div 12$s; the deep water wave steepness s_{0p} varies between 0.013 ÷ 0.041. The hydraulic characteristics at the toe of the walls have been measured without the structures.

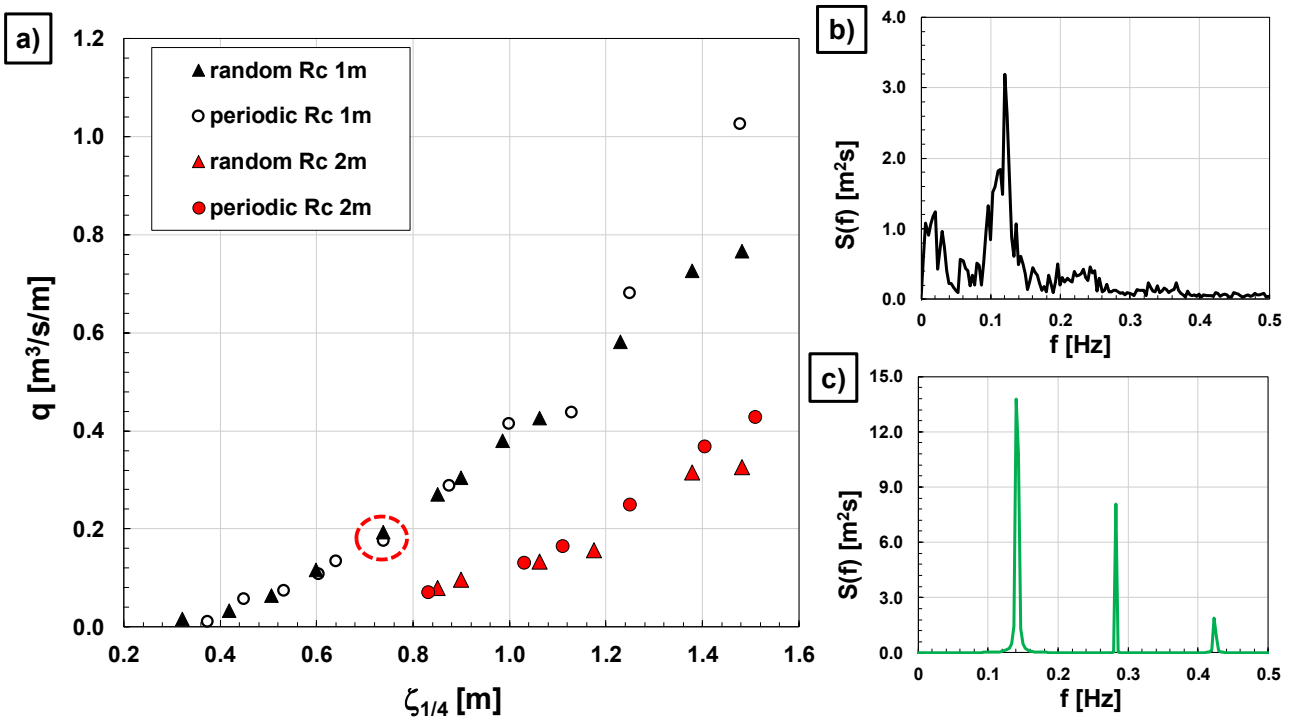

Figure 7.11 - *Panel a): mean overtopping discharge as function of the average of the highest one-fourth wave displacements obtained with random (triangle points) and periodic (circle points) waves. Panels b) and c) illustrate the wave energy spectra of random and periodic waves, respectively, at toe of the structure; these energy spectra relate to the data circled in red in panel a).*

The numerical outcomes are plotted in Figure 7.11a; the graph depicts the mean overtopping discharges as a function of the measured average of the highest one-fourth of wave displacements at the toe of the wall, $\zeta_{1/4}$. For each seawall's height, the flow rates of random and periodic waves remarkably follow a unique trend, confirming the crucial role of the new variable. Indeed, for a given value of $\zeta_{1/4}$ and R_C, periodic and random sea states provide the same discharge (the data circled in red in Figure 7.11a) despite their dramatic difference in the spectral distribution (see the random and periodic energy spectra in Figures 7.11b and 7.11c, respectively).

Therefore, such a result suggests that the discharge depends essentially on the upper tail (low probability exceedance) of the distribution of wave elevation rather than on the energy spectral distribution.

7.3. Discussion

The statistical analysis on the MT dataset performed in the previous Chapter has questioned the established role of the harmonic spectral period in the wave-structure interaction processes in shallow water conditions.

Specifically, a deep insight into the evolution of spectral moments has revealed that T_{m-10} affects wave overtopping because of a spurious correlation; the influence of spectral periods exists as long as their mutual relationship with the wave energy exists.
On the other hand, a new hydraulic variable has been introduced. Laboratory and numerical MT flow rates were well predicted using $\zeta_{1/4}$, the average of the highest one-fourth water levels in a Gaussian wave process.
Overall, the conclusions of the analysis performed on the MT data suggest that the mean overtopping discharge strongly depends on the water elevation distribution at the toe of the wall instead of the energy spectral distribution.

This may be a significant result for the coastal scientific and engineering community; however, it requires more piece of evidence. To this end, the present Chapter resorts to statistical and empirical approaches that corroborate the above assumptions.

The Added Variable Plot method, described in Section 6.3.1., has been applied to the run-up data collected at the Scheldt-flume (Delft Hydraulics) by Van Gent (1999b). As discussed in Chapter 3, this experimental campaign aimed to assess the more suitable wave period in describing wave-structure interaction processes in very shallow water regardless of the shape of wave energy spectrum; the conclusions crowned T_{m-10} as the characteristic wave period.

However, regarding run-up data, the AVP has demonstrated that the measured run-up heights depend significantly on the incident wave height and the dikes' slope (these explain more than 90% of the data variance) and on the nearshore peak period. Once these dependencies have been removed, the residuals of the regression models appear completely unaffected by the spectral periods at the toe of the structure (see Figure 7.3).
The assumed role of the harmonic spectral period is due to spurious correlations, which may arise when dimensionless output variables are used to examine the data. The presence of a common variable in the non-dimensional output and input may suppress the scattering, so confusing a statistical artefact with a physical relationship (Figure 7.6).

The Van Gent overtopping data confirm these findings. Specifically, $T_{m-10,TOE}$ does not influence the overtopping discharges since there is no correlation between q and $H_{m0,TOE}$ (Figure 7.7). Nonetheless, analogously to the run-up data analysis, using the relative mean overtopping discharge, $q/\sqrt{(gH_{m0,TOE}^3)}$, produces an artificial relationship with the harmonic spectral period (Figure 7.8), which appears as a good predictor because of its correlation with the incident wave height.

Nevertheless, it is worth pointing out that the influence of the wave period on wave-structure interaction processes is undoubted, as stated by the literature (e.g. Goda et al., 1975; Owen, 1980; Lashley et al., 2021) and observed in Van Gent data (see Figure 7.2), but – according to these work's results – differs from the influence of T_{m-10}.

From a physical point of view, these results suggest that the spectral distribution of wave energy does not affect the wave overtopping. Two arrays of *ad hoc* numerical experiments have corroborated these findings. The non-hydrostatic model SWASH has been used since the analysis of Chapter 6 has demonstrated its ability to reproduce the physics of these coastal phenomena.

The first array of experiments evaluates the mean overtopping discharges related to two incident wave spectra characterized by the same energy but different values of the harmonic spectral period. The type of experiment has been repeated by varying the value of incident wave height and the crest freeboard.
Unexpectedly, the greater $T_{m\text{-}10,TOE}$, the lower the mean overtopping discharge (Figure 7.10); the larger flow rate is instead due to a higher water level at the toe of the wall. Therefore, the new variable $\zeta_{1/4}$ seems to be a more suitable predictor.

A more evident proof is shown in Figure 7.11, which depicts the overtopping discharges as a function of $\zeta_{1/4}$ obtained during the second array of experiments. The latter examines the flow rates related to sea states that experience drastically different energy distribution in the spectral bandwidth, namely random and periodic waves (see panel b) and c) in Figure 7.11). Results indicate that, for a given R_C and water depth at the toe of the structure, flow rates remarkably follow a consistent trend regardless the spectral shape.
Therefore, following a similar experimental procedure to Van Gent (1999b), which examined wave run-up and overtopping on varying the spectral energy distribution to identify the characteristic period that describes these coastal phenomena regardless of the shape of wave spectra, the second array of experiments has demonstrated that the wave overtopping is actually governed by the water elevation distribution at the toe of the wall rather than the energy spectral distribution.

In light of these findings, the next chapters will derive a new predictive model that relates the mean overtopping discharge to the upper tail of wave elevation distribution at the toe of the structure. Therefore, the predictive model will adopt the average of the highest one-fourth of wave elevation as a new hydraulic variable.
It is worth highlighting that the use $\zeta_{1/4}$ is physically consistent with the use of extreme run-up statistics (e.g., $R_{2\%}$) for estimating the mean overtopping discharge (e.g. Mase et al., 2013), but its estimation is much simpler as it is inferred without the presence of the structure.

8. NUMERICAL INVESTIGATION ON WAVE OVERTOPPING OF VERTICAL WALLS WITH SHALLOW FORESHORES

The state-of-the-art analysis presented in Chapter 4 has revealed the uncertainties related to the available predictive formulae for wave overtopping at vertical walls in shallow waters. The paucity of reliable data highlights our inadequate knowledge about this process.

Furthermore, the hydraulic predictors employed in the existing empirical tools are characterized by some drawbacks that could affect the performances of the overtopping models. The use of the run-up height as a hydraulic variable brings along doubts about which are the more suitable run-up models (e.g. Hughes, 2004; Pillai et al., 2019; EurOtop 2018) and the uncertainties related to the empirical model itself (see Yuhi et al., 2021); moreover, the necessity of iterative procedures to assess the run-up level in order to estimate the overtopping discharge makes tedious their feasibility (e.g. Mase et al., 2013). On the other hand, results obtained in Chapter 6 have shown that the spectral wave parameters adopted so far by the literature are not strictly necessary and rough to estimate as well. Specifically, the Added Variable Plot analysis has suggested that the harmonic spectral period influences the flow rate as long as it is correlated to the wave height at the toe of the structure; T_{m-10} affects q just because of a spurious correlation. Finally, the overtopping models based on deepwater wave conditions (Lashley et al., 2021) overcome all the above drawbacks, but they may be unsuitable when complex bathymetries are involved.

In Chapter 6, a new hydraulic variable has been introduced. Results of *ad hoc* numerical experiments have confirmed that the mean overtopping discharge is affected by the water displacement distribution rather than the spectral energy distribution. The idea is that the wave overtopping is related to high percentiles of the surface elevation distribution at the toe of the wall, which can be expressed by the highest one-fourth of wave elevation, $\zeta_{1/4}$. Therefore, this Chapter will provide a new overtopping model based on this hydraulic variable.

An extensive parametric study has been carried out with the non-hydrostatic model SWASH to develop a design formula that uniformly predicts the overtopping rate at vertical seawalls for both breaking and non-breaking wave conditions.

The use of the numerical model indeed allows the experimental conditions to vary smoothly and thus create a wide and varied dataset, avoiding the typical limitation of laboratory experiments. Specifically, SWASH ensured the investigation of different geometrical features (by easily varying either the foreshore's slope and characteristics or the seawall's location and crest freeboard) and the examination of a wide range of shallowness conditions.

Therefore, the predictive formula has been derived by gathering an assorted dataset.

8.1. SWASH modelling of coastal processes

Over the last decade, the numerical model developed by Zijlema et al. (2011) has been increasingly used to analyze wave-structure interaction processes (e.g. Suzuki et al., 2017; Gruwez et al., 2020; Zhang et al., 2016;

Zhang et al., 2020; Buckley et al., 2022). Suzuki et al. (2023) have dealt with wave overtopping in port environments; a comparison with physical model tests has shown the capability of SWASH to predict the mean overtopping discharge with both perpendicular and oblique incident waves. Henderson et al. (2022) have validated the estimation of run-up and number of overtopping events of an extreme storm with field observations. The authors have obtained consistent results between numerical and field data, although the overtopping events have been overestimated by a factor of 2. Several studies have focused on the wave overtopping modelling of sloping dikes with very shallow foreshores (see Suzuki et al., 2014; 2011); among them, Suzuki et al. (2017) represents one of the most essential work. The authors accomplished an extensive and detailed analysis of wave overtopping in shallow water by numerically reproducing 124 tests from four different physical model campaigns. Both wave evolution and overtopping have been carefully examined, as the authors stated that an accurate estimation of the mean overtopping discharge requires a good reproduction of the incident wave properties. Then, the suitability of SWASH to predict the flow rate in very shallow waters has been proved, although the model performance worsened as the discharge decreased. In this work, the non-hydrostatic model has used to investigate the wave overtopping on vertical walls in shallow waters along with the relationships between the flow rate and incident wave characteristics. Beyond the mere validation, the aim was to verify the model's capabilities to describe the physics of wave transformation and overtopping in depth. Results have demonstrated that, as much as the RANS model, SWASH is able to describe the correlations relating to spectral moments within the surf zone and the relationships between the overtopping rate and the wave properties at the toe of the wall.

However, although the literature has gathered satisfactory validations, SWASH experiences some biases concerning wave transformation and overtopping.

Indeed, despite the non-hydrostatic model well capturing the dominant features of the spectral evolution from deep waters up to the shore, it tends to overestimate wave energy at high frequencies. This behavior has been underlined in Section 6.6, but has already been noticed in Zjilema et al. (2011) and Zjilema and Stelling (2008), where two different laboratory experiments of Boers (1996) were reproduced. Even if two types of foreshore – a multi-slope and a mild barred beach, respectively – and different wave steepness values have been involved, the studies agree that the energy is well reproduced at low frequencies and overpredicted at higher. Nevertheless, such bias does not seem to be systematic. Suzuki et al. (2017) indeed observed a fairly good agreement between numerical and laboratory outcomes on the steeper foreshore investigated ($tan(m)$ = 1/35), while an underprediction of wave energy along the entire bandwidth has been obtained with the 1/50 slope.

On the other hand, the tendency of SWASH to systematically underestimate the mean overtopping discharge has been established by several studies (Lashley et al., 2020b; Suzuki et al., 2017, 2011) and observed in Figure 6.25 of this work.

Although some biases have been found, many studies have ascertained the reliability of SWASH in modelling wave-structure interaction phenomena. Hence, based on its validity largely proved by the literature, some

researchers have employed SWASH in an exploratory way. Suzuki et al. (2020) have investigated the overtopping related variables (e.g. flow thickness and velocity) that affect human safety since the numerical model facilitates challenging measurements compared to the laboratory. Nguyen et al. (2020) have adopted SWASH to analyze the spectral wave evolution and the overtopping at dikes on very gentle foreshores (*tan(m)*>1/250) that have never been investigated during physical experimental campaigns.

Overall, such a non-hydrostatic model is characterized by some attractive peculiarities concerning numerical modelling. First of all, no treatments (e.g. VOF) are required to track the free surface motion as it is described by a single-valued function of the horizontal plane; moreover, few grid cells are necessary to represent the vertical structure of the motion. Hence, its inherent trade-off between correctly reproducing wave-related phenomena and saving computational costs has ensured that SWASH can compete with more sophisticated phase-resolving models, such as CFDs. Therefore, SWASH is an optimal tool to deepen the analysis of wave overtopping of seawalls in shallow waters.

8.2. Numerical experimental campaign

8.2.1. *D_U*. Planar beach experiments

The numerical experimental campaign encompasses 74 experiments performed on planar beaches with different slopes. In particular, the *D_U* dataset includes a steeper foreshore inclined by 1/10 to the horizontal and two milder profiles characterized by *tan(m)* equal to 1/30 and 1/50. This ensures the investigation of the seabed slope effect on wave overtopping and the generalization of the predictive formula as well.

Figure 8.1 depicts a sketch of the layout examined. The flat bottom in front of the beach allows the proper development of the generated waves; it is long 180 m, which is approximately equal to one deep water wavelength of the longer wave investigated, and has a water depth equal to 20.5m.
During the experiments, the location of the wall has been varied as well as the crest freeboard. Specifically, the variation of h_{TOE} led to overtopping tests in shallow waters ($h_{TOE}/ H_{m0,N}$ = 1.4, 2 and 2.7), very shallow waters ($h_{TOE}/ H_{m0,N}$ = 0.5 and 0.8) and in extremely shallow waters ($h_{TOE}/ H_{m0,N}$ = 0.2 and 0.3). The crest freeboard has been raised from the ratio $R_C/ H_{m0,TOE}$ = 0.5 up to 2, which is the typical design range.

Random sea states driven by mean JONSWAP spectra have been generated, which are characterized by a deep water wave steepness of about 0.035 (the typical value of wind-sea conditions).
It is worth noting that the wave parameters at the toe of the wall have been determined without the structure in the numerical channel. Hence, in addition to the tests on wave overtopping, wave propagation experiments have been carried out as well.

Wave propagation simulations run for 200 waves, while overtopping tests run for 500 waves (according to the findings of Romano et al., 2015).

The main hydraulic and geometric features are listed in Table 8.1.

Table 8.1. - *Main features of the D_U overtopping tests.*

cot(m)	# tests	$H_{m0,N}$ [m]	$T_{p,N}$ [s]	$h_{TOE}/ H_{m0,N}$ [-]	R_C [m]
10	40	1.3, 2.4, 5.3	5.3, 7, 10	0.2 – 2.7	0.4 – 5.8
30	24	2, 5.3	7, 10	0.2 – 2	0.4 – 3.4
50	10	5.3	10	0.2 – 0.5	0.8 – 4.4

.

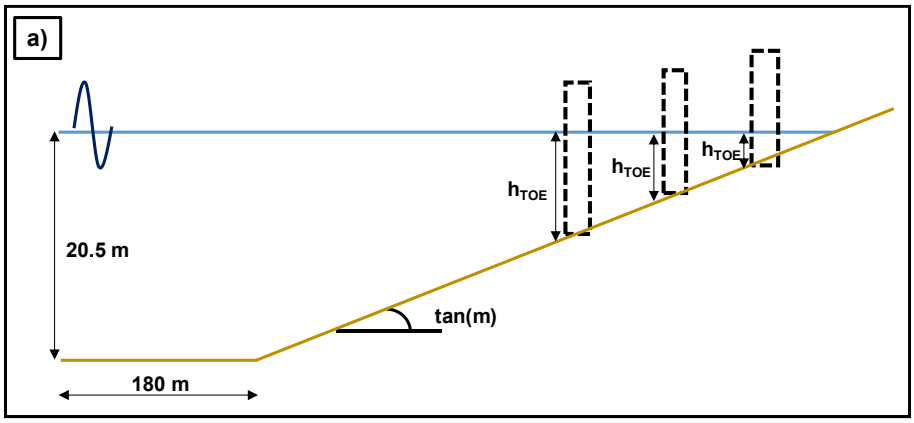

Figure 8.1 *– Sketch of the experimental layout of dataset D_U. Panel (a): schematization of the beach profile characteristics and the several water depths at toe of the wall investigated; panel (b): four different relative crest freeboard values examined for each wall position.*

8.2.2. Numerical setup

The numerical experiments have been conducted in a 1-D mode using the non-hydrostatic pressure term.

At the up-wave edge of the numerical flume, in addition to the wave generation tool adopted (mean JONSWAP spectra), a weakly reflective boundary condition has been imposed, which radiates the waves propagating from onshore. Rear the vertical wall, a Sommerfield condition minimized wave reflection at the end of the channel.

The water depth has been divided into two layers; the horizontal discretization has guaranteed at least 70 points per nominal wavelength at the incipient breaking, L_{nb}, which is defined as $L_{nb} = \sqrt{gH_{m0,N}} \cdot T_p$. Here, the hypothesis is that that $H_{m0,N}$ is of the same order as the incipient breaker height, H_b , and that, in turn, $H_b \cong h_b$. However, the results should be affected by the grid size. To verify this issue, 9 experiments of *D_U* have been randomly selected to perform a grid sensitive analysis.

These nine tests have been repeated with a coarser and a finer discretization. Specifically, the grid spacing has been doubled and halved, obtaining $L/\Delta x$ equal to 140 and 35, respectively. Figure 8.2 plots the variation in the flow rate, expressed as the ratio between the mean overtopping discharge computed with the coarser/finer grid, *q'*, and that obtained with $L/\Delta x = 70$. Figure 8.2a clearly shows that the coarser grid produces significant variations in the mean overtopping discharge, especially for lower flow rates (Figure 8.2b). On the other hand, the halved grid does not have a significant effect; the discharges vary between +0.46 and -0.35 with regard to

the original grid (+3% on average). These variation rates do not weigh more than the typical uncertainties related to the wave overtopping phenomena (e.g. Romano et al., 2015).

Therefore, according to the sensitive analysis conclusions, the discretization employed in this work ensures that the results obtained can be considered almost unaffected by the grid size.

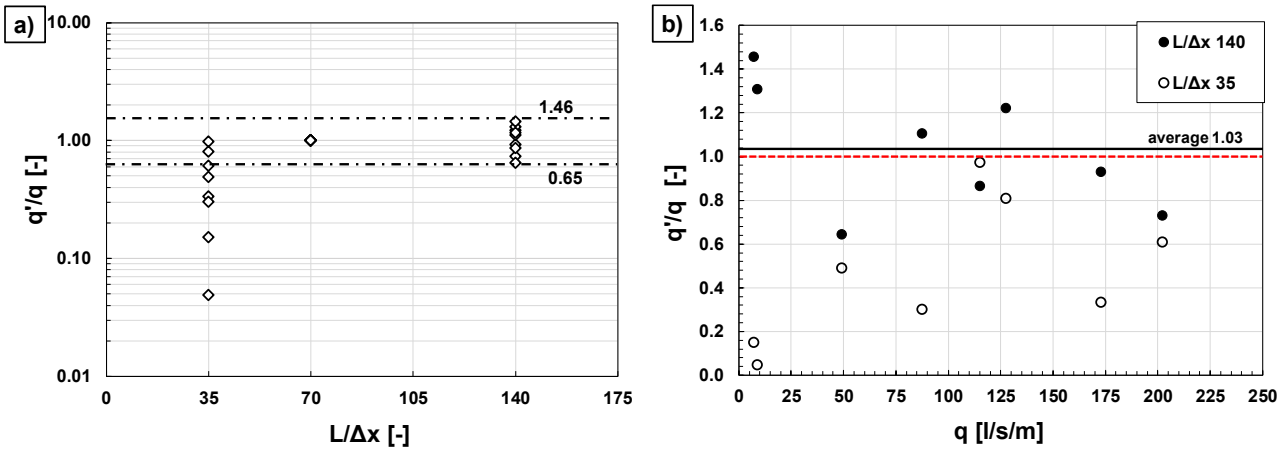

Figure 8.2 *– Variation in mean overtopping discharge due to the numerical discretization. Panel a): variation vs grid point per wave length; panel b): variation as a function of the flow rate.*

It is worth noting that the grid sensitivity analysis only concerns the mean overtopping discharge; based on the results obtained in Section 6.1.4.2. (see Figure 6.6) and on previous works' findings (Suzuki et al., 2011; 2014), it can be assumed that the grid size has no much influence on wave evolution.

The HFA approach has been used (Smit et al., 2013); the breaking parameters are set to the default values (i.e. $\alpha = 0.6$, $\beta = 0.3$). A zero value of the Manning coefficient has been adopted since greater values can reduce the mean overtopping discharge and affect the wave transformation process (Figure 6.7). The maximum Courant number assigned was 0.5.

8.3. A new formula for very and extremely shallow waters

The purpose of this section is to setup a relationship that predicts the mean overtopping rate at a vertical seawall in a surf zone, based on phase-averaged quantities only; these include the wave setup, $\bar{\zeta}$, and the wave variance, $m_{0,TOE}$. Thus, a predictive formula that adopts the new hydraulic variable, $\zeta_{1/4}$.

This section only considers seawalls with very and extremely shallow foreshores, i.e. $h_{TOE}/H_{m0,N}<1$ (according to the classification of Hofland et al., 2017 reported in Chapter 4); thus, the analysis refers to 53 out of 74 data.

As usual, the formula will be relating a dimensionless flow rate q^* and a relative crest freeboard R_C^*:

$$q^* = F(R_C^*) \tag{8.1}$$

where the function F can be of either exponential or power type.

The dimensionless crest freeboard is:

$$R_C^* = \frac{R_C}{\zeta_{1/4}} \tag{8.2}$$

where for simplicity $\zeta_{1/4}$ is calculated according to the Eq. (6.10), i.e. neglecting the skewness of wave displacements.

As for q^*, it is convenient to refer to the EurOtop formula, which under very shallow waters conditions reads:

$$q^* = \frac{q}{\sqrt{g \cdot H_{m0,TOE}^3} \cdot \sqrt{\frac{L_{m-10,TOE}}{h_{TOE}}}} = \frac{q}{\left(g \cdot H_{m0,TOE} \cdot T_{m-10,TOE}\right)\sqrt{\frac{H_{m0,TOE}}{h_{TOE}}}} \tag{8.3}$$

It is worth noticing that the term in the round parentheses at the right hand side of Eq. (8.3) is in effect the reference flow rate used in the pioneering work of Owen (1980).

However, the harmonic spectral period in Eq. (8.3) can be certainly substituted by the offshore (nearshore) peak period, $T_{p,N}$. This for twofold reasons: according to the findings obtained in the previous Chapter, the spectral shape does not affect the overtopping process; moreover, the state-of-the-art analysis reveals that the EurOtop reliable data for vertical seawalls all have $T_{m-10,TOE}/T_{p,DEEP}$ included between 0.8 and 1.1 (see Figure 4.6). Hence, the role of surf beats have not been assessed, and the variable $T_{m-10,TOE}$ is practically nothing else than the offshore peak period.

Furthermore, in a surf-zone the wave height to water depth ratio can be set as:

$$\frac{H_{m0,TOE}}{h_{TOE}} = \gamma(m) \tag{8.4}$$

where the breaking index depends on the slope of the foreshore, m. Therefore, Eqs. (8.2) and (8.3) lead finally to:

$$q^* = \frac{q}{g \cdot h_{TOE} \cdot T_{p,N}\gamma(\mathrm{m})^{\frac{3}{2}}} = F\left(\frac{R_C}{\zeta_{1/4}}\right) \tag{8.6}$$

8.3.1. Dimensionless flow rate: new parametrization

This Chapter will discuss two hypotheses of parametrizations regarding the dimensionless overtopping discharge. The first is more theoretically consistent, whereas the second one leans on empirical observations. However, both derive from Eq. (8.6).

The performances of the proposed empirical models will be assessed via their correlation coefficients and the residuals behaviors; moreover, two additional statistics indexes will be evaluated, namely the geometric mean (Eq. (8.7)) and the geometric standard deviation (Eq. (8.8)):

$$Geo = exp\left[\frac{1}{N}\sum_{N} ln\left(\frac{x_{est,i}}{x_{meas,i}}\right)\right] \tag{8.7}$$

$$GSD = exp\left\{\left[\frac{1}{N}\sum_{N}\left(ln\left(\frac{x_{est,i}}{x_{meas,i}}\right)^2 - \ln(Geo)^2\right)\right]^{0.5}\right\} \tag{8.8}$$

The geometric mean verifies the empirical model's accuracy (i.e., the presence of any bias), while the geometric standard deviation inspects the data scatter (see Goda, 2009). Assuming a normal distribution of the data, 90% of them will fall within the confidence interval [Geo·GSD$^{-1.65}$; Geo·GSD$^{+1.65}$].

- **Hypothesis 1:**

The first parametrization proposal adopts the breaking index formulation of Kamphuis (1991); the product of water depth and breaking index represents the breaking wave height. Thus, Eq. (8.6) becomes:

$$\frac{q}{g \cdot T_{p,N} \cdot h_{TOE} \cdot (\gamma_0 \cdot exp[p \cdot \tan(m)])} = \frac{q}{g \cdot T_{p,N} \cdot H_{br}} = F\left(\frac{R_C}{\zeta_{1/4}}\right) \tag{8.9}$$

where γ_0 and p are equal to 0.56 and 8, respectively. Compared to the original Kamphuis's formula, the coefficient p has been modified in order to obtain the best fit with numerical data.

The 53 data can be fitted with an exponential function (Eq. (8.10)) or, alternatively, with a double power function (Eq. (8.11)), as shown in Figure 8.3.
The exponential law reads:

$$\frac{q}{g \cdot T_{p,N} \cdot h_{TOE} \cdot (\gamma_0 \cdot exp[p \cdot \tan(m)])} = 0.007 \cdot \exp\left(-1.013 \cdot \frac{R_C}{\zeta_{1/4}}\right) \tag{8.10}$$

while the double power function is:

$$\frac{q}{g \cdot T_{p,N} \cdot h_{TOE} \cdot (\gamma_0 \cdot exp[p \cdot \tan(m)])} = min\left[0.003 \cdot \frac{R_C}{\zeta_{1/4}}^{-1.81}; 0.016 \cdot \frac{R_C}{\zeta_{1/4}}^{-3.6}\right] \tag{8.11}$$

Both the empirical formulae have high R^2 statistics, equal to 0.96 for Eq. (8.10) and 0.97 for Eq. (8.11). Moreover, the log residuals are approximately Gaussian, showing a quite homoscedastic behavior (Figure 8.3c refers to Eq. (8.10), while Figure 8.3d plots the log residuals of the double power function).

Both the empirical models are unbiased (Geo = 0.98 and 0.967 for Eq. (8.10) and Eq. (8.11), respectively) and have a low level of scattering. In particular, the exponential function has a GSD equal to 1.307, which means that if the overtopping data follow a normal distribution, 90% of the flow rates would located within a range of values between 0.63 and 1.52 times the measured overtopping discharge; similarly, the double power formula has a GSD = 1.269.

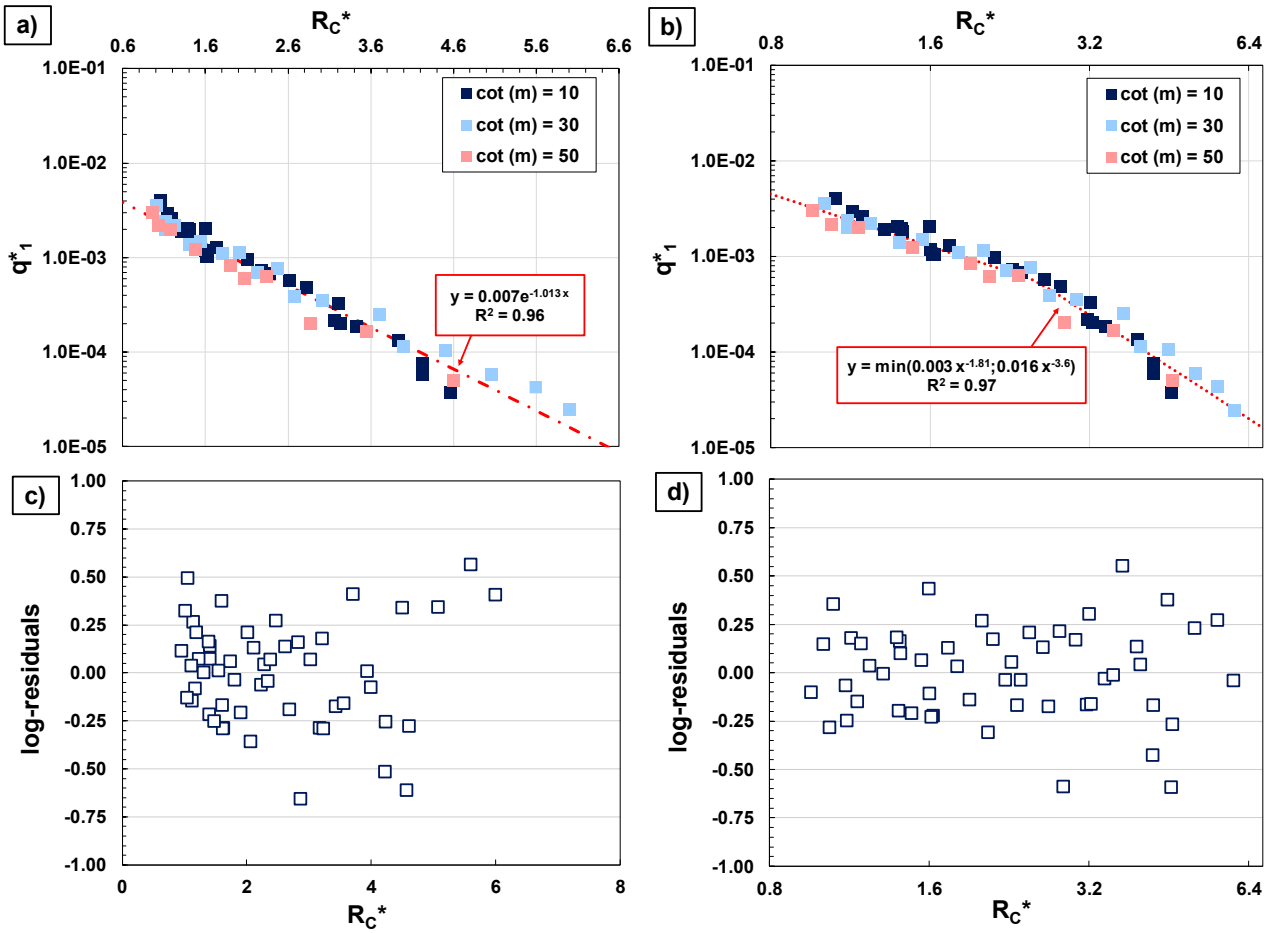

Figure 8.3– *Panel a): planar beach data fitted by an exponential function (Eq. (8.10)); panel b): planar beach data fitted by a double power function (Eq. (8.11)); panels c) and d) plot the log residuals of the Eq. (8.10) and Eq. (8.11), respectively.*

❖ **Hypothesis 2:**

The second parametrization proposal for the dimensionless flow rate is:

$$q^* = \frac{q}{g \cdot h_{TOE} \cdot T_{p,N} \cdot \tan(m)^{0.5}} \tag{8.12}$$

It is worth noting that a clear influence of the foreshore slope has been empirically observed; indeed, the presence of *tan(m)* in the dimensionless flow rate avoids stratification of the data according to their own slope.

Analogously, an exponential or a double power function can be used to fit the 53 data, as shown in Figure 8.4a and 8.4b, respectively.

The exponential formula reads:

$$\frac{q}{g \cdot h_{TOE} \cdot T_{p,N} \cdot \tan(m)^{0.5}} = 0.03 \cdot \exp\left(-1.03 \cdot \frac{R_C}{\zeta_{1/4}}\right) \tag{8.13}$$

to which corresponds an R^2 statistics of 0.97. Figure 8.4c plots the log-residuals, which are approximately Gaussian.

On the other hand, the double power function is:

$$\frac{q}{g \cdot h_{TOE} \cdot T_{p,N} \cdot \tan(m)^{0.5}} = min\left[0.013 \cdot \frac{R_C}{\zeta_{1/4}}^{-1.77} ; 0.07 \cdot \frac{R_C}{\zeta_{1/4}}^{-3.68}\right] \tag{8.14}$$

with an R^2 statistics of 0.98. Figure 8.6d shows no evident relationships between predictor and log-residuals.

Analogous to the performances of the predictive models derived in Hypothesis 1, Eq. (8.13) and Eq. (8.14) have no bias (Geo = 0.985 and 0.996, respectively) and are characterized by low values of GDS (1.289 and 1.247, respectively).

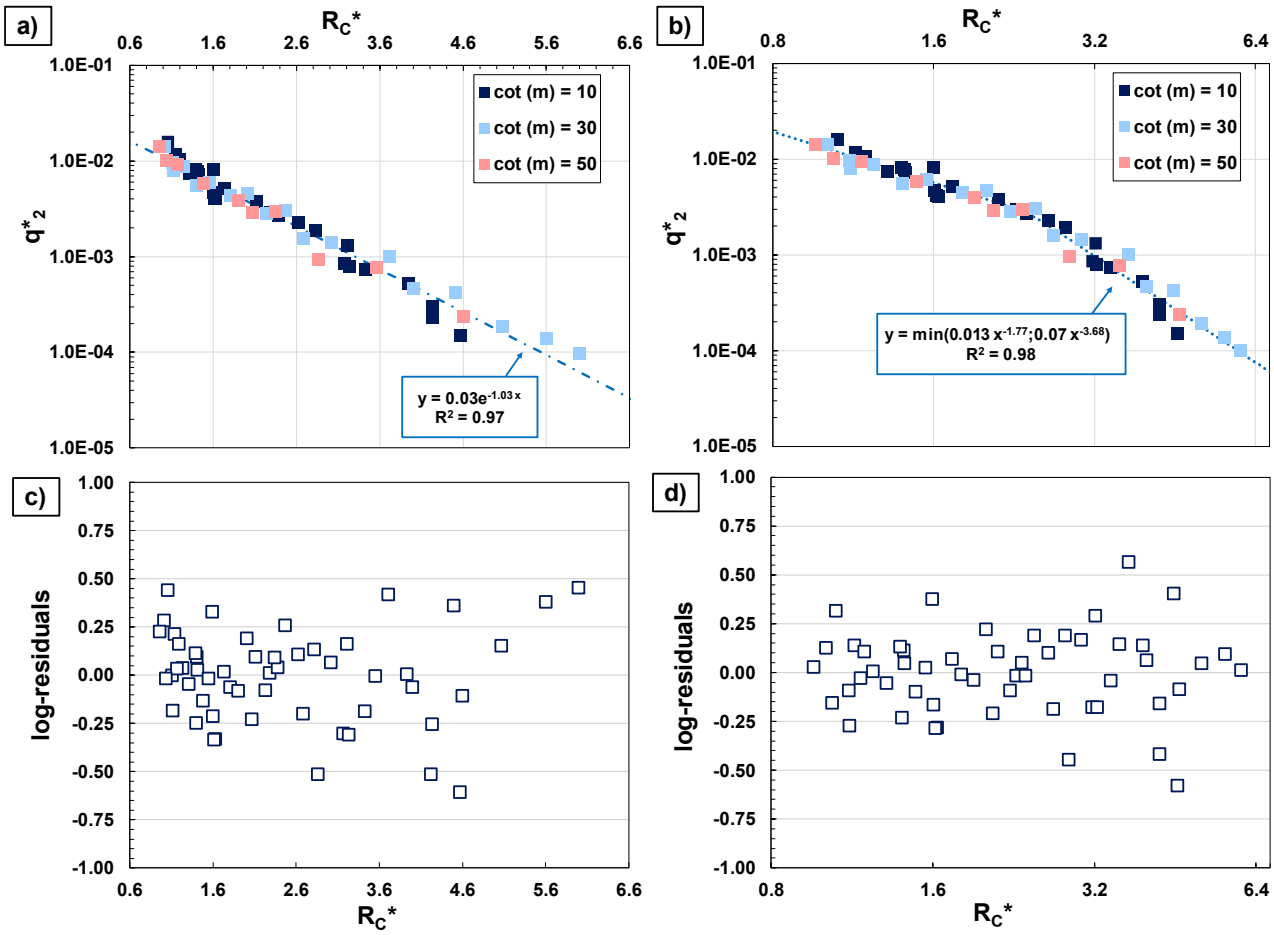

Figure 8.4 *– Panel a): planar beach data fitted by an exponential function (Eq. (8.13)); panel b): planar beach data fitted by a double power function (Eq. (8.14)); panels c) and d) plot the log residuals of the Eq. (8.13) and Eq. (8.14), respectively.*

Hence, beyond the fitting formula, both the hypotheses of parametrizations make data remarkably well gathered. Such a peculiarity will be confirmed in the next Section.

It is worth pointing out that the valid range for the empirical equations derived is $1 \leq R_C^* \leq 6$.

8.3.2. Uniform slope beaches: behavior of the new parametrization

The previous Section has demonstrated that the new parametrization makes the data very little scattered (beyond the dimensionless flow rate adopted among the two proposals). This has been confirmed by the high correlation coefficients related to the inferred empirical overtopping models and the low values of the geometric standard deviation.

However, a comparative analysis with the existing tools helps to understand the effective improvement. To this end, the behavior of the new parametrization has been evaluated compared to that of the EurOtop formula (Eq. (4.3)).

For the sake of brevity, the second hypothesis of parametrization will be shown; analogous results have been obtained with the other proposal. The data relative to the steeper beach (*tan(m) = 1/10*) are used to perform this comparison.

As can be appreciated in Figure 8.5, where the data are plotted on standardized graphs (by subtracting the mean from the variables and dividing by the standard deviation), the parametrization used herein led to grouping the data far more efficiently than with the EurOtop formula. This becomes even clearer by comparing this new formulation with the envelope (red dash-dotted lines) derived from data in Figure 8.5b. Such a reduction in data scattering indicates the better capabilities of the new parametrization in describing the overtopping in shallow water; Figure 8.5a seems to confirm that the parameters involved are crucial to estimating the mean overtopping discharge.

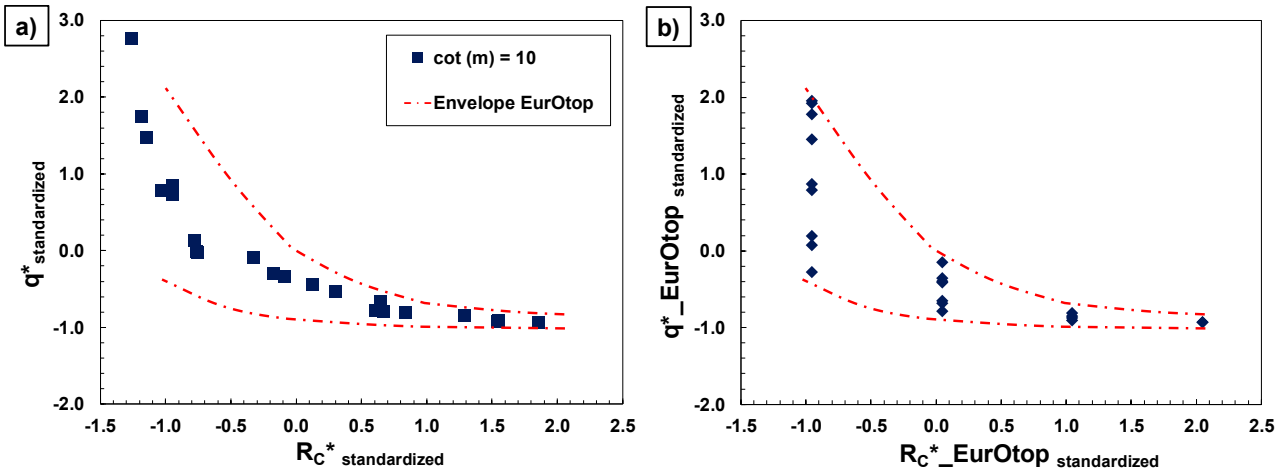

Figure 8.5 – *Numerical data characterized by cot(m) = 10 are plotted on standardized variables. Panel a): parametrization suggested in this work, Eqs. (8.2, 8.12). Data are compared to the envelope obtained using the EurOtop formulation shown in panel b) as well.*

A similar result has been obtained in Section 6.5., where the new relative crest freeboard, $R_C/\zeta_{1/4}$, has significantly reduced the MT overtopping discharge scattering compared to the R_C* used in the EurOtop formulation.

8.3.3. A comparison with Lashley et al. (2021) formula

This Section compares the performances of the predictive formulae previously derived and the overtopping model recently proposed by Lashley et al. (2021). As described in Section 4.1, the latter is valid for vertical seawalls with very and extremely shallow foreshores.

A qualitative comparison can be appreciated in Figure 8.6, which depicts the measured flow rates against that estimated with the double power formula, Eq. (8.14), and the Lashley et al.' model (Eq. (4.9). Although this comparison only includes Eq. (8.14) for the sake of clarity, analogous results concern the other predictive models inferred in the previous Section.

Figure 8.6 points out that, unlike the performance of the double power model, which guarantees that the 53 data of *D_U* are quite close to the perfect agreement line, the Lashley et al. formula provides contradictory results. Specifically, the analysis reveals a different behavior depending on the beach slope; indeed, measured and estimated flow rates agree fairly well for *cot(m)* = 10, whereas significant underestimations occur as the beach becomes milder. In particular, a drop in linearity and correlation is observed. Nonetheless, given the characteristics of the database used to calibrate their formula, this result is not really surprising. In fact, as shown in Figure 9 of Lashley et al. (2021), a large part of the data includes steeper beaches, while little information is available for gentle beaches (especially for foreshores milder than 1/30).

However, it is worth specifying that higher underpredictions have been observed in the so-called "transition region" ($h_{TOE}/ H_{m0,DEEP}$ included between 0.1 and 0.5), where the authors suggest an interpolation to estimate the mean overtopping discharge (Figure 8.7).

The performance of the existing model has been quantitatively evaluated using the two statistic indexes of Eqs. (8.7, 8.8) reported in Table 8.2. These confirm that the performance Lashley et al.' model worsens as the beach becomes gentler.

Overall, the model shows a significant bias and a high level of data scatter compared to Eq. (8.14). The better performance of the proposed predictive model can be further appreciated in Figure 8.8, which plots the measured to estimated flow rate ratio as a function of q. Results show that the Lashley et al. model can underestimate the flow rate of an order of magnitude.

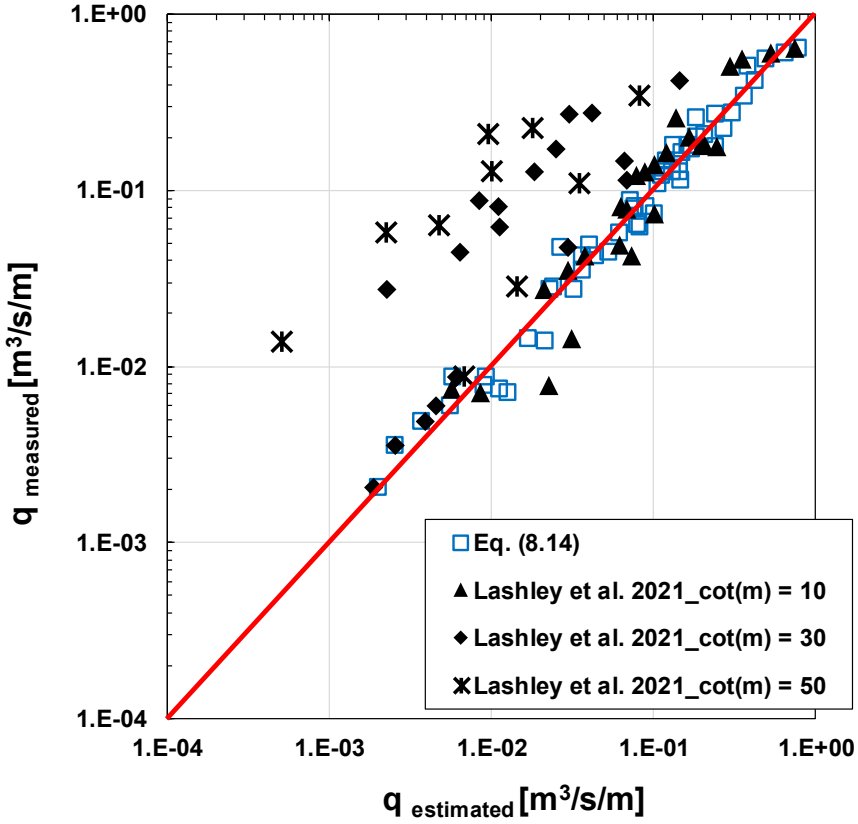

Figure 8.6 - *Comparison between performances of Eq. (8.14) (square blue points) and Lashley et al. (2021) formula (black symbols). The red line represents the perfect agreement between measured and estimated flow rates.*

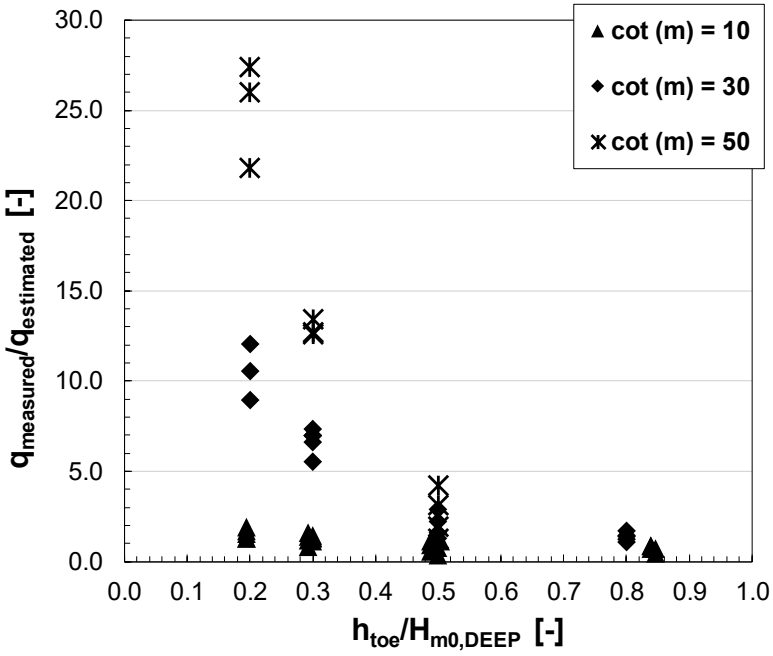

Figure 8.7. *– Ratio between the mean overtopping discharge measured and that estimated via the Lashley et al.' model vs the relative water depth.*

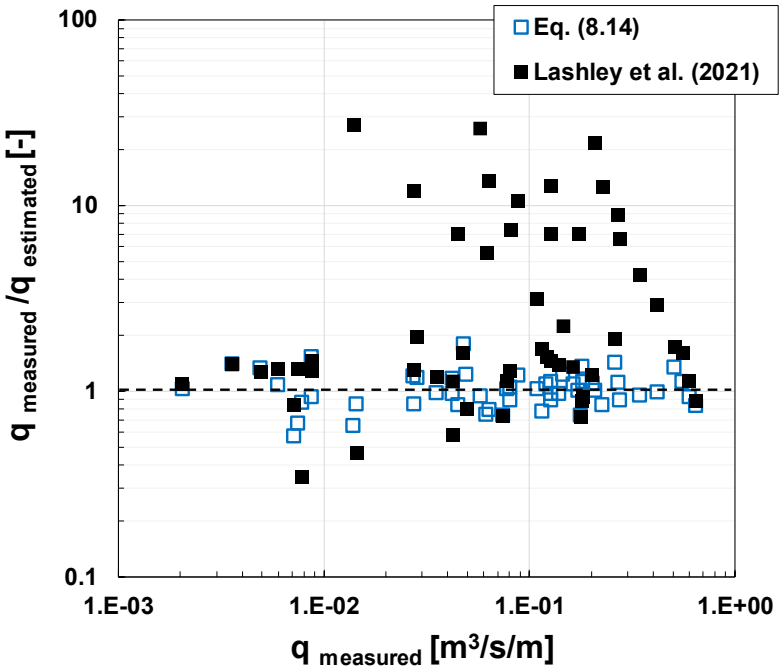

Figure 8.8. *– Ratio between the mean overtopping discharge measured and estimated as a function of q.*

Table 8.2 *– Statistic indexes of the Lashley et al.' overtopping model in evaluating the flow rate of D_U in very and extremely shallow waters.*

		# data	*Geo*	*GSD*
Lashley et al., 2021	*cot(m) = 10*	25	0.963	1.498
	cot(m) = 30	18	0.284	2.304
	cot(m) = 50	10	0.124	2.879
	Total	53	0.432	2.934

8.4. Extension to waves in shallow waters

This Section aims to extend the previous analysis to the overtopping of seawalls with shallow foreshore ($0.2 \leq h_{TOE}/H_{mo,DEEP} < 4$).

In case of limited or very limited breaking, the condition of Eq. (8.4) is no longer valid. Thus, Eqs. (8.2) and (8.3) need to be re-manipulated:

$$q^* = \frac{q}{g \cdot h_{TOE} \cdot T_{p,N}} = \left(\frac{h_{TOE}}{H_{m0,TOE}}\right)^{-\frac{3}{2}} \cdot F\left(\frac{R_C}{\zeta_{1/4}}\right) \tag{8.15}$$

Hence, neglecting the effect of shoaling we may set the general relationship:

$$q^* = \frac{q}{g \cdot h_{TOE} \cdot T_{p,N}} \cong F'\left(\frac{R_C}{\zeta_{1/4}}; \frac{h_{TOE}}{H_{m0,DEEP}}\right) \tag{8.16}$$

The formulation in Eq. (8.16) depends only on the deep water climate, and should hold in general in the absence of breaking. Moreover, the beach slope angle does not appear among the variables.

❖ **Hypothesis 1:**

The Eq. (8.15), for cases of very limited breaking, is here re-written as:

$$q^* = \frac{q}{g \cdot H_{m0,DEEP} \cdot T_{p,N}} = \left(\frac{h_{TOE}}{H_{m0,TOE}}\right)^{-\frac{1}{2}} \cdot F\left(\frac{R_C}{\zeta_{1/4}}\right) \cong F'\left(\frac{R_C}{\zeta_{1/4}}; \frac{h_{TOE}}{H_{m0,DEEP}}\right) \tag{8.17}$$

However, as this work aims to derive a unique model valid for extremely to shallow water conditions, a more generalized formulation can be obtained:

$$\frac{q}{g \cdot {H_{m0}}^* \cdot T_{p,DEEP}} = F\left(\frac{R_C}{\zeta_{1/4}} \cdot \gamma_{br}\right) \tag{8.18}$$

in which the wave height at the left-hand side is:

$${H_{m0}}^* = min\{H_{m0,DEEP};\ h_{TOE} \cdot (\gamma_0 \cdot exp[p \cdot \tan(m)])\} \tag{8.19}$$

Using Eq. (8.19) results in a non-dimensional flow rate similar to that proposed by Owen (1980). On the other hand, the coefficient at the right-hand side of Eq. (8.18) is:

$$\gamma_{br} = max\left\{1; \frac{h_{TOE}}{H_{m0,DEEP}} \cdot tanh\left(8 \cdot \pi \cdot \frac{h_{TOE}}{L_{p,N}}\right)\right\}^{0.33} \tag{8.20}$$

that recalls the term used in the parameter map (Calabrese and Buccino, 2000; Calabrese and Vicinanza, 1999; Calabrese, 1997) to distinguish between impulsive and pulsating waves. The loading condition somehow affects the overtopping rate; impulsive waves hitting the wall produce a higher vertical jet, increasing the overtopping discharge. Therefore, the coefficient γ_{br} amplifies the relative crest freeboard for seawalls located towards deep water (waves tending to pulsating conditions) to compensate for the lower flow rate of the non-impulsive waves.

According to this first parametrization proposal, the whole dataset *D_U* (74 data) follows rather well a unique trend regardless of the shallowness condition (Figure 8.9a); numerical data can be fitted with a double power function:

$$\frac{q}{g \cdot {H_{m0}}^* \cdot T_{p,DEEP}} = min\left\{0.003 \cdot \left(\frac{R_C}{\zeta_{1/4}} \cdot \gamma_{br}\right)^{-1.89}; 0.014 \cdot \left(\frac{R_C}{\zeta_{1/4}} \cdot \gamma_{br}\right)^{-3.45}\right\} \tag{8.21}$$

which has an R^2 statistic equal to 0.96. The model is unbiased (Geo = 0.988) and has a low level of scattering (GSD = 1.274); moreover, the log-residuals of Eq. (8.21) show a homoscedastic behavior (Figure 8.9b).

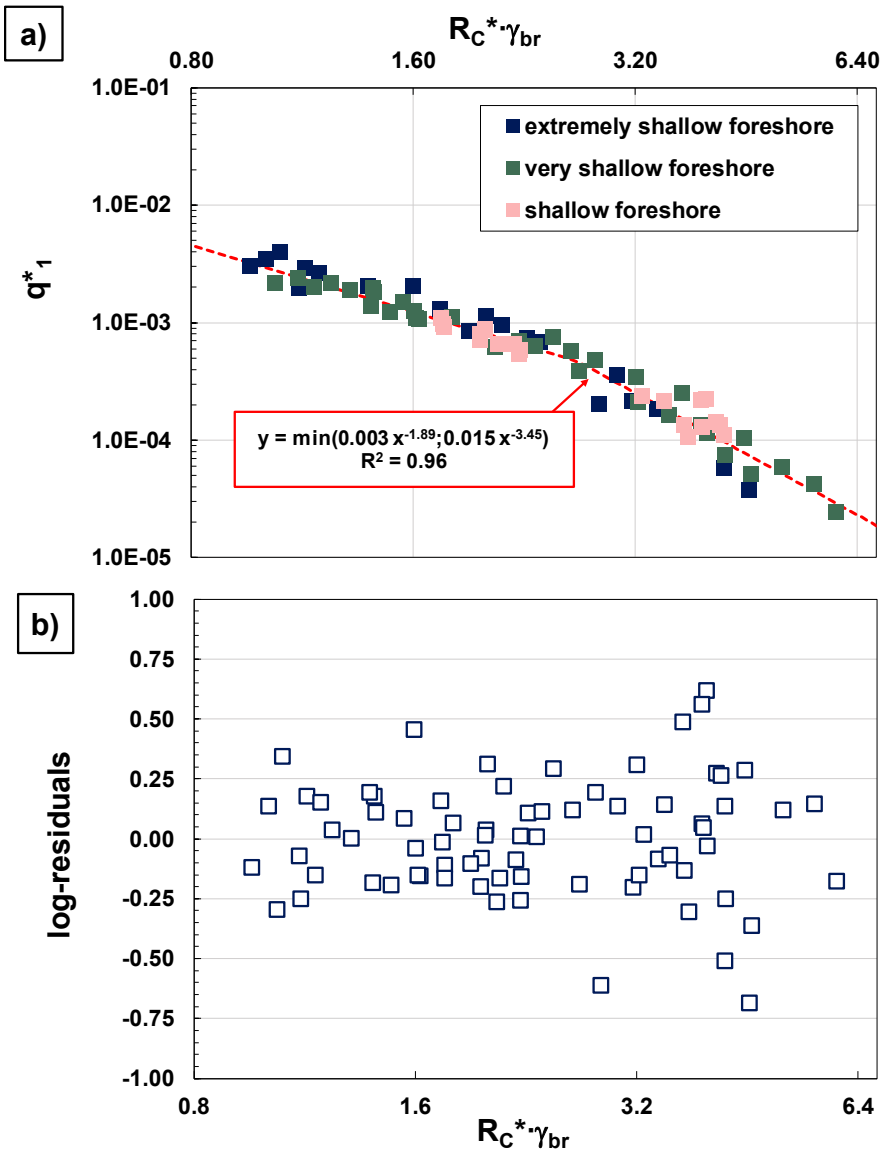

Figure 8.9 *– Panel a): D_U numerical data fitted by the double-power function (Eq. (8.21)); panel b) plots the log-residuals of the predictive model.*

❖ **Hypothesis 2:**

The second parametrization proposal takes into account the gradual shift between breaking and non-breaking waves (from Eq. (8.12) to Eq. (8.16)) by hypothesizing the following general formula:

$$q^* = \frac{q}{g \cdot h_{TOE} \cdot T_{p,N} \cdot \tan(m)^P} \cong F'\left(\frac{R_C}{\zeta_{1/4}} \cdot \gamma'_{br}\right) \tag{8.22}$$

in which the additional parameters γ'_{br} and P depend on the degree of stability of the waves. Specifically, when the wall is located in very or extremely shallow waters, γ'_{br} =1 and P = 0.5; vice versa, in deep waters, P tends

to 0 and $\gamma'_{br} = h_{TOE}/H_{m0,DEEP}$. The comparison with the whole dataset *D_U* led to the following transition equations:

$$\gamma'_{br} = \max\left\{1; \frac{h_{TOE}}{H_{m0,DEEP}} \cdot tanh\left(10 \cdot \pi \cdot \frac{h_{TOE}}{L_{p,N}}\right)\right\} \tag{8.23}$$

$$P = \frac{0.5}{\left[1 + 50 \cdot exp\left(-10 \cdot \frac{H_{m0,DEEP}}{h_{TOE}}\right)\right]} \tag{8.24}$$

Eq. (8.24) expresses the seaward diminishing influence of the foreshore slope on the overtopping process, while Eq. (8.23) amplifies the relative crest freeboard of walls with shallow foreshores, as explained above. However, it is worth pointing out this formulation differs from Eq. (8.20) because of the dimensionless flow rate proposed in the second hypothesis of parametrization; indeed, the coefficient γ'_{br} has the additional role of compensating empirically for the artificial reduction of q^* caused by the increase of h_{TOE} for deepwater structures.

Numerical data are plotted against the non-dimensional variables of Eq. (8.22) in Figure 8.10a. A double power function fits the data:

$$\frac{q}{g \cdot h_{TOE} \cdot T_{p,N} \cdot \tan(m)^P} = min\left\{0.013 \cdot \left(\frac{R_C}{\zeta_{1/4}} \cdot \gamma'_{br}\right)^{-1.91}; 0.031 \cdot \left(\frac{R_C}{\zeta_{1/4}} \cdot \gamma'_{br}\right)^{-2.96}\right\} \tag{8.25}$$

to which corresponds a R^2 value of 0.96. The log-residuals are quite randomly scattered, demonstrating the homoscedasticity of the model (Figure 8.10b). The geometrical mean and standard deviation are 0.997 and 1.321, respectively.

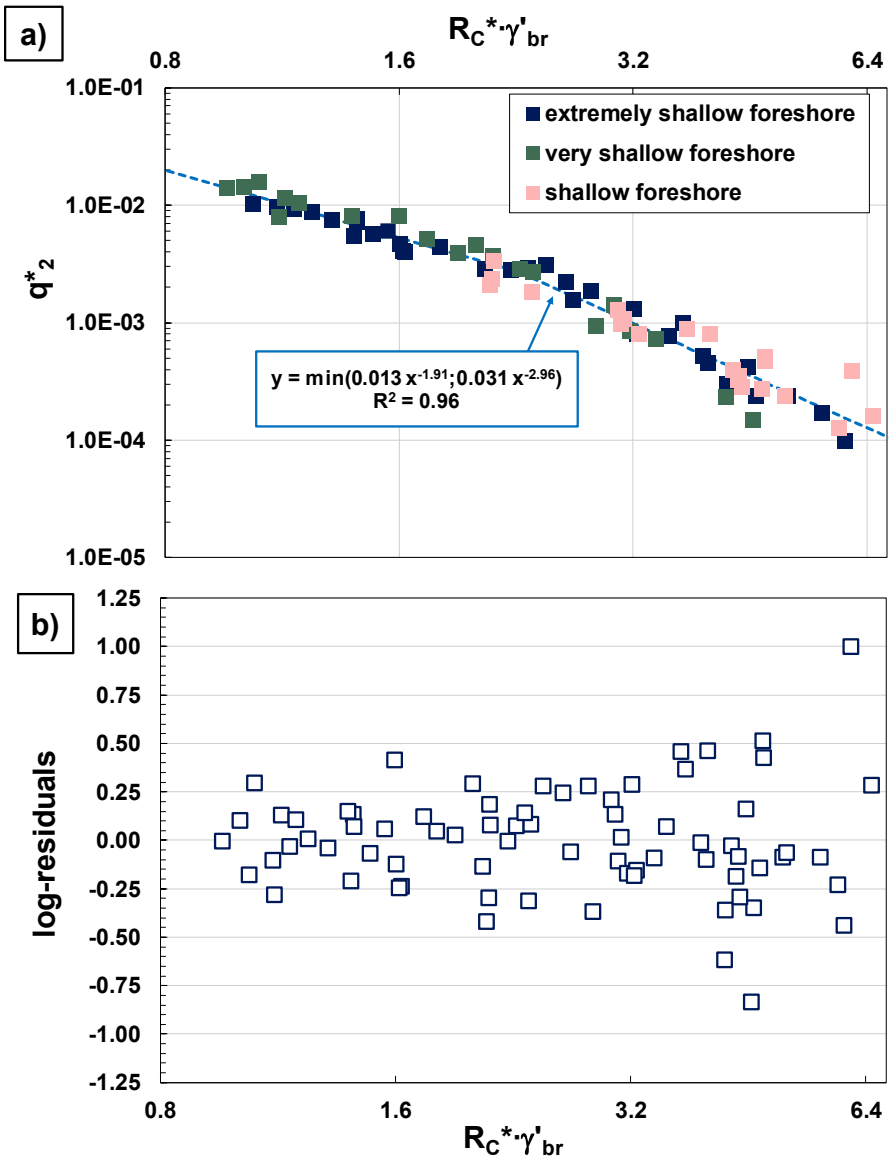

Figure 8.10 *– Panel a): D_U numerical data fitted by the double-power function (Eq. (8.25)); panel b) plots the log residuals of the predictive model.*

8.5. Discussion

The analysis performed in Chapter 6, along with previous studies in literature, has demonstrated the capability of SWASH to reproduce satisfactorily the physics of coastal processes. Therefore, the non-hydrostatic model has been employed as an explorative tool for a deeper comprehension of wave overtopping of seawalls in shallow water conditions.

In particular, the present Chapter aimed to derive a new predictive model based on the new hydraulic variable $\zeta_{1/4}$. Previous Chapters' results demonstrated that the flow rate depends on the upper tail of wave displacement distribution at the toe of the structure, which can be expressed by the highest one-fourth of $\zeta(t)$. This concept is physically consistent with the empirical models that relate the overtopping to a run-up level (Etemad-Shahidi

et al., 2022; Yuhi et al., 2021; Hedge and Reis, 1998). Nonetheless, $\zeta_{1/4}$ is determined without the presence of the structure and can be easily estimated via Eq. (6.10) (see Chapter 6).

The numerical analysis ensured the gathering of a wide and varied dataset (i.e. 74 data), which encompasses three different planar beaches ($tan(m)$ = 0.02 ÷ 0.1), a relative crest freeboard R_C* that varies between 1.0 and 6.0 (different order of magnitude of the flow rate), and many water depths at the toe of the wall ($0.2 \leq h_{TOE}/H_{m0,DEEP} \leq 2.7$). Indeed, using a numerical model allows the geometrical and hydraulic features to vary smoothly, overcoming the limitations of a physical experimental campaign.

For the predictive model, two hypotheses of new parametrization have been introduced; although conceptually similar, the first hypothesis is more theoretically consistent, while the second one leans on empirical observations. However, the new parametrization includes the main variables involved in wave overtopping. Specifically, $\zeta_{1/4}$ has been used to obtain the relative crest freeboard, while the dimensionless flow rate recalls that of Owen (1980), except for the foreshore slope. Hence, the parametrization includes the influence of the peak period, $T_{p,N}$; indeed, consistent with the literature (Lashley et al., 2021; Owen, 1980; Goda et al., 1975), a larger wave period produces a greater discharge. Furthermore, the role of foreshore slope for wave overtopping in very shallow water has been pointed out. As previously stated by Altomare et al. (2016) in their extensive analysis regarding the overtopping of sloping dikes with very shallow foreshores, the seabed slope seems to be a crucial variable that affects the wave overtopping in shallow water conditions, while its influence becomes weaker as deeper the waters. However, except for the Goda's model (2009), the predictive formulae for vertical seawalls do not consider the seabed slope's influence so far. EurOtop formulae neglect this variable (see Eq. (4.3)), while the deepwater-based-model of Lashley et al. (2021) takes it into account primarily as the foreshore slope, along with h_{TOE}, would merely express the foreshore effect on the wave evolution process.

Overall, the new parametrization accounts for the main features concerning the physics of the process (Eqs. (8.18, 8.22)); furthermore, it significantly reduces the scattering typically observed in the overtopping empirical models (Figure 8.5).

Finally, a unique generalized formula has been derived (see either Eq. (8.21) or Eq. (8.25)) that ensures estimating the mean overtopping discharge of walls with different foreshore conditions, i.e. from shallow to extremely shallow waters.
It is worth noting that among the two model derived, Eq. (8.25) requires more empirical coefficients compared to Eq. (8.21) because of the empirical approach adopted.

9. UNEVEN BEACH PROFILES: THE EQUIVALENT SLOPE

The numerical investigation performed in the previous Chapter has pointed out the crucial role of the seabed slope in estimating the flow rate of breaking waves.

The overtopping predictive model has been derived from planar beach data. However, real foreshores are rarely so regular and exhibit a variable inclination instead. Hence, an equivalent slope is necessary for applying the equations previously derived to natural beaches, avoiding any uncertainties related to the foreshore slope parameter.

To this end, a further numerical experimental campaign has been performed. As previously pointed out, SWASH is able to capture the physics of coastal phenomena (despite some biases) with low computational costs compared to more sophisticated phase-resolving models (e.g. CFD-RANS). Furthermore, a numerical investigation ensures a straightforward examination of different conditions compared to physical model campaigns.
In particular, the numerical experiments discussed in this Chapter concern two uneven foreshores: a convex-type profile and a multi-slope beach.

The analysis will evaluate four different approaches to define the equivalent slope for beaches characterized by irregular bathymetries.

9.1. Numerical investigation

Numerical tests have been carried out on different beach profiles so that two subsets can be distinguished: *S_EP* refers to tests with convex beaches, and *S_MT* that includes the numerical experiments performed on the Malecòn multi-slope foreshore (already discussed in Section 6.1.4.2).

9.1.1. *S_EP*. Equilibrium profile experiments

The subset *S_EP* includes four different convex profiles, which are described by the well-known power function of Bruun (1954) and Dean (1977):

$$h = A \cdot x^{\frac{2}{3}} \tag{9.1}$$

where h is the water depth and x is the horizontal distance from the shoreline. The peculiarity of such a profile lies in the variation of the local slope along the beach, which becomes steeper and steeper shoreward. Furthermore, these takes the sediment size into account through the scale parameter A (Moore, 1982); the coarser the sediment the greater A, that means a steeper beach. Hence, the use of different types of sediments allows to consider both mild and steep profiles.

Specifically, four different sediment sizes (d_{50} equals to 0.5, 1.8, 5, and 30mm) have been investigated, related to sand and gravel beaches. The convex profile follows the Brunn-Dean equation up to the local slope relative

to a water depth of 0.4m; then, it reaches a berm crest of 2m above the MWL with a uniform slope. The offshore water depth of 20.5m guarantees a wave generation in intermediate waters (Figure 9.1). The local slope range is 1/12 ÷ 1/85 and 1/7 ÷ 1/46 for the fine and coarse sand, respectively, while $cot(m)_i = 4 \div 28$ and 2 ÷ 15 for the two types of pebble beaches.

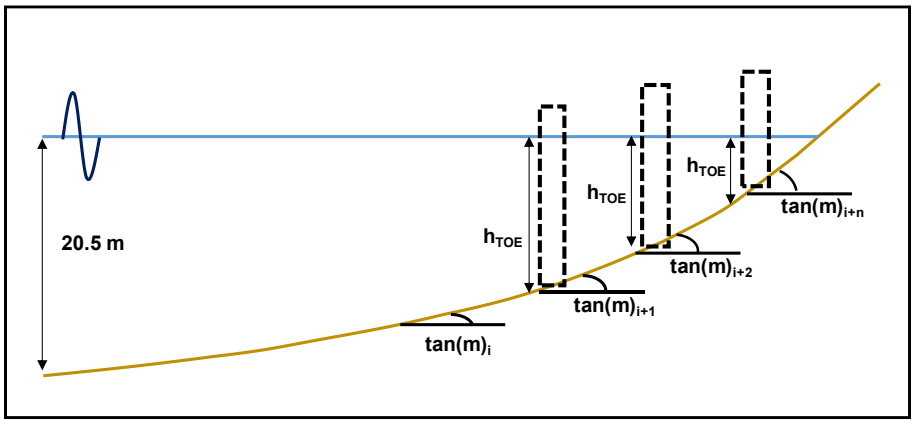

Figure 9.1 *– Schematization of the investigated layout in S_EP.*

Similar to the procedure exploited with the *D_U* data, the seawall's location and the height have been varied to analyze both different shallowness conditions and relative crest freeboards (Figure 9.1). In particular, wave overtopping has been investigated in shallow, very shallow and extremely shallow foreshore conditions ($h_{TOE}/H_{m0,DEEP} = 0.2 \div 2.7$) for 45 experiments. Two mean JONSWAP spectra characterized by $H_{m0,DEEP} = 2.4$ and 5.3m and $T_p = 7$ and 10s have been used (s_{0p} is about 0.03). The crest freeboard to incident wave height ratios varies between 0.5 and 1.5 ($R_C = 0.7 \div 5.6$ m). These main characteristics are summarized in Table 9.1.

In addition to the wave overtopping experiments, which have been run for 500 waves according to Romano et al. (2015), wave propagation tests have been carried out without the structure in the channel to derive the wave characteristics at the toe of the walls.

Table 9.1 - *Main features of the S_EP wave overtopping tests.*

subset-ID	# tests	$H_{m0,N}$ [m]	$T_{p,N}$ [s]	$h_{TOE}/ H_{m0,N}$	$R_C/ H_{m0,TOE}$
S_EP	45	2.4, 5.3	7, 10	0.2 ÷ 2.7	0.5 ÷ 1.5

For the numerical setup, refer to Section 8.2.2.

9.1.2. *S_MT*. The Malecon Tradicional experiments

Laboratory experiments carried out at the University of Naples "Federico II" in a 2D framework (Còrdova Lopez et al., 2015; 2016) have been numerically replicated at prototype scale using SWASH (see Section 6.1.4.1).

Eleven irregular waves have been tested on the Havana foreshore (Figure 9.2); 8 out of 11 correspond with the laboratory wave conditions discussed in Chapter 6. The additional tests were performed to extend the analysis to different wave periods (5.5s, 7s and 14s). The related significant wave heights ensure a deepwater wave

steepness about 0.035; a JONSWAP generation has been used. Three different crest freeboards have been examined, namely 2.23m (original height of the Malecon), 2.73m and 3.23m above the MWL.

The main characteristics of *S_MT* are listed in Table 9.2.

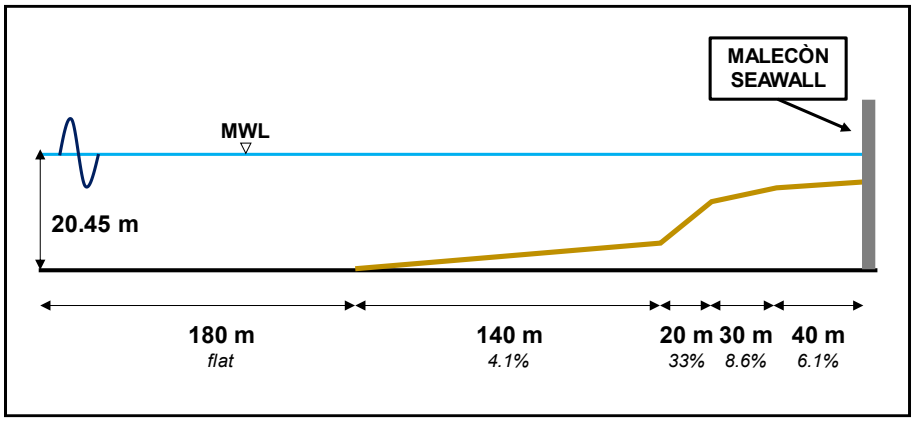

Figure 9.2 *– Multi-slope foreshore of S_MT experiments.*

Table 9.2 - *Main features of the S_MT wave overtopping tests.*

subset-ID	# tests	$H_{m0,N}$ [m]	$T_{p,N}$ [s]	$h_{TOE}/ H_{m0,N}$	$R_C/ H_{m0,TOE}$
S_MT	30	1.7 ÷ 6.5	5.5 ÷ 14	0.5 ÷ 2	0.52 ÷ 1.64

9.2.The equivalent slope

As mentioned above, this work examines four different equivalent slopes.

A common assumption is an averaged slope over a certain length (e.g. EurOtop, 2018). Hence, it can be supposed that the equivalent slope is averaged over some kind of distance $\mathcal{L}$ equals to either twice the local wavelength, $2L_p$, or one deepwater wavelength, $L_{p,DEEP}$. In both cases, the wavelength is calculated considering the offshore peak period.

According to the Bruun-Dean profile (Eq. 9.1), these two definitions of averaged slope for a given position x of the wall read:

$$\overline{\tan(m)} = \frac{1}{\mathcal{L}}[y(x+\mathcal{L}) - y(x)] = \frac{A}{\mathcal{L}}\left[(x+\mathcal{L})^{\frac{2}{3}} - (x)^{\frac{2}{3}}\right] \tag{9.2}$$

The third hypothesis considers the local foreshore slope at the toe of the wall. Thus, for a multi-slope beach, such as the MT profile (Figure 9.2), the local slope at the toe of the structure can be easily determined. On the other hand, for the convex profiles, it can be defined as:

$$\tan(m)_i = \frac{2}{3}\sqrt{\frac{A^3}{h}} \tag{9.3}$$

Finally, the hypothetical foreshore slope, m_i, recently proposed by Lashley et al. (2023) has been examined; it is a constant slope extending from a depth equal to $H_{m0,DEEP}$ to the toe of the structure (not applicable for seawalls located in shallow waters, $h_{TOE} / H_{m0,DEEP} \geq 1$). Unlike other equivalent slope definitions provided by the literature, m_i can be easily assessed since it does require neither iterative procedures nor the previous estimation of hydraulic parameters, such as $R_{2\%}$ (see Altomare et al., 2016; Mase et al., 2013).

Figure 9.3 shows a sketch of the four different equivalent slope's hypotheses investigated in this Chapter.

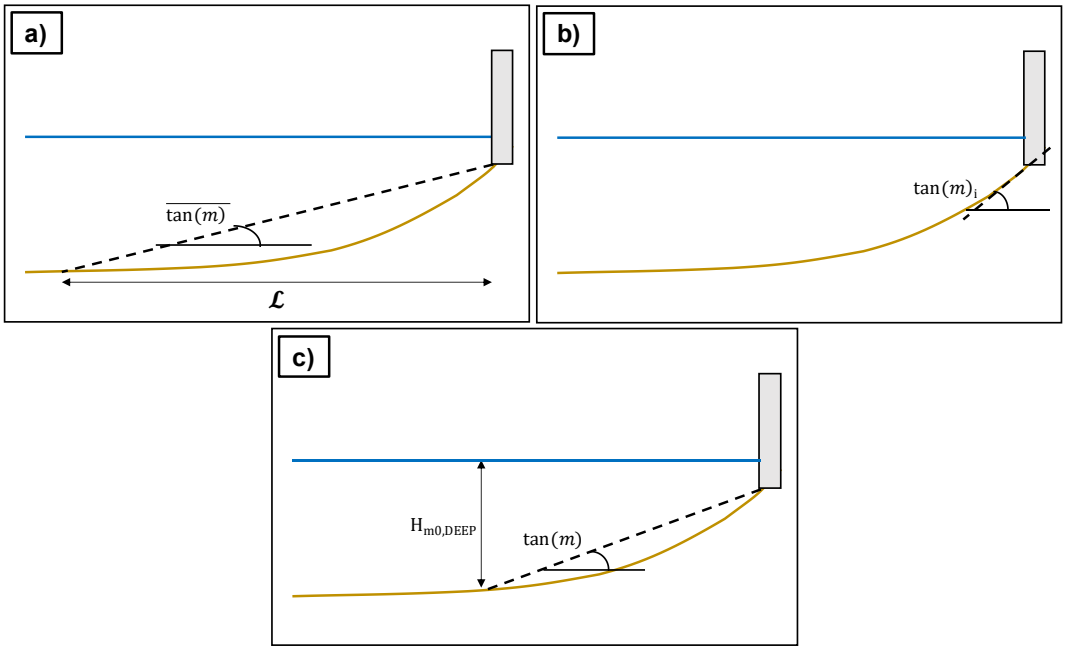

Figure 9.3 *– Sketch of the four equivalent slopes investigated. Panel a) refer to the slope averaged over some kind of distance $\mathcal{L}$ (whether twice the local wave length or $L_{p,DEEP}$); panel b) refer to the local slope, while panel c) depicts the equivalent slope proposed by Lashley et al. (2023).*

9.3. Results

This paragraph compares the performances of the four equivalent slope definitions to establish the most suitable one for describing irregular foreshores.

Figures 9.4 – 9.7 plot the dimensionless flow rates obtained by varying the equivalent slope; panels a) and b) refer to the first and second parametrization hypothesis, respectively. The envelope of *D_U* (planar beach data) is depicted as well.

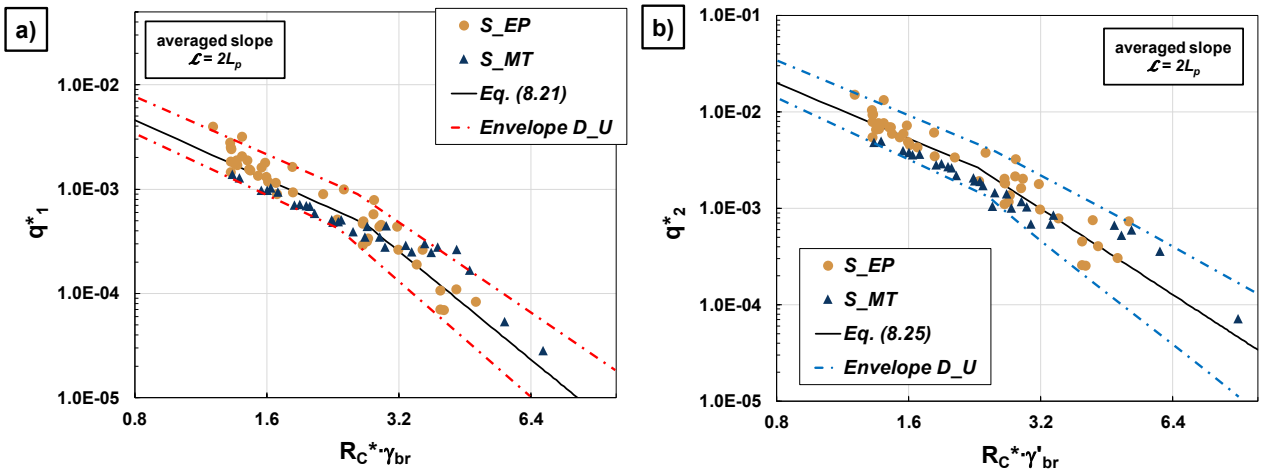

Figure 9.4 *– Comparison of numerical data of subsets S_EP and S_MT (obtained using the equivalent slope averaged on twice the local wavelength) with the overtopping formula (black solid line) and the envelope of planar beach data, D_U (dash-dotted lines). Panel a) refers to the first hypothesis of parametrization, while panel b) refers to the second one.*

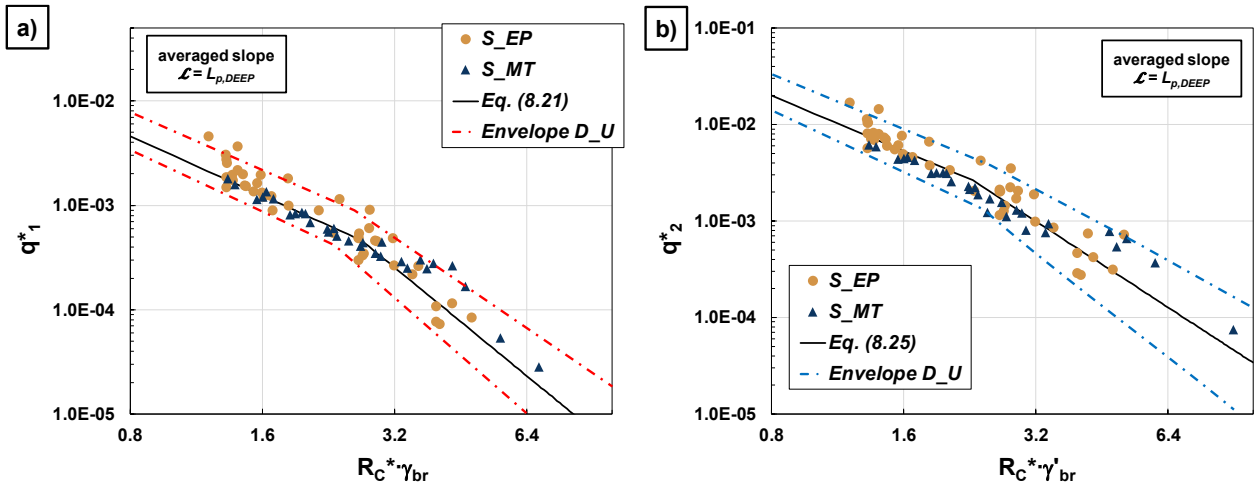

Figure 9.5 *– Comparison of numerical data of subsets S_EP and S_MT (obtained using the equivalent slope averaged on the deepwater wavelength) with the overtopping formula (black solid line) and the envelope of planar beach data, D_U (dash-dotted lines). Panel a) refers to the first hypothesis of parametrization, while panel b) refers to the second one.*

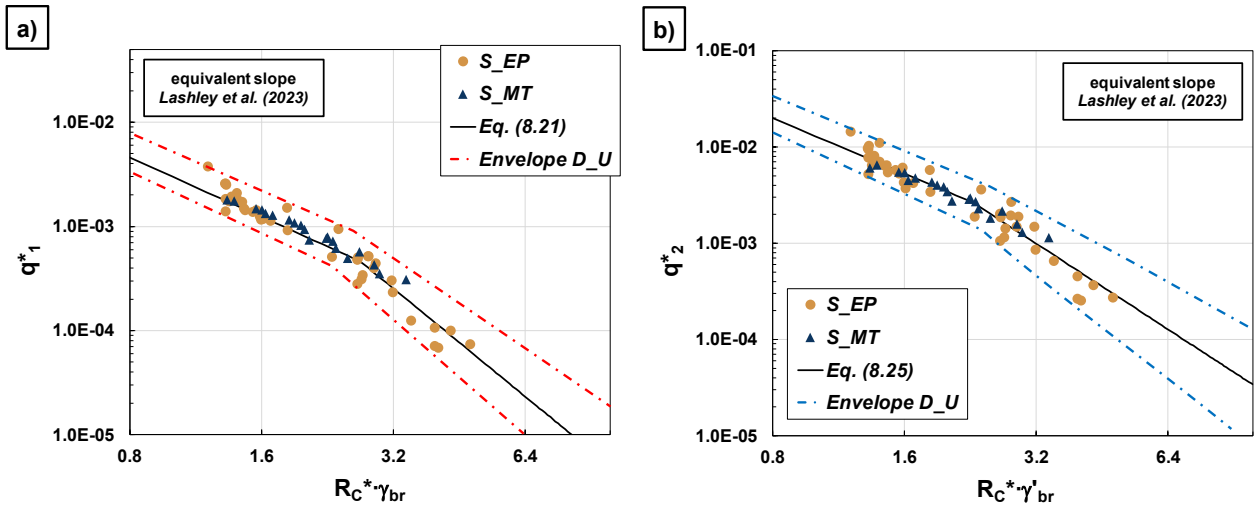

Figure 9.6 *– Comparison of numerical data of subsets S_EP and S_MT (obtained using the equivalent slope proposed by Lashley et al., 2023) with the overtopping formula (black solid line) and the envelope of planar beach data, D_U (dash-dotted lines). Panel a) refers to the first hypothesis of parametrization, while panel b) refers to the second one.*

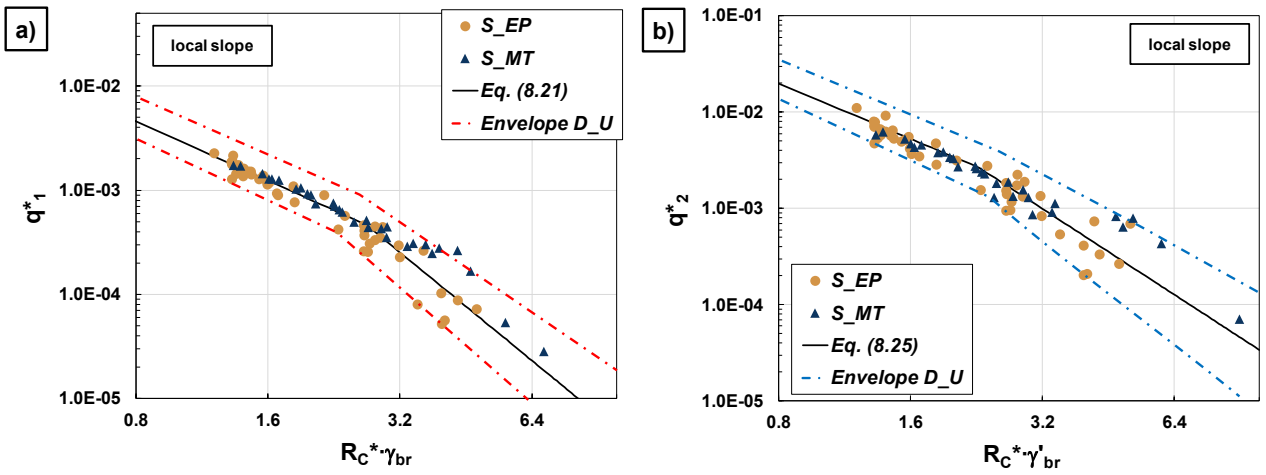

Figure 9.7 *– Comparison of numerical data of subsets S_EP and S_MT (obtained using the local slope, Eq. (9.3)) with the overtopping formula (black solid line) and the envelope of planar beach data, D_U (dash-dotted lines). Panel a) refers to the first hypothesis of parametrization, while panel b) refers to the second one.*

From a visual inspection of numerical results, no remarkable differences appear between the four equivalent slopes investigated. The *S_EP* and *S_MT* data fall within the envelope of the planar beach dataset whether the equivalent slope adopted.

Nevertheless, the slight differences in the performances should be pointed out.

The averaged equivalent slope (Eq. (9.2) lead to a larger scatter for the convex profiles, regardless of the wavelength used, while the multi-slope foreshore data of *S_MT* lie beneath the predictive model curve, especially for $\mathcal{L} = 2L_p$.

On the other hand, both the local slope and the equivalent slope of Lashley et al. provide more satisfactory results; indeed, both the subsets are characterized by a little scatter and no significant biases are observed. However, the Lashley et al. proposal cannot be applied on the entire dataset.

Therefore, this focus on uneven profiles has ensured the assessment of the equivalent slope necessary for estimating the flow rate at vertical seawalls when natural beaches are involved. The numerical study described in the previous Chapter has indeed pointed out the essential role of the seabed slope, especially for overtopping in very shallow water conditions.

Among the four option analyzed, results suggest to use of local slope at the toe of the structure. It is worth noting that the use of the local slope is theoretically consistent with Eq. (8.21), where the dimensionless flow rate includes a sort of breaking wave height, $H_{br} = h_{TOE} \cdot \gamma(m)$.

In the case of uneven foreshore characterized by a convex profile, Eq. (9.3) can be used. The scale parameter A can be easily identified by schematizing the convex profile with the power model of Bruun (1954) and Dean (1977). Moreover, Eq. (9.3) takes the beaches characteristics into account since A depends on the sediment size. On the other hand, the local slope at the toe of the wall can be easily used for irregular profiles that can be schematized like a multi-slope foreshore (e.g. Malecòn beach).

Nevertheless, the study reveals that the hypothetical slope recently suggested by Lashley et al. (2023) may be a valid alternative. Although the authors verified it on a single mildly-varying foreshore, its use gives satisfactory results. However, such a slope has limited validity; it cannot be applied to seawalls located in shallow waters ($h_{TOE} / H_{mo,DEEP} \geq 1$), where the foreshore slope could still (slightly) affect the overtopping process.

10. THE PHYSICAL EXPERIMENTAL CAMPAIGN

In this chapter, the experimental campaign carried out at the Department of Civil, Architectural and Environmental Engineering (DICEA) of the University of Naples "Federico II", Italy, will be described. Physical model tests have been performed to investigate the wave overtopping at vertical seawalls with very and extremely shallow foreshores.

The experimental campaign is organized into two phases: the first examines the wave propagation, while the second phase handles wave overtopping measurements.

10.1. Experimental set-up

10.1.1. Wave flume and main equipment features

The experimental tests have been conducted in the small-scale flume of the DICEA laboratory, which is a 0.75 m high, 26 m long and 0.5m width (Figure 10.1). From the wave maker, after a first stretch long 9 m, the flume has glass walls that allow the visual observation of the experiments.

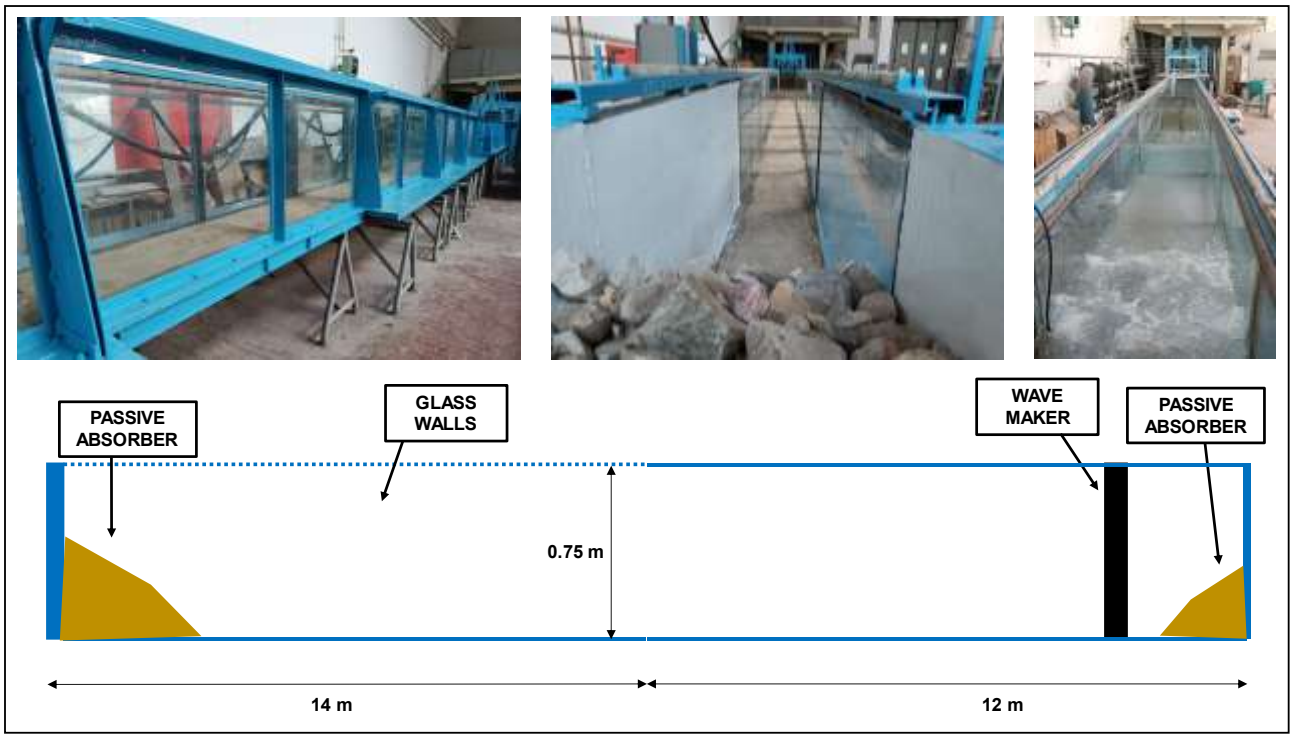

Figure 10.1 *– Small-scale flume of the DICEA laboratory.*

The wave maker is a piston-type one located at 3 m from the end of the channel (Figure 10.2a), controlled by a position sensor. An oil dynamic pump powered by an electric motor moves the paddle, allowing a maximum semi-stroke of 0.2 m. The software WAVEGEN (developed by HR Wallingford) generates the signal sent to the control cabinet, which transfers it to the wave maker. Regular and irregular sea states can be reproduced. At the channel's extremities, two passive absorbers usually minimize the effect of wave reflection.

Furthermore, the wave maker is equipped with an active-absorption system to avoid any undesired interference due to the presence of re-reflected waves. Such a system is based on a dual signal control algorithm in the frequency domain (Schaffer & Jakobsen, 2003; HR Wallingford, 2005). To appreciate the performance of the absorber, Figure 10.2c shows an example of reflection analysis; the latter refers to an overtopping test performed with one of the highest seawalls investigated (namely, low overtopping rate). In particular, the Figure depicts the incident wave height determined using the Zelt and Skjelbreia (1992) method for 10 stretches of nearshore wave signal (i.e., the wave elevation time series was divided into overlapping segments of 100 waves); the analysis shows that the incident wave height oscillates around a constant value, indicating no accumulation of energy in the flume.

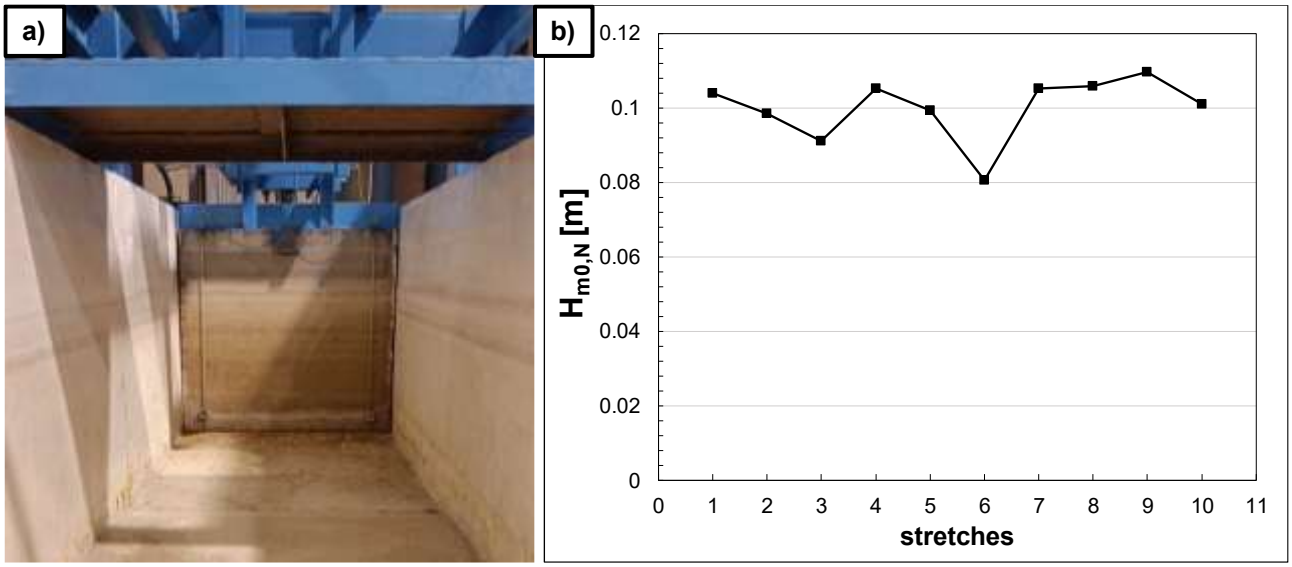

Figure 10.2 *– Panel a): wave maker. Panel b): incident wave height (determined using the method of Zelt and Skjelbreia, 1992) for 10 stretches of the nearshore wave elevation signal. The analysis refer to the test with* T_{pN} *= 1.3s,* $H_{m0,N}$ *= 0.13m, h=0.44m and* R_C*=0.2m.*

Twin-wire resistive probes and a pressure transducer have measured the water level displacements and wave characteristics (Figure 10.3); the wave probe has been employed to measure the mean overtopping discharge as well.

Each wave probe comprises two parallel stainless steel rods with a plastic head and foot, powered by a dual-power supply operating at a differential voltage of about ±10V. These measure the current that flows between two stainless steel wires that are immersed in water; then, the current is converted to an output voltage, directly proportional to the immersed depth, that is transferred to a control cabinet. The pressure transducers are piezoresistive sensors characterized by a voltage range of 0 ÷ 10V.

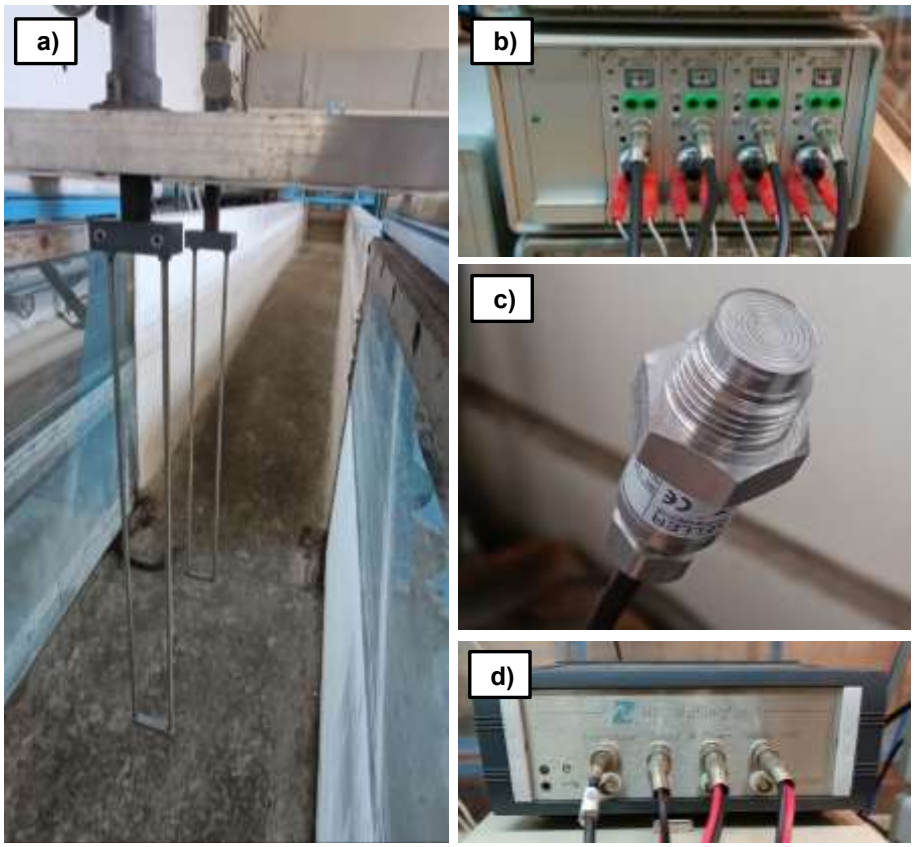

Figure 10.3 – *Measurement instruments. Panels a) and b) show the wave probes and their power supply, respectively; panels c) and d) depict the wave transducer and its power supply*.

The wave overtopping discharge has been measured through a probe located in a tank rear of the seawall (Figure 10.4). Using a probe allowed for measuring the temporal evolution of the overtopped water volume; thus, to minimize the unwanted noise due to the fluctuations following each overtopping event, we have divided the container with a partition wall that allows the water to pass underneath and reaches a zone unaffected by the fluctuations mentioned above. The tank size is 0.6m x 0.47m x seawall's height.

Finally, a pressure transducer has been located near the still water level to measure the pressures at the wall to characterize the impulsiveness of the waves (Figure 10.5).

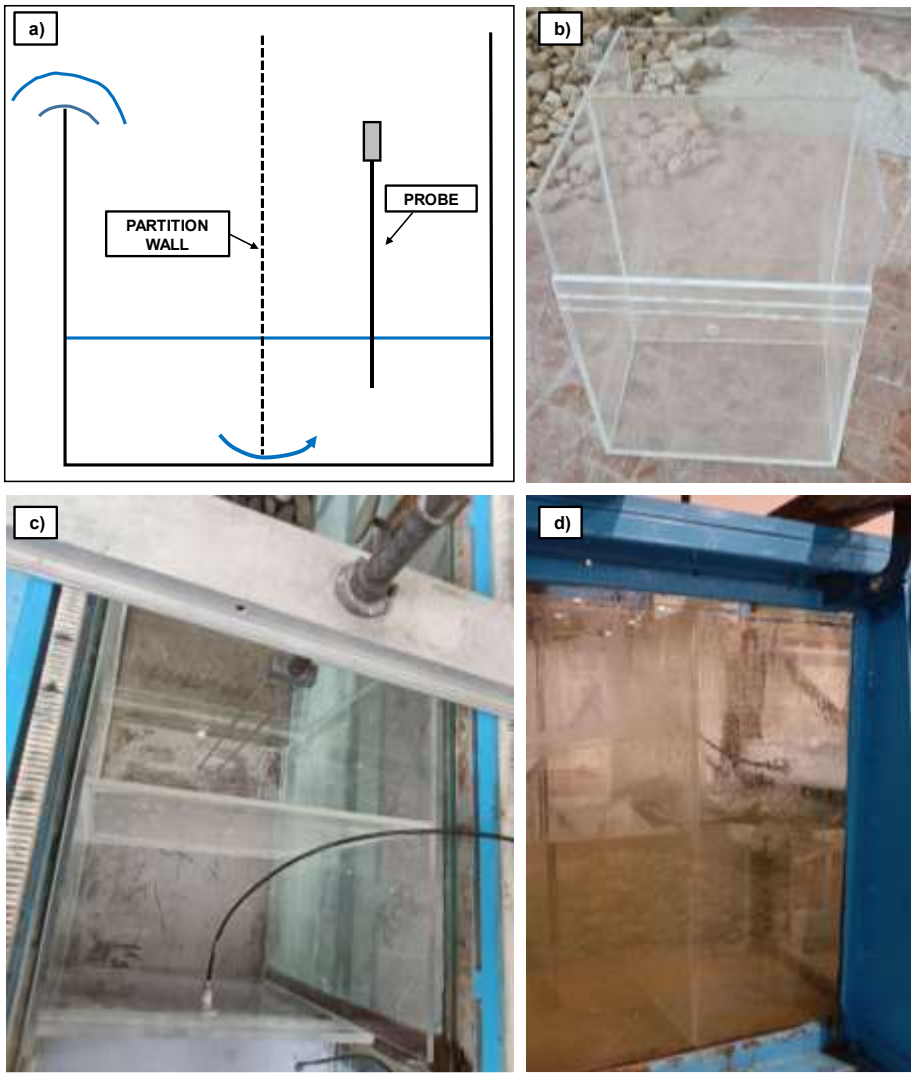

Figure 10.4 – *Panel a): sketch of the overtopping measurement equipment; panel b) and c): overtopping tank; panel d): the helpful effect of the partition wall in reducing the fluctuations due to overtopping events.*

Figure 10.5 – *Pressure transducer at the wall.*

10.1.2. Gauges' calibration

In order to obtain reliable measurements of wave transformation during the tests, a previous calibration of wave gauges is required. Such a calibration has been performed on a daily base, or whenever required by external conditions.

This procedure essentially establishes a correspondence between the position of the gauge with respect to the water level and the voltage returned. Thus, starting from a reference value, the water level in the flume was raised and reduced and, at each step, the correspondent voltage returned by gauges was recorded.
Simultaneously, the signal to noise ratio, *S/N*, has checked to verify that gauges were properly working. This ratio is expressed as:

$$\frac{S}{N} = 20 \log_{10} \left(\frac{\mu}{\sigma}\right) \tag{10.1}$$

where μ is the average of the signal acquired for 5 seconds with a sampling frequency of 25 Hz, while σ is the standard deviation of the signal (i.e. the noise). It is worth noting that the minimum value of *S/N* obtained during the experimental campaign was about 38.8 db, which ensures the correct operation of gauges.

After the calibration process, for each gauge the obtained points were fitted with a linear regression line characterized by a determination index, R^2, always greater than 0.99 (Figure 10.5).

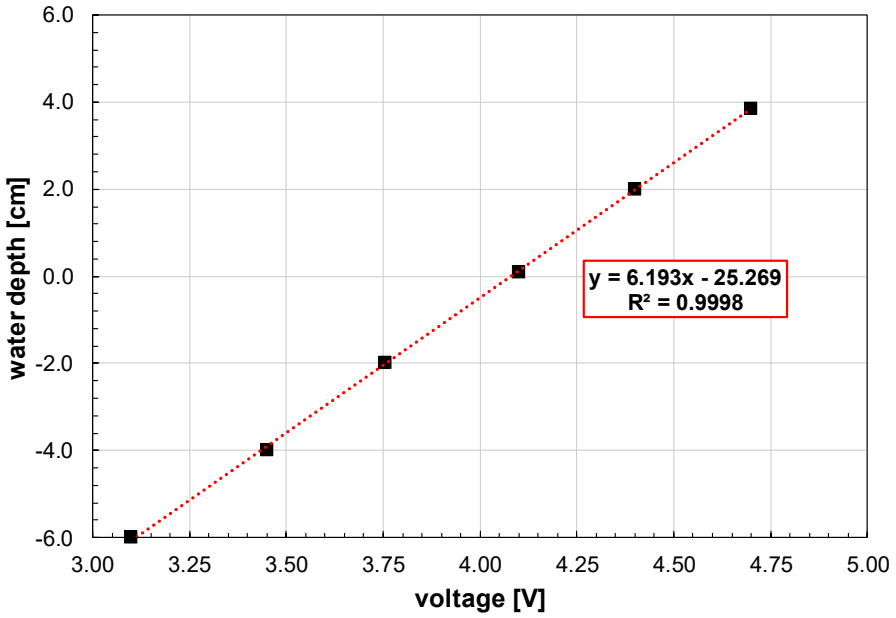

***Figure 10.5** – Probes calibration and fitting operation.*

It is worth noting that, during the overtopping experiments, the calibration of the probe located in the overtopping tank (Figure 10.4a) involved relating a volume of water to the voltage returned by the instrument.

The pressure transducers were calibrated at the beginning of the experimental campaign by means of a water column system (Figure 10.6). Analogously to the probes' calibration, the voltage read by the instruments was related to a water column level (Figure 10.7).

Figure 10.6 – *Water column system for calibrating pressure transducers.*

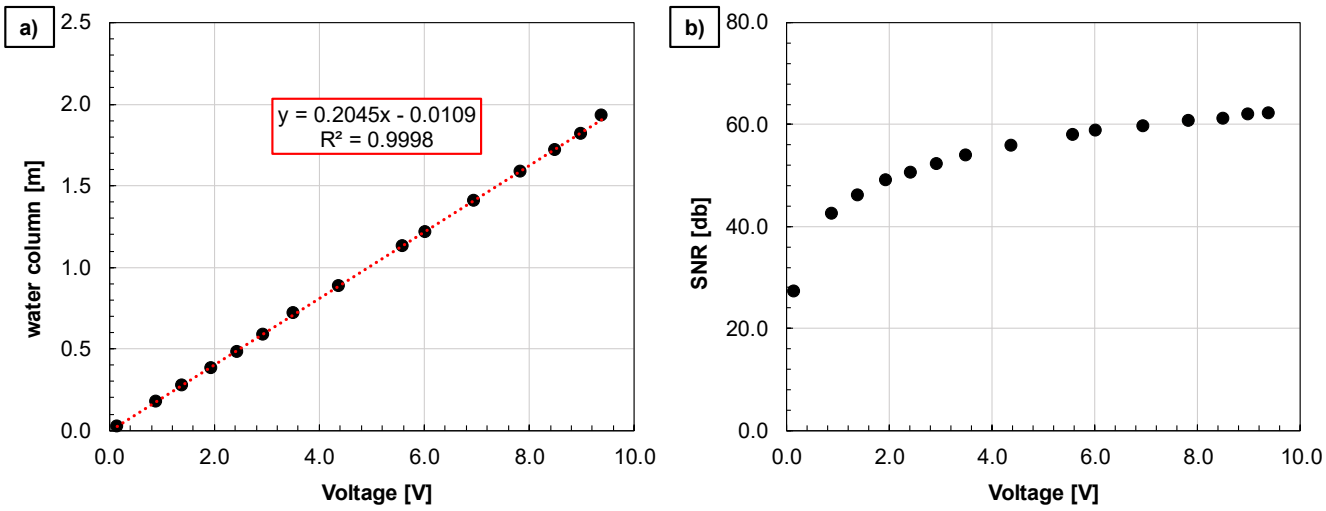

Figure 10.7 – *Panel a): pressure transducers calibration; panel b): signal to noise ratio related to the voltage values.*

10.1.3. Description of the physical model

In the DICEA small-scale channel, a steep foreshore inclined 1/10 to the horizontal has been reproduced (Figure 10.8). In front of the smooth slope, a flat bottom that is long 13m guarantees the proper development of the generated waves. Then, the foreshore raises up until + 0.4 m from the channel's bottom, where the vertical wall is located.

Figure 10.8 – *The steep foreshore characterized by tan(m)=1/10 reproduced in the small-scale channel of the DICEA laboratory.*

However, the hydraulic characteristics at the toe of the structure been measured without the wall in the flume. Hence, the foreshore has been extended up to +0.5 m from the channel's bottom to execute the wave propagation tests (Figure 10.9).

During this first experimental phase, four wave probes on the flat bottom have been used for the wave reflection analysis. The first probe is 9.3 m from the paddle, while the others have been arranged at a distance of +0.27m, +0.59m and +1.09m, respectively, from the first one. The Zelt and Skjelbria method (1992) has been employed to separate incident and reflected waves.

The pressure transducer has measured the wave parameters at the toe of the wall, while an additional probe has been located in the surf-zone, at +3.25 m from the beginning of the slope (Figure 10.9a). Furthermore, during 3 out of 27 experiments, the wave transformation has been recorded along the entire foreshore length (Figure 10.9b).

On the other hand, the second experimental phase concerns the wave overtopping experiments of vertical seawalls with very and extremely shallow foreshores (Figure 10.10). The vertical wall has been located at the end of the 4.0 m foreshore slope; its crest height has been gradually raised in order to model seven different seawall heights (Figure 10.11). As indicated in the next section, the experiments have been executed with four different water levels. Thus, 19 different crest freeboards have been investigated; specifically, R_C varies between 0.03 and 0.26 m.

It is worth noting that during wave overtopping tests that involve significant discharges, the generated time series has been divided into more sections, and for each of them, the overtopping variables have been measured. At the end of each test, a pump has re-introduced the lost volume of water in the flume. Otherwise, the whole time series would have reduced the water level in the flume and compromised the measurements.

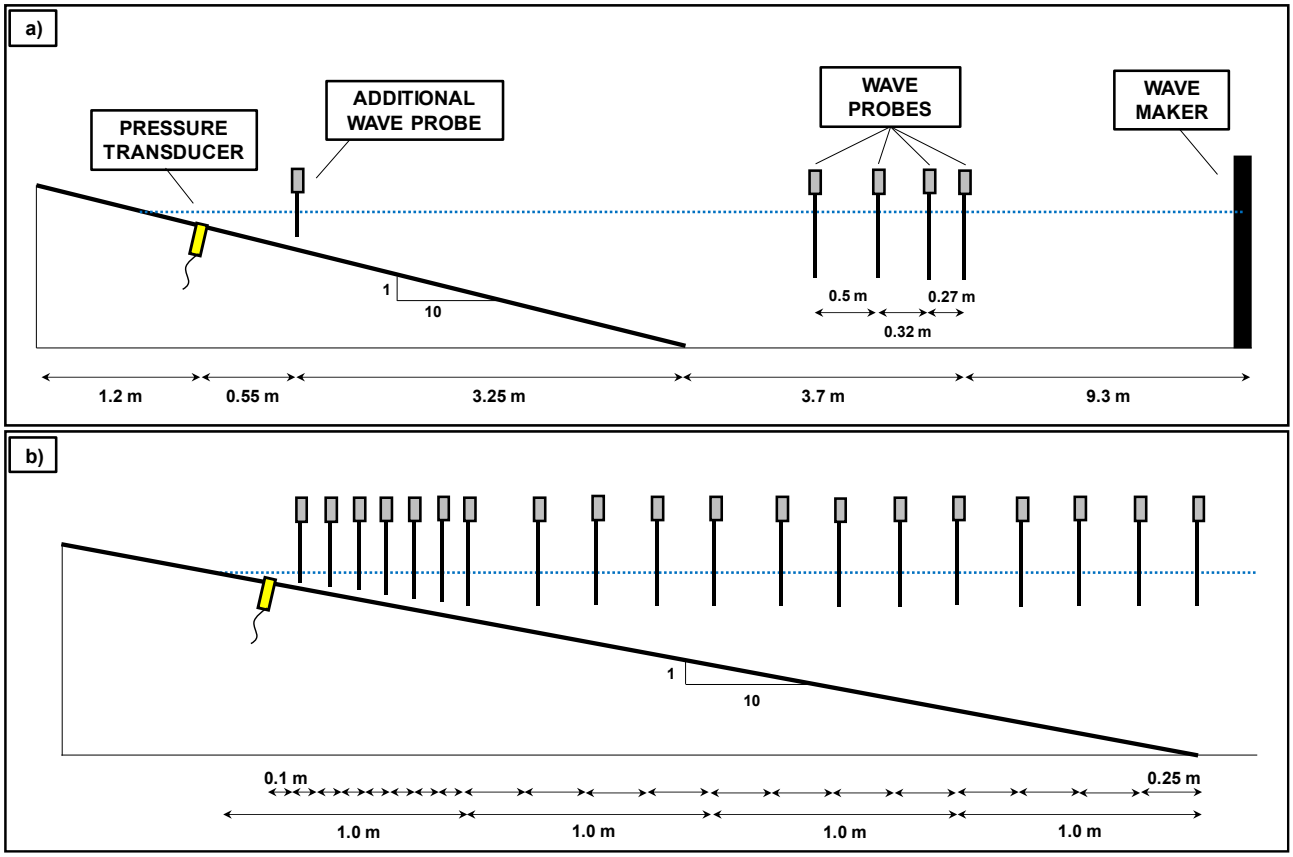

Figure 10.9 – *Panel a): sketch of the physical model setup during wave propagation tests: panel b) measurement points during 3 out of 2 wave propagation tests.*

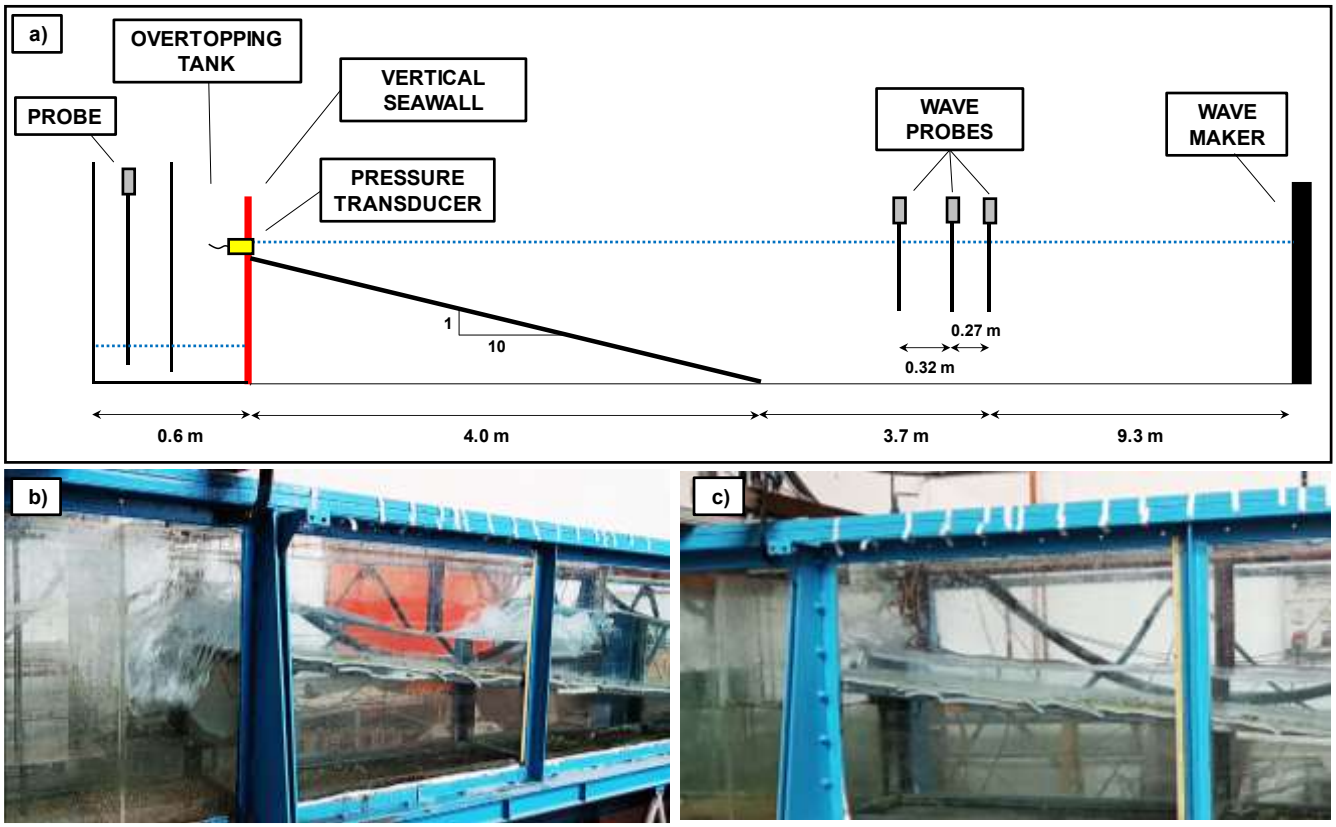

Figure 10.10 – *Panel a): sketch of the physical model setup during wave overtopping tests; panel b) and c): wave overtopping experiments.*

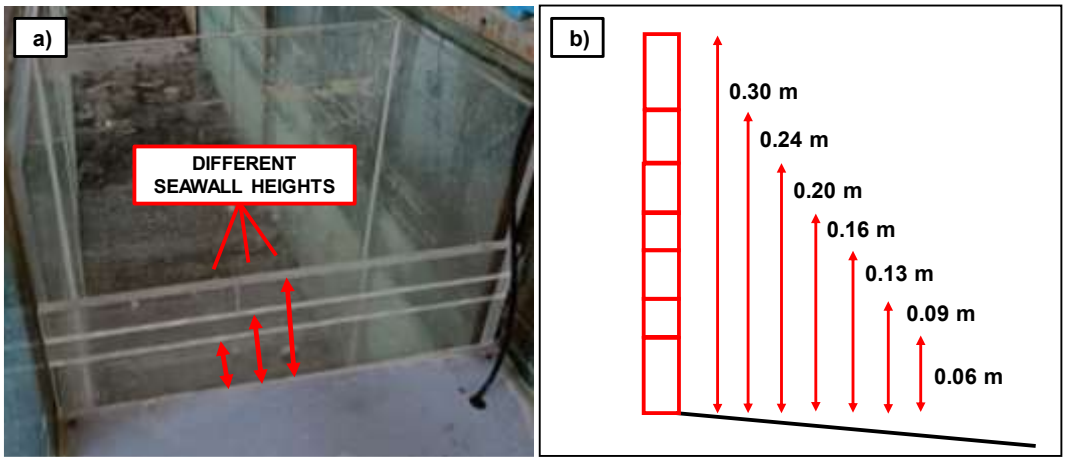

Figure 10.10 – *Panel a): seawall height gradually raised up; panel b): the seven different seawall heights investigated during the overtopping tests.*

10.2. Tests program

10.2.1. Wave propagation tests

The first phase of the experimental campaign concerns the wave propagation tests, namely the measurements of the incident wave parameters without the structure in the flume.

It is worth specifying that the test program has been organized to investigate the main variables (except for the foreshore slope) that, according to the numerical analysis of Chapter 8, affect the mean overtopping discharge of vertical walls in shallow water.

Irregular waves driven by mean JONSWAP spectra have been reproduced. In particular, 9 different sea states with 4 different water levels assemble the test program for a total of 27 experiments. Therefore, these have been performed by varying both the water depth and the generated wave conditions. Specifically, the water depth levels are 0.41, 0.42, 0.44 and 0.46m; the ranges of target significant wave height, $H_{m0,N}$, and peak period, $T_{p,N}$, are 0.08 ÷ 0.13 m and 1.3 ÷ 1.8 s, respectively. Thus, the wave steepness at the paddle varies between 0.016 to 0.049. Table 10.1 summarizes the characteristics of the tests program.

Each test has been conducted with a duration of 450 s in order to collect at least 250 waves.

Table 10.2 *– Wave propagation tests program.*

Test Code	**h [m]**	**h_{TOE} [m]**	**$H_{m0,N\ target}$ [m]**	**$T_{p,N\ target}$ [s]**	**s_{0p} [-]**
T13H13h42	0.42	0.02	0.13	1.3	0.049
T15H13h42	0.42	0.02	0.13	1.5	0.040
T18H13h41	0.41	0.01	0.13	1.8	0.026
T13H10h41	0.41	0.01	0.10	1.3	0.038
T15H10h41	0.41	0.01	0.10	1.5	0.028
T18H10h41	0.41	0.01	0.10	1.8	0.020
T13H08h41	0.41	0.01	0.08	1.3	0.030
T15H08h41	0.41	0.01	0.08	1.5	0.023
T18H08h41	0.41	0.01	0.08	1.8	0.016
T13H13h44	0.44	0.04	0.13	1.3	0.049
T15H13h44	0.44	0.04	0.13	1.5	0.037
T18H13h44	0.44	0.04	0.13	1.8	0.026
T13H10h44	0.44	0.04	0.10	1.3	0.038
T15H10h44	0.44	0.04	0.10	1.5	0.028
T18H10h44	0.44	0.04	0.10	1.8	0.020
T13H08h44	0.44	0.04	0.08	1.3	0.030
T15H08h44	0.44	0.04	0.08	1.5	0.023
T18H08h44	0.44	0.04	0.08	1.8	0.016
T13H13h46	0.46	0.06	0.13	1.3	0.049
T15H13h46	0.46	0.06	0.13	1.5	0.037
T18H13h46	0.46	0.06	0.13	1.8	0.026

T13H10h46	0.46	0.06	0.10	1.3	0.038
T15H10h46	0.46	0.06	0.10	1.5	0.028
T18H10h46	0.46	0.06	0.10	1.8	0.020
T13H08h46	0.46	0.06	0.08	1.3	0.030
T15H08h46	0.46	0.06	0.08	1.5	0.023
T18H08h46	0.46	0.06	0.08	1.8	0.016

10.2.2. Wave overtopping tests

The second phase represents the core of the experimental campaign, as the aim to gather reliable information on the overtopping of vertical walls with very shallow foreshores.

70 wave overtopping tests have been performed, which are almost equally divided between very and extremely shallow water conditions (Figure 10.11). The shallowness parameter, $h_{TOE}/H_{m0,DEEP}$, varies between 0.065 and 0.63 ($H_{m0,DEEP}$ has been obtained via de-shoaling). It is worth highlighting that the whole range investigated is quite below the range of the EurOtop reliable data (Figure 10.12); therefore, this new experimental campaign provides an essential dataset for comprehending the overtopping phenomenon in very shallow water.

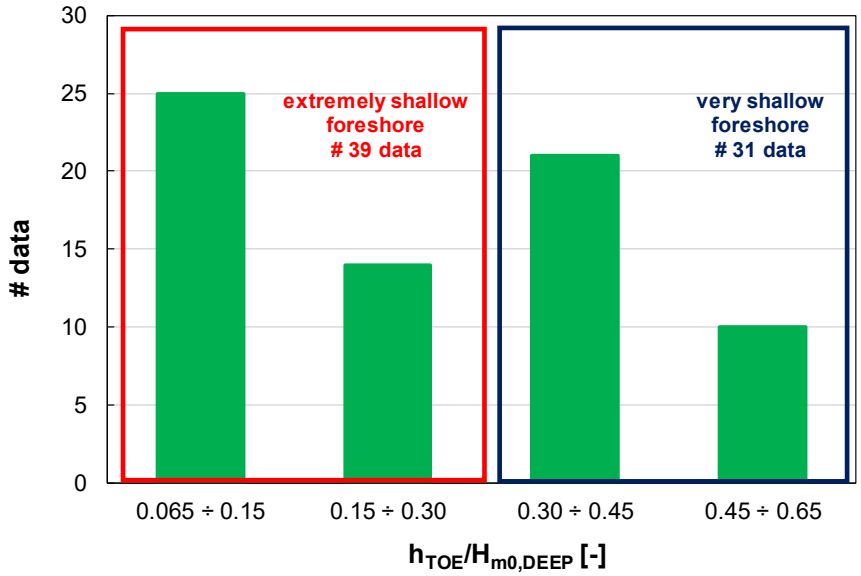

***Figure 10.11** – Shallow foreshore characteristics of the 70 wave overtopping tests performed.*

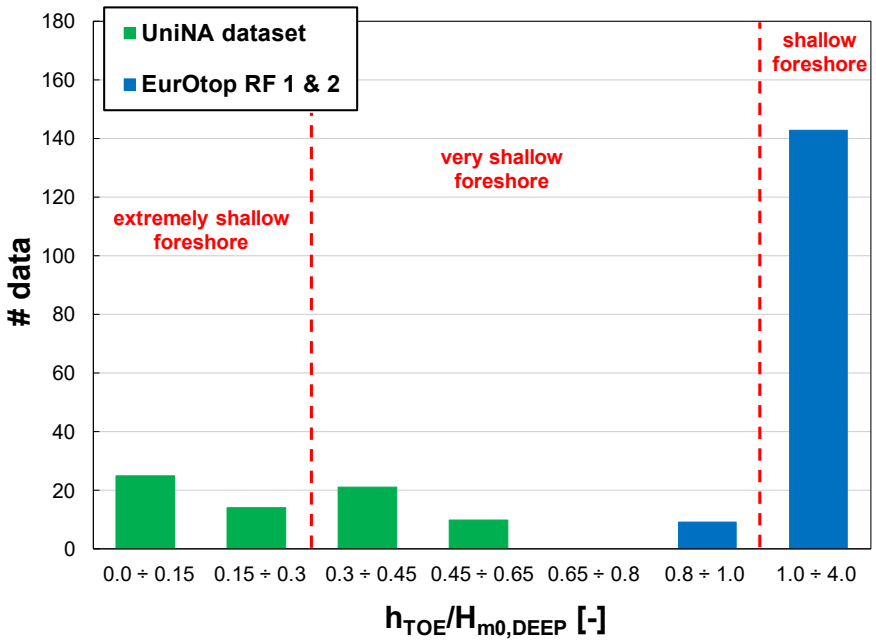

***Figure 10.12** – Shallow foreshore characteristics of the UniNa and EurOtop reliable datsets.*

As specified in the previous Section, the overtopping experiments involve seven different seawall heights (Figure 10.10b); the four different water levels adopted during the experiments lead to 19 crest freeboard values that vary between 0.03 and 0.26 m. Such an extended range allows for examining the wave overtopping of low-crested seawalls up to very high walls. In particular, the relative crest freeboard $R_C/\zeta_{1/4}$ varies quite uniformly between 1.28 and 14.16, while for $R_C/H_{m0,TOE}$ the range is 0.46 ÷ 4.48.

The characteristics of the seawalls investigated for each water depth at the toe of the structure are summarized in Table 10.2.

As mentioned above, the seawall has been equipped with a pressure transducer that allowed to investigated the nature and magnitude of the loadings exerted by waves on the structure. These measurements confirm the impulsive wave conditions examined.

***Table 10.2** – Seawalls' characteristics investigated during the experimental campaign.*

h_{TOE} [m]	$h_{SEAWALL}$ [m]	R_C [m]	$R_C/\zeta_{1/4}$[-]	$R_C/H_{m0,TOE}$ [-]	# seawall	# tests
0.01	0.06 ÷ 0.2	0.05 ÷ 0.19	1.7 ÷ 9.3	0.84 ÷ 4.34	5	19
0.02	0.06 ÷ 0.2	0.04 ÷ 0.18	1.28 ÷ 5.76	0.62 ÷ 2.78	5	6
0.04	0.09 ÷ 0.3	0.05 ÷ 0.26	1.48 ÷ 14.16	0.58 ÷ 4.48	5	29
0.06	0.09 ÷ 0.3	0.03 ÷ 0.24	1.55 ÷ 9.3	0.46 ÷ 3.11	5	16

11. ANALYSIS OF UniNA LABORATORY DATA

The present Chapter aims to analyze the UniNA laboratory data and, contemporarily, to verify the findings derived from the numerical study.

11.1. Behavior of the new parametrization in very and extremely shallow water conditions

It is worth recalling that the new parametrization previously introduced has been developed according to two different hypotheses (see Section 8.3.1). Although both account for the physics of the process, the first hypothesis is based on a more theoretical approach rather than the empirical character of the second one. However, the difference between them is trivial for the UniNA data because of the features investigated (i.e. $h_{TOE}/H_{m0,DEEP} < 1$ and a single value of foreshore slope). For the sake of brevity, only the first hypothesis's outcomes will be discussed; however, the second proposal leads to analogous results.

The dimensionless variables proposed in this work are here reported:

$$\frac{q}{g \cdot {H_{m0}}^{*} \cdot T_{p,N}} = F\left(\frac{R_C}{\zeta_{1/4}} \cdot \gamma_{br}\right) \tag{11.1}$$

where H_{m0}* is the minimum value between $H_{m0,DEEP}$ and a sort of breaking wave height, $H_{br} = h_{TOE} \cdot \gamma(m)$, while γ_{br} considers that waves tend to non-impulsive conditions towards deeper water.
As the UniNA dataset includes only data in very and extremely shallow waters, Eq. (11.1) can be simplified to:

$$\frac{q}{g \cdot h_{TOE} \cdot (\gamma_0 \cdot exp[p \cdot \tan(m)]) \cdot T_{p,N}} = F\left(\frac{R_C}{\zeta_{1/4}}\right) \tag{11.2}$$

Figure 11.1, plots the laboratory data according to this new parametrization. Furthermore, the predictive model inferred from numerical data (Eq. (8.11)) is depicted as well.

Numerical outcomes are consistent with physical model results, supporting the parametrization efficacy found during the numerical analysis. Moreover, the predictive model describes the decreasing trend of the measured q^* well, which confirms the SWASH capabilities to capture the physics of the process, besides a systematic underestimation already observed and discussed in this work.

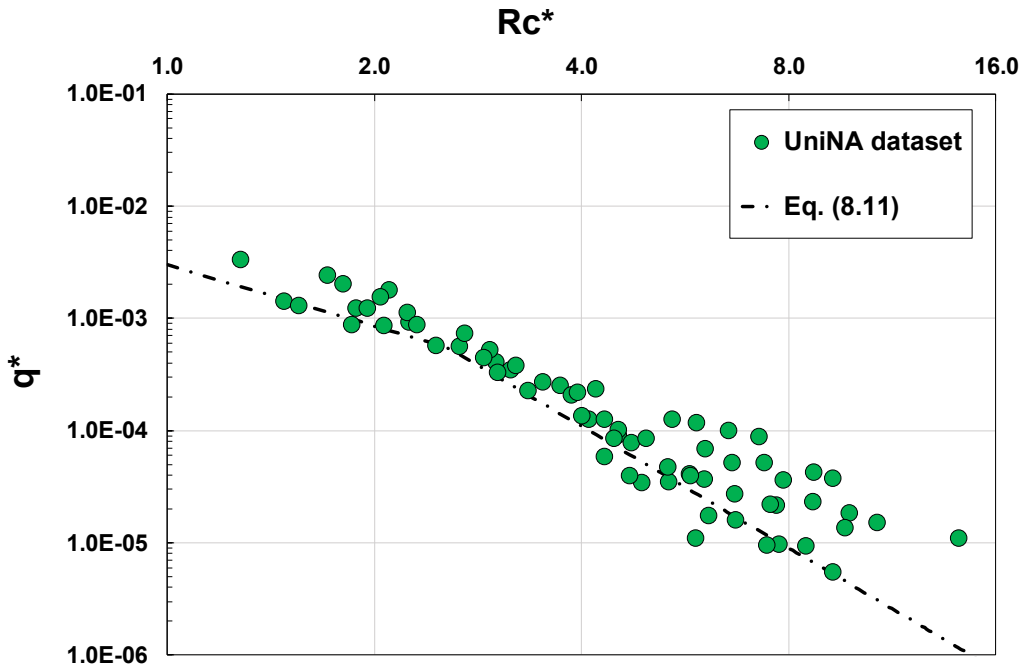

Figure 11.1 – *UniNA laboratory data plotted according to the new dimensionless variables; the overtopping predictive model, Eq. (8.21), is plotted as well.*

Overall, the laboratory data are characterized by a low level of scattering for R_C* lower than about 5, which is the typical design range of these defense structures (corresponding to $0.5 \leq R_C/H_{m0,TOE} \leq 2.5$ for the present dataset), whereas the scattering increases for higher values of relative crest freeboards. This aspect will be discussed in the following. However, it is worth noting that the numerical analysis has investigated a narrower range of dimensionless crest freeboards compared to that in UniNA. While $R_C/\zeta_{1/4}$ varied between 1 and 6 for the numerical dataset *D_U*, the physical experimental campaign has extended the analysis to higher seawall heights, up to $R_C/\zeta_{1/4}$ equals 14.

Nevertheless, the noteworthy improvement due to the new parametrization can be further appreciated in Figure 11.2, which plots the UniNA dataset on standardized dimensionless variables to compare the behaviors of Eq. (11.2) and the EurOtop parametrization. As observed for the numerical data in Section 8.3.2, results show that the parametrization proposed in this work significantly reduces the scattering compared to the EurOtop; indeed, the envelope of the EurOtop parametrization is quite larger compared to that of the new one.
Tis substantiates the validity of these new dimensionless variables in describing the overtopping phenomenon in very shallow water conditions.

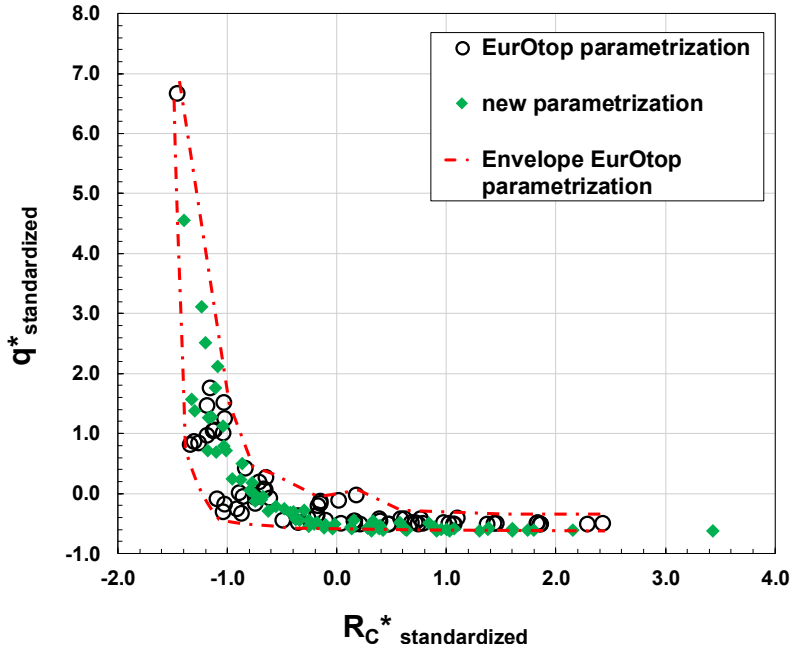

***Figure 11.2** – Comparison between the new parametrization (Eq. (8.2)) and that used in the EurOtop manual for the UniNA dataset.*

Finally, Figure 11.3 corroborates the inadequacy of the EurOtop formulae (Eq. (4.1)) to estimate the mean overtopping discharges of seawalls in very shallow water. The graph plots the measured to estimated flow rate ratio as a function of the UniNA flow rates; the EurOtop model significantly underestimates the laboratory discharges (up to one order of magnitude). This result is not surprising since the EurOtop database does not include reliable data for vertical walls in extremely shallow water (see Figure 4.4).

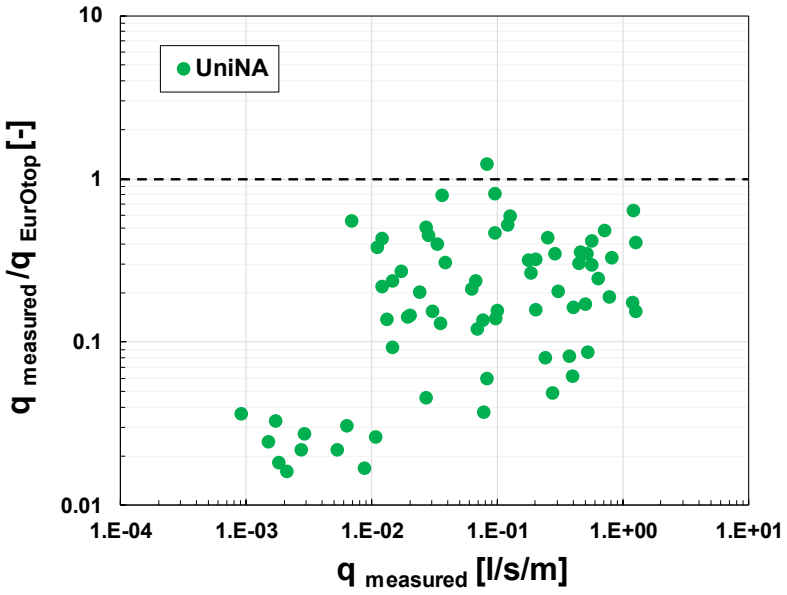

***Figure 11.3** – EurOtop model's performance: measured to estimated flow rate ratio as a function of UniNA discharges.*

11.2. Comparison with Lashley et al. (2021) predictive model

The present paragraph exploits the UniNA laboratory data to compare the performances of Eq. (8.11) and that of the empirical model proposed by Lashley et al. (2021).

It is worth remembering that, among the existing empirical tools, Lashley et al. specifically focuses on vertical seawalls with very and extremely shallow foreshores, such as those investigated during the physical experimental campaign.

Figure 11.4 plots measured against estimated mean overtopping discharges.

Results shows that the existing model well predicts the higher flow rates, data are quite close to the perfect agreement line for values of q between 10^{-1} and 10^{0} l/s/m, approximately. On the other hand, the performance weakens as the discharge diminishes. As clearly shown in Figure 11.5, Lahley et al.' formula provides satisfactory results as long as $R_C/H_{m0,DEEP}$ is lower than 1.5, whereas it underpredicts q for higher values. The higher the relative crest freeboard, the greater the underestimation. However, it is worth noting that the model has been mostly inferred from data characterized by $R_C/H_{m0,DEEP} \leq 1.5$, and there were few vertical walls with higher relative crest freeboard.

On the other hand, the new predictive model shows more satisfactory results; although the data lie mostly above the perfect agreement line because of the systematic underestimation previously mentioned (Figure 11.1), Eq. (8.11) exhibits more steady performances. This can be clearly appreciated in Figure 11.6, which plots the measured to estimated flow rates ratio as a function of the laboratory discharges. The graph demonstrates that, unlike Eq. (8.11), the Lashley et al. formula provides remarkable underestimations (different orders of magnitude) for the lower overtopping regime. It is worth noting that such underestimations have been already observed in the numerical analysis (Section 8.3.3).

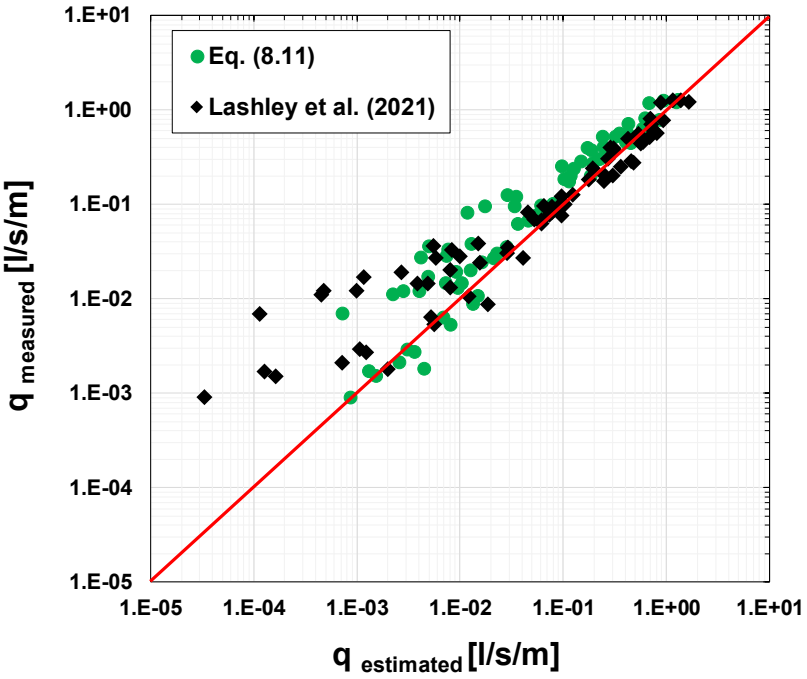

Figure 11.4 *– Comparison between Eq. (8.11) and Lashley et al. model.*

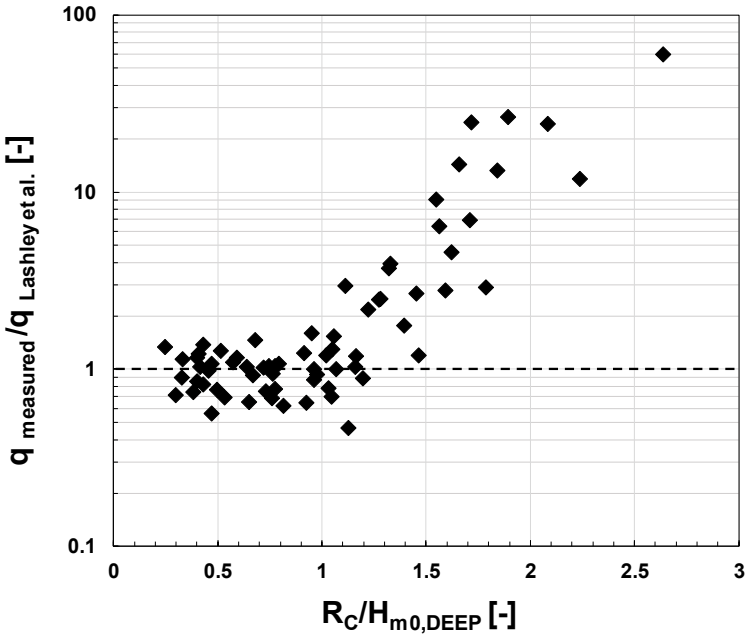

Figure 11.5 *– Lashley et al. model's performance: measured to estimated flow rate ratio as a function of the relative crest freeboard.*

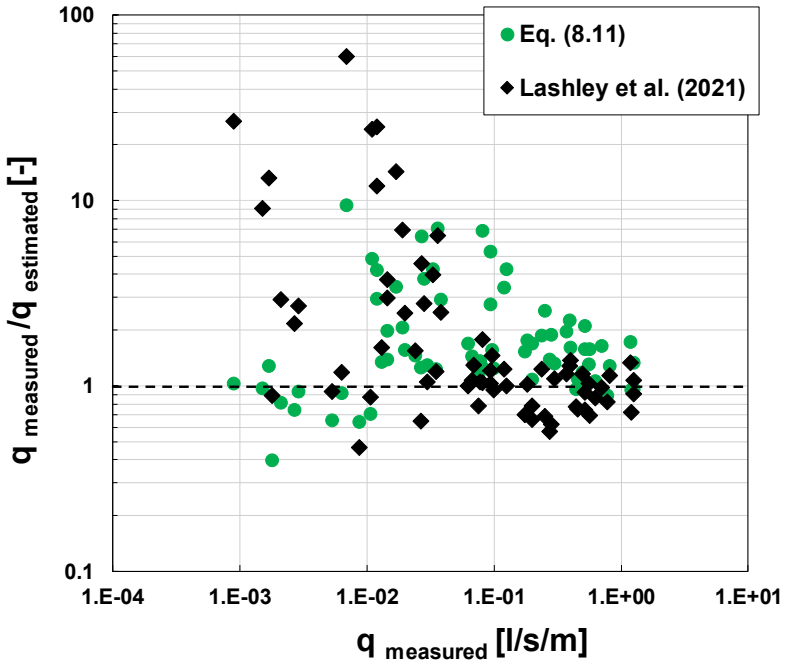

***Figure 11.6** – Measured to estimated flow rate ratio as a function of q.*

11.3. Wave overtopping in extremely shallow water: a deeper insight

As observed in Figure 11.1, the laboratory data exhibit a considerably narrow envelope for R_C* up to about 5, while the scattering increases for higher values of relative crest freeboards.

However, a closer inspection reveals a slightly different behavior for seawalls in extremely shallow water with $h_{TOE}/H_{m0,DEEP} < 0.2$ (Figure 11.7); indeed, these data apparently follow a steeper power-law compared to that related to the laboratory data with $h_{TOE}/H_{m0,DEEP} > 0.2$ (blue dash-dotted line). Nevertheless, the high R^2 statistic (0.98) confirms the effectiveness of this new parametrization.

It is worth noting that this peculiarity could not have emerged from the numerical analysis as it has examined the range $0.2 \leq h_{TOE}/H_{m0,DEEP} \leq 2.7$.

The data analysis has demonstrated that, for these shallowness conditions, the dimensionless flow rate decays with a power function in which the coefficients A and B depend on $h_{TOE}/H_{m0,DEEP}$ (Eq. (11.3)):

$$q^* = A \cdot \left(\frac{R_C}{\zeta_{1/4}} \right)^{-B} \tag{11.3}$$

Specifically, as $h_{TOE}/H_{m0,DEEP}$ increases, as A and B decrease, up to the values obtained for the data with the relative water depth larger than 0.2 (Figure 11.7).

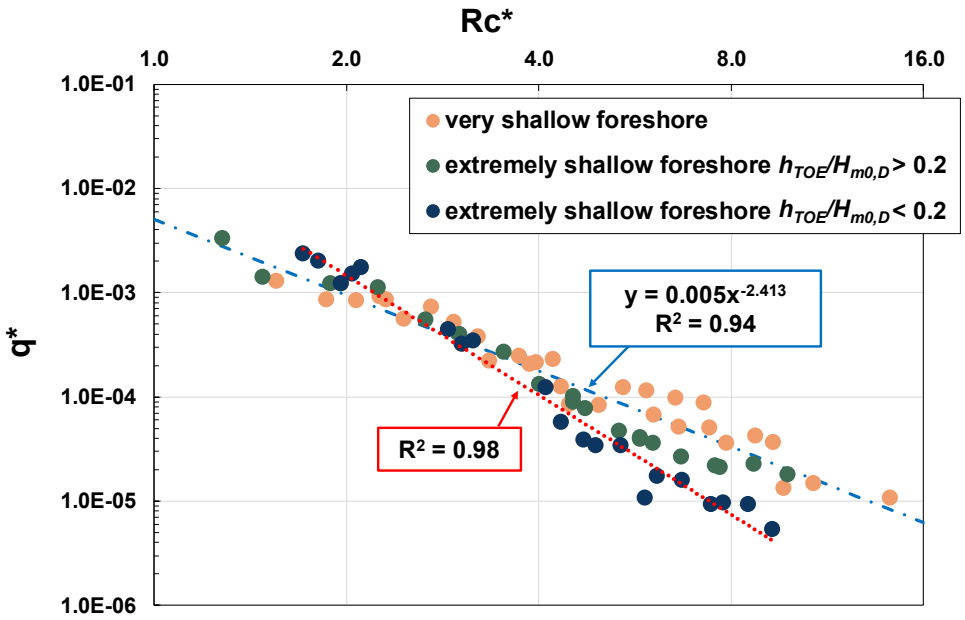

***Figure 11.7** – UniNA dataset plotted according to the new parametrization (Eq. (Y.2)). The red line is the regression curve for data with $h_{TOE}/H_{m0,DEEP} < 0.2$, while the blue line fits the data wih $h_{TOE}/H_{m0,DEEP} > 0.2$.*

Therefore, a unique predictive power formula can be derived for seawall with very and extremely shallow foreshores (Eq. (11.4)), in which, according to the UniNA laboratory data, the coefficients A and B can be estimated as follows:

$$\frac{q}{g \cdot h_{TOE} \cdot (\gamma_0 \cdot exp[p \cdot \tan(m)]) \cdot T_{p,N}} = A \cdot \left(\frac{R_C}{\zeta_{1/4}}\right)^{-B} \tag{11.4a}$$

$$A = max\left\{0.005\,;\,0.0013 \cdot \left(\frac{h_{TOE}}{H_{m0,DEEP}}\right)^{-1.06}\right\} \tag{11.4b}$$

$$B = max\left\{2.413\,;\,1.63 \cdot \left(\frac{h_{TOE}}{H_{m0,DEEP}}\right)^{-0.32}\right\} \tag{11.4c}$$

Analogously, using the second parametrization proposal, the predictive power formula reads:

$$\frac{q}{g \cdot h_{TOE} \cdot T_{p,N} \cdot \tan(m)^{0.5}} = A \cdot \left(\frac{R_C}{\zeta_{1/4}}\right)^{-B} \tag{11.5a}$$

$$A = max\left\{0.02\,;\,0.005 \cdot \left(\frac{h_{TOE}}{H_{m0,DEEP}}\right)^{-1.06}\right\} \tag{11.5b}$$

$$B = max\left\{2.413\,;\,1.63 \cdot \left(\frac{h_{TOE}}{H_{m0,DEEP}}\right)^{-0.32}\right\} \tag{11.5c}$$

To evaluate the effectiveness of the predictive model, Figure11.8 plots the measured flow rates against the estimated ones; panel a) and panel b) refer to Eqs. (11.4) and (11.5), respectively.

The estimated discharges are consistent with the laboratory ones (the data are quite uniformly close to the best agreement line). Therefore, using Eq. (11.3) significantly enhances the model predictive capabilities.

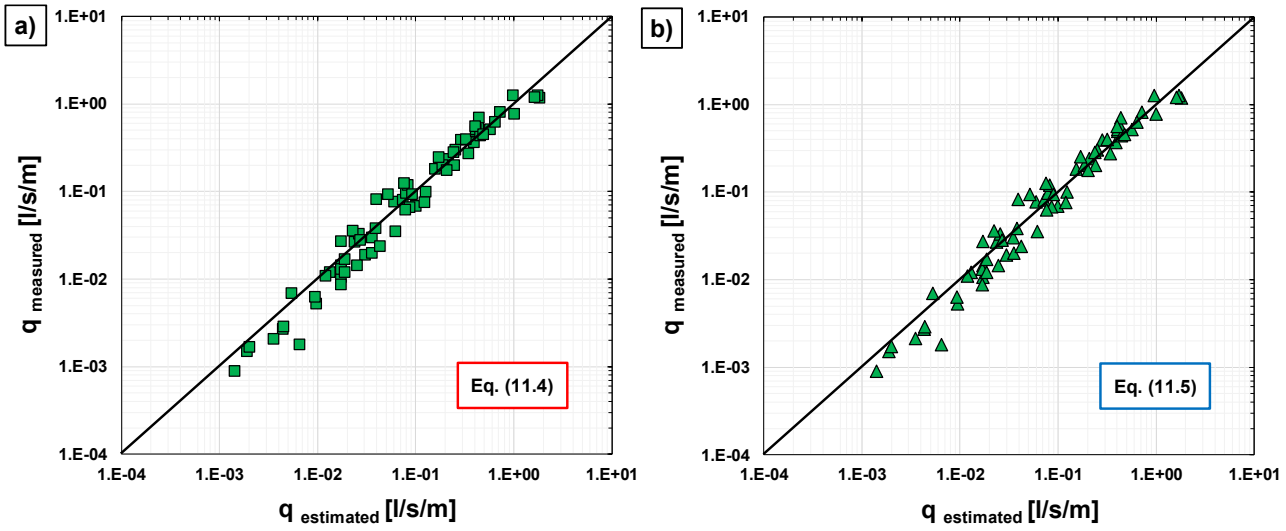

Figure 11.8 *– Measured flow rates vs. that one estimated via Eqs.(11.4, 11.5) in panel a) and b), respectively.*

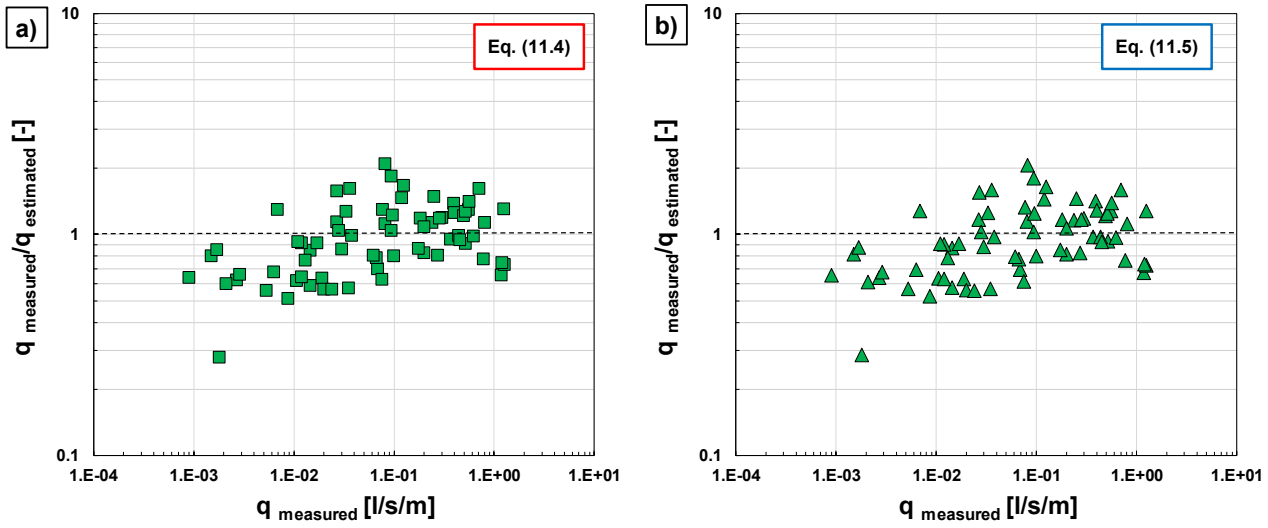

Figure 11.9 *– Eqs. (11.4, 11.5) performances: measured to estimated flow rate ratio as a function of q.*

It is worth pointing out that the model tends to slightly overestimate the low overtopping regimes (Figure 11.9). Such behavior probably results from the model adopted (Eq. 11.3); a single-power function has been suggested due to the limited amount of laboratory data. However, either a double-power formula or a combined exponential/power law may describe the process more accurately.

Furthermore, the physical experimental campaign has investigated only one foreshore slope; future research must extend this analysis to other seabed inclinations to verify the applicability of this predictive model.

Therefore, the unique formula suggested in this Chapter for estimating the overtopping at seawalls with very and extremely shallow water should be used with extreme caution.

12. A TENTATIVE GENERAL FORMULA

The present Chapter aims to evaluate the new parametrization's performance in extended shallowness conditions and provide a more generalized formula for estimating the wave overtopping of seawalls in shallow water. To this end, three different laboratory datasets have been gathered, namely:

- EurOtop reliable data (RF 1 & 2);
- experiments conducted at University of Naples Federico II on the Malecòn multi-slope profile (Cordova et al., 2015; 2016);
- laboratory tests described in Chapter 10.

12.1. General features of laboratory datasets

The EurOtop reliable dataset encompasses 152 laboratory tests, including both impulsive and pulsating wave conditions, with very and shallow foreshores ($0.8 \leq h_{TOE}/H_{m0,DEEP} < 4$).
However, it is worth noting that the wave setup is unknown for the EurOtop data, and thus, its role is neglected here. This assumption should be adequate for laboratory tests with $h_{TOE}/H_{m0,DEEP} \geq 1$, while it makes the data with very shallow foreshores, 9 out of 152, slightly uncertain (they may have a set-down that is ignored in this analysis).

The MT dataset contains 48 data characterized by a shallowness condition between 0.52 and 1.48 (i.e. very and shallow water). These data require the use of an equivalent slope since the laboratory tests were performed on the Malecòn multi-slope profile.

Finally, the UniNA dataset provides information on vertical seawalls with very and extremely shallow foreshores.

Table 12.1 summarized the main features of the three datasets.

Table 12.1 *– Datasets main characteristics.*

dataset ID	*# tests*	*foreshore*	$h_{TOE}/H_{m0,DEEP}$ *[-]*	*Impulsive condition*
EurOtop RF 1&2	152	planar	0.82 ÷ 3.9	impulsive / pulsating
Malecòn	48	uneven	0.52 ÷ 1.48	impulsive
UniNA	70	planar	0.07 ÷ 0.66	impulsive

12.2. Wave overtopping of seawalls in shallow water ($0.2 \leq h_{TOE}/H_{m0,DEEP} < 4$)

The first phase of the analysis concerns the 250 laboratory data characterized by $0.2 \leq h_{TOE}/H_{m0,DEEP} < 4$.

The analysis of the UniNA laboratory tests have demonstrated that, in shallower water ($h_{TOE}/H_{m0,DEEP} < 0.2$), the dimensionless flow rate is characterized by a higher decay rate (Figure 11.6). Therefore, 25 out of 70 UniNA laboratory data are disregarded here.

12.2.1. EurOtop parametrization

The laboratory data are plotted on the EurOtop plane in Figure 12.1. The (log-log) graph has $R_C/H_{m0,TOE}$ on the abscissas, while, on the ordinates, there is either $q/\sqrt{(g\,H_{m0,TOE}^3)}$ or $q/\sqrt{(g\,H_{m0,TOE}^3)}/\sqrt{(L_{m-10,TOE}/h_{TOE})}$ depending on whether the data fall in the non-impulsive or impulsive loading case.

The data are quite scattered, and UniNA lies well beneath the main cloud. Also, the Malecòn data seem to follow a slightly different trend. Moreover, the graph shows that, for a given value of relative crest freeboard, Malecòn and UniNA may differ from up to one or even two orders of magnitude. Finally, the non-impulsive data are located around the upper bound of the cloud, reasonably because they actually refer to a different formula.

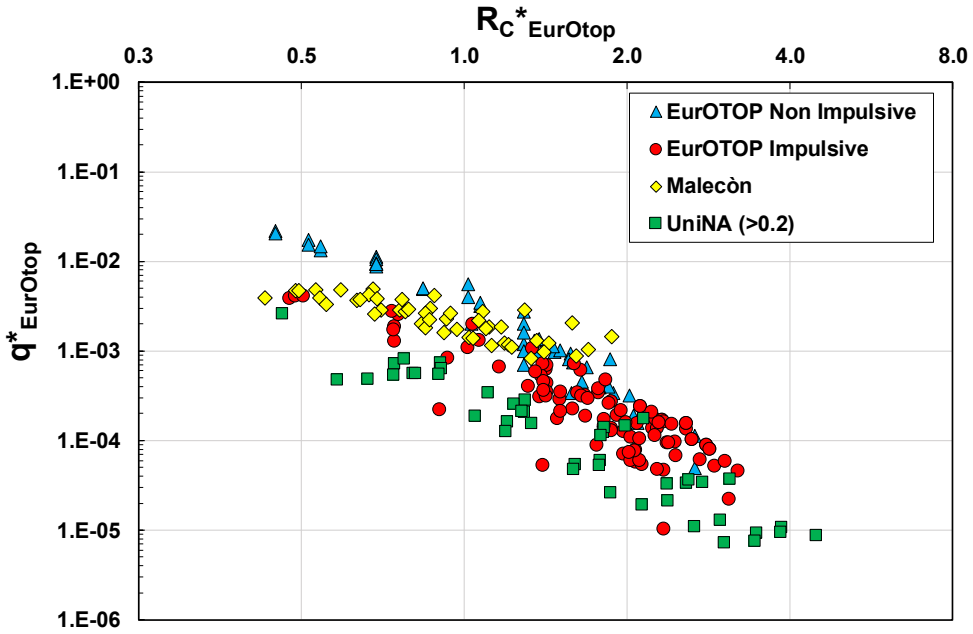

Figure 12.1 *– The three datasets plotted on the EurOtop plane.*

The reason for the observed behavior is that UniNA experiments were conducted with values of the walls' toe depth significantly less than other data. This is either in terms of $h_{TOE}/L_{m-10,TOE}$ or $h_{TOE}/H_{m0,TOE}$, as shown in the Figure 12.2. Accordingly, the distance from the other data is destined to increase as the extremely shallow water data with $h_{TOE}/H_{m0,TOE} < 0.2$ are added (see Figure 12.3).

Thus, these results suggest that EurOtop parametrization is not robust enough to explain the whole database. Interestingly, the large scattering (one order of magnitude) for a given relative crest freeboard in the EurOtop plane is consistent with the SWASH experiments, as cane be seen in Figure 12.4.

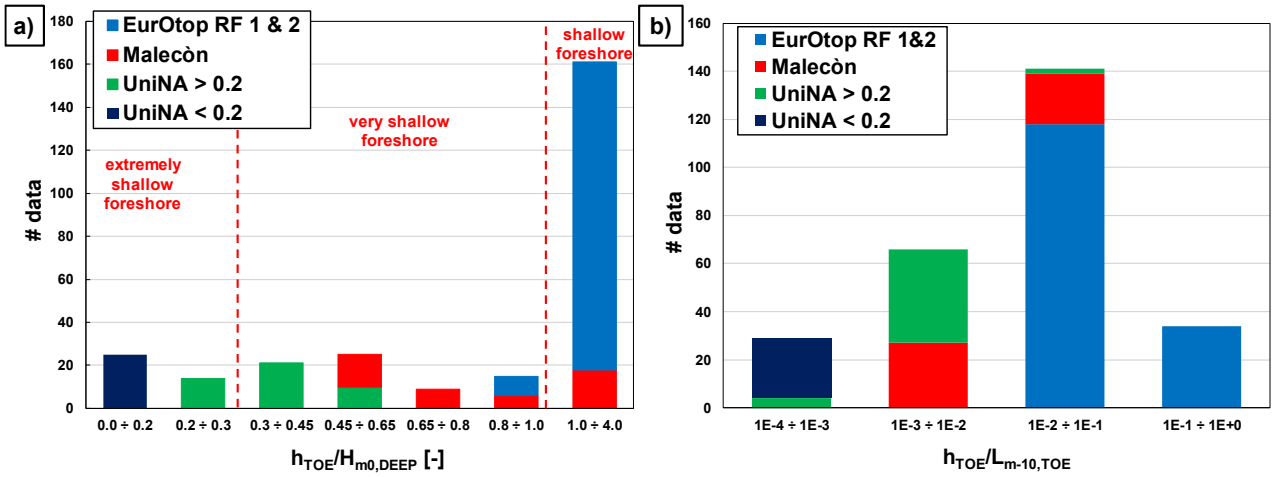

Figure 12.2 *– Shallowness characteristics for the three datasets. Panel a) and b) plot the number of data in terms of $h_{TOE}/H_{m0,TOE}$ and $h_{TOE}/L_{m-10,TOE}$, respectively.*

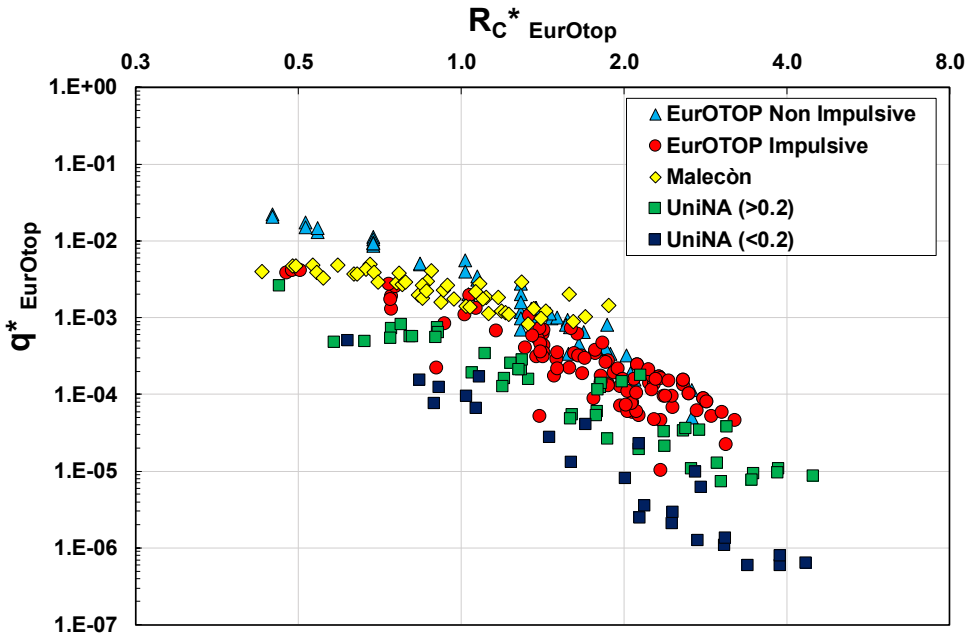

Figure 12.3 *– The three datasets plotted on the EurOtop plane; the graph also plots UniNA data with a relative water depth $h_{TOE}/H_{m0,TOE}$ less than 0.2.*

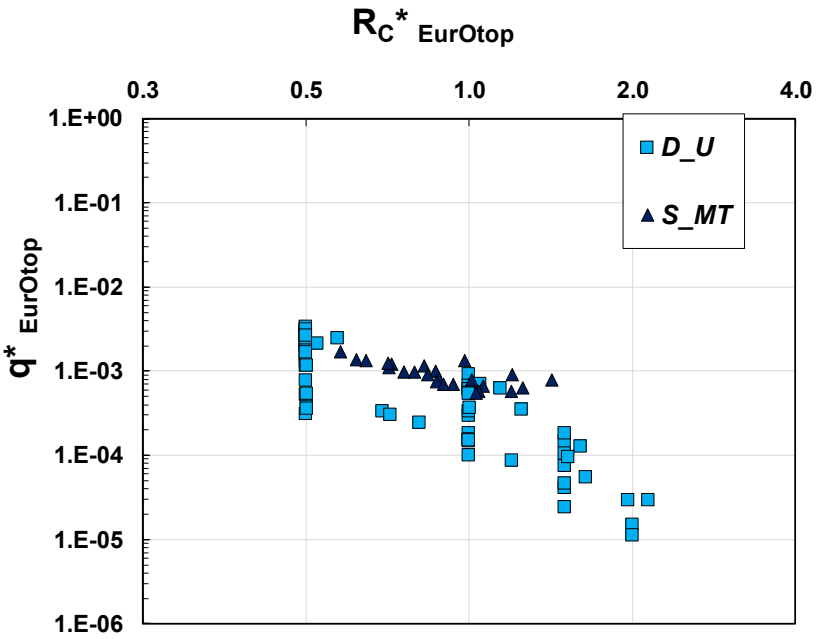

Figure 12.4 *– SWASH outcomes on the EurOtop plane; cross symbols refer to the experiments with planar beaches (D_U), while triangles indicate the MT numerical experiments (S_MT).*

12.2.2. New parametrization

The present paragraph evaluates the parametrization proposed in this work against the laboratory database. Both the two parametrization proposals are showed and discussed.

Figures 12.5 and 12.6 plot the three datasets according to the first and second parametrization proposals, respectively. Moreover, the graphs also depict the empirical formulae (black solid curve) derived from numerical outcomes as well as their upper envelopes (red solid curve).

It is worth remembering that the numerical study did not investigate the parametrization's behavior for relative crest freeboards higher than 6; thus, the extrapolated formula and upper envelope are depicted in the Figures as dash-dotted curves.

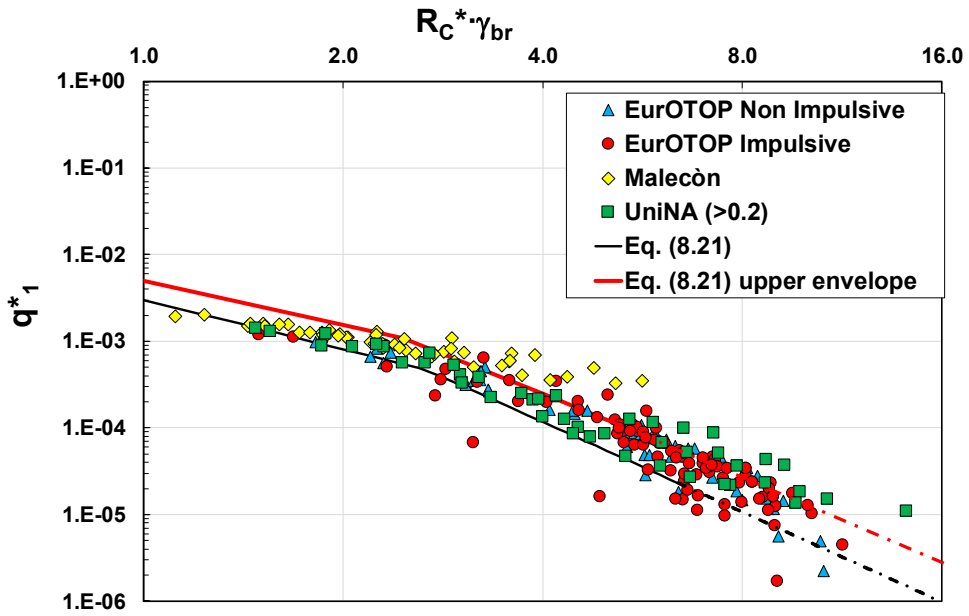

Figure 12.5 *– The three laboratory datasets plotted according to the new parametrization; the dimensionless variables refer to the first hypothesis.*

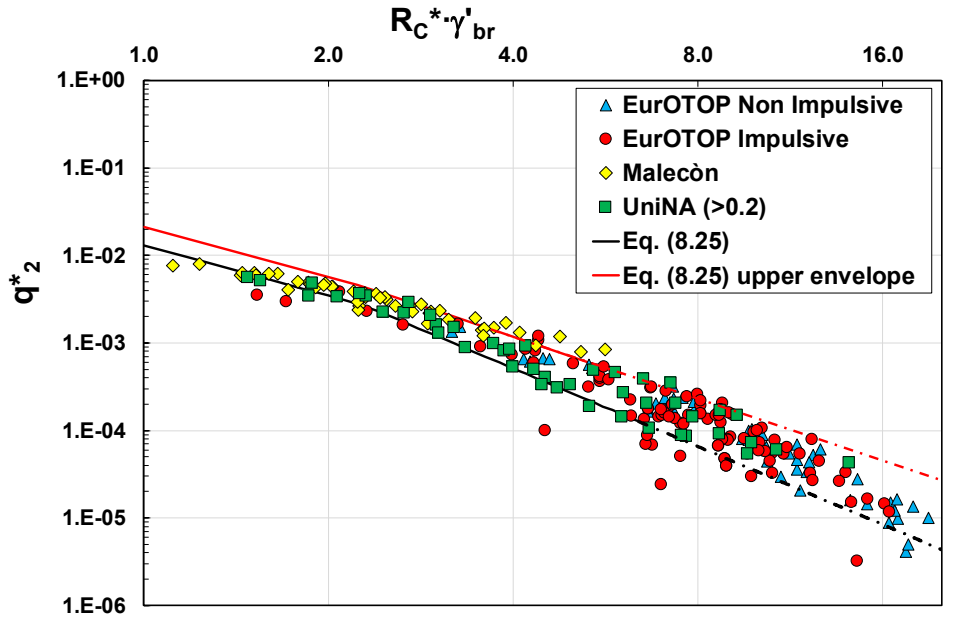

Figure 12.6 *– The three laboratory datasets plotted according to the new parametrization; the dimensionless variables refer to the second hypothesis.*

Several significant conclusions can be drawn from Figures 12.5 and 12.6.

The results clearly show a remarkable reduction in the data scattering compared to the EurOtop parametrization (Figure 12.1). The three laboratory datasets exhibit a uniform behavior and a narrow envelope. This significant improvement indicates that the new dimensionless variables better explain the physics of the process. Moreover, unlike the literature statement, the new parametrization does not discern between the overtopping

of breaking and non-breaking waves. As underlined in Figure 12.7, the present parametrization assembles impulsive and pulsating EurOtop data, which follow a unique trend.

The numerical findings are corroborated. The numerical-derived formulae describe a q^* decreasing trend consistent with the physical model results (beyond the systematic underestimation already discussed in this work). Furthermore, it is worth observing that the upper envelope of the empirical formulae includes a large part of laboratory data, especially for the second parametrization proposal (Figure 12.6).

For the Malecòn uneven profile, the slope averaged on twice the local wavelength is adopted instead of the local slope suggested by the numerical analysis (Chapter 9). The former equivalent slope indeed provides more satisfactory results. However, it should be specifying that using the local slope does not alter the global result; indeed, the Malecòn data would rise slightly up in Figures 12.5 and 12.6, but not produces a scatter of one order of magnitude from the other datasets (as observed in the EurOtop parametrization).

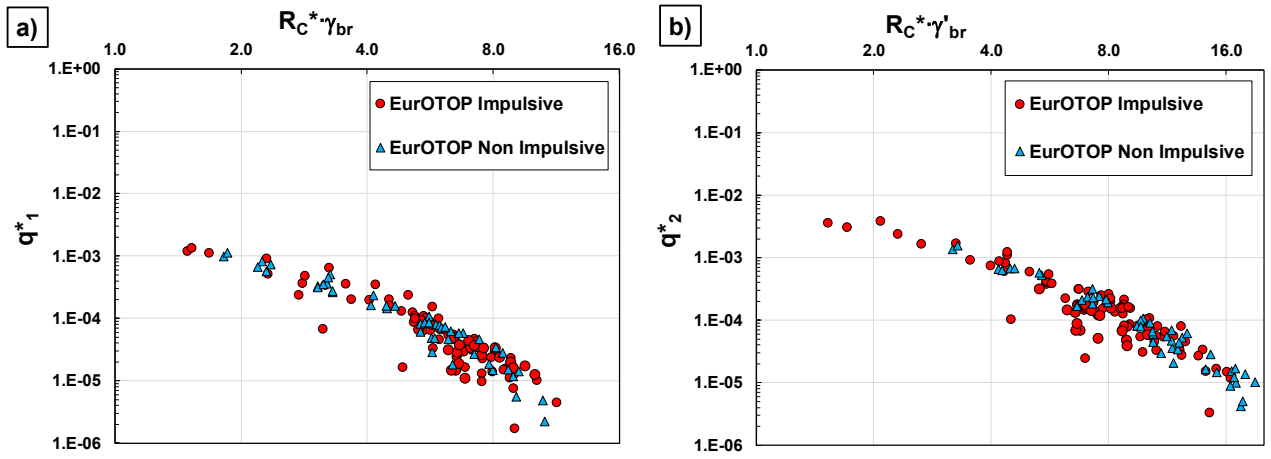

***Figure 12.7** – Impulsive and non-impulsive EurOtop data plotted according to the new dimensionless variables; panels a) and b) refer to the first and second parametrization proposal, respectively.*

Among the two hypotheses, the "empirical-type" formulation provides more satisfactory results (Figure 12.5). Although no substantial differences can be appreciated, a few data lie slightly far from the cloud.

The different performances substantially result from the two ways of accounting for the foreshore slope in the dimensionless flow rate. Indeed, the first hypothesis takes this variable into account as long as $h_{TOE} \cdot \gamma(m) < H_{m0,DEEP}$; whereas the logistic function adopted in the second hypothesis considers that the seabed effect gradually reduces towards deep water.

This result further confirms the crucial role of the foreshore slope in describing the wave overtopping in shallow water properly.

12.2.2.1. Empirical formulae

The predictive models inferred from the numerical analysis tend to underestimate the mean overtopping discharge, as shown in Figures 12.4 and 12.5. Thus, the double-power functions are here recalibrated to fit the

three laboratory datasets. It is worth specifying that the re-calibration phase only concerns the coefficient of the double-power formulae but not the dimensionless variables.

The following overtopping predictive models ensure estimating the flow rate at vertical seawall in shallow water. Specifically, the validity range is $0.2 \leq h_{TOE}/H_{m0,DEEP} < 4$.

❖ **Hypothesis 1**

For the first parametrization proposal, the re-calibrated predictive model (Figure 12.8) reads:

$$\frac{q}{g \cdot {H_{m0}}^* \cdot T_{p,N}} = min\left\{0.0033 \cdot \left(\frac{R_C}{\zeta_{1/4}} \cdot \gamma_{br}\right)^{-1.78}; 0.028 \cdot \left(\frac{R_C}{\zeta_{1/4}} \cdot \gamma_{br}\right)^{-3.44}\right\} \quad (12.1)$$

which has a R^2 statistic equal to 0.91.

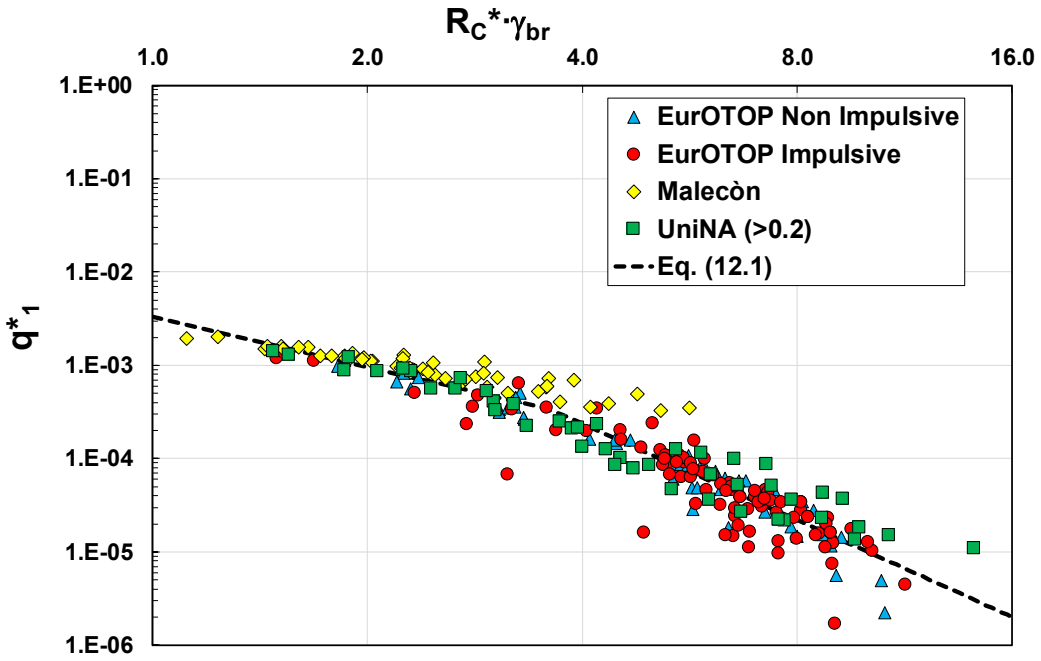

Figure 12.8 *– The three laboratory datasets fitted by the new predictive model (Eq. (12.1)).*

❖ **Hypothesis 2**

According to the second hypothesis of parametrization, the new predictive model (Figure 12.9) is:

$$\frac{q}{g \cdot h_{TOE} \cdot T_{p,N} \cdot m^P} = min\left\{0.011 \cdot \left(\frac{R_C}{\zeta_{1/4}} \cdot \gamma'_{br}\right)^{-1.56}; 0.0515 \cdot \left(\frac{R_C}{\zeta_{1/4}} \cdot \gamma'_{br}\right)^{-2.914}\right\} \quad (12.2)$$

with a R^2 statistic equal to 0.94.

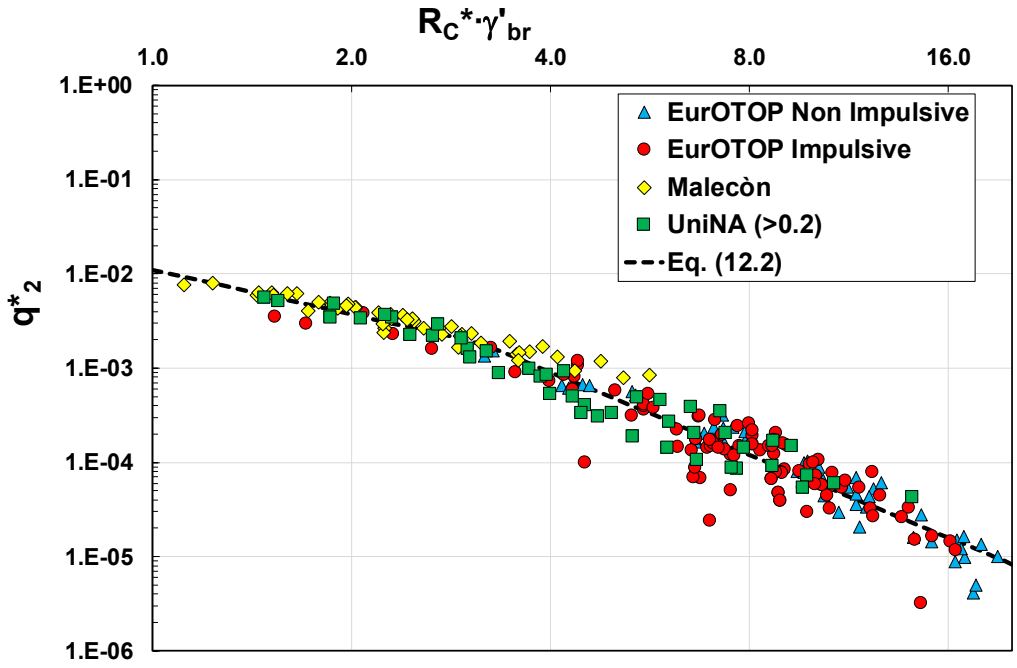

Figure 12.9 *– The three laboratory datasets fitted by the new predictive model (Eq. (12.2)).*

Overall, the new parametrization provides satisfactory results up to $R_C^* \leq 5$, while the envelope of data slightly increases for higher values. The reason of this behavior needs to be deepen in future research.

As specified above, these predictive model can be applied for vertical seawalls in shallow water with $h_{TOE}/H_{m0,DEEP}$ included between 0.2 and 4.

However, it should be noted that both the predictive models can be extended in more extremely shallow water conditions as long as the relative crest freeboard is lower than 5. In fact, the UniNA data with $h_{TOE}/H_{m0,DEEP} <$ 0.2 and $R_C/\zeta_{1/4} \leq 5$ lie within the cloud of the other laboratory data and follow the predictive models' trend fairly well.

Therefore, Eq. (12.1) or (12.2) may be a valid alternative to the overtopping model for seawalls with extremely shallow foreshores derived in Chapter 11. The latter, indeed, has been derived with few laboratory data; moreover, the effect of milder foreshore slopes has not been investigated. Thus, it brings along some uncertainties.

Furthermore, it is worth highlighting that the limit of $R_C^* \leq 5$ guarantees that Eqs. (12.1) and (12.2) are valid for the typical design ranges. Specifically, $R_C/\zeta_{1/4} = 5$ corresponds to $R_C/H_{m0,TOE} = 1.6$ when the wave setup is negligible (in deeper water); otherwise, as the seawall is located shoreward, as the limit value of $R_C/H_{m0,TOE}$ increases because of the wave decay and the wave setup growth.

13. THE WIND EFFECT ON WAVE OVERTOPPING PROCESS

The primary aim of this work was to analyze in depth the wave overtopping process of vertical walls in shallow water conditions. However, the comprehension of the phenomenon to a greater extent requires the analysis of secondary factors that can affect it. Among them, the onshore wind that blows during storms can significantly enhance wave run-up and overtopping, increasing the risk of coastal flooding and jeopardizing people and vehicles safety.

Hence, the present Chapter aims to assess the role of the wind on the mean overtopping discharge at vertical seawalls.

As indicated in the EurOtop Manual (2018), the influence of wind on green water overtopping is negligible, while it might increase by up to four times discharges of the order of 1 l/s/m, namely the order of magnitude of thresholds for structural and functional damages (e.g. EurOtop, 2018; Rock Manual, 2007). Therefore, the wind should be an essential variable to account for in the design of coastal defenses against flooding.

However, although researchers have been studying the influence of wind on wave overtopping since the end of the last century, the full understanding and correct assessment of its effects are still fraught with uncertainty. The lack of sufficient knowledge is due to shortcomings in the laboratory investigation and difficulties associated with field measurements. Physical models experience complications in studying a phenomenon that requires two different scale laws (i.e., Froude and Reynolds), while field measurements are limited to the local wave and wind conditions. On the other hand, numerical analysis has the advantage of avoiding scale effects associated with physical model experiments and of extending wave, wind and geometric characteristics investigated as compared to field tests.

This study, therefore, resorts to a numerical modeling of the phenomenon; the CFD numerical experiments performed in Di Leo (2021, PhD Thesis), along with SWASH experiments, have been analyzed. In particular, the Di Leo approach considered the wind through the shear stress it exerts on the sea surface. Analogously, this simplified wind modelling has been used in this work to perform the numerical analysis via SWASH. It is worth noting that, to the best of the author's knowledge, this non-hydrostatic model has never been used to study the influence of wind on wave overtopping.
The aim is twofold:

- to verify the ability of this simplified wind modelling to reproduce the influence of wind on the overtopping rate correctly;
- to clarify how the wind acts and how its effect on the enhancement of the overtopping rate changes depending on the overtopping regime.

Finally, by gathering numerical results along with laboratory data carried out by Durbridge (2021), a new predictive formula to estimate the wind effect on the mean overtopping discharge is provided.

13.1. Literature background

The impact on the overtopping process has been studied mainly through physical model experiments so far (e.g. Inagaki et al., 2024; Durbridge, 2021; Wolters and Van Gent, 2007; de Waal et al., 1996), although some numerical research has been published in recent times (Di Leo et al., 2022; Kiku and Kawasaki, 2014; Hieu et al., 2014).

Among the physical model studies, de Waal et al. (1996) used a paddle wheel to "push ahead" the water reaching the crest of a vertical wall. The authors observed that part of the breaker spray, which would have fallen back into the sea without wind, was blown over the structure instead. According to their findings, this effect can increase the mean overtopping discharge by a factor of 3.2. Wolters and Van Gent (2007) employed the same experimental approach and found a greater enhancement factor (about 6.2) for sloping structures than vertical walls.

Pullen et al. (2009) modelled the wind by setting up four fans in front of an upright structure; the results showed that the wind only affects discharge lower than 10 l/s/m approximately. Moreover, the authors gathered field and laboratory data to provide a predictive equation for estimating the influence of wind on wave overtopping, expressed as the wind transport factor f_{WIND} (i.e. the ratio of mean overtopping discharge with and without wind). Specifically, Pullen et al. related the wind factor to the overtopping regime, observing a variation between 1 (negligible effect of wind) and 4. However, they neglected the possible influence of other variables, such as wind speed.

More recently, Murakami et al. (2020) proposed a new equation based on laboratory experiments in which the wind factor is a function of wind speed, wave characteristics and the crest freeboard of the structure. However, it might underestimate the effect of wind since only the water flow on the seawall crown was taken into account (neglecting the advection of splash beside the structure due to the wind).

The effect of wind speed on the variation in flow rate has been subsequently corroborated by experiments conducted by Durbridge at the University of Plymouth to examine the response of a shallow water vertical seawall under both regular and irregular waves. Furthermore, Durbridge showed that high wind transport factors could occur even for an overtopping regime as high as 10 l/s/m.

Inagaki et al. (2024; 2023) performed a physical model experimental campaign to investigate the process's hydrodynamics. Using a wind tunnel along the flume allowed the study of the wind effects on both wave transformation and overtopping. The authors indeed observed that the presence of wind anticipates the onset of wave breaking, resulting in a greater energy dissipation that may reduce the flow rate. Furthermore, a Particle Image Velocimetry analysis showed that the wind enhances the overtopping discharge through a lift-up effect on the up-rushing jet along the wall and a shoreward transport effect over the structure as well.

As already mentioned, the literature has recently focused on numerical modelling of wind. Kiku and Kawasaki (2014) adopted the single-phase numerical model CADMAS-SURF to analyze the response of both vertical

and sloping walls, pointing out the role of wind speed on the flow rate growth. Analogously to the Di Leo (2021) approach, CADMAS-SURF accounts for the presence of wind via the shear stress on the water surface. On the other hand, Hieu et al. (2021) employed a two-fluids Navier Stokes model and observed that the wind field may significantly affect the wave profile. In particular, the authors found a maximum wind factor of 1.25, which is consistent with the CFD analysis findings of Xie (2014). Implementing a two-fluid approach, Xie studied the effect of wind on a breaking solitary wave. Results demonstrated that wind alters the air flow structure above the water, increases the generation of vorticity and turbulent stress, and affects the wave shoaling, breaking and run-up processes.

13.2. SWASH wind modeling

SWASH models the wind effect through the shear stress that transfers the momentum flux from wind to surface waves.

The wind stress depends on the drag coefficient and wind velocity relative to the wave celerity; it is expressed as:

$$\overrightarrow{\tau_s} = \rho_a C_D \left|\overrightarrow{U_{10}} - c\right| (U_{10} - c) \tag{13.1}$$

Concerning the drag coefficient, C_D, seven different formulations are available in SWASH (e.g. a constant value, a linear or a second order polynomial relationship between C_D and wind velocity). Among them, this study adopts a constant drag coefficient value.

According to Chen et al. (2004), a heterogeneous distribution of the wind stress over a wavelength allows the reproduction of wave growth due to the wind in a phase-resolving model. The wind stress may vary with a larger wind drag on the wave crest than that on the trough. Therefore, the wind stress is applied only on the wave crest.

13.3. Numerical experiments

The numerical experiments have been performed on the multi-slope Malecòn foreshore (see Section 6.1.4.) at the prototype scale. The next Sections will describe the characteristics of the experiments performed in Di Leo (2021) and the SWASH test program.

13.3.1. CFD tests

The work of Di Leo (2021) investigated the wind effect on the mean overtopping discharge of a vertical seawall. Hence, numerical experiments with and without the presence of wind were performed.

As mentioned above, the wind has been modelled introducing in the RANS equations the shear stress that it exerts on the sea surface. Assuming a logarithmic vertical distribution of the sea wind, the shear stress acting on the sea surface is typically estimated by:

$$\overrightarrow{\tau_s} = \rho_a C_{D10} |\overrightarrow{U_{10}}| U_{10} \tag{13.2}$$

where ρ_a is the density of air (1.225 kg/m3), U_{10} is the wind velocity at 10 m above the sea surface and C_{D10} is the wind shear coefficient (or drag coefficient). The latter was determined with predictive equation suggested by Andreas et al. (2012), namely:

$$\sqrt{C_{D10}} = \frac{0.239 + 0.0433 \cdot \{(U_{10} - 8.271) + [0.120 \cdot (U_{10} - 8.271)^2 + 0.181]^{0.5}\}}{U_{10}} \tag{13.3}$$

Obviously, since the drag coefficient varies with wind speed, the effects of the Reynolds number are theoretically accounted for.

According to the literature, the wind effect increases as the flow rate diminishes. Therefore, the crest freeboard was varied to obtain different order of magnitude of overtopping discharge (10^{-1} ÷ 10^{2} l/s/m). Specifically, seven different R_C were investigated, ranging from 2.23 to 9.27 m (Figure 13.1).
The analysis involved four different periodic waves; the wave height varied from 1.5 m to 8 m, and two wave periods (10 and 12 s) were analyzed. Specifically, three breaking waves and one non-breaking wave were examined.

The wind speeds implemented vary between 1.9 and 31.2 m/s. These values guarantee a sea age parameter β (i.e. deepwater wave celerity to wind speed ratio) between 0.5 and 9.86 (Table 13.1). The sea age ratio characterizes the wave condition under the action of wind (Bretschneider, 1964); in particular, values of β ranging from 0.5 to 1.25 represent seas under the dominant effect of tangential wind stress, while larger values (up to 10) characterize swells under weak winds.

The characteristics of the 34 experiments performed are reported in Table 13.2. Further details can be found in Di Leo (2021) and Di Leo et al. (2022).

Table 13.1 *– Wind speeds and relative sea age ratio simulated.*

T = 10 s		***T = 12 s***	
β [-]	**U_{10} [m/s]**	**β [-]**	**U_{10} [m/s]**
0.50	31.2	0.62	30.0
0.82	19.0	1.00	18.7
1.25	12.5	2.00	9.4
3.00	5.2	3.07	6.1
5.04	3.1	9.86	1.9

Table 13.2 - *Main features of the CFD experiments (Di Leo, 2021).*

H [m]	**T [s]**	**R_C [m]**	**β [-]**	**U_{10} [m/s]**
8.0	10	8.27, 9.27	0.5 ÷ 5.04	3.1 ÷ 31.2
8.0	12	2.23	0.62 ÷ 9.86	1.9 ÷ 30.0
5.4	10	2.23, 9.27	0.5 ÷ 5.04	3.1 ÷ 31.2
1.5	10	2.23 ÷ 9.27	0.5 ÷ 5.04	3.1 ÷ 31.2

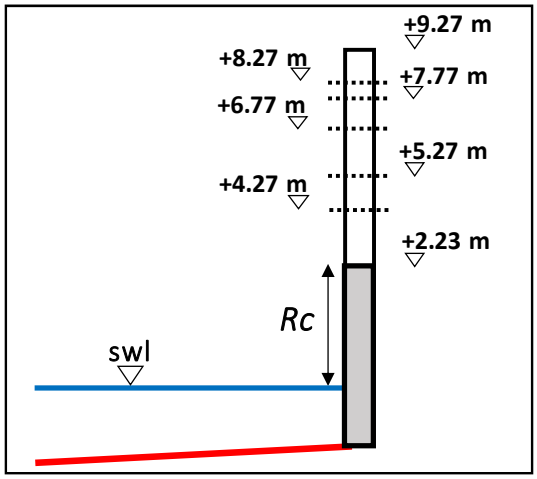

Figure 13.1 *– Crest freeboards value investigated in the CFD experiments.*

13.3.2. SWASH test program

The SWASH test program investigates the effect of the wind shear stress on the overtopping of monochromatic waves.

The program includes 23 experiments performed by varying wave conditions, crest freeboards and wind speeds. Analogously to the CFD analysis, the test program allowed the investigation of several orders of magnitude of the overtopping discharges ($10^{-2} \div 10^{2}$ l/s/m). Numerical experiments with and without the wind shear stress have been performed.

In particular, five periodic waves have been studied; the wave height varies between 0.6 and 5.4m, while the wave period has been kept constant (T=10s). Non-breaking wave conditions have been tested.
Two crest freeboards have been reproduced, namely R_C equal to 2.23 and 4.27m above the still water level. The wind conditions examined are those listed in Table 13.1. The drag coefficient in Eq. (13.1) has been determined according to the equation of Andreas et al. (Eq. (13.3)), which is one of the most recent and accurate formulations for the wind drag.

Table 13.3 summarizes the SWASH test program.

Table 13.3 - *Main features of the SWASH experiments.*

H [m]	T [s]	R_C [m]	β [-]	U_{10} [m/s]
1.5	10	2.23, 4.27	0.5 ÷ 3.0	5.20 ÷ 31.2
0.95	10	2.23	0.5 ÷ 3.0	5.20 ÷ 31.2
0.8	10	2.23	0.5 ÷ 1.25	12.5 ÷ 31.2
0.7	10	2.23	0.5 ÷ 1.25	12.5 ÷ 31.2
0.6	10	2.23	0.5 ÷ 1.25	12.5 ÷ 31.2

It is worth noting that SWASH analysis mainly focuses on seas under the dominant effect of tangential wind stress (low values of β).

For the numerical setup, refer to Section 6.1.4.1.

13.4. Results

13.4.1. Physical processes and basic definitions

As stated by the literature (de Waal et al., 1996; Resio, 1987), wind shear can affect wave overtopping either by raising the mean sea level or acting on the wave profile at the wall.

The effects on the wave profile encompass either the change in phase-averaged and time-domain wave properties (e.g., variation of the wave height and profile skewness), the deformation of the run-up wedge, or the onshore drift of the droplets produced during the up-rush process. The effect on the mean sea level includes wind and wave setups.

The amount of wind setup, , $\overline{\zeta_{WIND}}$, is governed by the cross-shore balance between the hydrostatic forces and the time-averaged wind stress, $\overline{\tau_w}$ (Dean and Darlymple, 2001):

$$\rho_w g[h\,(x) + \overline{\zeta_{WIND}}] \cdot \frac{d\overline{\zeta_{WIND}}}{dx} - \overline{\tau_w} = 0 \tag{13.4}$$

which can be integrated and parametrized in terms of the quantity:

$$A = (n \cdot \overline{\tau_w} \cdot l_D)/\rho_w g\, h_0^2 \tag{13.5}$$

where the variable A represents the shear to hydrostatic force ratio. In Eq. (13.5), $n \cong 1.5$ accounts for the effects of bottom friction, l_D is the domain's length and h_0 denotes the offshore water depth.

On the other hand, the effect on wave setup, $\overline{\zeta_{WAVE}}$, is related to a change in the radiation stress gradient caused by variation in the wave profile characteristics. According to (Longuet-Higgins and Stewart, 1962), the gradient is seawards for non-breaking waves, while it is directed towards the shore for breaking waves. Hence, a change in the breaking point due to the presence of the wind can produce a variation in $\overline{\zeta_{WAVE}}$; as the breaking point moves offshore the wave setup increases, and vice-versa.

13.4.1.1. On the role of the mean sea level

Despite the complexity of the processes that rule its variation in response to wind stress, the role of the mean sea level is subordinate in this study.

In fact, the length of the computational domain (l_D = 410 m) is too small for a significant wind setup to occur; indeed, the maximum wind speed investigated (U_{10} = 31.2 m/s) leads to a value of the parameter A equals $4.7 \cdot 10^{-4}$, indicating that the role of shear forces can be assumed to be negligible.

Concerning the wave setup, results are shown in Figure 13.2. The latter depicts the variation in the mean water level as a function of the profile variance ratio, $\sigma^2_{WIND}/\sigma^2_{NO\ WIND}$, which represents the wind effect on wave energy and, hence, it is proportional to the variation of the radiation stress.

Figure 13.2a shows that the variations of $\bar{\zeta}$ for non-breaking waves correlate reasonably well with $\sigma^2_{WIND}/\sigma^2_{NO\ WIND}$; values of the ratio lower than unity implies a reduction in dS_{xx}/dx, which, being seawards, leads the mean water level to increase (less set-down).

For breaking waves, the radiation stress gradient reverses, and so does the relationship between $\bar{\zeta}$ and $\sigma^2_{WIND}/\sigma^2_{NO\ WIND}$ (Figure 13.2b); this is except for two outliers circled in the figure, for which $\bar{\zeta}$ reduces due to a reforming/re-breaking process that occurs in the innermost part of the foreshore (not shown here for the sake of brevity).

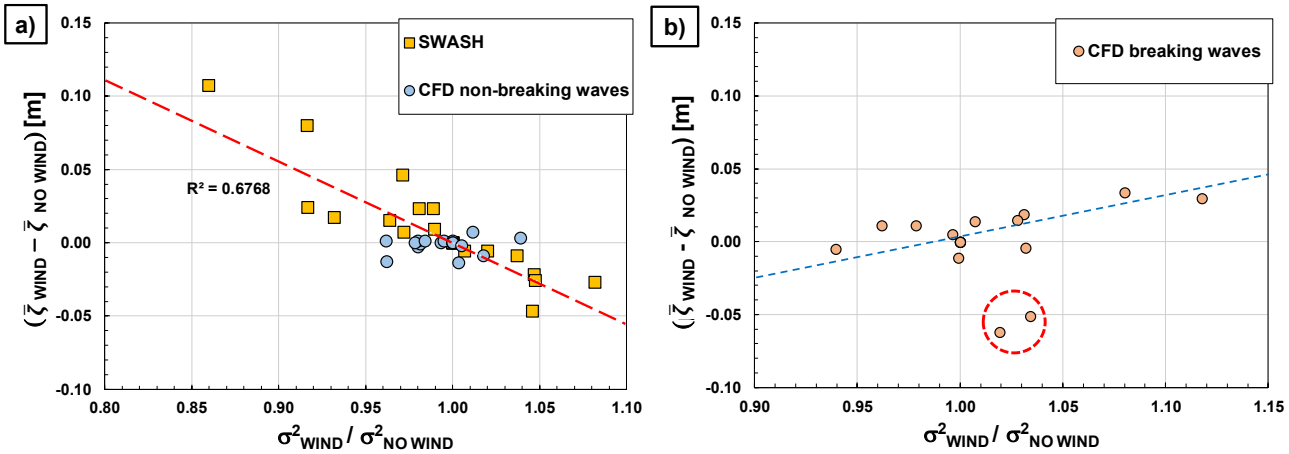

***Figure 13.2** – Variation of the mean sea level as a function of the variance ratio; panel a) refers to the non-breaking waves, while panel b) plots the results of the breaking waves.*

However, besides the tough previous analysis, it can be concluded that the observed variations of the mean sea level are too small to have a significant effect on the mean overtopping discharge. Indeed, the maximum variation is nearly 0.10 m, corresponding to 4.5% of the minimum crest freeboard $R_C = 2.23$ m. A further proof will be shown in Section 13.4.3.

13.4.1.2. Wind Stress, Wave Profiles and Overtopping Rates

It is worth noting that the results discussed in the present Section were produced with the CFD numerical model only. As will be shown later, SWASH does not allow a proper assessment of the wind effects from wave profile characteristics.

For non-breaking waves, Figure 13.3 shows that the wind enhances the run-up wedge and pushes forward the droplets that otherwise would fallen back into the sea (see panel a) vs. panel b)); such behavior is consistent with the wind effects observed by Kiku and Kawasaki (2014). Therefore, the presence of wind can cause an overtopping event that would not otherwise have occurred (Figure 13.3c).

On the other hand, the scenario may be different with breaking waves. As shown in Figure 13.4, in some cases the presence of wind may reduce the overtopping rate. As observed by the literature (Inagaki et al., 2024; Perlin et al, 2013), the wind brings forward the onset of wave breaking (see Figure 13.5 that refers to the

numerical data circled in green in Figure 13.4); the greater the surf zone, the greater the energy dissipation, which eventually results in a lower amount of wave overtopping. However, this is not a systematic behavior. A reduction in wave overtopping has not been observed for all breaking waves investigated. Indeed, as the order of magnitude of discharge reduces, the wind enhances the overtopping rate both for breaking and non-breaking waves, as can be appreciated in Figure 13.4.

Finally, Figure 13.4 demonstrates that higher wind velocities do not always produce a greater increase in the overtopping rate. This result is consistent with Inagaki et al. (2023) and Ward et al., (1996), that have found that the overtopping rate does not increase monotonically with the wind speed.

Furthermore, consistent with the literature (EurOtop 2018; Pullen et al. 2009; de Waal et al. 1996), the wind shear stress analysis confirms that the influence of wind is negligible for green wave overtopping (i.e. $q_{NO\ WIND}$ larger than 10^2 l/s/m).

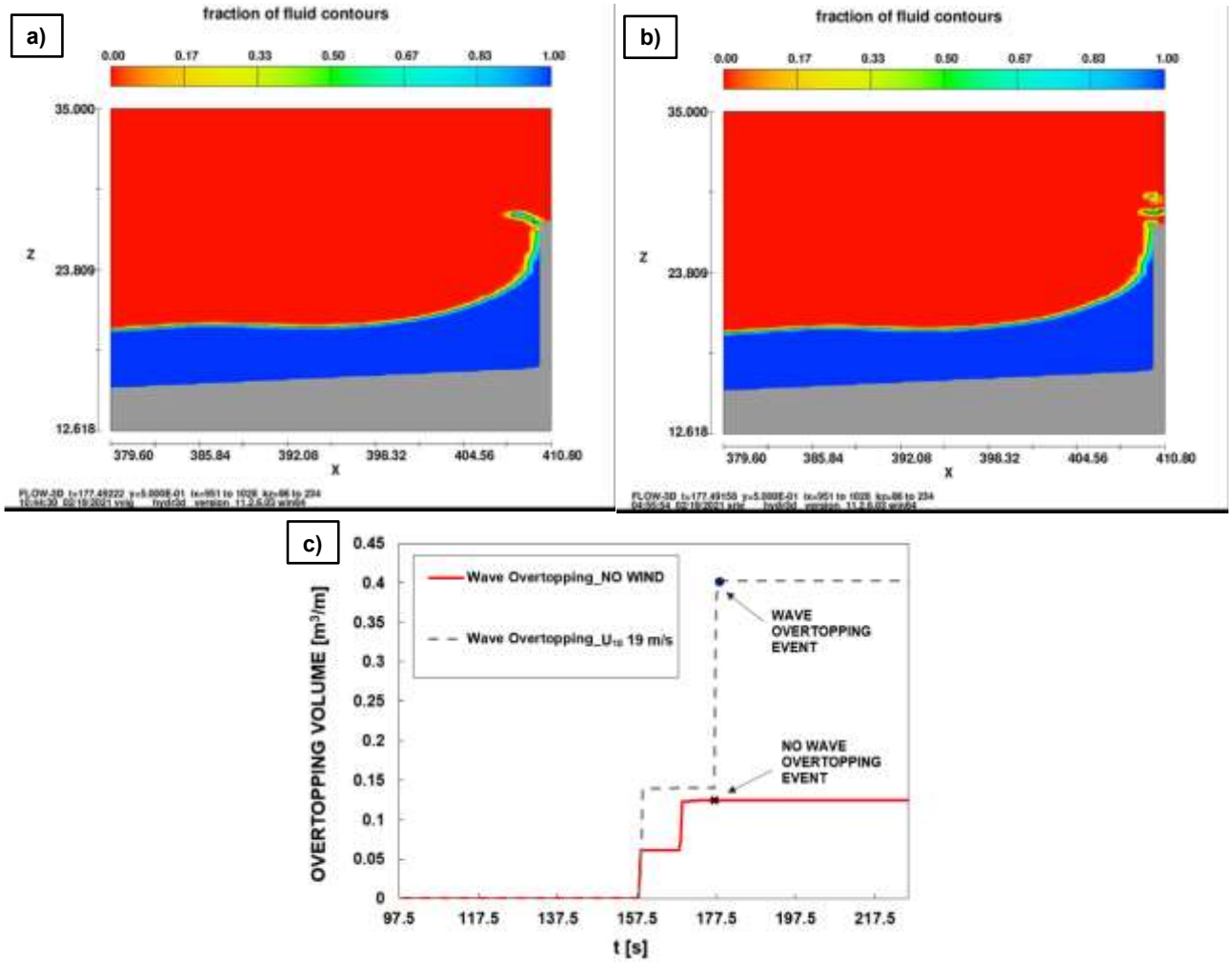

Figure 13.3 *– Effects of the wind either on the run-up wedge or on the advection of the droplets behind the seawall in case of non-breaking wave. Panel a) no wind condition; panel b) wind U_{10}=19.0 m/s; panel c) comparison between cumulative overtopping volume curves with and without wind.*

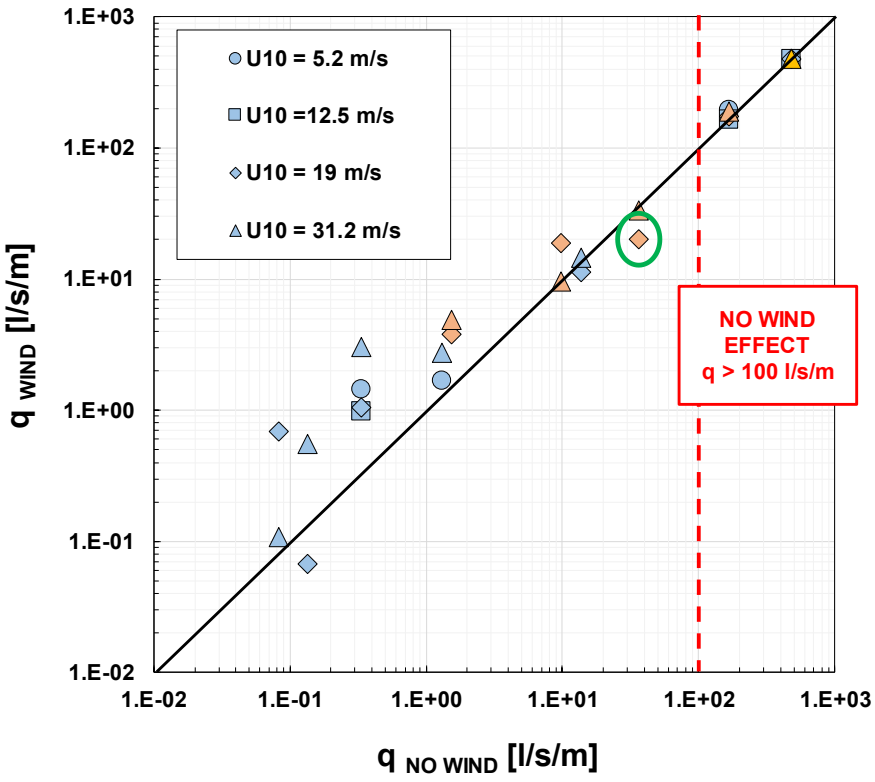

Figure 13.4 *– Comparison between CFD flow rates with and without wind; blue data refer to non-breaking waves, while orange data refer to breaking waves.*

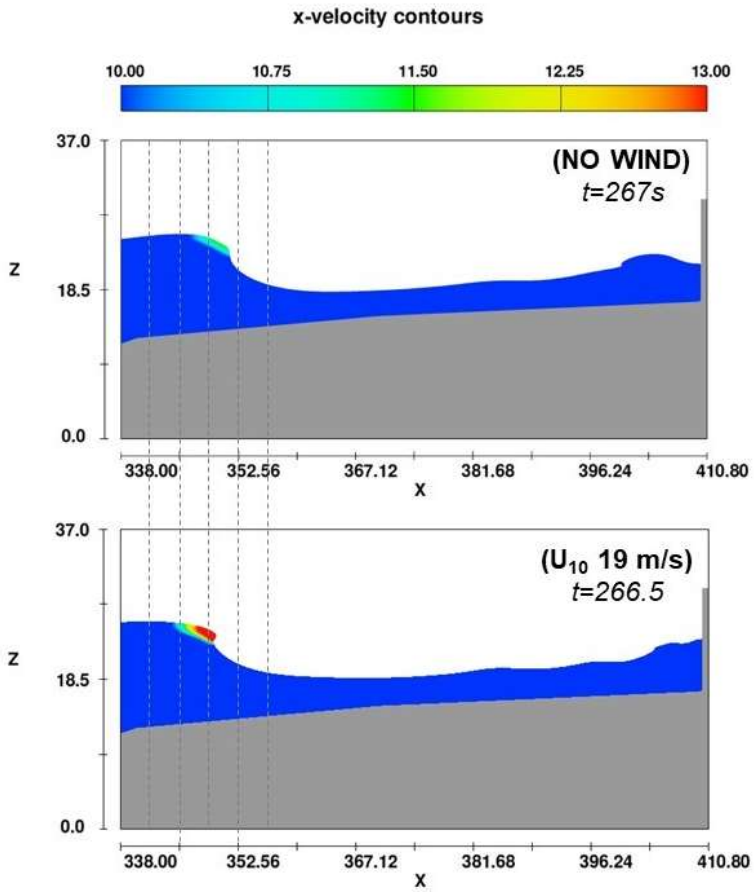

Figure 13.5 – *Variation in the onset of wave breaking due to the effect of the wind shear stress.*

Hence, numerical analysis suggests that the influence of wind on the overtopping process depends on the amount of the flow rate. This result has been explored by comparing three different orders of magnitude of discharges, namely 10^2 l/s/m, 10^0 l/s/m and 10^{-1} l/s/m, in order to understand the mechanisms that role the interaction wind-wave overtopping.

Figure 13.6 illustrates the wind effect on green water overtopping ($q_{NO\ WIND} > 10^2$ l/s/m). Negligible differences appear in the horizontal velocity and thickness of the overtopping layer when comparing wind and no wind conditions. The wind effect seems to be negligible as compared to the momentum of overtopping water, so that the mean overtopping discharge is not influenced by the wind.

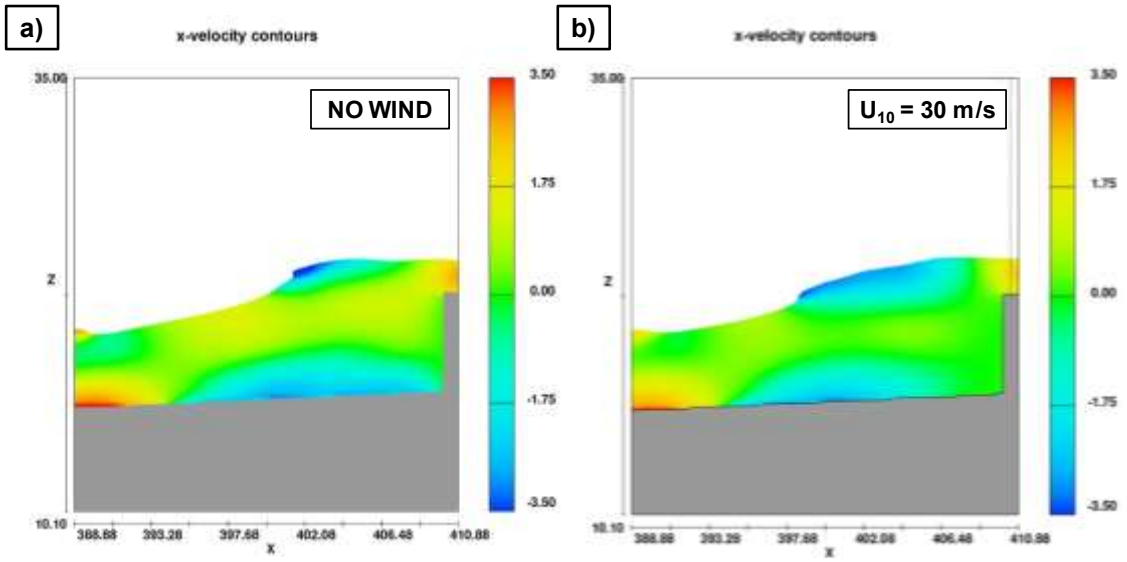

Figure 13.6 *– Influence of the wind on green wave overtopping; panel a) and b) shows an overtopping event with and without the presence of the wind, respectively.*

On the other hand, for a mean overtopping discharge of the order of 10^0 l/s/m, the comparison in Figure 13.7 shows that the wind effect cannot be neglected. The wind stress leads to a greater height of the up-rushing jet, with a difference of about 0.3 m (the water spray was not considered); moreover, unlike the no wind condition (Figure 13.7a), the fluid stream and the water spray were characterized by a shoreward velocity (Figure 13.7b), which ensured that the water crossed the wall instead of falling back into the numerical flume. Thus, the presence of wind increased the overtopping rate by inducing a greater height of the up-rushing jet and by transporting water spray over the seawall.

Still reducing the discharge to 10^{-1} l/s/m, for the "white" overtopping dynamics, the main overtopping mechanism seems to be the advection of the spray by the wind. In fact, as shown in Figure 13.8, the overtopping occurred when the spray crossed the seawall. The water spray may be carried over the wall under its own momentum without wind that otherwise falls back into the sea (Figure 13.8a). Onshore wind, on the other hand, significantly increases the amount of water that crosses the wall (Figure 13.8b) and thus plays a key role in the overtopping process. The difference between wind and no wind conditions is remarkable.

Therefore, the role of the wind becomes crucial as the flow rate diminishes.

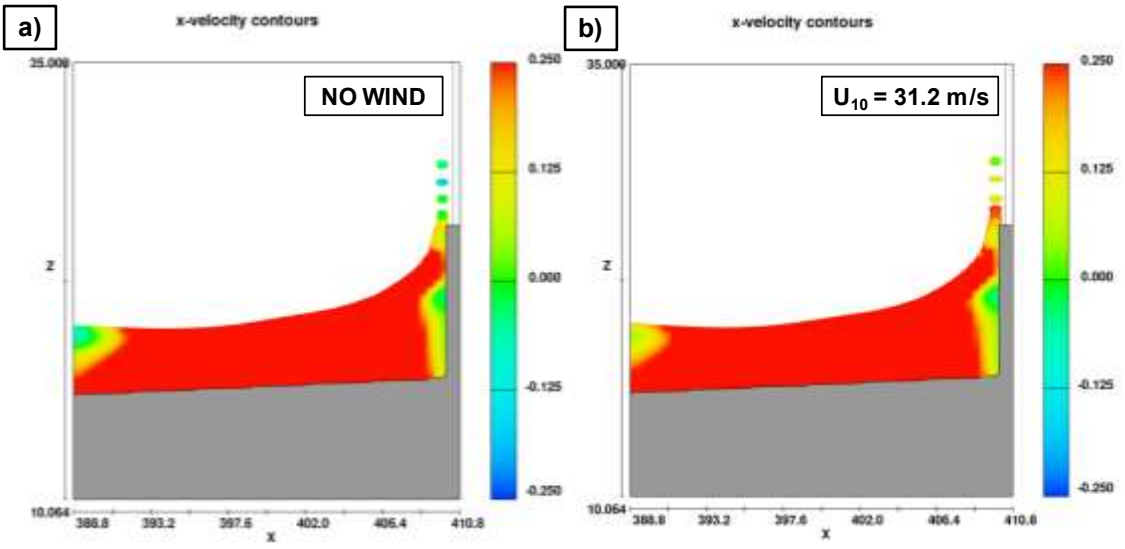

***Figure 13.7** – Influence of a mean overtopping discharge of the order of 10 l/s/m; panel a) and b) shows an overtopping event with and without the presence of the wind, respectively.*

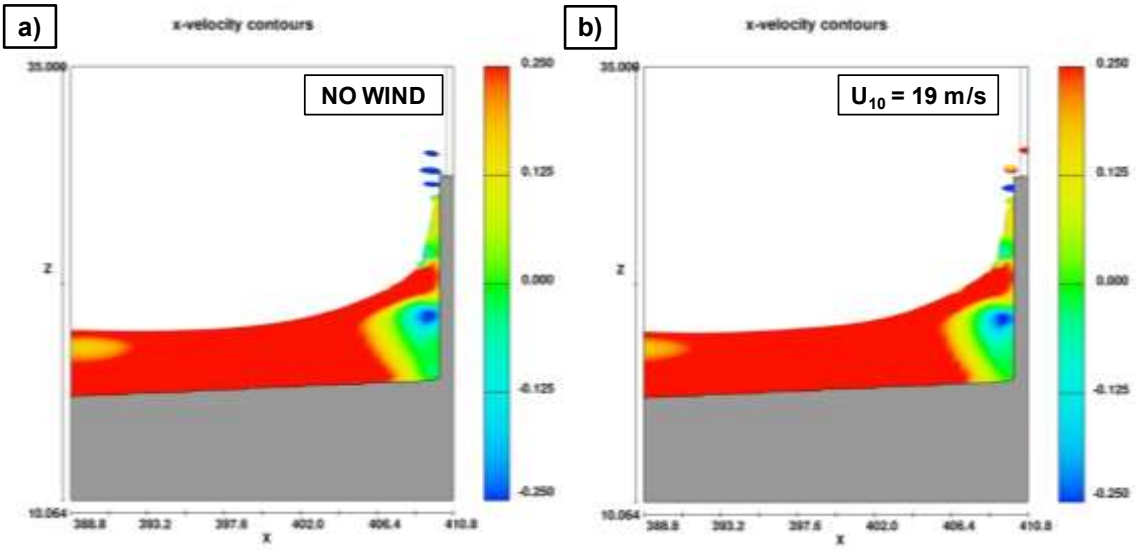

***Figure 13.8** – Influence of a mean overtopping discharge of the order of 1 l/s/m; panel a) and b) shows an overtopping event with and without the presence of the wind, respectively.*

13.4.2. Numerical experiments vs Pullen et al. physical model data

In Figure 13.9, numerical results carried out with FLOW-3D and SWASH are compared with the laboratory data reported in Pullen et al. (2009), which has investigated a quite similar range of wind speed (i.e., 15, 26 and 28 m/s).

FLOW-3D and SWASH confirm that the wind has no effect on the "green water" overtopping regime, as observed above.

On the other hand, the influence of the wind increases when the flow rate decreases. The CFD model reproduces this behavior well; its data spread within the same cloud as the laboratory data, though the

numerical outcomes appear to be somewhat more scattered (Figure 13.9). Thus, physical and CFD results are in good agreement, even though Pullen et al. only investigated the wind effect in front of the seawall (i.e., only the convective transport over the wall).

Conversely, SWASH is unable to reproduce the wind effect on the lower overtopping discharges. Analyzing different orders of magnitude of q, the effect of wind appears always negligible – an increase in discharge has not been observed (Figure 13.9). The slight variations in q_{WIND} indicated that the results were affected by the wind stress term, but not appropriately. SWASH appears unsuitable for reproducing the phenomenon dealt with in this study. This is probably due to the its structure since it is a depth-integrated model that cannot simulate the water separation phase in front of the wall. Therefore, it does not reproduce the increase in the overtopping rate due to the wind typical of the lower overtopping regime, where the spray blown over the wall is the predominant mechanism.

Thus, the quantitative analysis discussed in the next Section evaluates only the CFD data.

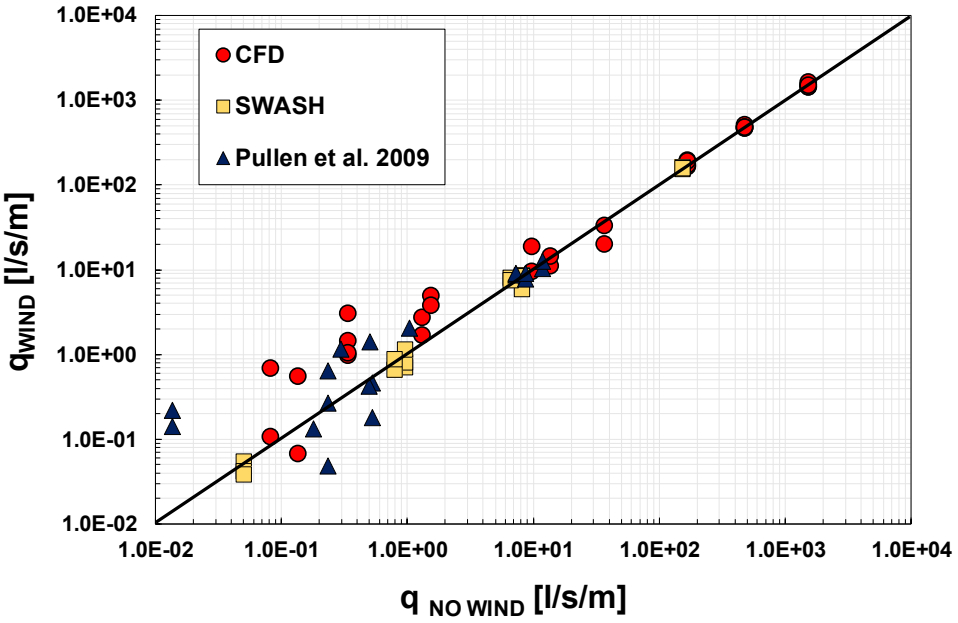

Figure 13.9 – *Numerical vs. laboratory flow rates (Pullen et al., 2009) obtained with and without wind.*

13.4.3. The wind transport factor

The wind factor quantitatively expresses the influence of wind on the mean overtopping discharge:

$$f_{WIND} = \frac{q_{WIND}}{q_{NO\,WIND}} \tag{13.6}$$

As mentioned in Section 13.1, Pullen et al. (2009) gathered laboratory and field measurements to provide a predictive formula for estimating the wind factor, that reads:

$$f_{WIND} = 1 + 3\left(\frac{-\log q_{NO\ WIND} - 2}{3}\right)^3 \tag{13.7}$$

According to the author, the validity range of Eq. (13.7) is $10^{-2} \div 10^{1}$ l/s/m.

Figure 13.10a shows the numerical wind factors as a function of q; the Pullen et al' formula is plotted as well. Similar to Eq. (13.7), numerical outcomes follow a decreasing trend with increasing overtopping discharge while remaining close to unity at higher rates.

Breaking and non-breaking waves appear to behave similarly, even if some breaking data lie above the non-breaking points.

The observed scatter is not surprising, since the wind factor is essentially controlled by the number of droplets produced during the up-rush phase, which is a highly random process. Since the incoming wave trains are identical with and without the wind (both in the frequency and time domains), the inherent uncertainty related to the overtopping phenomenon has likely a negligible impact on the observed results (Romano et al., 2015).

However, two main differences can be appreciated: CFD data provide a maximum value of f_{WIND} of 9 compared to 4 suggested by Pullen et al.; and, according to Eq. (13.7), the effect of wind may already be negligible at an overtopping discharge of 1 l/s/m, while the CFD results indicate a strong influence of wind even for larger rates.

It is worth highlighting that the observed behavior is practically independent of the variations in the mean water level due to the wind, as discussed in Section 13.4.1.1. In fact, Figure 13.11 clearly demonstrates that the largest values of the wind factor are attained when the wind effect on the mean sea level is negligible.

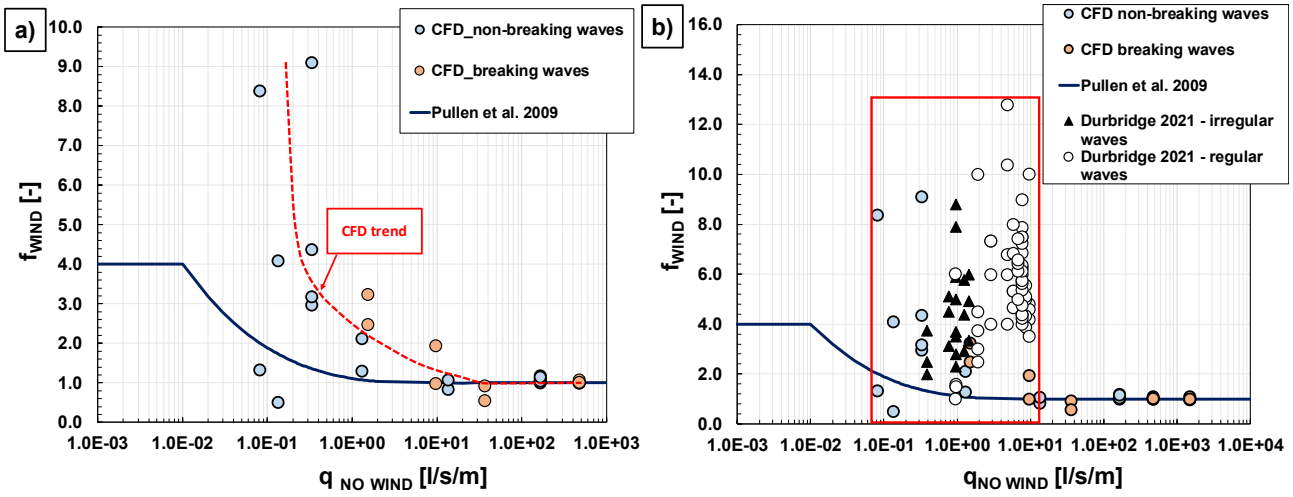

Figure 13.10 *– The wind factor as a function of the mean overtopping discharge. Panel a); CFD data vs Pullen et al.' formula; panel b): numerical and physical results obtained by Durbridge (2021) compared to the Pullen et al.' formula.*

In Figure 13.10 b, the laboratory data of Durbridge (2021) have been shown as well. The experiments were conducted at Plymouth University, where the author investigated random and periodic 2D-tests, at the scale of

1:21, on a shallow foreshore vertical seawall. Conversely to CFD experiments, the laboratory test examined the effect of wave frequency, analyzing regular and irregular waves, while the structure's freeboard and the offshore wave height were kept constant.

Nevertheless, numerical and physical results are consistent, showing a significant influence of the wind also for values of discharge of the order of 10 l/s/m. Moreover, the maximum measured f_{WIND} is of the order of 10. This results indicates the need for new predictive equations, which include more variables than the sole mean overtopping discharge.

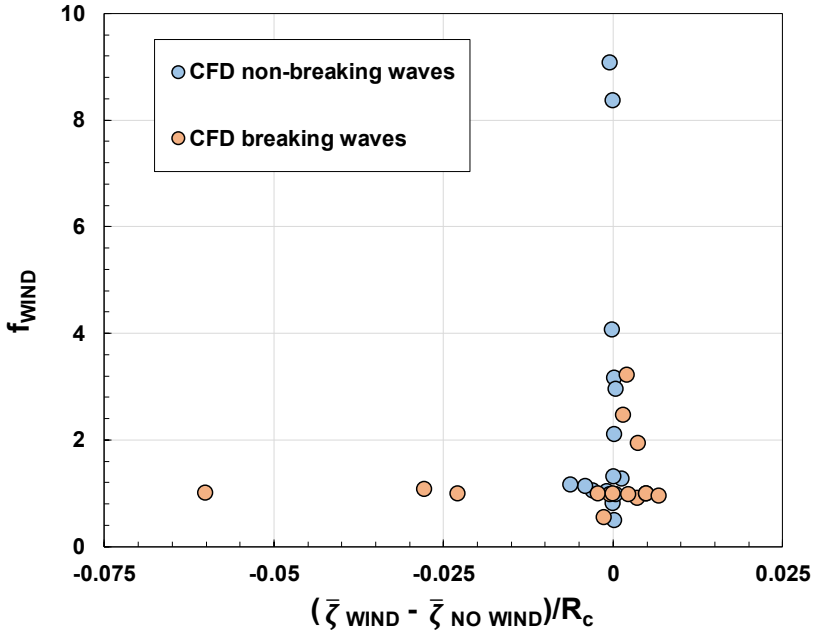

Figure 13.11 *– CFD wind factor as a function of the ratio between the variation in the mean sea level due to the wind and the crest freeboard.*

Hence, by gathering numerical and Durbridge's experimental data, a new predictive formula has been derived (Figure 3.12):

$$f_{WIND} = 1 + 0.00037 \cdot \max\{0.001, q^*\}^{-1.062} \; S_{s-a} \tag{13.8}$$

where q^* is the non-dimensional overtopping discharge and S_{s-a} is the shallow water sea age:

$$q^* = \frac{q}{\sqrt{gH_0^3}} \tag{13.9}$$

$$S_{s-a} = \frac{U}{\sqrt{gh}} \tag{13.10}$$

The expression above essentially relates the wind correction factor to the probability of occurrence of water droplets during the overtopping events. The presence of droplets clearly reduces with increasing the relative flow rate q^* (when the overtopping regime tends to "green overtopping") as well as with increasing water

depth. Oppositely, wave breaking occurrence in shallow water increases the generation of droplets, which explains the use of shallow water celerity $\sqrt{gh}$. Finally, the higher the wind speed the higher the wind factor.

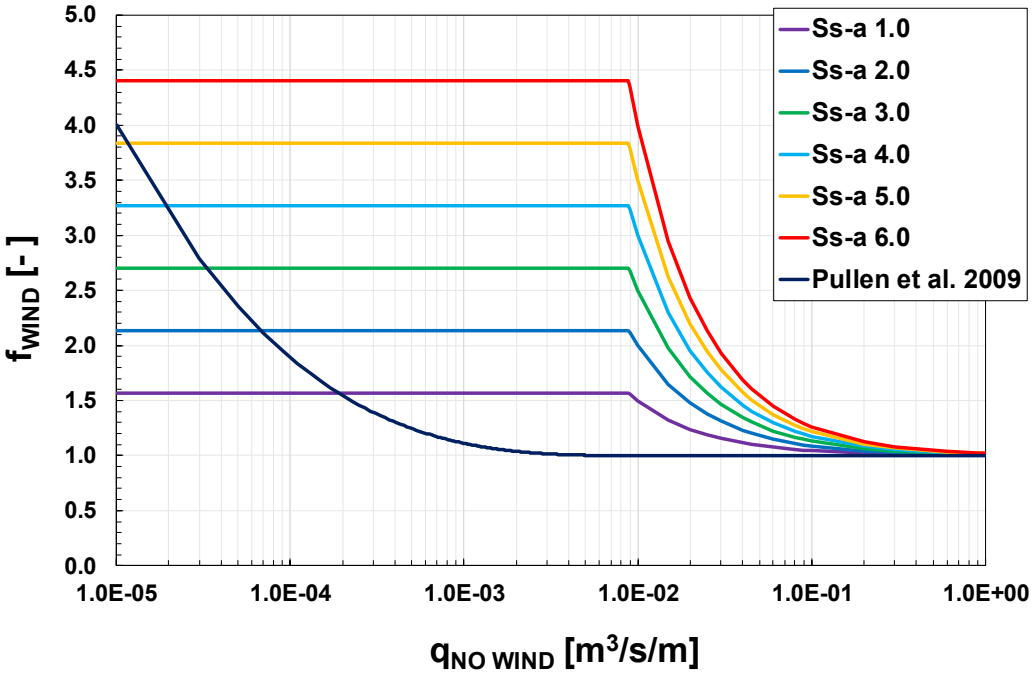

***Figure 13.12** – The new wind factor formula proposed, Eq. (13.8) compared to that of Pullen et al. (2009).*

Figure 13.13 shows calculated and measured wind factors; Eq. (13.8) has an R^2 statistics of 0.5 and is significant at a level of 5%. A low value of R^2 is not surprising since the process which governs the formation of droplets is highly random.

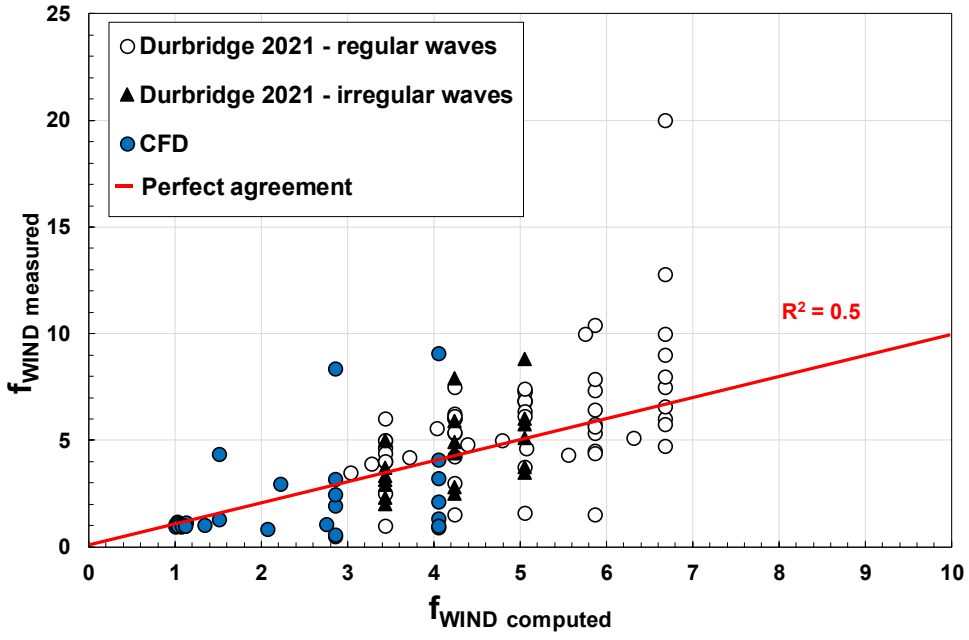

***Figure 13.13** – Computed vs- measured wind factors.*

Although the numerical data used to infer Eq. (13.8) derive from rough modelling (single-fluid approach), its reliability has been confirmed by comparing computed wind factors with those of Hieu et al. (2014). The latter were obtained by performing numerical experiments with the two-fluid technique. As further evidence of the ability of the single-fluid approach to reproduce the enhancement of the mean overtopping discharge due to the wind correctly, Figure 13.14 indeed shows that results are quite close to the perfect line of agreement.

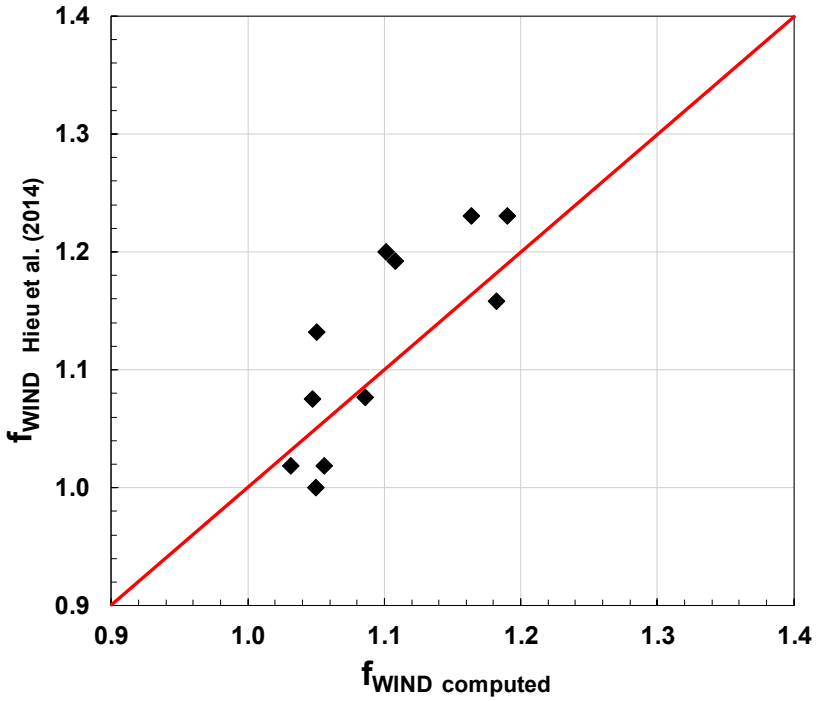

***Figure 3.14** – Comparison between wind factors estimated using Eq. (13.8) and those obtained by Hieu et al. (2014).*

13.5. Summary

The main purpose of this Chapter was to analyze the influence of the wind on wave overtopping at vertical seawalls in shallow water.

Simplified numerical modelling has been adopted to pursue this aim. In particular, a single fluid RANS model and the SWASH model have reproduced the presence of the wind by means of the shear stress that it exerts on the sea surface.

Hence, it was firstly verified the ability of simplified numerical models to capture the macro-processes involved in the phenomenon of wave overtopping in the presence of onshore wind; then, numerical results were exploited to understand the wind mechanism of action in increasing the mean overtopping discharge.

As general result, numerical analysis demonstrated that the application of wind stress induces negligible variations in the mean water level since the numerical flume employed measures only 410 m in length. Hence,

the process under study is essentially governed by the effects the wind shear exerts on the wave profile. These include:

- Deformation of the run-up wedge;
- Advection of the droplets formed in the uprush phase;
- Variation in the breaking point with wind.

The CFD RANS model was found to address all the above processes realistically.

CFD experiments have shown that the wind stress gives rise to higher up rushing jets, and pushes forward the water spray that would otherwise have fallen back into the sea. This can be considered one of the leading mechanisms for the increase of the overtopping rate by wind.
Concerning the effect of wave breaking, results suggest that it should be considered with some caution. On the one side, breaking waves may lead to larger wind enhancement factors by augmenting the number of droplets available for advection; however, as the wind moves the breaking point seawards, there might be a reduction in the overtopping volume as a consequence of the larger dissipation of energy.

Overall, the effect of wind increases with reducing the overtopping regime; this can be explained by the fact that the influence of the droplets' advection on the mean overtopping rate increases with reducing q. Despite Pullen et al. (2009) already pointed out this behavior, numerical data differ from their model in two essential points: numerical wind factors reach a value of 10 rather than a maximum of 4 assumed by Pullen et al., and the effect of wind does not vanish for overtopping discharges of the order of 1 l/s/m but persists for higher regimes. Laboratory data of Durbridge (2021) confirm these numerical findings.

On the other hand, numerical results carried out via SWASH show that it is probably unsuitable for reproducing the influence of the wind. The non-hydrostatic model does not reproduce the flow rate enhancement even with lower overtopping regimes. This is probably due to the structure of SWASH, which is a depth-integrated model that cannot simulate the water separation phase in front of the wall. Therefore, it does not reproduce the increase in the overtopping rate due to the wind typical of the lower overtopping regime, where the spray blown over the wall is the predominant enhancement mechanism.

Finally, by gathering numerical and physical experimental data (Durbridge, 2021), a new predictive equation was proposed to quantify the effect of the wind on the mean overtopping discharge. The new formula relates the wind factor to the mean overtopping discharge, the wind speed and the water depth.
It is worth commenting that the low correlation coefficient of the predictive model ($R^2 = 0.5$) is mainly due to the remarkable scatter related to the inherent randomness of the wind enhancement process, rather than to the wave overtopping phenomenon. The latter indeed may suffer from laboratory effects, measurement issues (at low rates) and time-domain differences among the wave series (Romano et al., 2015); however, none of the previous cases applies to the present numerical experiments.

14. CONCLUSIONS AND FUTURE DEVELOPMENTS

The present Thesis analyzed in depth the wave overtopping of seawalls in the surf-zone. Although this coastal process has fascinated and involved coastal scientific and engineering communities since the middle of the last century, a critical review of the literature has revealed that our knowledge about the overtopping of seawalls in shallow water is still rough and unaccomplished. In particular, a closer inspection of the literature database (i.e. CLASH) showed that a few reliable data are available on the overtopping of vertical walls in the surf zone. Therefore, the design process of these evergreen sea defense structures is affected by some uncertainties that may threaten seawalls' efficacy in protecting coastal zones from flooding risks.

The work, hence, moves from these shortcomings and aims to offer a deeper insight into the physics of the phenomenon. To pursue these objectives, the results of laboratory and numerical investigations are exploited. In particular, numerical experiments adopt two approaches that differ in the degree of complexity and computational time: CFD-RANS and SWASH.

The joint analysis of numerical and laboratory data of Chapter 6 has shown that both the phase-resolving models capture, to a good extent, the physical processes (despite different levels of accuracy) and, thus, can significantly contribute to extending our comprehension of the wave overtopping in the surf-zone.

This study firstly analyzed the laboratory data of an experimental campaign carried out at the University of Naples Federico II that examined the overtopping of the Malecòn Tradicional, the seawall that protects La Habana city (Cuba). The laboratory experiments have been numerically reproduced the non-hydrostatic model SWASH and the CFD-RANS model FLOW-3D.

The results analysis revealed that, contradictory to the literature assumption, the energy distribution in the frequency domain has not a crucial role in the wave overtopping process; the influence of the harmonic spectral period seems result from a spurious correlation due to the mutual relationships between spectral moments within the surf zone, as shown in Section 6.3. Specifically, T_{m-10} affects wave overtopping by virtue of the relationship between the flow rate and wave energy at the toe of the structure; the influence of the spectral period exists as long as its mutual relationship with the wave energy exists.

This unexpected result has been further confirmed via a statistical analysis performed in Chapter 7 on the run-up and overtopping laboratory data of Van Gent (1999b), which is the work that crowned T_{m-10} as the characteristic wave period in describing wave-structure interaction processes. It is worth noting that the influence of the wave period on wave-structure interaction processes is undoubted, as stated by the literature and observed in this work, but differs from the influence of T_{m-10}.

Nevertheless, questioning the role of T_{m-10} does not signify that the energy at low-frequency components (i.e. IG-waves) has no impact on the mean overtopping discharge. Indeed, the total variance of the wave process accounts for it.

On the other hand, the joint numerical and laboratory analysis of the Malecòn experiments pointed out the crucial role of the wave setup in the overtopping process within the surf zone, although the literature has treated it with some ambiguity.

Actually, the flow rate depends on a certain water level statistic at the toe of the wall. Therefore, the new hydraulic variable has been introduced, $\zeta_{1/4}$, which represents the average of the highest one-fourth of water levels in a Gaussian wave process. From a physical point of view, this result expresses the simple concept that the amount of wave overtopping cannot depend solely on the variance of the wave fluctuations but rather on the upper tail of the distribution.

Such a relationship is physically consistent with the approach of many authors in literature who relate overtopping rates and extreme run-up heights. However, the new hydraulic variable is much simpler to estimate compared to extreme run-up statistics. Indeed, for a Gaussian wave process, $\zeta_{1/4}$ can be easily derived from the mean wave setup and wave energy, and thus, by using simple empirical formulae or phase-averaged numerical models that inherently account for the effects of surf beats.

Consequently, the work attempted to provide a new overtopping model based on this hydraulic variable. To this end, an extensive parametric study descried in Chapters 8-9 has been carried out with the non-hydrostatic model SWASH, which has been employed as an explorative tool for a deeper comprehension of wave overtopping of seawalls in shallow water conditions. Indeed, SWASH has proved to be capable of reproducing the physics of coastal processes satisfactorily.

Furthermore, using a numerical model allowed the experimental conditions to vary smoothly, thus creating a wide and varied dataset and avoiding the typical limitations of laboratory experiments. It is worth mentioning that the numerical experimental campaign focuses on the wave overtopping of random sea states characterized by a wave steepness of about 0.035, so representing the typical wind-sea conditions. Nevertheless, different wave steepness values have been investigated during the physical experimental campaign.

The numerical analysis led to a new parametrization proposal, which has been developed according to two different hypotheses: the first is based on a more theoretical approach rather than the empirical character of the second one. Nevertheless, both of them account for the physics of the process.

Overall, the new parametrization includes the main variables involved in wave overtopping, such as the new hydraulic variable, $\zeta_{1/4}$, the deep water peak period, the relative crest freeboard and the water depth at the toe of the wall, and the foreshore slope. Particularly, the seabed slope's effect seems crucial for overtopping in very shallow water. Therefore, further numerical experiments have been performed to identify an equivalent slope necessary when natural beaches with irregular bathymetries are involved (Chapter 9).

Finally, a new generalized formula has been inferred from the numerical data to estimate the mean overtopping discharge of walls with different foreshore conditions, i.e. from shallow to extremely shallow waters.

The numerical findings have been verified against 270 laboratory data from different datasets, encompassing the EurOtop reliable data, the Malecòn and the UniNA experiments (Chapter 12). In particular, the UniNA dataset includes 70 physical model tests performed in this work to examine the wave overtopping of seawalls with very and extremely shallow foreshores and fill the void found in literature (as shown in Chapter 10).

The laboratory data corroborated the numerical findings and showed many interesting peculiarities of the parametrization proposed in this work. Specifically, the new dimensionless variables lead to a remarkable reduction in the data scattering compared to the EurOtop parametrization. Furthermore, unlike the literature statement, impulsive and pulsating wave conditions follow a unique trend; any difference appears between the overtopping of impulsive and pulsating waves. Overall, the laboratory data follow a unique trend, exhibiting a uniform behavior. These significant improvements indicate the large explanatory power of the new dimensionless variables.
Finally, the generalized predictive model (Eqs. (12.1) or (12.2)) derived from the numerical analysis has been re-calibrated according to the laboratory data, valid for both breaking and non-breaking waves.

It is worth pointing out that the laboratory data in extremely shallow water conditions ($h_{TOE}/H_{m0,DEEP} < 0.2$) exhibited a slightly different behavior (as observed in Chapter 11), and the generalized overtopping formula can be used as long as the relative crest freeboard, R_C^*, is lower than 5. Otherwise, an alternative overtopping model for seawalls in extremely shallow water has been proposed alternatively (Eqs. (11.4) or (11.5)). However, it should be used with extreme caution; indeed, this alternative formula derives from a few physical model tests carried out with a single value of the foreshore slope.

Therefore, further research is necessary to investigate in depth the wave overtopping of seawalls with extremely shallow foreshores in order to confirm the findings of this study and evaluate the influence of the seabed slope. In addition, the overtopping model proposed should be validated with a larger dataset.

Furthermore, the analysis should be extended towards lower values of the relative crest freeboard and seawalls located on the land (with an emerged toe), broadening our knowledge of wave overtopping at vertical seawalls.

The last phase of this study focused on the wind effect on wave overtopping at vertical seawalls in shallow water (Chapter 13). Indeed, although researchers have been studying the influence of wind on wave overtopping since the end of the last century, the full understanding and correct assessment of its effects are still uncertain.
Hence, the analysis of numerical investigations allowed us to understand the wind mechanism of action in increasing the flow rate.
Finally, by gathering numerical and physical experimental data, a new predictive equation has been proposed to quantify the effect of the wind on the mean overtopping discharge (Eq. (13.8)). The new formula relates the

wind factor to the mean overtopping discharge, the wind speed and the water depth. New laboratory experiments should be performed to validate this empirical formula.

REFERENCES

Ahrens, J., 1977. Prediction of Irregular Wave Overtopping, CETA 77-7, US Army Engineer Waterways Experiment Station, Coastal Engineering Research Center, Vicksburg, Miss.

Akbari, H., 2017. Simulation of wave overtopping using an improved SPH method. Coast. Eng. 126, 51–68 https://doi.org/10.1016/j.coastaleng.2017.04.010.

N. W. H. Allsop, P. Besley and L. Madurini, 1995. Overtopping performance of vertical and composite breakwaters, seawalls and low reflection alternatives, Paper 4.7 in MCS Project Final Report, University of Hannover.

Allsop, W., Bruce, T., Pearson, J., Besley, P., 2005. Wave overtopping at vertical and steep seawalls. In Proceedings of the Institution of Civil Engineers-Maritime Engineering, 158 (3), pp. 103-114. Thomas Telford Ltd. https://doi.org/10.1680/maen.2005.158.3.103

Allsop, W., Bruce, T. O. M., Pullen, T. A., and Van der Meer, J., 2008. Direct hazards from wave overtopping-the forgotten aspect of coastal flood risk assessment. HR Report.

Altomare, C., Suzuki, T., Chen, X., Verwaest, T., and Kortenhaus, A., 2016. Wave overtopping of sea dikes with very shallow foreshores. Coastal Engineering, 116, 236-257. https://doi.org/10.1016/j.coastaleng.2016.07.002

Altomare, C., Laucelli, D. B., Mase, H., and Gironella, X. 2020. Determination of semi-empirical models for mean wave overtopping using an evolutionary polynomial paradigm. Journal of Marine Science and Engineering, 8(8), 570.

Altomare, C., Gironella, X., Suzuki, T., Viccione, G., and Saponieri, A., 2020. Overtopping metrics and coastal safety: A case of study from the catalan coast. Journal of Marine Science and Engineering, 8(8), 556.

Altomare, C., Gironella, X., and Crespo, A. J., 2021. Simulation of random wave overtopping by a WCSPH model. Applied Ocean Research, 116, 102888. https://doi.org/10.1016/j.apor.2021.102888

Aminti, P., and Franco, L., 1988. Wave overtopping on rubble mound breakwaters. In Coastal Engineering 1988 (pp. 770-781).

Andreas, E.L., Mahrt, L., Vickers, D., 2012. A New Drag Relation for Aerodynamically Rough Flow over the Ocean. J. Atmos. Sci., 69, 2520–2537. https://doi.org/10.1175/JAS-D-11-0312.1.

Ball, J.E., Babister, M.K., Nathan, R., Weinmann, P.E., Weeks, W., Retallick, M., andTestoni, I., 2019. Australian Rainfall and Runoff-A guide to flood estimation. Commonwealth of Australia.

Baldock, T.E., Huntley, D.A., Bird, P.A.D., O'Hare, T., Bullock, G.N., 2000. Breakpoint generated surf beat induced by bichromatic wave groups. Coast. Eng. 39, 213–242.

Baldock, T.E., 2012. Dissipation of incident forced long waves in the surf zone – implications for the concept of bound wave release at short wave breaking. Coast. Eng. 60, 276–285.

Battjes, J., 1974. Computation of set-up, longshore currents, run-up and overtopping due to wind-generated waves. PhD thesis. Delft University of Technology.

Battjes, J. A., and Groenendijk, H. W., 2000. Wave height distributions on shallow foreshores. Coastal engineering, 40(3), 161-182. https://doi.org/10.1016/S0378-3839(00)00007-7

Battjes, J.A., Bakkenes, H.J., Janssen, T.T., van Dongeren, A.R., 2004. Shoaling of subharmonic gravity waves. J. Geophys. Res. 109http://dx.doi.org/10.1029/ 2003JC001863. C02009.

Battjes, J. A., and Janssen, J. P. F. M., 1978. Energy loss and set-up due to breaking of random waves. In Coastal engineering 1978, pp. 569-587.

Bertin, X., de Bakker, A., Van Dongeren, A., Coco, G., André, G., Ardhuin, F.,.. and Tissier, M, 2018. Infragravity waves: From driving mechanisms to impacts. Earth-Science Reviews, 177, 774-799.

Besley, P., 1999. Overtopping of seawalls—design and assessment manual. In R&D Technical Report W 178. Environment Agency: UK.

Boers, M., 1996. Simulation of a surf zone with a barred beach; part 1: wave heights and wave breaking. Communication on Hydraulic and Geotechnical Engineering, Report no. 96-5. Delft University of Technology, Delft, The Netherlands.

Bretschneider, C.L., 1964. Generation of Waves by Wind: State of Art; International Summer Course: Lunteren, The Netherlands, September 1964.

Buccino, M., and Calabrese, M., 2002. Wave height distribution in the surf zone: analysis of experimental data. Coastal engineering Proceedings, 2002.

Buckley, M.L., Lowe, R.J., Hansen, J.E., van Dongeren, A.R., Pomeroy, A., Storlazzi, C.D., Rijnsdorp, D.P., da Silva, R.F., Contardo, S., Green, R.G., 2022. Wave-driven hydrodynamic processes over fringing reefs with varying slopes, depths, and roughness: Implications for coastal protection. J. Geophys. Res. Oceans, 127, https://doi.org/10.1029/2022JC018857

Bruce, T., J. Pearson, and Allsop, W, 2002. Violent overtopping of seawalls-extended prediction methods. In Breakwaters, Coastal Structures and Coastlines: Proc. Int. Conf. Organized by the Institution of Civil Engineers, edited by N. W. H. Allsop, 245–255. London: Thomas Telford.

Bruun, P., 1954. Coast erosion and the development of beach profiles (Vol. 44). US Beach Erosion Board.

Calabrese, M., and Vicinanza, D., 1999. Prediction of wave impact occurrence on vertical and composite breakwaters. Excerpta, 13, 91-123.

Calabrese, M., and M. Buccino, 2000. Wave impacts on vertical and composite breakwaters. 10th nt. Conf. ISOPE. Seattle.

Chen, Q., Kaihatu, J.M., Hwang, P.A., 2004. Incorporation of wind effects into Boussinesq wave models. J. Waterw. Port Coast. Ocean Eng., 130, 312–321. https://doi.org/10.1061/(ASCE)0733-950X(2004)130:6(312).

Chen, W., Warmink, J. J., Van Gent, M. R. A., and Hulscher, S. J. M. H., 2021. Numerical modelling of wave overtopping at dikes using OpenFOAM®. Coastal engineering, 166, 103890. https://doi.org/10.1016/j.coastaleng.2021.103890

Crest Level Assessment of coastal Structures by full scale monitoring, neural network prediction and Hazard analysis on permissible wave overtopping. Fifth Framework Programme of the EU, Contract n. EVK3-CT-2001-00058.

Dean, R. G., 1977. Equilibrium beach profiles: US Atlantic and Gulf coasts.

Dean, R.G.; Dalrymple, R.A., 2021. Coastal Processes with Engineering Applications; Cambridge University Press: New York, NY, USA, 2001.

de Waal, J. P., and Van der Meer, J. W., 1993. Wave runup and overtopping on coastal structures. In Coastal Engineering 1992 (pp. 1758-1771).

de Waal, J.P.; Tönjes, P.; van der Meer, J., 1996. Wave overtopping of vertical structures including wind effect. In Proceedings of the 25th International Conference on Coastal Engineering, ASCE, Orlando, FL, USA, 2–6 September 1996. https://doi.org/10.1061/9780784402429.172.

De Bakker, A.T.M., Tissier, M.F.S., Marieu, V., Sénéchal, N., Ruju, A., Lara, J., Ruessink, B.G., 2013. Infragravity wave propagation and dissipation on a low-sloping laboratory beach. In: Proc. 7th Int. Conf. on Coastal Dynamics, pp. 443–452.

De Bakker, A.T.M., Brinkkemper, J.A., van der Steen, F., Tissier, M.F.S., Ruessink, B.G., 2016. Cross-shore sand transport by infragravity waves as a function of beach steepness. J. Geophys. Res. Earth Surf.

den Bieman, J. P., van Gent, M. R., van den Boogaard, H. F., 2021. Wave overtopping predictions using an advanced machine learning technique. Coast. Eng., 166, 103830. https://doi.org/10.1016/j.coastaleng.2020.103830

Di Leo, A. CFD Analysis of Coastal Flood Risk: Overtopping Related Phenomena. Ph.D. Thesis, 2021

Di Leo, A., Buccino, M., Dentale, F., Pugliese Carratelli, E., 2022. CFD Analysis of Wind Effect on Wave Overtopping. In Proceed-ings of the 32nd International Ocean and Polar Engineering Conference, June 2022.

Draper, N.,R., Smith, N., 1998. Applied Regression Analysis, pp. 1-716. http://onlinelibrary.wiley.com/book/10.1002/9781118625590

Durbridge, S., 2021.The effect of onshore wind on wave overtopping of a vertical sea wall. Plymouth Stud. Sci., 14, 311–355.

Etemad-Shahidi, A., Koosheh, A., and van Gent, M. R., 2022. On the mean overtopping rate of rubble mound structures. Coast. Eng. 177, 104150.

EurOtop Wave Overtopping of Sea Defenses and Related Structures—Assessment Manual. 181 pp. 2007

EurOtop, 2018. Manual on wave overtopping of sea defences and related structures. An overtopping manual largely based on European research, but for worldwide application. Van der Meer, J.W., Allsop, N.W.H., Bruce, T., De Rouck, J., Kortenhaus, A., Pullen, T., Schüttrumpf.

Fiedler, J.W., Brodie, K.L., McNinch, J.E., Guza, R.T., 2015. Observations of runup and energy flux on a low-slope beach with high-energy, long-period ocean swell. Geophys. Res. Lett. 42. http://dx.doi.org/10.1002/2015GL066124.

Franco, L., De Gerloni, M., and Van der Meer, J. W., 1994. Wave overtopping on vertical and composite breakwaters. In Coastal Engineering 1994 (pp. 1030-1045).

Franco, C., and Franco, L., 1999. Overtopping formulas for caisson breakwaters with nonbreaking 3D waves. J. Waterw. Port Coast. Ocean Eng., 125(2), 98-108.

Formentin, S.M., and Zanuttigh, B., 2019. Semi-automatic detection of the overtopping waves and reconstruction of the overtopping flow characteristics at coastalstructures. Coast. Eng 152, 103533. https://doi.org/10.1016/j.coastaleng.2019.103533.

Goda, Y., Kishara, Y., Kamiyama, Y., 1795. Laboratory investigation on the overtopping rate of seawalls by irregular waves. Report of the Port and Harbour Research Institute..

Goda, Y., 2000. Random Seas and Design of Maritime Structures, 2nd Edition. World Scientific, Singapore. 443pp.

Goda, Y. 2009. "Derivation of unified wave overtopping formulas for seawalls with smooth, impermeable surfaces based on selected CLASH datasets." Coastal Eng. 56 (4): 385–399. https://doi.org/10.1016/j.coastaleng.2008.09.007.

Griggs, G. B., 2009. The effects of armoring shorelines—the California experience. In Puget Sound Shorelines and the Impacts of Armoring—Proceedings of a State of the Science Workshop (pp. 77-84).

Gruwez, V., Altomare, C., Suzuki, T., Streicher, M., Cappietti, L., Kortenhaus, A., Troch, P., 2020. An inter-model comparison for wave interactions with sea dikes on shallow foreshores. J. mar. sci. eng., 8(12), 985. https://doi.org/10.3390/jmse8120985

Guza, R.T., Thornton, E.B., 1982. Swash oscillations on a natural beach. J. Geophys. Res. 87, 483–491.

Hansen, W., 1956. Theorie zur Errechnung des Wasserstandes und der Strömingen in Randmeeren nebst Anwendungen. Tellus 8, 289–300.

Harlow Francis H. and Nakayama Paul I.,1967. Turbulence Transport Equations. The Physics of Fluids 10, 2323.7.

Hasselmann, K., 1962. On the non-linear energy transfer in a gravity-wave spectrum Part 1. General theory. J. Fluid Mech. 12, 481–500.

Hedges, T. S., and Reis, M. T., 1998. Random wave overtopping of simple sea walls: A new regression model. Proc. Inst. Civ. Eng., Water Maritime Energ., 130(1), 1–10.

Henderson, C. S., Fiedler, J. W., Merrifield, M. A., Guza, R. T., Young, A. P., 2022. Phase resolving runup and overtopping field validation of SWASH. Coast. Eng,, 175, 104128. https://doi.org/10.1016/j.coastaleng.2022.104128

Herbert, D. 1993. Wave overtopping of vertical walls. Wallingford, UK:HR Wallingford.

Hirt C.W. and Nichols B.D., 1981. Volume of fluid (VOF) method for the dynamics of free boundaries, Journal Comp. Physics, Vol.39, pp. 201-225.

Hirt C. W. and Sicilian J. M.,1985. A porosity technique for the definition of obstacles in rectangular cell meshes.

Hieu, P.D., Vinh, P.N., Toan, D.V., Son, N.T., 2014. Study of Wave-wind Interaction at a Seawall Using a Numerical Wave Channel. Appl. Math. Model., 38, 5149–5159. https://doi.org/10.1016/j.apm.2014.04.038.

Hofland, B., Chen, X., Altomare, C., and Oosterlo, P., 2017. Prediction formula for the spectral wave period Tm-1, 0 on mildly sloping shallow foreshores. Coast. Eng., 123, 21-28. https://doi.org/10.1016/j.coastaleng.2017.02.005

HR Wallingford, 2005. Dynamic Wave Absorption System. Report available at: https://www.hrwallingford.com/sites/default/files/2020-06/eq-011_multielement_wavemaker-r6.pdf

Hughes, S. A., 2004. Estimation of wave run-up on smooth, impermeable slopes using the wave momentum flux parameter. Coast. Eng., 51(11-12), 1085-1104. https://doi.org/10.1016/j.coastaleng.2004.07.026

Hughes, S. A., Thornton, C. I., Van der Meer, J. W., and Scholl, B., 2012. Improvements in Describing Wave Overtopping Processes. In Proceedings of the 33rd International Conference on Coastal Engineering, pages 1–15, Santander, Spain.

Ibrahim, M. S., Baldock, T. E., 2020. Swash overtopping on plane beaches–Reconciling empirical and theoretical scaling laws using the volume flux. Coast. Eng., 157, 103668.

Inagaki, N., Shibayama, T., Ishibashi, K., Nakamura, R., Esteban, M., 2023. Experimental investigations into the effect of strong winds on wave overtopping at a vertical seawall. Coastal Engineering Proceedings, 26-26, December 2022.

Inagaki, N., Shibayama, T., Nakamura, R., Ishibashi, K., Esteban, M., 2024. Experimental investigation into the effects of strong winds on the transport of overtopping water mass over a vertical seawall. Coastal Engineering Journal, 1-15.

Inch, K., Davidson, M., Masselink, G., Russell, P., 2017b. Observations of nearshore infragravity wave dynamics under high energy swell and wind-wave conditions. Cont. Shelf Res. 138, 19–31. http://dx.doi.org/10.1016/j.csr.2017.02.010.

Janssen, T.T., Battjes, J.A., and van Dongeren, A.R., 2003. Long waves induced by short-wave groups over a sloping bottom. J. Geophys. Res. 108, 3252. http://dx.doi.org/10. 1029/2002JC001515.

Kamphuis, J. W., 1991. Incipient wave breaking. Coast. Eng., 15(3), 185-203. https://doi.org/10.1016/0378-3839(91)90002-X

Kamphuis, J.W., 1996. Experiments on Design Wave Height in Shallow Water. Proceedings of the International Conference on Coastal Engineering.

Kiku, M. and Kawasaki, K., 2014. Proposal of numerical wave flume for wave overtopping computation considering wind external force. In Proceedings of 34th Conference on Coastal Engineering, June 2014.

Koosheh, A., Etemad-Shahidi, A., Cartwright, N., Tomlinson, R., and van Gent, M. R., 2021. Individual wave overtopping at coastal structures: A critical review and the existing challenges. Applied Ocean Research, 106, 102476.

Kraus, N. C., McDougal, W. G., 1996. The effects of seawalls on the beach: Part I, an updated literature review. J. Coast. Res., 691-701.

Lashley, C. H., Zanuttigh, B., Bricker, J. D., Van der Meer, J., Altomare, C., Suzuki, T., Roeber, V. Oosterlo, P., 2020. Benchmarking of numerical models for wave overtopping at dikes with shallow mildly sloping foreshores: Accuracy versus speed. Environ. Model. Softw., 130, 104740. https://doi.org/10.1016/j.envsoft.2020.104740

Lashley, C. H. van der Meer, J.W., Bricker, J.D., Altomare, Suzuki, Hirayama, K., 2021. Formulating Wave Overtopping at Vertical and Sloping Structures with Shallow Foreshores Using Deep-Water Wave Characteristics. J. Waterw. Port Coast. Ocean Eng., Volume 147, Issue 6. https://doi.org/10.1061/(ASCE)WW.1943-5460.0000675

Lashley, C. H., Brown, J. M., Yelland, M. J., Van der Meer, J. W., Pullen, T., 2023. Comparison of deep-water-parameter-based wave overtopping with wirewall field measurements and social media reports at Crosby (UK). Coast. Eng., 179, 104241. https://doi.org/10.1016/j.coastaleng.2022.104241

Lam, D.C.L., Simpson, R.B., 1976. Centered differencing and the box scheme for diffusion convection problems. Journal of Computational Physics 220 (4), 486–500.

Le Mehaute, B, 1962. On non-saturated breakers and the wave run-up. Coastal Engineering Proceedings, (8), 6-6.

Lin, P., Liu, P. L. F. 1999. Internal wave-maker for Navier-Stokes equations models. J. Waterw. Port, Coast. Ocean Eng., 125(4), 207-215. https://doi.org/10.1061/(ASCE)0733-950X(1999)125:4(207)

Longuet-Higgins, M.S., Stewart, R.W., 1962. Radiation stress and mass transport in gravity waves, with application to 'surf beats'. J. Fluid Mech., 13, 481–504. https://doi.org/10.1017/S0022112062000877.

Lopez, L. F. C., Salerno, D., Dentale, F., Capobianco, A., Buccino, M., 2015. Experimental campaign on the overtopping of the seawall Malecòn Tradicional. In The Twenty-fifth International Ocean and Polar Engineering Conference, 2015, OnePetro.

Lopez, L. F. C., Salerno, D., Dentale, F., Capobianco, A., Buccino, M., 2016. Wave overtopping at Malecòn Tradicional, la Habana, Cuba. Coastal Engineering Proceedings 2016, (35), 24-24.

Lykke-Andersen, T., Burcharth, H.F., Gironella, F.X., 2009. Single wave overtopping volumes and their travel distance for rubble mound breakwaters. In: Proc. 5th International Conference Coastal Structures 2007. World Scientific, pp. 1241–1252.https://doi.org/10.1142/9789814282024_0109.

Liu, X., Liu, Y., Lin, P., and Li, A. J., 2021. Numerical simulation of wave overtopping above perforated caisson breakwaters. Coast. Eng., 163, 103795. https://doi.org/10.1016/j.coastaleng.2020.103795

Losada, I.J., Lara, J.L., Guanche, R., Gonzalez-Ondina, J.M., 2008. Numerical analysis of wave overtopping of rubble mound breakwaters. Coast. Eng. 55, 47–62 https://doi.org/10.1016/j.coastaleng.2007.06.003.

Lynett, PJ, Melby, JA, Kim, D-H. 2010. An application of Boussinesq modeling to Hurricane wave overtopping and inundation. Ocean Eng, 37, 135–153. https://doi.org/10.1016/j.oceaneng.2009.08.021

Mahmoudof, S. M., Eyhavand-Koohzadi, A., and Kazeminezhad, M. H., 2023. Field investigation of spectral wave period Tm-1, 0 on shallow and very shallow foreshores of the southern Caspian sea. Coastal Engineering, 181, 104277. https://doi.org/10.1016/j.coastaleng.2023.104277

Masselink, G., 1995. Group bound long waves as a source of infragravity energy in the surf zone. Cont. Shelf Res. 15, 1525–1547. http://dx.doi.org/10.1016/0278-4343(95)00037-2.

Mares-Nasarre, P., Argente, G., Gómez-Martín, M. E., Medina, J. R., 2019. Overtopping layer thickness and overtopping flow velocity on mound breakwaters. Coast. Eng., 154, 103561. https://doi.org/10.1016/j.coastaleng.2019.103561

Mase, H., T. Tamada, T. Yasuda, T. S. Hedges, and M. T. Reis., 2013. Wave runup and overtopping at seawalls built on land and in very shallow water. J. Waterw. Port Coastal Ocean Eng. 139 (5): 346–357. https://doi.org/10.1061/(ASCE)WW.1943-5460.0000199.

Masselink, G., 1995. Group bound long waves as a source of infragravity energy in the surf zone. Cont. Shelf Res. 15, 1525–1547. http://dx.doi.org/10.1016/0278-4343(95)00037-2.

Mahmoudof, S. M., Eyhavand-Koohzadi, A., and Kazeminezhad, M. H., 2023. Field investigation of spectral wave period Tm-1, 0 on shallow and very shallow foreshores of the southern Caspian sea. Coast. Eng., 181, 104277.

Mokos, A., Carmigniani, R., Leroy, A., and Violeau, D., 2020. Simulating wave overtopping on a complex coastal structure using SPH. Journal of Applied Water Engineering and Research, 8(1), 55-65. https://doi.org/10.1080/23249676.2020.171922

Munk, W., 1949. Surf beat. Eos Trans. AGU 30, 849–854.

Murakami, K., Maki, D., Ogino, K., 2020. Effect of Wind Velocity on Wave Overtopping. In Proceedings of the 10th International Conference on Asian and Pacific Coasts (APAC 2019), September 2019.

Nguyen, T. H., Hofland, B., Dan Chinh, V., Stive, M., 2020. Wave overtopping discharge for very gently sloping foreshores. Water, 12(6), 1695. https://doi.org/10.3390/w12061695

Ni, X. Y., and Feng, W. B., 2013. Numerical simulation of wave overtopping based on DualSPHysics. Applied Mechanics and Materials, 405, 1463-1471. https://doi.org/10.4028/www.scientific.net/AMM.405-408.1463

Nordstrom, K. F., 2014. Living with shore protection structures: a review. Estuarine, coastal and shelf science, 150, 11-23.

Nørgaard, J. Q. H., Andersen, T. L., Burcharth, H. F., Steendam, G. J., 2013. Analysis of overtopping flow on sea dikes in oblique and short-crested waves. Coast. Eng., 76, 43-54. https://doi.org/10.1016/j.coastaleng.2013.01.012

Nørgaard, J. Q. H., Andersen, T. L., and Burcharth, H. F., 2014. Distribution of individual wave overtopping volumes in shallow water wave conditions. Coast. Eng. , 83, 15-23.

Owen, M. W. 1980. Design of Seawalls Allowing for Wave Overtopping. Report No. Ex 924, Hydraulics Research Station, Wallingford, England.

Perlin, M., Wooyoung, C., Zhigang, T., 2013. Breaking Waves in Deep and Intermediate Waters. Annu. Rev. Fluid Mech., 45, 115–145.

Pedersen, J., and Burcharth, H. F., 1993. Wave forces on crown walls. In Coastal Engineering 1992, pp. 1489-1502.

Pillai, K., Etemad-Shahidi, A., and Lemckert, C., 2019. Wave run-up on bermed coastal structures. Appl. Ocean Res., 86, 188-194. https://doi.org/10.1016/j.apor.2019.02.006

Pomeroy, A., Lowe, R., Symonds, G., Van Dongeren, A., and Moore, C., 2012. The dynamics of infragravity wave transformation over a fringing reef. J. Geophys. Res. 117. http://dx.doi.org/10.1029/2012JC008310.

Pullen, T., Allsop, W., Bruce, T., and Pearson, J., 2009 Field and laboratory measurements of mean overtopping discharges and spatial distributions at vertical seawalls. Coast. Eng., 56, 121–140. https://doi.org/10.1016/j.coastaleng.2008.03.011.

Resio, D.T., 1987. Assesment of Wind Effects on Wave Overtopping of Proposed Virginia Beach Seawall. Technical memorandum to CERC.

Rijnsdorp, D. P., Smit, P. B.,and Zijlema, M., 2014. Non-hydrostatic modelling of infragravity waves under laboratory conditions. Coast. Eng., 85, 30-42. https://doi.org/10.1016/j.coastaleng.2013.11.011

Romano, A., Bellotti, G., Briganti, R., and Franco, L., 2015. Uncertainties in the physical modelling of the wave overtopping over a rubble mound breakwater: the role of the seeding number and of the test duration. Coast. Eng. 103, 15–21. https://doi.org/10.1016/j.coastaleng.2015.05.005

Salauddin, M., O'Sullivan, J. J., Abolfathi, S., Peng, Z., Dong, S., and Pearson, J. M., 2022. New insights in the probability distributions of wave-by-wave overtopping volumes at vertical breakwaters. Scientific Reports, 12(1), 16228.

Sandoval, C, Bruce, T., 2017. Wave overtopping hazard to pedestrians: video evidence from real accidents. In: Coasts, Marine Structures and Breakwaters 2017. ICE Publishing, pp. 501–512 https://doi.org/10.1680/cmsb.63174.0501.

Saville, T., Jr. 1955. "Laboratory Data on Wave Runup and Overtopping on Shore Structures," TM-64, US Army Corps of Engineers, Beach Erosion Board.

Schäffer, H.A., 1993. Infragravity waves induced by short wave groups. J. Fluid Mech. 247, 551–588.

Schäffer, H.A., Jakobsen, K., 2003. Non-linear wave generation and active absorption in wave flumes. In: Long Waves Symposium. Thessaloniki, Greece.

Schäffer, H. A. and Svendsen, I. A.. 1988 Surf beat generation on a mild slope beach. Proc. 21st Intl Conf. Coastal Engng, Malaga, Spain, 1988, vol. 2, pp. 1058– 1072.

Schoonees, T., Gijón Mancheño, A., Scheres, B., Bouma, T. J., Silva, R., Schlurmann, T., and Schüttrumpf, H., 2019. Hard structures for coastal protection, towards greener designs. Estuaries and Coasts, 42, 1709-1729.

Schüttrumpf, H., and Van Gent, M. R., 2003. Wave overtopping at seadikes. In Coastal Structures 2003 (pp. 431-443).

Shao, S., 2006. Incompressible SPH simulation of wave breaking and overtopping with turbulence modelling 597–621. https://doi.org/10.1002/fld.1068

Smit, P., Zijlema, M., and Stelling, G., 2013. Depth-induced wave breaking in a non-hydrostatic, near-shore wave model. Coast. Eng., 76, 1-16. https://doi.org/10.1016/j.coastaleng.2013.01.008

Smit, P., Janssen, T., Holthuijsen, L., and Smith, J., 2014. Non-hydrostatic modeling of surf zone wave dynamics. Coast. Eng., 83, 36-48. https://doi.org/10.1016/j.coastaleng.2013.09.005

Smith, G.P., Modra, B.D., and Felder, S., 2019. Full-scale testing of stability curves for vehicles in flood waters. J. Flood Risk Manag 12, e12527

Suzuki, T., Verwaest, T., Hassan, W., Veale, W., Reyns, J., Trouw, K., Troch, P., and Zijlema, M., 2011. The applicability of SWASH model for wave transformation and wave overtopping: A case study for the Flemish coast. In Proc. 5th Int. Conf. Advanced Computational Methods Engineering, Liège, Belgium, 14-17 November 2011.

Suzuki, T., Altomare, C., Verwaest, T., Trouw, K., and Zijlema, M., 2014. Two-dimensional wave overtopping calculation over a dike in shallow foreshore by SWASH. In ICCE 2014: Proceedings of 34th International Conference on Coastal Engineering, Seoul, Korea, 15-20 June 2014. Coastal Engineering Research Council.

Suzuki, T., Altomare, C., Veale, W., Verwaest, T., Trouw, K., Troch, P., and Zijlema, M. 2017. Efficient and robust wave overtopping estimation for impermeable coastal structures in shallow foreshores using SWASH. Coast. Eng., 122, 108-123. https://doi.org/10.1016/j.coastaleng.2017.01.009.

Suzuki, T., Altomare, C., Willems, M., Dan, S., 2023. Non-Hydrostatic Modelling of Coastal Flooding in Port Environments. J. mar. sci. eng., 11(3), 575. https://doi.org/10.3390/jmse11030575

Stagnitti, M., Lara, J. L., Musumeci, R. E., & Foti, E., 2023. Numerical modeling of wave overtopping of damaged and upgraded rubble-mound breakwaters. Ocean Engineering, 280, 114798. https://doi.org/10.1016/j.oceaneng.2023.114798

Symonds, G., Huntley, D. A., and Bowen, A. J. 1982. Two-dimensional surf beat: Long wave generation by a time-varying breakpoint. J. Geophys. Res. Oceans, 87(C1), 492-498. https://doi.org/10.1029/JC087iC01p00492

Tamada, T., M. Inoue, and T. Tezuka. 2002. "Experimental studies on diagrams for the estimation of wave overtopping rate on gentle slope-type seawalls and these reduction effects on wave overtopping." [In Japanese.] Proc.Coastal Eng. JSCE 49: 641–645. https://doi.org/10.2208/proce1989.49.641

Tamada, T., Mase, H., and Yasuda, T., 2015. Wave runup and overtopping integrated model for vertical seawall based on CLASH datasets. Proc. SCACR2015, Int. Short Course/Conf. on applied Coast. Res. 361–370.

Tayfun, M.A., Lo, J.M., 1989. Envelope, Phase, and Narrow-Band Models of Sea Waves. J. Waterw. Port Coast. Ocean Eng., 115, 5. https://doi.org/10.1061/(ASCE)0733-950X(1989)115:5(594)

Tissier, M., Bonneton, P., and Ruessink, B., 2017. Infragravity waves and bore merging. In: Proceedings of the Conference Coastal Dynamics 2017. ASCE, Helsingør, Denmark, pp. 451–460.

Tonelli, M., and Petti, M., 2013. Numerical simulation of wave overtopping at coastal dikes and low-crested structures by means of a shock-capturing Boussinesq model, Coast.Eng., 79, 75–88. https://doi.org/10.1016/j.coastaleng.2013.04.007

Tuozzo, S., Ciccaglione, M. C., Buccino, M., Ascione, G., and Calabrese, M., 2022. Wave overtopping at a vertical seawall by Boussinesq modeling. In ISOPE International Ocean and Polar Engineering Conference (pp. ISOPE-I). ISOPE.

Tucker, M., 1950. Surfbeats: sea waves of 1 to 5 minutes period. In: Proc. R.Soc. London A 202-565-573.

Van der Meer, J. and Janssen, J. P., 1994. Wave run-up and wave overtopping at dikes and revetments. Delft Hydraulics.

Van der Meer, J. W., 2002. Technical report wave run-up and wave overtopping at dikes. TAW report.

Van der Meer, J., and Bruce, T., 2014. New physical insights and design formulas on wave overtopping at sloping and vertical structures. Journal of Waterway, Port, Coastal, and Ocean Engineering, 140(6), 04014025. https://doi.org/10.1061/(ASCE)WW.1943-5460.0000221

Van der Meer, J., Steendam, G. J., Bruce, T., and Breteler, M. K., 2022. Admissible post-wave overtopping flow for persons on a horizontal surface. Journal of Coastal and Hydraulic Structures, 2.

Van Dongeren, A., Battjes, J., Janssen, T., van Noorloos, J., Steenhauer, K., Steenbergen, G., and Reniers, A., 2007. Shoaling and shoreline dissipation of low-frequency waves. J. Geophys. Res. 112http://dx.doi.org/10.1029/2006JC003701. C02011.

Van Gent, M. R. A., 1999a. Wave run-up and wave overtopping for double peaked wave energy spectra. H3351.

Van Gent, M. R. A., 1999b. Physical model investigations on coastal structures with shallow foreshores. Delft Hydraulics (Deltares) Report H3608.

Van Gent, M. R. A., 2001. Wave runup on dikes with shallow foreshores. Journal of waterway, port, coastal, and ocean engineering, 127(5), 254-262.

Van Gent, M. R. A., and Giarrusso, C. C., 2003. Influence of low frequency waves on wave overtopping. CLASH Report and Delft Hydraulics Rep. H4297.

Van Gent, M. R. A., van den Boogaard, H. F., Pozueta, B., and Medina, J. R., 2007. Neural network modelling of wave overtopping at coastal structures. Coast. Eng., 54(8), 586-593. https://doi.org/10.1016/j.coastaleng.2006.12.00

Verhaeghe, H., De Rouck, J., and van der Meer, J., 2008. Combined classifier–quantifier model: a 2-phases neural model for prediction of wave overtopping at coastal structures. Coast. Eng., 55(5), 357-374.

Victor, L., Van der Meer, J.W., and Troch, P., 2012. Probability distribution of individual wave overtopping volumes for smooth impermeable steep slopes with low crest freeboards. Coast. Eng., 64:87–101.

Xie, Z., 2014. Numerical modelling of wind effects on breaking solitary waves. Eur. J. Mech. B-Fluid, 43, 135–147. https://doi.org/10.1016/j.euromechflu.2013.08.001.

Yakhot V. and Smith L. M., 1992. The renormalization group, the ε-expansion and derivation of turbulence models. J. Sci. Comput. 7, 35.

Yuhi, M.,H.Mase, S. Kim, S. Umeda, and C.Altomare. 2021. "Refinement of integrated formula of wave overtopping and runup modeling." Ocean Eng. 220: 108350. https://doi.org/10.1016/j.oceaneng.2020.108350.

Ward, DL., Zhang, J., Wibner, C.G., and Cinotto, C.M., 1996 Wind effects on runup and overtopping. In Proceedings of the 25th International Conference on Coastal Engineering, September 1996.

Weggel, J. R., 1976. Wave Overtopping Equation, Proceedings of the 15th J. Coastal Engineering Conference, Honolulu, pp 2737-2755.

Wilcox, D. C., Turbulence Modeling for CFD, 2nd edition, DCW Industries, Inc., La Canada CA, 1998.

Wolters, G.; and van Gent, M.R.A., 2007. Maximum wind effect on wave overtopping of sloped coastal structures with crest elements. In Proceedings of 5th International Coastal Structures, July 2007; pp. 1263–1274.

Zanuttigh, B., van der Meer, J., Bruce, T., and Hughes, S., 2013. Statistical characterisation of extreme overtopping wave volumes. Sea to Shore–Meeting the Challenges of the Sea: (Coasts, Marine Structures and Breakwaters 2013) (pp. 442-451). ICE Publishing.

Zanuttigh, B., Formentin, S., and Van der Meer, J.W., 2016. Prediction of extreme and tolerable wave overtopping discharges through an advanced neural network. Ocean Eng. 127, 722. https://doi.org/10.1016/j.oceaneng.2016.09.032

Zelt, J. A., Skjelbreia, J. E., 1992. Estimating incident and reflected wave fields using an arbitrary number of wave gauges. Coast. Eng., pp. 777-789. https://doi.org/10.1061/9780872629332.058

Zijlema, M., and G.S. Stelling, G., 2008. Efficient computation of surf zone waves using the nonlinear shallow water equations with non-hydrostatic pressure. Coast. Eng., 55, 780–790. http://dx.doi.org/10.1016/j.coastaleng.2008.02.020.

Zijlema, M., Stelling, G., and Smit, P., 2011. SWASH: An operational public domain code for simulating wave fields and rapidly varied flows in coastal waters. Coast. Eng., 58(10), 992-1012. https://doi.org/10.1016/j.coastaleng.2011.05.015

Zhang, N., Zhang, Q., Zou, G., Jiang, X., 2016. Estimation of the transmission coefficients of wave height and period after smooth submerged breakwater using a non-hydrostatic wave model. Ocean Eng., 122, 202-214. https://doi.org/10.1016/j.oceaneng.2016.06.037

Zhang, N., Zhang, Q., Wang, K. H., Zou, G., Jiang, X., Yang, A., and Li, Y., 2020. Numerical simulation of wave overtopping on breakwater with an armor layer of accropode using SWASH model. Water, 12(2), 386. https://doi.org/10.3390/w12020386